Dissecting Dopaminergic Neuron Specification at Single Cell Resolution - Insights from 3D brain organoids and xenograft models

Sozzi, Edoardo

2025

Document Version:
Publisher's PDF, also known as Version of record

Dissecting Dopaminergic Neuron Specification at Single Cell Resolution

Insights from 3D brain organoids and xenograft models

EDOARDO SOZZI
DEPARTMENT OF EXPERIMENTAL MEDICAL SCIENCE | FACULTY OF MEDICINE | LUND UNIVERSITY

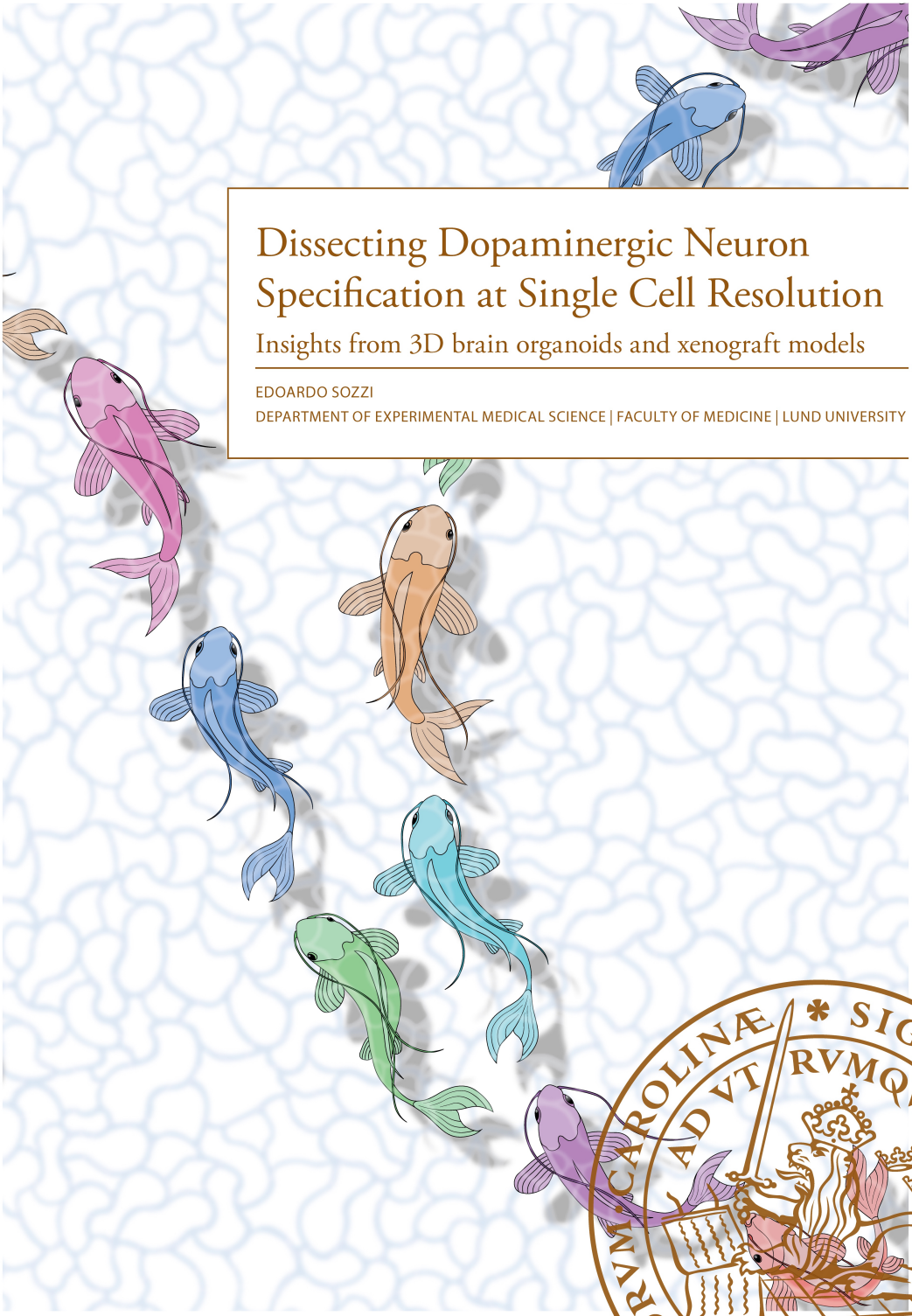

Dissecting Dopaminergic Neuron Specification at Single Cell Resolution

Insights from 3D brain organoids and xenograft models

Edoardo Sozzi

LUND UNIVERSITY

DOCTORAL DISSERTATION

Doctoral dissertation for the degree of Doctor of Philosophy (PhD)
at the Faculty of Medicine at Lund University
to be publicly defended on 7th of February 2025
at 09.00 in Segerfalksalen, Sölvegatan 17, 223 62, Lund, Sweden

Faculty opponent:

Professor Gonçalo Castelo-Branco
Department of Medical Biochemistry and Biophysics,
Karolinska Institutet, Stockholm

Organization
LUND UNIVERSITY
Developmental and Regenerative Neurobiology, Department of Experimental Medical Science, Faculty of Medicine, Sweden

Document name
DOCTORAL DISSERTATION

Date of issue
2025-02-07

Sponsoring organization

Author(s)
Edoardo Sozzi

Title and subtitle: Dissecting Dopaminergic Neuron Specification at Single Cell Resolution
- Insights from 3D brain organoids and xenograft models

Abstract Midbrain dopaminergic neurons exhibit a wide diversity in their projection patterns, disease vulnerability, and functions, playing key roles in voluntary motor control, cognition, and reward processing. Parkinson's Disease, one of the most common neurodegenerative disorders, is characterized by the selective degeneration of the A9 dopaminergic neuron subtype, leading to severe motor dysfunction. Despite advancements in symptomatic treatments, current approaches fail to halt disease progression, highlighting the need for novel therapeutic strategies such as cell replacement therapy. Generating authentic human dopaminergic neurons for transplantation and therapeutic purposes relies on a comprehensive understanding of the factors driving their development. However, the molecular mechanisms underlying the specification of midbrain dopaminergic neurons into distinct subtypes remain poorly understood. Due to the inaccessibility of developing and adult human brain tissue, novel methodologies are needed for investigating these processes in a human-relevant context.

This thesis investigates the development, diversity, and specification of human dopaminergic neurons using advanced human stem cell models, with a particular focus on their application in cell replacement therapies for Parkinson's Disease. In the first part, I established ventral midbrain-patterned organoids that recapitulate developmental trajectories and the molecular identities of distinct dopaminergic neuron subtypes. To overcome limitations in conventional organoid technology, silk scaffolding was also introduced, enhancing cell viability and neuronal maturation. In the second part, I linked the molecular identities of human dopaminergic neurons to their projection patterns using homotopic transplantation models. Finally, co-grafting experiments examined the influence of support cell types on dopaminergic neuron maturation and lineage commitment, identifying critical factors shaping subtype identity. These findings advance our understanding of human dopaminergic neuron development and subtype specification, offering valuable insights for refining cell replacement therapies for Parkinson's Disease.

Key words: Dopaminergic neurons, human brain organoids, single cell RNA sequencing, cell replacement therapy for Parkinson´s Disease, human pluripotent stem cells.

Classification system and/or index termes (if any):

Supplementary bibliographical information:

Language
English

ISSN and key title:
1652-8220

ISBN
978-91-8021-665-4

Recipient's notes

Number of pages
231

Price

Security classification

Signature  Date 2025-01-10

Dissecting Dopaminergic Neuron Specification at Single Cell Resolution

Insights from 3D brain organoids and xenograft models

Edoardo Sozzi

2025

Developmental and Regenerative Neurobiology
Department of Experimental Medical Science
Faculty of Medicine, Sweden

LUND
UNIVERSITY

Cover art by Edoardo Sozzi, illustrating the differentiation and specification of human midbrain dopaminergic neurons into the A9 and A10 subtypes. Each koi fish represents a single cell, its color reflecting the uniqueness revealed by single-cell RNA sequencing. Just like koi fish navigate shifting currents, these neurons follow dynamic developmental trajectories as they mature and differentiate into their final identities.

ISSN 1652-8220
ISBN 978-91-8021-665-4
Lund University, Faculty of Medicine, Doctoral Dissertation Series 2025:12

Printed by Exakta printing AB, Malmö, Sweden
Lund 2025

Tè e manga contro caffè e giornale:
l'eleganza e l'incanto
contro la triste aggressività
dei giochi di potere degli adulti.

- Muriel Barbery, L´eleganza del riccio

TABLE OF CONTENTS

ORIGINAL PAPERS AND MANUSCRIPTS INCLUDED IN THE THESIS 9
ORIGINAL PAPERS NOT INCLUDED IN THE THESIS 11
RESEARCH REVIEW ARTICLES NOT INCLUDED IN THE THESIS 13
ABSTRACT 15
LAY SUMMARY 17
POPULÄRVETENSKAPLIG SAMMANFATTNING 19
RIASSUNTO IN ITALIANO 21
ABBREVIATIONS 23
INTRODUCTION 25
- Parkinson´s Disease 25
- Cell replacement therapy for Parkinson´s Disease 26
  - **The rationale** 26
  - **Fetal cell transplantation – paving the way** 26
  - **Stem cell-based therapies for Parkinson´s Disease** 27
- Development of midbrain dopaminergic neurons 28
  - **Early midbrain specification** 28
  - **Dopaminergic neuron differentiation** 29
- Diversity of midbrain dopaminergic neurons 30
- Stem cell models of human dopaminergic neuron development 32
- Bridging the gap between *in vitro* and *in vivo* studies: the rise of human brain organoids 33
- Emerging frontiers in brain organoid technology 34
  - **Bioengineered brain organoids** 34
  - **Integrated organoid systems** 35
  - **Multi-region brain organoids** 35

AIMS OF THE THESIS 37
SUMMARY OF RESULTS AND DISCUSSION 39
- Brain organoid cultures mimic key features of human vMB development (Paper I and II) 40
- Advancing brain organoid technology with recombinant silk microfibers (Paper I and III) 47
- Defining molecular profile of human DA neuron subtypes by their target specificity (Paper IV) 56
- Extrinsic modulation of DA neuron maturation and specification in co-grafts (Paper V) 60

Modelling vMB-STR neuron long range interactions in a multi-organoid system (ongoing study) 67
CONCLUSIONS AND FUTURE PERSPECTIVES 73
SUMMARY OF KEY METHODS 77
Human pluripotent stem cell culture 77
Monolayer differentiation of human pluripotent stem cells 77
Surgical procedures and cell transplantation 78
Human brain organoid culture 78
Ventral midbrain organoid differentiation 79
Forebrain organoid differentiation 80
Striatal organoid differentiation 80
Generation of bioengineered silk organoids 81
Connectoid formation 81
RNA extraction and qRT-PCR 82
Isolation of xenografts from the host rat brain and nuclei extraction 82
Organoid cryosectioning and immunofluorescence 85
Histology and immunohistochemistry 86
Image acquisition and quantifications 87
Cell viability analysis 87
Bioinformatic analysis of bulk sequencing data 88
Single cell RNA sequencing sample preparation 88
Library preparation, sequencing, and raw data processing 88
Bioinformatic analysis of single cell/nuclei sequencing data 89
Barcode library analysis and lineage tracing 89
Data availability 90
ACKNOWLEDGEMENTS 91
REFERENCES 95
APPENDIX 115
Paper I 115
Paper II 145
Paper III 165
Paper IV 189
Paper V 205

ORIGINAL PAPERS AND MANUSCRIPTS INCLUDED IN THE THESIS

Paper I

Fiorenzano, A., **Sozzi, E.,** Birtele, M., Kajtez, J., Giacomoni, J., Nilsson, F., Bruzelius, A., Sharma, Y., Zhang, Y., Mattsson, B., Emnéus J., Ottosson, DR., Storm, P., Parmar, M. (2021).

Single-cell transcriptomics captures features of human midbrain development and dopamine neuron diversity in brain organoids.

Nature Communications

Paper II

Sozzi, E., Nilsson, F., Kajtez, J., Parmar, M., Fiorenzano, A. (2022).

Generation of human ventral midbrain organoids derived from pluripotent stem cells.

Current Protocols

Paper III

Sozzi, E., Kajtez, J., Bruzelius, A., Wesseler, MF., Nilsson, F., Birtele, M., Larsen, NB., Ottosson, DR., Storm, P., Parmar, M., Fiorenzano, A. (2022).

Silk scaffolding drives self-assembly of functional and mature human brain organoids.

Frontiers in Cell and Developmental Biology

Paper IV

Fiorenzano, A.*, Storm, P.*, **Sozzi, E.,** Bruzelius, A., Corsi, S., Kajtez, J., Mudannayake, J., Nelander, J., Mattsson, B., Åkerblom, M., Björklund, T., Björklund, A., Parmar, M. (2024).

TARGET-seq: Linking single cell transcriptomics of human dopaminergic neurons with their target specificity.

Proceedings of the National Academy of Sciences

Paper V

Sozzi, E., Mudannayake, J., Garcia Garrote, M., Ramos Passarello, G., Bruzelius, A., Corsi, S., Galeotti, G., Habekost, M., Scaramuzza, L., Besusso, D., Björklund, A., Cattaneo, E., Fiorenzano, A., Storm, P., Parmar, M.

Extrinsic modulation of co-grafted neural progenitors enhances dopamine neuron specification and functional maturation.

Manuscript

ORIGINAL PAPERS NOT INCLUDED IN THE THESIS

Reumann, D., Krauditsch, C., Novatchkova, M., **Sozzi, E.,** Wong, SN., Zabolocki, M., Priouret, M., Doleschall, B., Ritzau-Reid, KI., Piber, M., Morassut, I., Fieseler, C., Fiorenzano, A., Stevens, MM., Zimmer, M., Bardy, C., Parmar, M., Knoblich, JA. (2023).

In vitro modeling of the human dopaminergic system using spatially arranged ventral midbrain – striatum – cortex assembloids.

Nature Methods

Rezaei, B., Giacomoni, J., Nilsson, F., **Sozzi, E.,** Fiorenzano, A., Parmar, M., Keller, SS., Kajtez, J. (2023).

Modular 3D printed platform for fluidically connected human brain organoid culture.

Biofabrication

Birtele, M., Sharma, Y., Storm, P., Kajtez, J., Nelander, J., **Sozzi, E.,** Nilsson, F., Stott, S., He, XL., Mattsson, B., Ottosson, DR., Barker, R., Fiorenzano, A., Parmar, M. (2022).

Single-cell transcriptional and functional analysis of human dopamine neurons in 3D fetal ventral midbrain organoid-like cultures.

Development

Johansson, PA., Brattås, PL., Douse, CH., Hsieh, P., Adami, A., Pontis, J., Grassi, D., Garza, R., **Sozzi, E.,** Cataldo, R., Jönsson, ME., Atacho, DAM., Pircs, K., Eren, F., Sharma, Y., Johansson, J., Fiorenzano, A., Parmar, M., Fex, M., Trono, D., Eichler, EE., Jakobsson, J. (2022).

A cis-acting structural variation at the ZNF558 locus controls a gene regulatory network in human brain development.

Cell Stem Cells

Nilsson, F., Storm, P., **Sozzi, E.,** Hidalgo Gil, D., Birtele, M., Sharma, Y., Parmar, M., Fiorenzano, A. (2021).

Single-cell profiling of coding and noncoding genes in human dopamine neuron differentiation.

Cells

RESEARCH REVIEW ARTICLES NOT INCLUDED IN THE THESIS

Fiorenzano, A., **Sozzi, E.,** Parmar, M., Storm, P. (2021).

Dopamine neuron diversity: Recent advances and current challenges in human stem cell models and single cell sequencing.

Cells

ABSTRACT

Midbrain dopaminergic neurons exhibit a wide diversity in their projection patterns, disease vulnerability, and functions, playing key roles in voluntary motor control, cognition, and reward processing. Parkinson's Disease, one of the most common neurodegenerative disorders, is characterized by the selective degeneration of the A9 dopaminergic neuron subtype, leading to severe motor dysfunction. Despite advancements in symptomatic treatments, current approaches fail to halt disease progression, highlighting the need for novel therapeutic strategies such as cell replacement therapy. Generating authentic human dopaminergic neurons for transplantation and therapeutic purposes relies on a comprehensive understanding of the factors driving their development. However, the molecular mechanisms underlying the specification of midbrain dopaminergic neurons into distinct subtypes remain poorly understood. Due to the inaccessibility of developing and adult human brain tissue, novel methodologies are needed for investigating these processes in a human-relevant context.

This thesis investigates the development, diversity, and specification of human dopaminergic neurons using advanced human stem cell models, with a particular focus on their application in cell replacement therapies for Parkinson's Disease. In the first part, I established ventral midbrain-patterned organoids that recapitulate developmental trajectories and the molecular identities of distinct dopaminergic neuron subtypes. To overcome limitations in conventional organoid technology, silk scaffolding was also introduced, enhancing cell viability and neuronal maturation. In the second part, I linked the molecular identities of human dopaminergic neurons to their projection patterns using homotopic transplantation models. Finally, co-grafting experiments examined the influence of support cell types on dopaminergic neuron maturation and lineage commitment, identifying critical factors shaping subtype identity. These findings advance our understanding of human dopaminergic neuron development and subtype specification, offering valuable insights for refining cell replacement therapies for Parkinson's Disease.

LAY SUMMARY

Parkinson's Disease is the second most common neurodegenerative disorder after Alzheimer's disease, affecting about 1% of individuals over the age of 60. Patients with this condition primarily experience motor symptoms such as resting tremors, muscle rigidity, and difficulty initiating movements, which can profoundly impact the quality of life. While the precise causes of Parkinson's Disease remain unclear, we now know that these symptoms result from the progressive degeneration of a specific group of brain cells located in the midbrain. In a healthy brain, these neurons produce dopamine, a neurotransmitter essential for initiating and regulating movement. Therefore, the motor symptoms of Parkinson's disease are often treated with medications aimed at increasing dopamine levels, restoring balance in the brain. However, this approach is not effective in the long term and does not alter or halt the disease's progression.

Cell replacement therapy represents an alternative approach for treating Parkinson's Disease and is currently being explored in clinical trials. The concept behind this strategy is to replace the dopamine-producing neurons lost due to the disease with healthy, functional cells that can integrate into the patient's brain and restore lost motor functions. These new dopamine neurons are derived from human stem cells, which are directed through a differentiation process to mimic the developmental steps necessary to become neurons. Therefore, advancements in cell replacement therapy are inextricably linked to our understanding of dopamine neuron development.

Due to the human brain's inaccessibility, most of our current knowledge has been built on parallels with findings from animal models, which, while valuable, can sometimes fail to fully capture human-specific processes. However, recent breakthroughs in neurobiology have led to the development of advanced human stem cell models, including *brain organoids*. These organoids represent a powerful tool for studying the complexities of the human brain, as they can replicate the developmental processes of specific neuronal populations in an accessible system.

In this thesis, I describe how we established a human organoid model designed to study midbrain dopamine neuron differentiation and diversity, gaining new insights into the mechanisms underlying their development. Also, we have explored the possibility of incorporating biomaterials, creating a more supportive microenvironment that promotes neuron maturation and functionality. In the second part of the thesis, we have investigated the identity of two distinct subtypes of dopaminergic neurons: A9 neurons, which are implicated in Parkinson's Disease, and A10 neurons, which are associated with addiction and cognitive disorders. Using transplantation models, we explored how the interactions with other cell types influence the specification and maturation of these neuronal subtypes, revealing key factors that shape their identity and function. These findings have significant implications for advancing cell replacement therapies for Parkinson's Disease, as understanding the precise characteristics of A9 neurons is essential for refining current treatments.

POPULÄRVETENSKAPLIG SAMMANFATTNING

Parkinsons sjukdom är den näst vanligaste neurodegenerativa sjukdomen efter Alzheimers sjukdom och drabbar cirka 1% av alla personer över 60 år. Patienter med denna sjukdom upplever främst motoriska symtom som skakningar, muskelstelhet och svårigheter att initiera rörelser, vilket kan ha en djupgående inverkan på livskvaliteten. Även om de exakta orsakerna till Parkinsons sjukdom fortfarande är oklara, vet vi nu att dessa symtom beror på en progressiv degeneration av en specifik grupp hjärnceller i mellanhjärnan. I en frisk hjärna producerar dessa neuroner dopamin, en neurotransmittor som är nödvändig för att initiera och reglera rörelser. Därför behandlas de motoriska symtomen i Parkinsons sjukdom ofta med läkemedel som syftar till att öka dopaminnivåerna och återställa balansen i hjärnan. Denna metod är dock inte effektiv på lång sikt och förändrar eller stoppar inte sjukdomsförloppet.

Cellersättningsterapi är ett alternativt sätt att behandla Parkinsons sjukdom och utforskas för närvarande i kliniska prövningar. Konceptet bakom denna strategi är att ersätta de dopaminproducerande nervceller som förlorats på grund av sjukdomen med friska, funktionella celler som kan integreras i patientens hjärna och återställa förlorade motoriska funktioner. Dessa nya dopaminneuroner har sitt ursprung från mänskliga stamceller, som styrs genom en differentieringsprocess för att efterlikna de utvecklingssteg som krävs för att neuroner ska bildas. Framstegen inom cellersättningsterapi är därför direkt kopplade till vår förståelse av dopaminneuronernas utveckling.

På grund av den mänskliga hjärnans otillgänglighet har merparten av vår nuvarande kunskap byggt på paralleller med resultat från djurmodeller, som visserligen är värdefulla, men som ibland inte helt kan fånga människospecifika processer. De senaste genombrotten inom neurobiologin har dock lett till utvecklingen av avancerade modeller för mänskliga stamceller, bland annat hjärnorganoider. Dessa organoider utgör ett kraftfullt verktyg för att studera komplexiteten i den mänskliga hjärnan, eftersom de kan återskapa utvecklingsprocesserna hos specifika neuronala populationer i ett tillgängligt system.

I den här avhandlingen beskriver jag hur vi etablerade en mänsklig organoidmodell utformad för att studera differentiering och mångfald av dopaminneuron i mellanhjärnan och få nya insikter i de mekanismer som ligger till grund för deras utveckling. Vi har också undersökt möjligheten att inkorporera biomaterial för att skapa en mer stödjande mikromiljö som främjar neuronens mognad och funktionalitet. I den andra delen av avhandlingen har vi undersökt identiteten hos två distinkta subtyper av dopaminerga nervceller: A9-neuroner, som är inblandade i Parkinsons sjukdom, och A10-neuroner, som är förknippade med missbruk och kognitiva störningar. Med hjälp av transplantationsmodeller har vi undersökt hur interaktionen med andra celltyper påverkar specifikationen och mognaden av dessa neuronala subtyper och avslöjat nyckelfaktorer som formar deras identitet och funktion. Dessa resultat är betydelsefulla för utvecklingen av cellersättningsterapier för Parkinsons sjukdom, eftersom det är viktigt att förstå de exakta egenskaperna hos A9-neuroner för att kunna vidareutveckla nuvarande behandlingar.

RIASSUNTO IN ITALIANO

La malattia di Parkinson è la seconda malattia neurodegenerativa più comune dopo la malattia di Alzheimer e colpisce circa l'1% delle persone di età superiore ai 60 anni. I pazienti affetti da questa patologia manifestano principalmente sintomi motori come tremori, rigidità muscolare e difficoltà a iniziare i movimenti, che possono incidere profondamente sulla qualità della vita. Sebbene le cause precise della malattia di Parkinson non siano ancora chiare, oggi sappiamo che questi sintomi derivano dalla progressiva degenerazione di uno specifico gruppo di cellule cerebrali situate nel mesencefalo. In un individuo sano, questi neuroni producono dopamina, un neurotrasmettitore essenziale per avviare e regolare il movimento. Pertanto, i sintomi motori della malattia di Parkinson sono spesso trattati con farmaci che aumentano i livelli di dopamina, ripristinando l'equilibrio cerebrale. Tuttavia, questo approccio non è efficace a lungo termine e non contribuisce ad alterare o arrestare la progressione della malattia.

La terapia di sostituzione cellulare rappresenta un approccio alternativo per trattare la malattia di Parkinson ed è attualmente in fase di sperimentazione clinica. Il concetto alla base di questa strategia è quello di sostituire i neuroni dopaminergici persi a causa della malattia con cellule sane e funzionali che possano integrarsi nel cervello del paziente e ripristinare le funzioni motorie perdute. Questi nuovi neuroni dopaminergici sono derivati da cellule staminali umane, che vengono indirizzate attraverso un processo di differenziamento basato sullo sviluppo umano a diventare neuroni. Pertanto, i progressi nella terapia cellulare sono indissolubilmente legati alla comprensione dello sviluppo dei neuroni dopaminergici.

A causa dell'inaccessibilità del cervello umano, la maggior parte delle nostre conoscenze attuali è costituita da paralleli con risultati ottenuti su modelli animali che, pur essendo validi, a volte non riescono a cogliere appieno i processi specifici dell'uomo. Tuttavia, le recenti scoperte nel campo della neurobiologia hanno portato allo sviluppo di modelli avanzati derivati su cellule staminali umane, tra cui gli organoidi cerebrali. Questi organoidi rappresentano un potente strumento per studiare le complessità del cervello umano, in quanto possono replicare i meccanismi dello sviluppo di specifiche popolazioni neuronali in un sistema piu accessibile.

In questa tesi, descrivo come abbiamo creato un modello di organoide umano per studiare il differenziamento dei neuroni dopaminergici del mesencefalo, ottenendo nuove conoscenze sui meccanismi alla base del loro sviluppo. Inoltre, abbiamo esplorato la possibilità di incorporare biomateriali, creando un microambiente più favorevole per promuovere la maturazione e la funzionalità dei neuroni. Nella seconda parte della tesi, abbiamo studiato l'identità di due sottotipi distinti di neuroni dopaminergici: i neuroni A9, implicati nella malattia di Parkinson, e i neuroni A10, associati alle dipendenze e a determinati disturbi cognitivi. Trapiantando questi neuroni in animali modello, abbiamo esplorato come le interazioni con altri tipi di cellule influenzino la specificazione e la maturazione di questi sottotipi neuronali, rivelando i fattori chiave che ne modellano identità e funzioni.

Questi risultati hanno implicazioni significative per il progresso delle terapie di sostituzione cellulare per la malattia di Parkinson, poiché capire le rprecise caratteristiche dei neuroni A9 èessenziale per perfezionare i trattamenti attuali.

ABBREVIATIONS

AAV	Adeno-associated vector
ALDH1A1	Aldehyde dehydrogenase
CALB1	Calbindin 1
DA	Dopamine
DBS	Deep brain stimulation
DDC	L-aromatic amino acid decarboxylase
dlSTR	Dorso-lateral striatum
EN1	Engrailed 1
ESCs	Embryonic stem cells
FB	Forebrain
FGF8	Fibroblast growth factor 8
FP	Floor plate
GDNF	Glial-derived neurotrophic factor
GIRK2	G protein-activated inward rectifier potassium channel
GMP	Good Manufacturing Practice
GO	Gene Ontology
GPCs	Glial progenitor cells
GRN	Gene regulatory network
GSEA	Gene set enrichment analysis
hPSCs	Human pluripotent stem cells
iPSCs	Induced pluripotent stem cells
IZ	Intermediate zone
MFB	Medial forebrain bundle
MSNs	Medium spiny neurons
MZ	Mantle zone
NGN2	Neurogenin 2
NTN1	Netrin 1
OPCs	Oligodendrocyte precursor cells
PD	Parkinson´s Disease
PDMS	Polydimethylsiloxane
PFA	Paraformaldehyde
PFC	Prefrontal cortex
PLGA	Poly-lactic-co-glycolic acid
qRT-PCR	Quantitative real-time polymerase chain reaction
ROBO2	Roundabout guidance receptor 2
SEM	Scanning electron microscope
SHH	Sonic hedgehog

SNpc	*Substantia nigra pars compacta*
STR	Striatum
TF	Transcription factor
TH	Tyrosine hydroxylase
UMAP	Uniform manifold approximation and projection for dimension reduction
vFB	Ventral forebrain
VLMCs	Vascular leptomeningeal cells
vMB	Ventral midbrain
VTA	Ventral tegmental area
VZ	Ventricular zone

INTRODUCTION

Parkinson´s Disease

Parkinson's Disease (PD), first described by James Parkinson in his 1817 publication "An Essay on the Shaking Palsy", is a chronic and progressive neurodegenerative disorder of the central nervous system (Parkinson, 2002). Affecting over 1% of individuals over 60 years of age, it is recognized as the second most common neurodegenerative disease after Alzheimer's Disease (de Lau & Breteler, 2006). As aging represents the primary risk factor, the prevalence of PD is expected to rise in the near future in the aging western populations (WHO, 2022). However, it´s important to notice that about 10% of cases are classified as early-onset PD, affecting individuals under 45 years of age (Lees et al., 2009; Taylor et al., 2006). Despite being first documented over two centuries ago, the root causes of PD remain elusive. It is now known that its etiology is highly complex, involving a combination of genetic and environmental factors. While genetic studies have linked specific mutations to the disease, approximately 90% of all PD cases are idiopathic, meaning without a known cause (Lees et al., 2009).

Clinical manifestations of PD impact both motor and non-motor functions, significantly diminishing patients' quality of life. The cardinal motor symptoms of PD - resting tremors, rigidity, bradykinesia (slowness of movement), and postural instability - result from the focal and progressive degeneration of dopaminergic (DA) neurons in the midbrain (Bernheimer et al., 1973). In particular, the most vulnerable DA neurons are localized in the *substantia nigra pars compacta* (SNpc), projecting to the dorsolateral striatum (caudate-putamen), where they modulate the motor activity via the basal ganglia circuits (Bjorklund & Dunnett, 2007). Beyond motor symptoms, PD patients often experience a range of non-motor conditions, including hyposmia (reduced sense of smell), constipation, sleep disturbances, and cognitive impairments, such as memory deficits (Duncan et al., 2014; Fu et al., 2012). As PD progresses, the degeneration extends to non-DA cells, like the basal forebrain cholinergic neurons, leading to dementia and the associated symptoms of depression and anxiety (Bjorklund & Barker, 2024).

Currently, the primary strategy for managing PD motor symptoms is the pharmacological elevation of DA levels. Common treatments include the DA precursor l-3,4-dihydroxyphenylalanine (L-DOPA), DA agonists, and inhibitors of DA-degrading enzymes such as monoamine oxidase type B (MAO-B) and catechol-O-methyltransferase (COMT) (Connolly & Lang, 2014). These therapies effectively restore DA activity in the striatum, providing efficient symptomatic relief in the early disease stages. However, their efficacy diminishes over time and prolonged use often results in severe side effects, including dyskinesias and motor fluctuations (Kalia & Lang, 2015). These complications primarily arise from the systemic, uncontrolled, and non-physiological elevation of DA levels, causing off-target effects (Jankovic, 2005; Thanvi & Lo, 2004). Additionally, DA pharmacological therapies do not address non-motor symptoms, which are often linked to dysfunctions in other brain regions be-

yond the DA system (Bjorklund & Barker, 2024; Braak et al., 2004). Deep brain stimulation (DBS) is another established intervention for PD, involving the implantation of electrodes into the subthalamic nucleus/internal globus pallidus to deliver controlled high-frequency electrical pulses. These signals modulate the network dynamics, mitigating motor fluctuations, reducing tremors, and alleviating L-DOPA-induced dyskinesias (Okun, 2012). However, DBS requires an invasive surgical procedure that limits its suitability for some patients, and the restricted range of the electrodes hampers a broader application for PD (Rossi et al., 2018). Furthermore, DBS has been associated with potential behavioral and cognitive side effects, due to the unintended stimulation of off-target structures (Bronstein et al., 2011; Castrioto et al., 2014).

While current therapies for PD effectively manage motor symptoms, they mainly provide symptomatic relief without addressing the underlying neurodegenerative processes (AlDakheel et al., 2014; Kalia & Lang, 2015). Cell replacement therapy offers a promising restorative approach, by replacing the lost DA neurons with healthy, functional, DA-producing cells to restore DA signaling and potentially repair the impaired motor circuitry (Lindvall & Kokaia, 2010).

Cell replacement therapy for Parkinson´s Disease

The rationale

While the concept of replacing impaired or lost cells extends beyond the brain (e.g. type I diabetes, clinical trial #NCT04786262), this therapeutic option is being actively explored for several neurodegenerative disorders (Steinbeck & Studer, 2015; Tabar & Studer, 2014). In particular, PD has long been considered a well-suited candidate for this approach, due to its hallmark feature: the focal and selective loss of DA neurons within a defined brain region, the SNpc (Barker et al., 2013; Barker, Studer, et al., 2015; Lindvall et al., 1990). Importantly, it is now known that replacing only a relatively small number of DA neurons can significantly alleviate motor symptoms and achieve meaningful therapeutic effects (Lindvall et al., 1990). In this context, DA progenitors derived from fetal tissue or pluripotent stem cells are transplanted into the caudate/putamen of PD patients to reinnervate these structures, restore physiological DA levels, and provide sustained therapeutic effects (Barker, Drouin-Ouellet, et al., 2015; Li et al., 2016). A major advantage of this approach is the localized, self-regulating release of DA directly at the target site, minimizing the chance of off-target effects often seen with systemic pharmacological treatments. (Connolly & Lang, 2014). Cell replacement therapy is particularly promising for early-onset PD patients, who face the prospect of living with the disease for a significant portion of their lives. By addressing the underlying loss of DA neurons, cell replacement therapy holds the potential to become a truly restorative treatment rather than merely mitigate motor symptoms, thus achieving long-lasting relief in a broad cohort of PD patients (Parmar et al., 2020).

Fetal cell transplantation – paving the way

The history of cell transplantation in the brain began in Sweden in the 1970s and 1980s, pioneering modern grafting strategies for PD. Early experimental studies demonstrated that tissue pieces from rat fetal ventral midbrain (vMB) could not only survive transplantation in the rat brain but

also successfully reinnervate the host striatum (Bjorklund et al., 1980; Bjorklund & Stenevi, 1979; Bjorklund et al., 1981; Dunnett et al., 1981; Perlow et al., 1979). Furthermore, these grafts were able to restore DA signaling and reverse motor deficits, including rotational asymmetry, in PD animal models (Bjorklund et al., 1981; Dunnett et al., 1981). Crucially, evidence that human vMB-derived cells could also survive and integrate into the rat striatum paved the way for the first clinical trials in PD patients (Brundin et al., 1986; Brundin et al., 1988). In 1987, the first transplantation of human fetal vMB into PD patients was performed in Lund, Sweden, showing promising proof-of-concept efficacy and promoting the initiation of additional clinical investigations in Europe and USA (Brundin et al., 2000; Hagell et al., 1999; Lindvall et al., 1990; Lindvall et al., 1989; Lindvall et al., 1994; Wenning et al., 1997; Widner et al., 1992). In these initial trials, graft integration and significant motor improvements were observed in a subset of patients, with a few even being able to discontinue the pharmacological treatments (Brundin et al., 2000; Piccini et al., 1999; Piccini et al., 2000). Long-term follow-up studies confirmed that transplanted fetal tissue survived and maintained its identity for over 24 years, providing durable motor benefits (Barker et al., 2013; Kefalopoulou et al., 2014; Li et al., 2016). Building on these early successes, the TRANSEURO clinical trial was launched in 2009 with the aim of identifying factors that could influence the positive clinical outcomes of human fetal vMB grafts (Barker & consortium, 2019; Barker, Drouin-Ouellet, et al., 2015). In this study, 11 PD patients were bilaterally grafted with fetal cells at medical centers in Lund and Cambridge, UK (Barker & consortium, 2019). However, despite advances in technology and biological knowledge, ethical and logistical challenges surrounding the use of fetal tissue for cell replacement therapy have become increasingly evident. In particular, the limited availability of human fetal tissue resulted in the cancellation of 87 planned surgeries due to insufficient tissue supply (Barker et al., 2024). This highlighted the need for a scalable, reliable, and standardized cell source to make cell replacement therapy accessible to a broader cohort of patients.

Stem cell-based therapies for Parkinson´s Disease

Human pluripotent stem cells (hPSCs) possess two defining characteristics that make them ideal candidates for cell-based therapies: pluripotency and self-renewability (Takahashi & Yamanaka, 2006; Thomson et al., 1998; Yu et al., 2007). By providing the necessary developmental cues, hPSCs can be theoretically differentiated *in vitro* into any adult cell type, including DA neurons. A pivotal breakthrough in this field came in the late 2000s, driven by the discovery that these neurons originate from floor plate (FP) progenitors rather than neuroepithelial cells (Bonilla et al., 2008; Joksimovic et al., 2009; Kirkeby et al., 2012; Kriks et al., 2011; Ono et al., 2007). This insight revolutionized the field, promoting numerous efforts to refine differentiation protocols through optimized culture conditions, the precise timing of key patterning factors, or the incorporation of cell sorting (Kim et al., 2021; Kirkeby et al., 2017; Maimaitili et al., 2023). These advancements have enabled the production of hPSC-derived midbrain DA neurons under Good Manufacturing Practice (GMP) guidelines, leading to the development of an off-the-shelf product for PD treatment (Doi et al., 2020; Kirkeby et al., 2023; Nolbrant et al., 2017; Piao et al., 2021). Importantly, these cells can be cryopreserved for extended periods of time without losing their identity or functionality after transplantation (Barker et al., 2017; Nolbrant et al., 2017). Compared to fetal tissue, stem cell-derived DA neurons offer significant advantages, including extensive and rigorous prior-to-graft testing, enhancing both safety and efficacy (Kirkeby et al., 2023; Piao et al., 2021).

Despite these advancements, over a decade has passed between the initial discovery and the initiation of clinical trials. Today, numerous trials are underway or in preparation, utilizing either embryonic (ESCs) or induced pluripotent stem cells (iPSCs) as starting material. Examples of such efforts include the academic STEM-PD trial in Europe and the CiRA trial in Japan, as well as initiatives driven by companies such as BlueRock Therapeutics and Aspen Neuroscience (US), S. Biomedics (South Korea), and Novo Nordisk (Denmark), which is preparing for a global trial (Barker et al., 2024). Although these trials are based on slightly different protocol adaptations, they all rely on the same key principles of DA neuron development. Continued advancements in our understanding of DA neurogenesis will further refine the clinical differentiation protocols, advancing the field of cell replacement therapy for PD.

Development of midbrain dopaminergic neurons

Early midbrain specification

The development of an organism from a fertilized egg to a fully formed individual is finely orchestrated by precise molecular mechanisms that regulate cell differentiation and specialization. These processes ensure that each cell assumes its role at the right time, harmonizing with neighboring cells to form tissues and organs. Similarly to all other cells, midbrain DA neurons arise from the combination of tightly regulated signaling pathways, transcription factors (TFs), and extrinsic cellular interactions.

During early embryogenesis, cells within the inner cell mass of the blastocyst undergo gastrulation, an organizational process that ultimately leads to the formation of the three primary germ layers: endoderm, mesoderm, and ectoderm. The nervous system originates from a domain of the neuroectoderm, known as the neural plate (Marikawa & Alarcon, 2009; Solnica-Krezel & Sepich, 2012). Under the influence of mesoderm-secreted factors, such as bone morphogenetic protein (BMP) inhibitors, the neural plate first elongates and folds into the neural groove, and later closes to form a hollow neural tube (Colas & Schoenwolf, 2001; Harland, 2000). At the anterior end of the neural tube, three primary brain vesicles emerge: the forebrain (prosencephalon), midbrain (mesencephalon), and hindbrain (rhombencephalon) (Leibovitz et al., 2022). Around five weeks post-conception, the forebrain further subdivides into the telencephalon and diencephalon, while the hindbrain forms the metencephalon and myelencephalon.

Neural tube regionalization is guided by signaling centers that release molecular cues to define positional identities along the dorsoventral and rostrocaudal axes (Kiecker & Lumsden, 2012; Lumsden & Krumlauf, 1996). In particular, early midbrain patterning is driven by concentration gradients of Wnt family members, the fibroblast growth factor 8 (Fgf8), and sonic hedgehog (Shh), released by the FP and the isthmic organizer (Echelard et al., 1993; Liu & Joyner, 2001). The secretion of Wnt1 in the most rostral part of the neural tube maintains the expression of Otx2 in both forebrain and midbrain while suppressing hindbrain development by inhibiting Nkx2.2 expression (Broccoli et al., 1999; Martinez-Barbera et al., 2001; Millet et al., 1996; Nordstrom et al., 2002; Ono et al., 2007; Puelles et al., 2004). In contrast, the caudal expression of the TF Gbx2 promotes the formation of the hindbrain and spinal cord, while inhibiting Otx2 and the midbrain domain (Liu & Joyner, 2001). The opposing

expression of the homeodomain TFs Otx2 and Gbx2 therefore establishes a sharp boundary between the midbrain and hindbrain, setting the positioning of the isthmus organizer (Broccoli et al., 1999; Martinez-Barbera et al., 2001). Here, signaling cells secrete Fgf8 to drive caudal midbrain development (Liu & Joyner, 2001), while the release of Shh from FP cells provides ventral positioning cues in a dose-dependent manner (Echelard et al., 1993). Although the FP was traditionally considered only as a signaling center, it is now known that FP radial glia-like cells in the midbrain also hold neurogenic potential (Bonilla et al., 2008; Hebsgaard et al., 2009; Nelander et al., 2009; Ono et al., 2007). Overall, the interplay of all these signals is essential in establishing the DA progenitor territory, from which midbrain DA neurons are born over a narrow temporal window (E10.5–12.5 in the mouse, and 6–8.5 weeks post conception in humans) (Arenas et al., 2015; Asgrimsdottir & Arenas, 2020).

Dopaminergic neuron differentiation

This vMB FP domain is organized into three distinct areas: the ventricular zone (VZ), housing proliferating DA progenitors; the intermediate zone (IZ), containing early postmitotic DA neurons; and the mantle zone (MZ), where maturing DA neurons reside (Kawano et al., 1995; Shults et al., 1990). During DA neurogenesis, developing neurons first migrate radially from the VZ through the IZ and toward the MZ, gradually acquiring mature DA transcriptional profiles along the way (Kawano et al., 1995; Shults et al., 1990). Upon reaching the MZ, these neurons migrate tangentially, to form the ventral tegmental area (VTA) and substantia nigra (SN) (Garritsen et al., 2023; Kawano et al., 1995). This intricate process is governed by the precise expression of numerous TFs, regulating different stages of neuronal differentiation and specification.

Key early determinants of DA neuron development include the TF Lmx1a and its downstream effector Msx1, as well as FP markers such as FoxA1, FoxA2, Corin, and Lmx1b (Andersson, Tryggvason, et al., 2006; Ferri et al., 2007; Marklund et al., 2014; Nelander et al., 2009). As DA progenitors expand in the VZ, FoxA1 and FoxA2 induce the activation of the pro-neural transcription factor Neurogenin 2 (Ngn2), initiating neurogenesis (Andersson, Jensen, et al., 2006; Ang, 2009; Ferri et al., 2007; Kele et al., 2006; Lin et al., 2009; Stott et al., 2013). During this process, additional factors crucial for DA specification start to be expressed, including Engrailed 1 and 2 (En1, En2) and Pbx1, which expression is sustained throughout DA neurogenesis (Kouwenhoven et al., 2017; Simon et al., 2001). As progenitors exit the cell cycle and neurons complete their migration toward the MZ, Nurr1 expression drives DA identity by inducing the enzymes required for DA synthesis - Tyrosine hydroxylase (TH) and L-aromatic amino acid decarboxylase (Ddc) - and transporters involved in DA release, such as Dat and Vmat2 (Asgrimsdottir & Arenas, 2020; Chakrabarty et al., 2012; Miller, Erickson, et al., 1999; Miller, Gainetdinov, et al., 1999; Molinoff & Axelrod, 1971; Nelander et al., 2009; Saucedo-Cardenas et al., 1998; Smidt et al., 2000; Smits et al., 2003). The TF Pitx3 further supports the survival and terminal differentiation of postmitotic DA neurons, completing neurogenesis (Hong et al., 2014; Jacobs et al., 2009; Nunes et al., 2003). The developmental trajectory of midbrain DA neurons is further complicated by their segregation into distinct subtypes, each with distinct projection patterns and functional characteristics (Garritsen et al., 2023; La Manno et al., 2016; Poulin et al., 2020; Poulin et al., 2014; Tiklova et al., 2019).

Diversity of midbrain dopaminergic neurons

Midbrain DA neurons, despite sharing a common neurotransmitter and being in close anatomical proximity, form a heterogeneous group with distinct functions, vulnerabilities to degeneration, and axonal projection targets (Adams et al., 2023; Bjorklund & Dunnett, 2007; Farassat et al., 2019; Fiorenzano, Sozzi, et al., 2021; Fu et al., 2012). Overall, these neurons play critical roles in many aspects of our lives, including motor control, reward processing, and cognition (Meyer-Lindenberg et al., 2002; Milton & Everitt, 2012). The canonical classification by Dahlström and Fuxe organizes midbrain DA neurons into three groups: A8 (located in the retrorubral field), A9 (in the SNpc), and A10 (in the VTA) (Dahlström & Fuxe, 1964). Among these, A9 and A10 DA neurons have drawn significant research attention due to their selective vulnerabilities in different diseases, including PD (Brochier et al., 2008; Garritsen et al., 2023).

A9 DA neurons, crucial for voluntary motor control, project from the SNpc to the dorsolateral striatum via the nigrostriatal pathway and are selectively degenerated in PD (Adams et al., 2023; Freund et al., 1984; Hegarty et al., 2013; Kalia & Lang, 2015; Maiti et al., 2017). They develop first (around E11.5 in mice), and exhibit large, angular somas (Bayer et al., 1995; Damier et al., 1999; Grealish et al., 2014). In contrast, A10 DA neurons residing in the VTA, are born slightly later (around E12.5), display smaller, round somas (Grealish et al., 2014; Morales & Margolis, 2017), and have broader axonal projections to the amygdala, *nucleus accumbens* (mesolimbic pathway) and prefrontal cortex (PFC, mesocortical pathway) (Beier et al., 2019; Beier et al., 2015; Lammel et al., 2008). Their role in reward and cognition makes A10 neurons central to studies on addiction and related disorders (Menegas et al., 2018).

Midbrain DA neurons are defined by unique electrical properties that support neurotransmitter release, including characteristic pace-making firing activity (Hyland et al., 2002). This regular firing pattern is driven by a subthreshold calcium current during the after-hyperpolarization phase, inducing a slow depolarization (Puopolo et al., 2007; Wilson & Callaway, 2000). Additionally, studies in rat midbrain have identified at least two distinct firing patterns between A9 and A10 DA neurons, with the latter marked by more burst firing and less regular discharge compared to the more regular firing pattern of A9 neurons (Ungless & Grace, 2012). Mature A9 DA neurons are further distinguished by the presence of D2 autoreceptors on their dendrites and axons, which tightly regulate striatal input activity (Groves et al., 1975).

Historically, certain gene expression patterns have been identified as more enriched in either A9 or A10 DA neurons (Chung et al., 2005; Greene et al., 2005; Grimm et al., 2004). Specifically, the G protein-activated inward rectifier potassium channel (Girk2, encoded by the gene *Kcnj6*) and aldehyde dehydrogenase (Aldh1a1) are prevalent in SNpc DA neurons, while A10 DA neurons in the VTA express Otx2 and the calcium-binding protein Calb1 (Chung et al., 2005; Di Salvio et al., 2010; Greene et al., 2005; Grimm et al., 2004). Although relevant, these markers are not exclusive to a single subtype, reflecting a more complex molecular landscape within midbrain DA neurons (Garritsen et al., 2023; La Manno et al., 2016; Poulin et al., 2020; Tiklova et al., 2019).

Histological and anatomical studies have tried to further subdivide the SNpc and VTA into distinct subnuclei in both rodents and humans. Advances in single-cell RNA sequencing have expanded

our understanding of DA neuron diversity, moving beyond the classical A9/A10 framework (Agarwal et al., 2020; Braun et al., 2023; Fiorenzano, Sozzi, et al., 2021; Kamath et al., 2022; La Manno et al., 2016; Poulin et al., 2020; Poulin et al., 2014; Siletti et al., 2023; Tiklova et al., 2019). Novel markers, including Sox6 (preferentially expressed in the lateral SNpc), vGlut2 (localized in VTA and medial SNpc), and others such as vGat, Gad2, Vip, NeuroD6, Grp, Lmo3, Nfia, Nfib, Zbtb20, Nrip3, and Bcl11a, have been consistently identified across studies, and helped refining DA neuron classification (Kramer et al., 2018; Panman et al., 2014; Pereira Luppi et al., 2021; Saunders et al., 2018; Steinkellner et al., 2018; Tolve et al., 2021). Based on the combinatorial expression of these genes and others, numerous subdivisions of SNpc and VTA have been proposed over the years.

However, differences in annotation across studies have hindered the establishment of a unified classification of midbrain DA neurons based solely on differential marker expression and anatomical localization (Garritsen et al., 2023, Poulin et al., 2020). Furthermore, significant developmental differences between rodent and human DA neurons limit the direct translation of findings to humans (Agarwal et al., 2020; Birtele et al., 2022; Hook et al., 2018; Kamath et al., 2022; La Manno et al., 2016; Poulin et al., 2014; Saunders et al., 2018; Tiklova et al., 2019; Yaghmaeian Salmani et al., 2024). The developmental or adult stage at which tissue is sampled also impacts molecular classifications. For example, while vGlut2 is transiently expressed in most developing DA neurons, only certain subtypes retain its expression in adulthood (Steinkellner et al., 2018). Moreover, neurodegeneration and pathological alterations in postmortem tissue from PD patients can further obscure the identity of adult human DA neurons (Agarwal et al., 2020; Kamath et al., 2022).

The emergence of DA neuron diversity during development is also not fully understood (Brignani & Pasterkamp, 2017). Some studies suggest temporal differences in response to Shh and Wnt1 during DA neurogenesis (as early as E7.5 in mice) (Blaess et al., 2011; Hayes et al., 2011; Joksimovic et al., 2009; Nouri et al., 2020), while others propose that SNpc and VTA identities are shaped by interactions with the surrounding environment (Brignani et al., 2020; Kabanova et al., 2015; Van den Heuvel & Pasterkamp, 2008). Indeed, it has been proposed that A9 and A10 neurons initially project broadly throughout the striatum, but as development progresses, non-specific connections are selectively pruned (Hu et al., 2004). In this context, A9 and A10 DA neuron subtypes seem to be differentially responsive to the chemokine receptor Cxcr4, the axon guidance cue Netrin1 (Ntn1) and Roundabout guidance receptor 2 (Robo2), which are known to be involved in neuron migration and target-specific connectivity (Bodea et al., 2014; Chabrat et al., 2017; Li et al., 2014; Lin et al., 2005; Lo et al., 2022; Yang et al., 2013). Additionally, recent findings suggest that the glial-derived neurotrophic factor (GDNF) promotes SNpc DA innervation of the striatum, with important implications in cell replacement therapy for PD (Gantner et al., 2020; Moriarty, Gantner, et al., 2022; Moriarty, Kauhausen, et al., 2022; Thompson et al., 2009).

Despite significant advancements, studying human DA neuron diversity at single-cell resolution remains challenging (Fiorenzano, Sozzi, et al., 2021). A key obstacle is the lack of consensus on molecular classifications and the absence of a clear correlation between the classical A9/A10 anatomical/functional classification and emerging molecular subdivisions (Poulin et al. 2020). Species differences further complicate these investigations, particularly when transferring knowledge from rodents to humans (La Manno et al. 2016). Additionally, limited access to human tissue (both fetal and adult) and the inability to perform genetic manipulations hinder the investigation of the intrinsic and extrinsic

mechanisms that regulate DA neuron development and diversity. These challenges highlight the need for alternative sources of mature human DA neurons, such as hPSC-derived cultures and organoid models, to bridge these gaps and advance our understanding of human-specific DA neuron biology.

Stem cell models of human dopaminergic neuron development

The first reports of hESC-derived neurons followed shortly after the isolation of hESCs from the inner cell mass of the blastocyst (Reubinoff et al., 2001; Thomson et al., 1998; Zhang et al., 2001). Since then, considerable efforts have been made to recapitulate the cellular diversity of the human brain *in vitro*, including midbrain DA neurons. Between 2004 and 2005, the first protocols for differentiating hESCs into DA neurons were developed, taking advantage of insights from midbrain developmental biology (Park et al., 2005; Perrier et al., 2004; Zeng et al., 2004). These early protocols produced heterogeneous cell populations, including TH-positive neurons (Sonntag et al., 2007), but lacked co-expression of key midbrain markers like LMX1A, FOXA2, and OTX2, raising concerns about their midbrain identity. Later on, the introduction of dual SMAD inhibition, targeting the Lefty, Activin, and Transforming Growth Factor β (TGF-β) signaling pathways, allowed for more efficient and synchronized neural induction (Chambers et al., 2009). Combined with WNT pathway activation (via GSK3 inhibition) and exposure to SHH and FGF8, these protocols successfully patterned hESCs into DA progenitors with midbrain identity (Kirkeby et al., 2012; Kriks et al., 2011; Xi et al., 2012). Just a few years later, similar methods were adapted for iPSCs, enabling disease modeling and autologous cell replacement therapies (Doi et al., 2014). These protocols generated DA neurons from a FOXA2+/PAX6- intermediate, resembling *in vivo* differentiation from midbrain FP progenitors (Arenas et al., 2015; Bonilla et al., 2008; Ono et al., 2007). Upon terminal differentiation *in vitro*, these neurons were electrophysiologically active, capable of DA release, and co-expressed key markers such as TH, FOXA2, and EN1 (Kim et al., 2021; Kirkeby et al., 2012; Kriks et al., 2011; Nilsson et al., 2021). Ongoing refinements in differentiation protocols aim to improve the purity of DA progenitors, including the separation from cell types in close lineage relations, like subthalamic neurons (Kee et al., 2017; Kirkeby et al., 2017).

The homogeneity, accessibility, relative low cost, and ease of maintenance of monolayer cultures have made them the preferred system for *in vitro* human studies. Their high reproducibility has enabled the use of 2D hPSC-derived neurons in large-scale drug screening and early-stage DA neuron development research (Nilsson et al., 2021; Xu et al., 2022). Upon transplantation, hPSC-derived DA progenitors can survive, mature, reinnervate the host striatum, and integrate functionally into host neural circuits (Adler et al., 2019; Cardoso et al., 2018; Denham et al., 2012; Grealish et al., 2015). The ability to precisely control differentiation using defined factors ensures a scalable and standardized source of DA neurons for clinical applications. Functional studies demonstrate that transplanted DA neurons release DA *in vivo* and mediate motor recovery in PD animal models (Chen et al., 2016; Doi et al., 2014; Grealish et al., 2014; Grealish et al., 2015; Kikuchi et al., 2017; Steinbeck & Studer, 2015; Wakeman et al., 2017). Notably, hPSC-derived DA neurons show comparable graft outcomes, properties, and functionality to human fetal vMB tissue (Grealish et al., 2014). Current GMP-compatible protocols also allow the cryopreservation of differentiated progenitors, offering greater flexibility for cell replacement therapies (Nolbrant et al., 2017).

Transplantation models can be useful not only to assess the therapeutic potential of DA neurons in a preclinical setting but also to obtain insights into DA neuron development. The host brain's environmental signals, molecular cues, and anatomical landmarks can unveil the mechanisms driving DA neuron maturation *in vivo*, including long-range axonal projections, identity refinement (e.g., subtype specification), and cell-cell interactions. With the advent of single-cell RNA sequencing in transplantation studies, these questions can now be addressed at single-cell resolution, enabling the reconstruction of developmental trajectories and paving the way for more effective therapeutic strategies (Tiklova et al., 2020).

Bridging the gap between *in vitro* and *in vivo* studies: the rise of human brain organoids

While monolayer cultures are invaluable for developmental and therapeutic research, they remain a reductionist system, that replicates only certain aspects of brain development (Kadoshima et al., 2013; Lancaster et al., 2013). Specifically, 2D cultures often fail to capture the complex architecture of human brain tissue and the non-cell-autonomous mechanisms that arise from interactions between diverse cell types. These limitations hinder the study of later stages of DA neuron differentiation and maturation (Fiorenzano, Sozzi, et al., 2021). Nevertheless, monolayer studies have laid a critical foundation for the development of more complex human stem cell-based models, such as 3D brain organoids (Kadoshima et al., 2013; Lancaster & Knoblich, 2014b).

Human brain organoids exploit the intrinsic self-organization and self-patterning capabilities of hPSCs, generating multiple cell types in a fully humanized system (Kadoshima et al., 2013; Lancaster & Knoblich, 2014b). By modeling human brain development in a three-dimensional, physiologically relevant context, brain organoids bridge the gap between homogeneous monolayer cultures and the vast diversity of the human brain (Lancaster et al., 2013; Quadrato et al., 2017). Furthermore, they provide a platform to investigate unique and complex features of neurodegeneration and associated mental disorders (Renner et al., 2017). The first human brain organoids, which relied on limited extrinsic differentiation cues, were mainly utilized to study early neurodevelopmental processes and cellular organization (Kanton et al., 2019). These systems, as they are mostly driven by the self-patterning properties of hPSCs, are often described as *unguided* (Pasca et al., 2022). Recent organoid protocols have now shifted towards *guided* approaches, incorporating extrinsic patterning factors to direct the formation of specific brain regions, including, but not limited to, the cortex, striatum, cerebellum, and midbrain (Atamian et al., 2024; He et al., 2024; Jo et al., 2016; Kanton et al., 2019; Kwak et al., 2020; Miura et al., 2020; Pasca et al., 2015; Quadrato et al., 2017; Velasco et al., 2019). Notably, human brain organoids can now be patterned to recreate the distinct cellular layers of the developing human vMB, mirroring key aspects of DA neuron development observed *in vivo* (Jo et al., 2016; Qian et al., 2016; Renner et al., 2020). Directed organoid protocols can therefore recapitulate region-specific features of the human brain making them an effective tool for studying individual brain regions in isolation.

The primary applications of vMB organoids include developmental studies, drug screening, and disease modeling. With the advent of iPSC technology, researchers can now recapitulate disease-relevant phenotypes in vMB organoids derived from PD patients (Hiller et al., 2022; Laperle et al., 2020). For instance, recent studies have shown that vMB organoids carrying the PD-associated *LRRK2-G2019S* mutation exhibited increased vulnerability to induced neurotoxic damage, a reduced number of DA neurons, and accumulation of alpha-synuclein (α-syn) in endosomes, compared to isogenic controls (Kim et al., 2019; Smits et al., 2019). Importantly, iPSC-derived vMB organoids provide a platform to explore the effects of known PD-causing genetic mutations and to investigate the mechanisms underlying sporadic PD cases, which remain far more challenging to model with existing systems (Dawson et al., 2010; Vadodaria et al., 2020). Generating patient-specific vMB organoids for drug screening could also lead to the development of targeted and personalized therapies. By automating workflows, it is now possible to achieve precise, high-throughput analysis of drug effects at the single-cell level, all within the human-relevant context of vMB organoids (Renner et al., 2020).

Emerging frontiers in brain organoid technology

Although brain organoids have the potential to bridge the gap between monolayer cultures and *in vivo* models, this technology still faces significant limitations. Emerging technologies and organoid-based models aim to overcome these challenges, advancing our understanding of human brain function and dysfunction.

Bioengineered brain organoids

A critical limitation of brain organoids is represented by the lack of an internal vascular system to effectively deliver oxygen and nutrients. Due to their size and biophysical properties, this limitation often results in hypoxia, the formation of necrotic cores, and impaired organoid growth and maturation, thus reducing their physiological relevance (Bhaduri et al., 2020; Vertesy et al., 2022). To address these issues, spinning bioreactors have been implemented to enhance oxygen and nutrient diffusion within brain organoids (Adams et al., 2023; Cho et al., 2021; Seiler et al., 2022). Additionally, advanced 3D-printed microfluidic systems enable long-term organoid maintenance by facilitating gas exchange and diffusion, ultimately reducing necrotic core formation (Khan et al., 2021; Qian et al., 2016; Rezaei et al., 2023; Spitz et al., 2023). The incorporation of scaffolds into 3D cultures also shows promise in improving neuron viability and maturity within brain organoids (Lancaster et al., 2017; Rothenbucher et al., 2021; Tejchman et al., 2020). Biocompatible and biodegradable materials, such as poly-lactic-co-glycolic acid (PLGA) fibers, can promote hPSC self-organization into neuroectodermal structures, enhancing maturation and reducing intra-organoid variability (Lancaster et al., 2017; Rothenbucher et al., 2021). However, synthetic scaffolds are functionally inert and cannot form microchannels within the organoid tissue, limiting their utility as facilitators of oxygen, nutrient, and patterning factor diffusion in the organoid inner core (Lancaster et al., 2017; Rothenbucher et al., 2021).

Integrated organoid systems

Another key limitation of human brain organoids is the absence of microglia and endothelial cells which originate from lineages not recapitulated in neuroectodermal differentiation (Cserep et al., 2021). While initial efforts to incorporate vasculature cells into brain organoids have been recently published (Adams et al., 2023; Bergmann et al., 2018; Sun et al., 2022), these methods remain technically challenging. Developing vascularized organoids is crucial for drug discovery and modeling diseases with vascular components, such as stroke, blood-brain barrier dysfunction, and glioblastomas. Similarly, the lack of microglia - a key player in neuroinflammation, synaptic pruning, and brain homeostasis - limits organoids' ability to model critical aspects of brain development and disease. A pioneering study demonstrated that injecting microglia into vMB-patterned organoids enhanced synaptic remodeling and increased DA neuron activity, opening avenues to more comprehensive PD modeling (Sabate-Soler et al., 2022).

Transplantation represents another promising strategy to address these limitations. Forebrain organoids transplanted into the mouse cortex not only generated neurons and astrocytes, but also integrated host microglia, extended axonal projections to multiple brain regions, and displayed functional connections (Mansour et al., 2018; Revah et al., 2022). These transplanted human organoids can also modulate host neural circuits and influence behavioral responses (Kelley et al., 2024; Revah et al., 2022). Recently, a transplantation model using iPSC-derived vMB organoids achieved motor recovery in a mouse model of PD (Zheng et al., 2023). Transplantation not only facilitates interactions with other cell types absent in conventional organoids but also supports the formation of long-range neuronal connections, allowing the study of complex brain functions mediated by human cells.

Multi-region brain organoids

Recreating cell-cell interactions, neuronal migration, and axonal projection patterns across different brain regions *in vitro* has been a long-standing challenge. The development of *assembloids*, a 3D culture system combining organoids with distinct regional identities, represents a significant breakthrough in the field (Pasca, 2019). By fusing region-specific organoids, assembloids address the lack of anatomical references in conventional brain organoids, enabling the study of the interactions between specific brain regions. For instance, assembloids have been successfully used to model cortical interneuron migration by merging ventral and dorsal forebrain organoids (Bagley et al., 2017; Birey et al., 2017; Sloan et al., 2018). This system provides a humanized platform to investigate specific regional interactions, such as the corticostriatal or corticothalamic connections, within a simplified yet physiologically relevant context.

Assembloids have also proven invaluable for dissecting pathological mechanisms at the cellular level, offering insights into complex brain disorders. One notable example is Timothy syndrome, a rare condition caused by mutations in the CACNA1C gene encoding for the calcium channel Ca v1.2 alpha subunit. Using assembloids, researchers have identified alterations in neural migration and synaptic activity associated with this disorder (Birey et al., 2017; Birey et al., 2022). In the context of DA neurons, assembloids represent an innovative platform for recapitulating DA circuitry *in vitro*, by combining vMB, striatal, and cortical organoids (Reumann et al., 2023). This triple-fusion model enables the study of late-stage DA neuron differentiation, maturation, and dysfunctions in key DA circuits, such as the nigrostriatal, mesolimbic, and mesocortical pathways. For example, it has been used to model cocaine addiction and related DA circuitry alterations (Reumann et al., 2023).

In addition to assembloids, innovative organoid-based systems are being developed to model interactions between anatomically distant brain regions. The combination of microfluidic devices and regionalized organoids has promoted the development of complex models for long-range synaptic connectivity, where the two cultures are not fused together but maintained spatially separated (Kirihara et al., 2019). Proof-of-concept studies have demonstrated the potential of these systems in modeling cortico-cortical interactions and disorders such as agenesis of the corpus callosum (Kirihara et al., 2019; Martins-Costa et al., 2024). While current systems have primarily focused on cortico-cortical connections, this technology holds great promise for modeling other long-range neural interactions, including those involving midbrain DA neurons. Advances in these systems offer exciting opportunities to study axon guidance, circuitry formation, and the mechanisms underlying associated pathologies.

AIMS OF THE THESIS

The overall aim of this thesis has been to investigate the molecular profile of developing human dopaminergic neurons *in vitro* and *in vivo*, within the context of cell replacement therapy for Parkinson´s Disease.

The specific aims of this thesis were to:

- Develop a 3D cell culture system to model features of human ventral midbrain development and investigate dopamine neuron diversity *in vitro* (**Paper I** and **II**).
- Explore the use of recombinant silk scaffolding to enhance cell viability and functional maturity of human brain organoids (**Paper I** and **III**).
- Link the molecular identities of dopaminergic neuron subtypes with their projection patterns in a homotopic transplantation model (**Paper IV**).
- Assess the influence of support cell types on the development, maturation, and specification of human dopaminergic neurons (**Paper V**).

SUMMARY OF RESULTS AND DISCUSSION

Midbrain DA neurons play a central role in voluntary motor control, cognitive functions, and reward processing (Bjorklund & Dunnett, 2007). Historically, they have been classified into A9 and A10 subtypes, exhibiting distinct projection patterns and functional roles in the human brain (Fiorenzano, Sozzi, et al., 2021). The selective vulnerability of A9 DA neurons in PD underscores the importance of understanding the molecular mechanisms driving their development and diversity. Furthermore, insights into DA neuron specification could also refine therapeutic approaches, including cell replacement therapies for PD (Parmar et al., 2020). Recent advances in hPSC-based models provide a unique opportunity to study DA neuron development in a human-relevant context. Three-dimensional human brain organoids, which recapitulate key aspects of brain architecture and cellular complexity, have become a powerful tool for investigating molecular and cellular processes in specific neuronal populations (Lancaster et al., 2013; Pasca, 2018).

This section summarizes key findings from the studies included in this thesis, exploring midbrain DA neuron development and diversity using single-cell transcriptomics and advanced hPSC-based models. In **Papers I** and **II**, we developed a robust protocol for generating vMB-patterned brain organoids. Single-cell RNA sequencing revealed developmental trajectories of different cell types, including molecularly distinct DA neuron subtypes. **Papers I** and **III** addressed some limitations of conventional organoid technology introducing silk scaffolds, with the aim of improving cellular viability and neuronal maturation. These organoid models bridge the gap between reductionist monolayer cultures and the complexity of the human brain, providing valuable insights into DA neuron differentiation and specification.

Despite recent advances, linking the molecular profiles of hPSC-derived DA neurons to their functional and anatomical characteristics, such as the classical A9/A10 classification, is still challenging. In **Paper IV,** we introduced *Target-Seq*, a novel methodology that correlates the molecular profiles of grafted human DA neurons with their projection patterns toward either the dorsolateral striatum (dlSTR, A9 target) or the PFC (one of A10 targets). Finally, in **Paper V**, we investigated the influence of support cells on DA neuron lineage commitment and subtype specification through co-grafting experiments. Collectively, these studies lay the groundwork for a deeper understanding of human DA neuron development and subtype differentiation, leveraging bioengineered organoids, single-cell RNA sequencing, and xenograft models.

Brain organoid cultures mimic key features of human vMB development (Paper I and II)

The ability to direct the differentiation of hPSCs toward specific cell fates has revolutionized the study of human brain development *in vitro*. By adapting guided differentiation protocols, human brain organoids have now emerged as effective systems to recapitulate cellular processes of distinct brain regions in a physiologically relevant context. In **Papers I** and **II**, we adapted a widely used protocol for generating whole-brain organoids, incorporating exposure to extrinsic signaling cues to achieve precise patterning of a vMB identity. In particular, this protocol employs dual SMAD inhibition for neural induction, SHH signaling for ventralization, and the activation of FGF8 and WNT signaling pathways to establish a caudal fate, mimicking the *in vivo* temporal sequence (Figure 1).

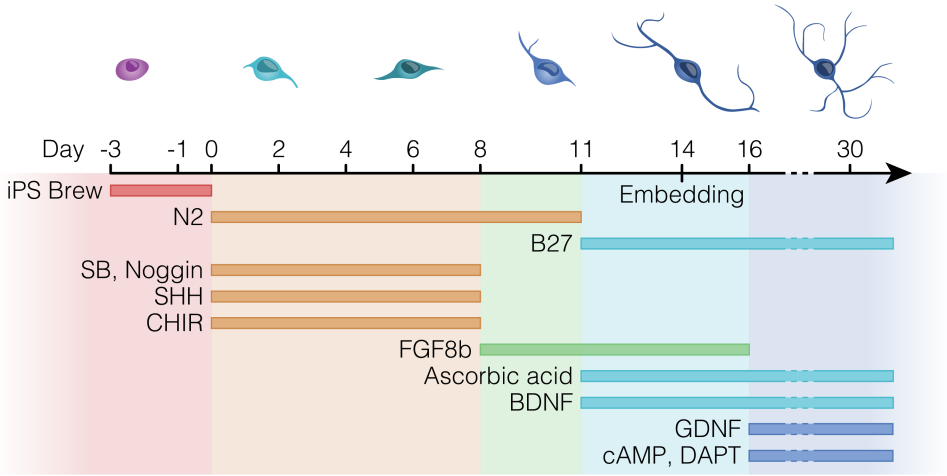

Figure 1 | Schematic overview of the differentiation protocol for the generation of vMB-patterned organoids. The procedure starts with the seeding of hPSCs into U-bottom low-attachment plates three days before the beginning of differentiation. On day 14, developing vMB organoids are embedded in Matrigel to mimic the extracellular matrix of the brain, providing structural support and extrinsic signaling cues.

vMB-patterned brain organoids recapitulate midbrain developmental program

The characterization of these organoids revealed a progressive acquisition of midbrain identity, marked by the expression of key genes, including SOX2, OTX2, FOXA2, and CORIN (Figure 2A-F). At later stages, in parallel with a reduction of growth rate, vMB organoids began expressing markers associated with DA neurogenesis, such as NURR1, NGN2, and TH (Figure 2A-F). While directly aligning the timing of organoid growth *in vitro* with human vMB development *in vivo* remains challenging, the sequential expression of early- and late-stage genes suggests a developmental progression

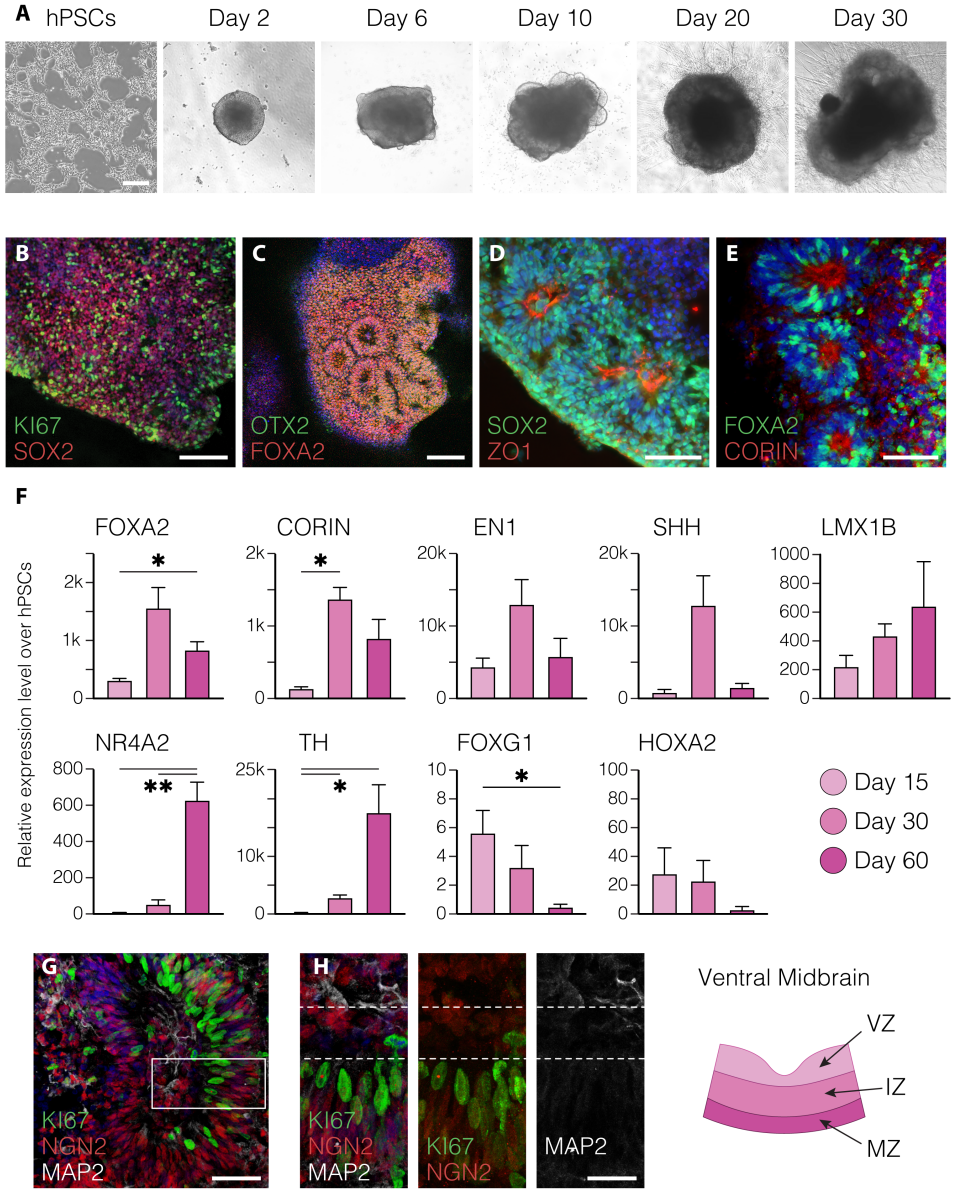

Figure 2 | Cellular organization of developing vMB organoids.

A) Representative bright field pictures of vMB organoids at different stages of maturation. Scale bars 200 µm. B-E) Immunofluorescence staining of key markers of developing vMB (FOXA2, OTX2, CORIN) as well as cycling progenitors (SOX2, KI67, ZO1). Scale bars 100 µm (B,C,E), 50 µm (D). F) Relative expression (qRT-PCR) of selected vMB, FB, and hindbrain genes across vMB organoid differentiation. Data is presented as mean ± SEM and normalized over undifferentiated hPSCs. G,H) Immunohistochemistry of KI67, NGN2 and MAP2 in vMB organoids at day 15. Scale bar 100 µm (G), 50 µm (H).

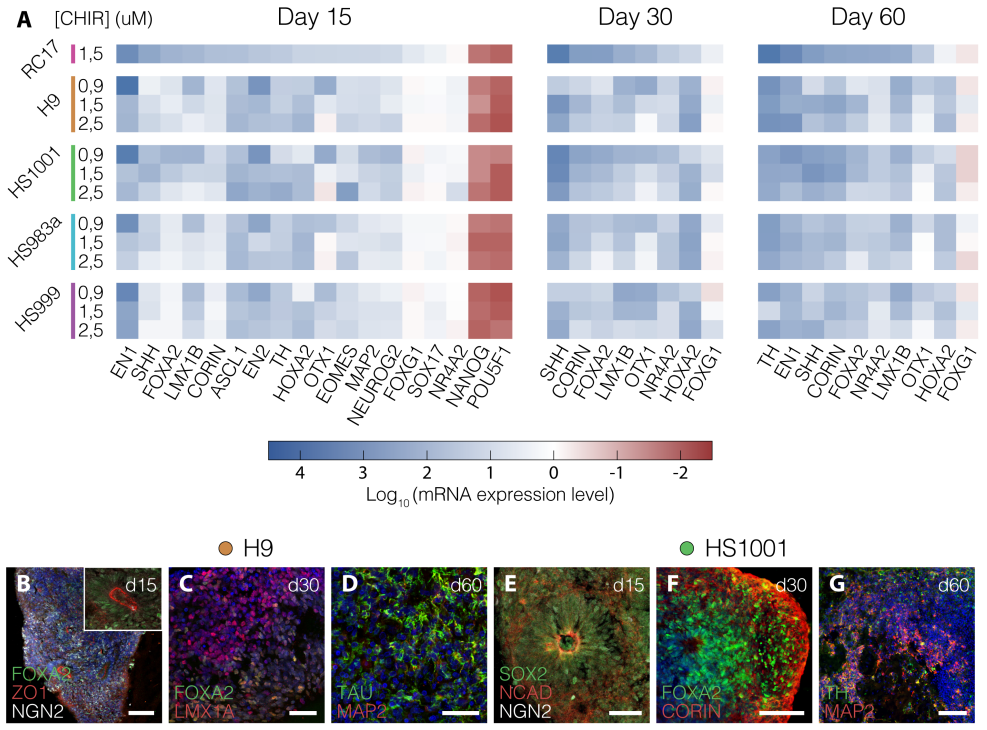

Figure 3 | Patterning of multiple hPSC lines into vMB organoids.

A) Heatmap depicting expression levels of selected markers in vMB organoids generated from four hPSC lines (H9, HS1001, HS983a, HS999). RC17 values are here reported as an internal control. Three different concentrations (0.9 μM, 1.5 μM, and 2.5 μM) of CHIR99021 were tested for each cell line. B-G) Immunohistochemistry of vMB organoids at different developmental stages derived from H9 (B-D) or HS1001 (E-G). Scale bars 100 μm (B,F), 40 μm (C,D,E) and 200 μm (G).

similar to what is observed during the patterning of human midbrain (Arenas et al., 2015). The expression of midbrain markers during early stages coincided with the formation of radially organized structures, resembling the layered cytoarchitecture of neural rosettes (Figure 2C-E). These structures mirrored the organization of the developing human vMB, including the spatial segregation of $KI67^{+}$ cycling cells in the basal layer and the enrichment of progenitors undergoing neurogenesis ($NGN2^{+}$ and $MAP2^{+}$) on the apical side (Figure 2G,H).

To assess the robustness of our protocol, we generated vMB organoids from four additional hPSC lines, achieving similar results (Figure 3A-G). This is particularly relevant for disease modeling purposes, where it is essential that differentiation protocols work equally in cell lines derived from both healthy individuals and patients. Monolayer differentiations (Nolbrant et al., 2017) showed that different cell lines could exhibit varying sensitivities to the GSK3 inhibitor CHIR99021, here used to activate the WNT pathway and refine the patterning along the anteroposterior axis. To address this, we tested different CHIR99021 concentrations to optimize culturing conditions for each line. At the right concentration, all lines consistently expressed vMB markers, with minimal to no expression

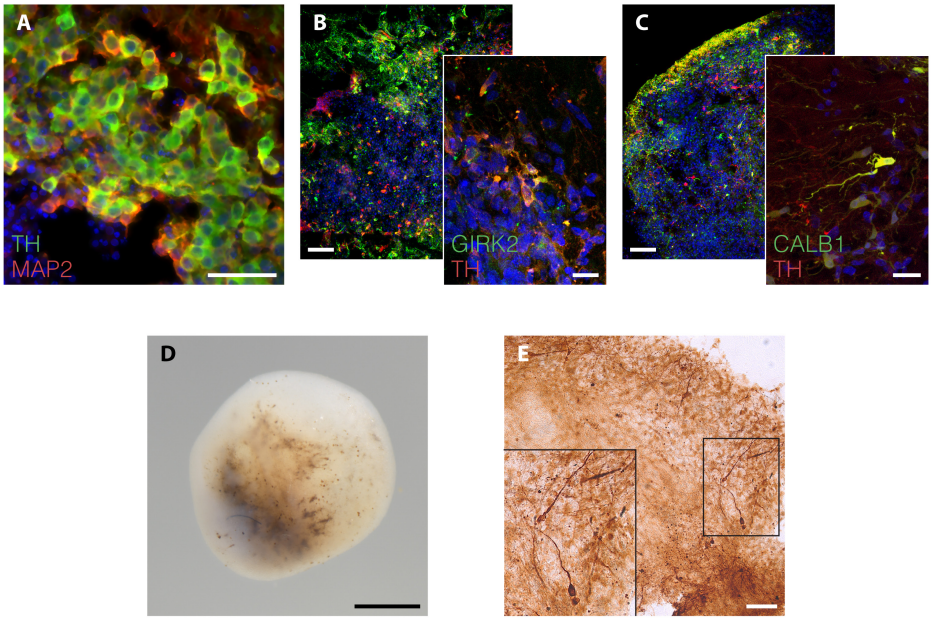

Figure 4 | DA neurogenesis in vMB organoids.

A) Immunohistochemistry of TH and MAP2 in vMB organoids after 60 days of differentiation. Scale bar 50 µm. B,C) Expression of GIRK2 (B) and CALB1 (C) in midbrain DA neurons at day 60. Scale bars 100 µm, inset 50 µm. D) Representative overview of pigmented vMB organoids after 8 months in culture. Scale bar, 1 mm. E) Immunohistochemistry staining of neuromelanin and TH in vMB organoids at day 120 of differentiation. Scale bar, 20 µm.

of forebrain, hindbrain, or pluripotency genes, and maintained the characteristic cytoarchitectural organization (Figure 3A-G).

After 60 days of differentiation, the co-expression of TH and MAP2 indicated the presence of post-mitotic DA neurons in vMB organoids (Figure 4A). Immunostaining for GIRK2 and CALB1, markers traditionally associated with A9 and A10 DA neuron subtypes respectively, confirmed the presence of diverse DA neuron subpopulations in the organoids (Figure 4B,C). Moreover, the detection of intra- and extracellular neuromelanin granules suggested the specification of a subset of DA neurons toward an A9-like identity (Figure 4D,E). These characteristic dark granules, which give the *substantia nigra* its name, are typically considered one of the features of mature DA neurons and have been observed in vMB organoids after at least 4 months in culture (Figure 4D,E).

Single-cell transcriptomics reveals DA neuron diversity in vitro

To characterize the cellular composition of vMB organoids over time (days 15–120), we profiled their transcriptome at single-cell resolution, revealing an array of different cell types (Figure 5A).

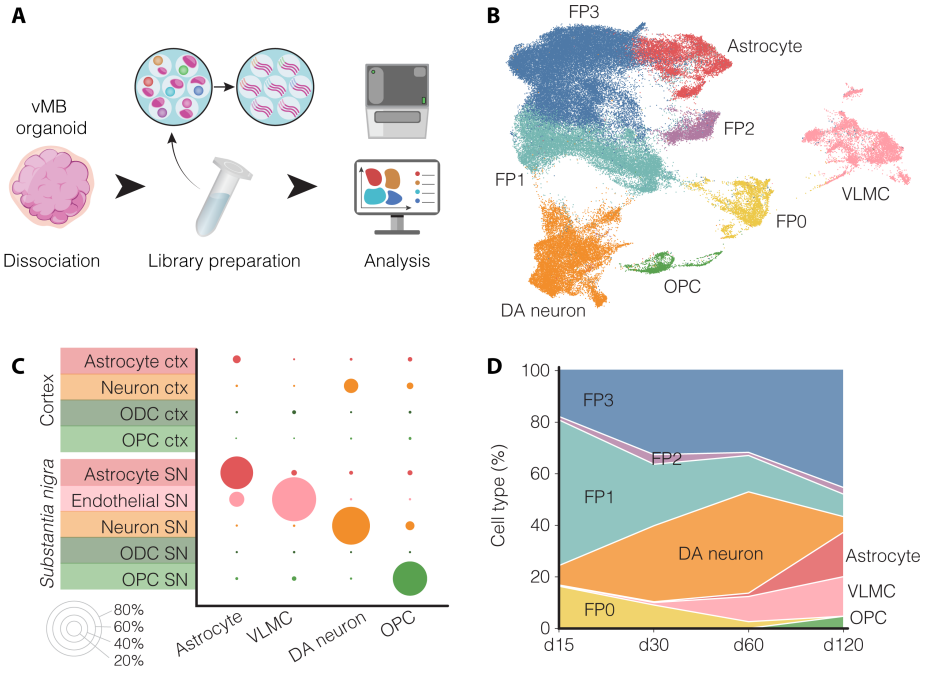

Figure 5 | Single-cell profiling of vMB organoid differentiation.

A) Schematic illustration of the time course profiling strategy. vMB organoids were collected at day 15, 30, 60, 90, and 120 of differentiation, and analyzed via single-cell RNA sequencing. B) Scatterplot of uniform manifold approximation and projection (UMAP) embeddings showing cellular heterogeneity in vMB organoids. C) Transcriptional similarity between vMB organoid populations and human vMB and cortex. ODC, oligodendrocytes. D) Relative proportions of cell types during vMB organoid differentiation, from day 15 to day 120.

The majority of cells identified were FP progenitors at various stages of maturation and cell cycle (FP0-FP3) (Figure 5B). Additionally, mature cell populations were detected, including DA neurons, oligodendrocyte precursor cells (OPCs), astrocytes, and vascular leptomeningeal cells (VLMCs) (Figure 5B). Interestingly, nearly all neurons expressed markers related to DA neurogenesis. This indicates that while the differentiation protocol can successfully recapitulate many cellular components of the vMB niche, neuronal differentiation is restricted to the DA lineage, reflecting a more limited diversity than the neuronal populations typical of adult human vMB. To validate the midbrain identity of the identified cell types, we compared their transcriptomic profiles with published data from human midbrain and cortex (Agarwal et al., 2020) (Figure 5C). Notably, all cell types in the vMB organoids demonstrated significantly higher transcriptional similarity to their counterparts in the human midbrain than to the cortex, thus confirming their correct patterning (Figure 5C). Moreover, as previously observed via immunohistochemistry, the emergence of cell types followed a specific temporal progression: FP progenitors appeared first, followed by DA neurons, and later on by VLMCs, astrocytes, and OPCs (Figure 5D).

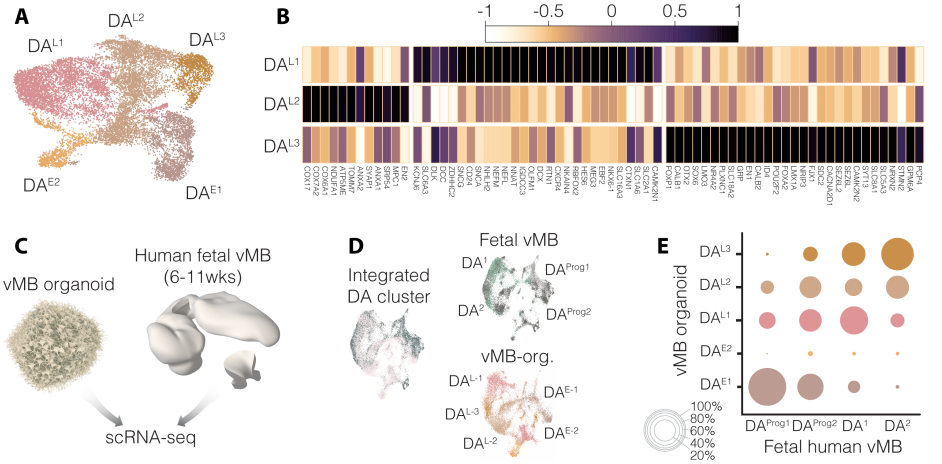

Figure 6 | Mapping DA neuron diversity in vMB organoids.

A) UMAP plot of DA neuron cluster in isolation, subdivided into 5 distinct molecular populations. B) Heatmap depicting differentially expressed genes between the three *DA late* clusters. C) Illustration of the comparison strategy between vMB organoid and human fetal datasets. D,E) Integrated and individual UMAP plots representing DA neuron subtypes in vMB organoids and human fetal tissue (D) and relative overlapping quantification (E).

The emergence of mature DA neurons in high numbers in vMB organoids allowed an in-depth analysis of their developmental trajectories and diversity. While all DA neurons expressed *TH*, high-resolution analysis of this cluster in isolation revealed five distinct subpopulations: two with more immature features, termed *DA early*, and three more mature subtypes, named *DA late* (Figure 6A). Despite sharing a broadly similar expression profile, the clusters´ transcriptomes differed for a set of features (Figure 6A,B). Interestingly, markers enriched in the SNpc, such as *KCNJ6* (GIRK2), *SNCA*, and high levels of *SLC6A3* (DAT), were characteristic of the DA-late 1 cluster. In contrast, the DA-late 3 cluster expressed genes enriched in the VTA, including *CALB1, OTX2, FOXP1*, and *LMO3* (Figure 6B). DA-late 2 cluster instead displayed a different molecular profile that did not align with either A9 or A10-like cells, characterized by the expression of *EN2*, the synapse-associated protein *SYAP1*, and mitochondrial-related genes (*COX17, NDUF, MPC1,* and *ATP5ME*) involved in ATP production (Figure 6B). Many of the markers mentioned in this analysis were also identified in previously published datasets from bulk and single-cell RNA sequencing of mouse vMB DA neuron populations (Hook et al., 2018; Kramer et al., 2018; Poulin et al., 2014; Saunders et al., 2018; Tiklova et al., 2019). The correspondence between DA neuron subtypes in vMB organoids and data from human fetal vMB (6–11 weeks post-conception, (Birtele et al., 2022) further validated the authenticity of these neurons and underscores the relevance of these models to investigate human DA neurogenesis (Figure 6C-E). This dataset represents a powerful resource to investigate the mechanisms involved in human DA neurons subtype specification, fundamental for more targeted and effective differentiation strategies for cell replacement therapy for PD.

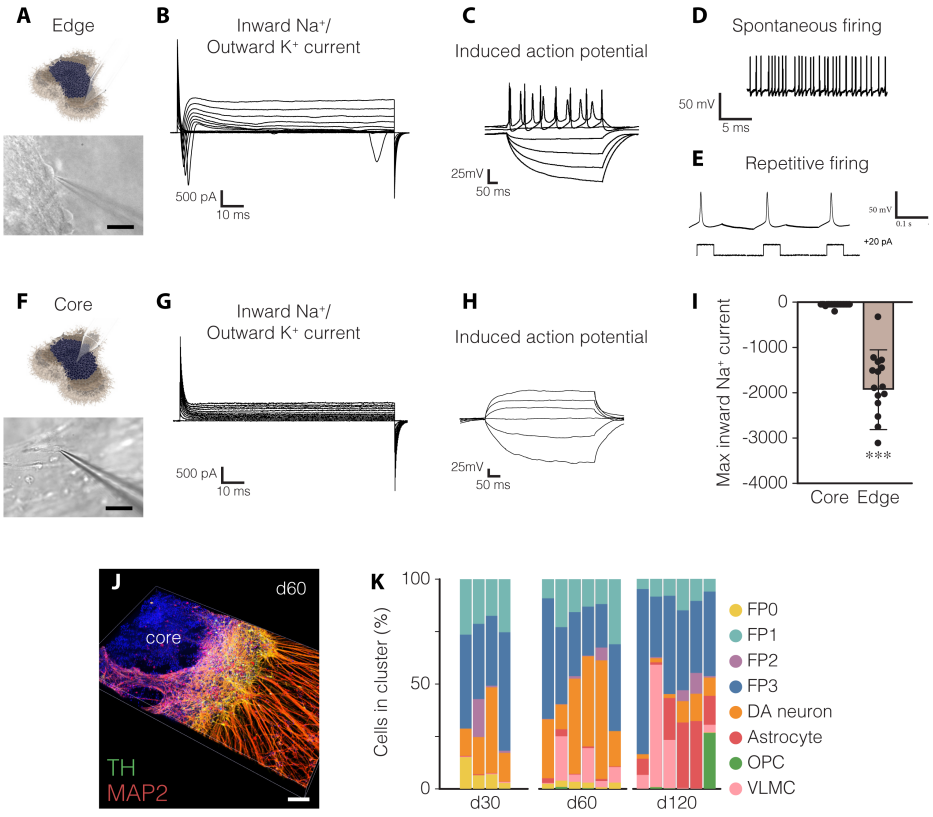

Figure 7 | Functional characteristics of vMB organoids.

A-E) Neurons on the edge of vMB organoids at day 90 displayed functional characteristics of DA neurons, including inward Na^+ and outward K^+ currents (B), multiple induced action potentials (C), spontaneous activity (D) as well as rebound depolarization (E). Scale bar 100 μm. F-H) Representative traces from whole-cell patch recordings of cells in the inner core of vMB organoids at day 90; inward Na^+/outward K^+ currents (G), evoked action potential (H). I) Maximum inward sodium current in neurons in the edge or the core of vMB organoids. Unpaired two-tailed t-test, p=0.0007. J) Confocal three-dimensional reconstruction of vMB organoid stained for TH and MAP2 at day 60. Scale bar 100 μm. K) Bar plots depicting relative cell composition of individual vMB organoids after 30, 60, and 120 days in culture.

Molecular and functional heterogeneity of conventional vMB organoids

In parallel with the characterization at the transcriptional level, we proceeded to investigate the functionality of DA neurons generated within vMB organoids. Whole-cell patch-clamp recordings of neurons in the outer regions of vMB organoids revealed mature electrophysiological properties, including Na^+ and K^+ currents, the ability to fire evoked action potentials, as well as spontaneous and repetitive firing – characteristic of mature DA neurons (Figure 7A-E). However, such features were absent in cells within the organoid core, which exhibited an immature phenotype lacking any sign of

activity (Figure 7F-I). This functional heterogeneity arises from structural limitations of vMB organoids, where incomplete differentiation in the inner regions is often accompanied by cell death (Figure 7J). Beyond this intra-organoid variability, we also observed significant inter-organoid differences in cell composition, hampering the use of vMB organoids for reliable modeling of developmental and physiological features (Figure 7K).

Advancing brain organoid technology with recombinant silk microfibers (Paper I and III)

The biophysical characteristics of human brain organoids limit oxygen and nutrient diffusion in the inner part of cell cultures, impairing cell viability and neuronal differentiation (Pasca, 2019). The introduction of biomaterial-based scaffolding can create a more favorable environment for hPSC self-organization and differentiation toward neuroectodermal fates, thus reducing hypoxia and incomplete differentiation in the inner organoid regions (Lancaster et al., 2017; Rothenbucher et al., 2021). In this context, spider silk represents a unique biomaterial with excellent mechanical properties and biocompatibility, easy to handle, and can be assembled in a three-dimensional scaffold to support organoid formation and maturation (Rising et al., 2011; Widhe et al., 2016).

Generation and characterization of silk-bioengineered organoids

Spider silk functionalized with full-length human laminin 111 - an extracellular matrix protein critical for neuronal adhesion in the brain - was utilized to generate bioengineered organoids. The scaffold was formed by introducing air bubbles into silk protein droplets through repeated pipetting, which induced the polymerization into fibers along the bubble walls (Figure 8A-C). This process gradually created a three-dimensional fiber network with microcavities that acted as a passive vasculature structure (Figure 8D). Then, hPSCs were dispersed into the foam, where they adhered to the self-supporting scaffold while anchored to the plate's surface (Figure 8A,C). Unlike floating scaffolds, this method offered better control over cell distribution within the foam, ensuring an optimal cell-to-silk ratio. The generation of bioengineered silk organoids is, therefore, a straightforward and versatile procedure, compatible with most high-throughput applications.

To evaluate the impact of silk scaffolds on hPSC self-organization and patterning, we employed an unguided protocol for generating mature cerebral organoids, providing minimal external cues to preserve the hPSC self-morphogenesis properties. Scanning electron microscopy (SEM) revealed that the silk fibers polymerized into flat sheets approximately 1 μm thick, exhibiting a nano topography that facilitates cell adhesion (Figure 8E,F). After 60 days of differentiation, the emergence of neurons was also observed, with the silk scaffold effectively supporting axonal outgrowth (Figure 8G).

Silk scaffolding enhances neural induction and maturation

While unguided differentiation protocols are ideal for studying the early stages of development and the self-organization of hPSCs, they are often hindered by spontaneous differentiation toward

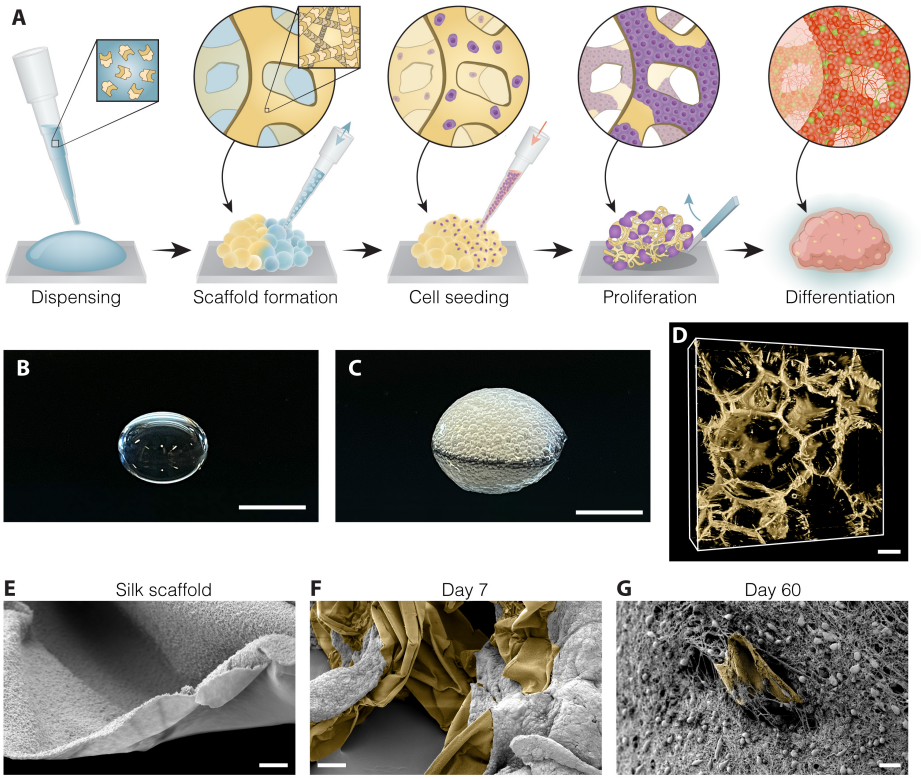

Figure 8 | Generation of silk bioengineered organoids.

A) Schematic illustration of the steps involved in spider silk organoid formation. B,C) Representative pictures of silk droplets before (B) and after (C) scaffold polymerization. Scale bar, 5 mm. D) Confocal image reconstruction of the polymerized 3D silk scaffold after bubbles burst. Scale bar, 100 μm. E-G) SEM imaging of silk scaffold alone (E), with adherent hPSCs (F), and neurons (G) at different stages of organoid differentiation. Scale bars 5 μm (E), 50 μm (F), 20 μm (G).

mesodermal and endodermal cell fates (Lancaster et al., 2017; Lancaster & Knoblich, 2014b; Lancaster et al., 2013) (Figure 9A-C). These "contaminant" cells are typically restricted to localized niches and represent a small proportion of the overall organoid. However, their maturation into undesired cell types can confound the interpretation of developmental and pathological studies and increase the variability of organoid models. Interestingly, such contaminant cells were absent in silk-based brain organoids, denoting a more homogeneous differentiation toward neuroectodermal fates (Figure 9D-F). Consistent with this observation, bulk RNA sequencing data comparing silk and non-silk organoids at day 20 revealed reduced expression levels of genes associated with pluripotency and mesodermal/endodermal-derived structures, such as kidney, skeletal system, and blood vessels in bioengineered silk organoids (Figure 9G). On the other hand, genes upregulated in silk brain organoids were consistently linked to early neuroectodermal differentiation and neurogenesis (Figure 9G).

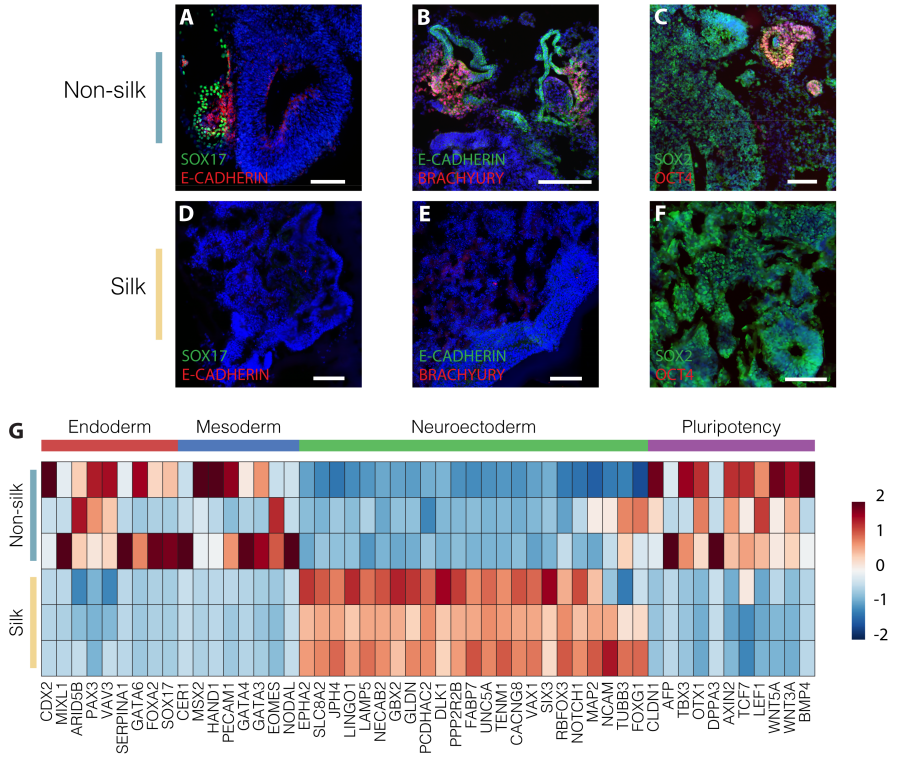

Figure 9 | Silk scaffolding reduce hPSC spontaneous differentiation in cerebral organoids.

A-F) Immunohistochemistry of SOX17 (endoderm), E-Cadherin (non-neural ectoderm), Brachyury (mesoderm), OCT4 (pluripotency) and SOX2 (pluripotency and neuroectoderm) in conventional (A-C) and silk (D-F) brain organoids at day 20. Scale bars 100 μm (A,C,D,E,F), 200 μm (B). G) Heatmap representing expression levels (bulk RNA-seq) of selected markers of pluripotency and neuroectoderm, mesoderm, and endoderm differentiation in three silk and three non-silk brain organoids at day 20.

Importantly, the presence of silk in bioengineered organoids did not appear to disrupt hPSC morphogenesis or the formation of early neural rosette-like structures, as confirmed by immunohistochemistry (Figure 10A,B). During the differentiation, the same dorsal and ventral progenitor populations emerged in both silk and non-silk brain organoids, following a similar temporal pattern (Figure 10C-F). Upon complete maturation, brain organoids from both groups contained diverse neuronal populations, including glutamatergic and GABAergic neurons (Figure 10G-L). Overall, silk scaffolding does not disrupt the inherent neuronal differentiation trajectories or the acquisition of forebrain identities.

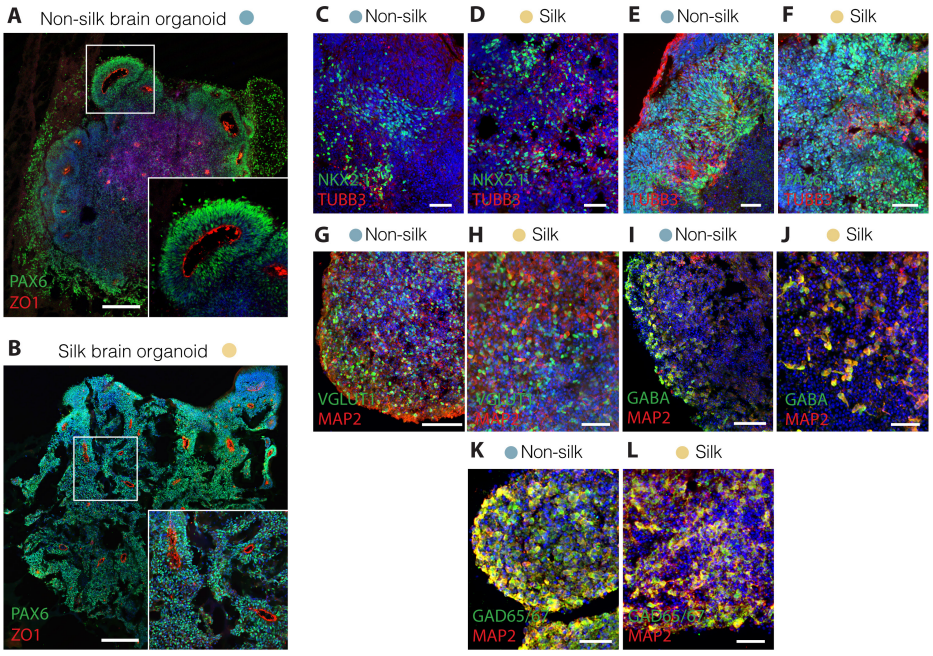

Figure 10 | Silk scaffolding supports hPSC self-organization and differentiation toward forebrain cell fates.

A,B) Neural rosette-like structures in conventional (A) and silk (B) brain organoids at day 20, positive for PAX6 and ZO1. Scale bars 200 µm. C-F) Cryosections of cerebral organoids at day 30 showing ventral (C,D; NKX2.1/TUBB3) or dorsal (E,F; PAX6/TUBB3) forebrain progenitors at day 30. Scale bars 50 µm. G-L) Immunohistochemistry of vGLUT1, GABA, GAD67 and MAP2 in silk and non-silk brain organoids at day 120 of differentiation. Scale bars 50 µm. Nuclei were stained with DAPI.

The presence of neuronal subtypes observed in silk and conventional organoids was further validated using single-cell RNA sequencing after four months in culture (Figure 11A,B). Transcriptomic profiling at single-cell level also identified additional cell populations in both silk and non-silk organoids, including astrocytes, OPCs, and mural cells (Figure 11A,B). Mural cells, a mesoderm-derived cell type associated with vasculature, are essential for maintaining the structural integrity of blood vessels and regulating vascular functions. Notably, this cell type was almost entirely absent in silk brain organoids, aligning with previous observations on the reduced presence of mesodermal progenitors, and further validated by immunofluorescence staining (Figure 11C-E). In contrast, silk brain organoids exhibited a significantly higher proportion of cells with neuronal identities, comprising approximately 80% of the total cell population (Figure 11C).

Notably, whole-cell patch-clamp recordings confirmed the functionality of neuronal populations in both organoid cultures at day 90. While neurons within conventional brain organoids could only fire single evoked action potentials at this stage, neurons grown on silk scaffolds fired multiple action potentials, indicating a higher degree of maturation (Figure 12A). Furthermore, the presence of spontaneous activity in silk brain organoids demonstrated the ability of such neurons to form functional synaptic networks and establish complex circuitries (Figure 12B).

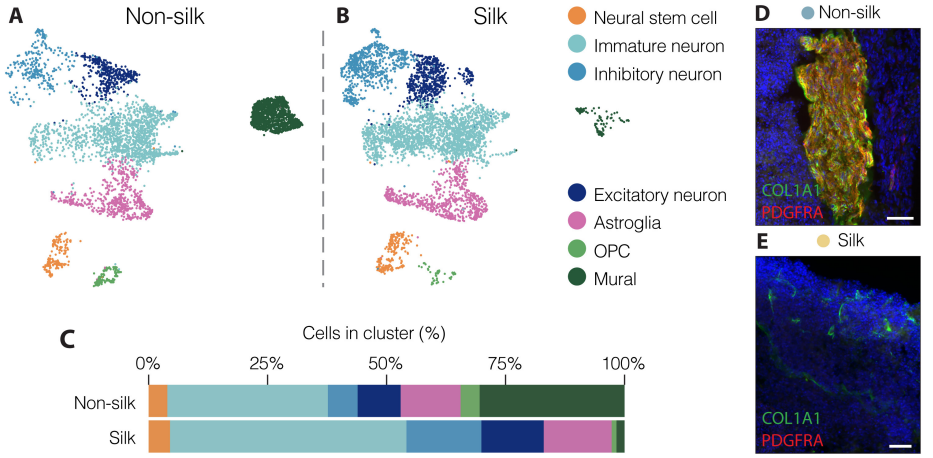

Figure 11 | Single cell transcriptomic profiling reveals a reduction of mural cells in silk brain organoids.

A-C) UMAP plots representing the cell populations composing silk and non-silk brain organoids after 120 days of differentiation, and their relative proportion. D,E) Sections of conventional (D) and bioengineered (E) brain organoids at day 120 stained for mural cell markers COL1A1 and PDGFRA. Scale bars 50 µm.

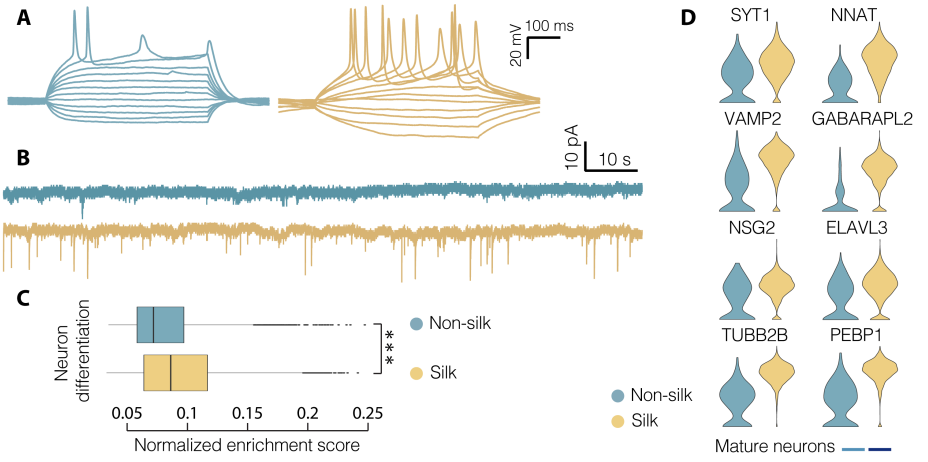

Figure 12 | Silk scaffolding promotes neurons' functional maturation.

A,B) Representative traces of induced action potential (A) and spontaneous activity (B) of cells in silk and non-silk organoids at day 90. C) Gene set enrichment analysis (GSEA) for genes associated with the Gene Ontology (GO) term Neuron maturation in the two organoid cultures. *** $p < 0.001$, two-tailed Wilcoxon rank sum test. D) Expression of selected mature neuronal markers in conventional and bioengineered cerebral organoids at day 120 of differentiation.

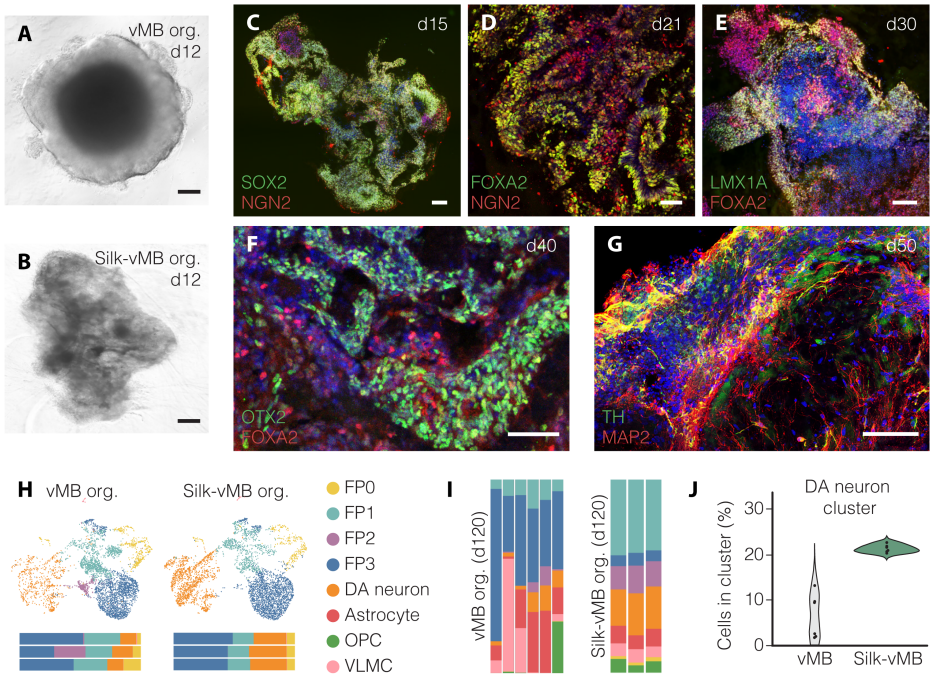

Figure 13 | Generation and molecular characterization of silk vMB organoids.

A,B) Brightfield images of vMB organoids at day 12, cultured with or without silk scaffold. Scale bars, 100 µm. C-G) Cryosections of silk vMB organoids at different stages of differentiation, stained for various markers: SOX2/NGN2 (C), FOXA2/NGN2 (D), FOXA2/LMX1A (E), OTX2/FOXA2 (F) and TH/MAP2 (G). Scale bars, 100 µm (D,F,G), 50 µm (C,E). H,I) UMAP plots showing the distinct cellular populations present in silk and non-silk vMB cultures at day 30 (H) or day 120 (I) of differentiation. Below, the bar charts display the relative cluster composition of individual organoids derived from the two culture conditions. J) Violin plot illustrating the percentage of DA neuron cluster in individual silk and non-silk vMB cultures.

These mature electrophysiological properties were also supported by transcriptional data, which revealed an upregulation of genes associated with neuronal maturation and synaptic activity in silk brain organoids (Figure 12C,D). Overall, these findings suggest that silk scaffolding promotes the formation of functionally mature neurons in unguided cerebral organoids, demonstrating the potential of this multidisciplinary approach to enhance the development and functionality of brain organoids.

Silk scaffolding is compatible with guided differentiation protocols and reduces inter organoid variability

The differentiation strategy employed for the generation of silk brain organoids showed so far relied on minimal external patterning cues. However, to ensure broad applicability, it is essential that silk scaffolding is also compatible with guided differentiation protocols, without interfering with developmental trajectories and the generation of desired cell types. To address this, we differentiated hPSCs on silk scaffolds functionalized with laminin-111 toward vMB fate, following the same differentiation protocol previously established for conventional 3D cultures (Figure 13A,B). Silk-based

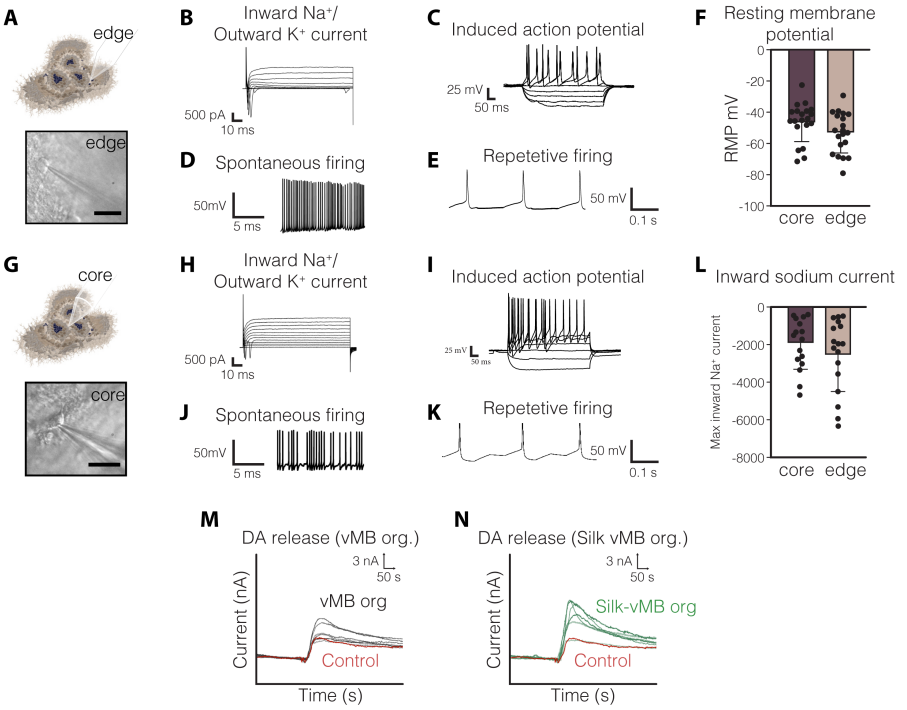

Figure 14 | Functional homogeneity of silk vMB cultures.

A-E) Representative traces from whole-cell patch recordings of neurons in the outer region of silk vMB organoids at day 90. At this stage, inward Na^+ and outward K^+ currents (B), multiple induced action potentials (C), spontaneous activity (D) and repetitive firing (E) were observed. Scale bar 100 µm. F) Resting membrane potentials of cells localized in the outer or inner layers of silk vMB organoids at day 90, presented as mean ± SD. G-K) Corresponding representative traces from cells in the inner core of silk vMB organoids at day 90. Unlike conventional non-silk cultures, these neurons exhibited mature electrophysiological properties, with virtually no differences with neurons recorded from outer organoid areas. Scale bar 100 µm. L) Quantification of maximum inward sodium currents in neurons across different regions of silk vMB organoids. M,N) Real-time DA exocytosis measurements via chronoamperometry in silk and non-silk vMB organoid cultures.

vMB organoids exhibited expression patterns consistent with previous observations on non-silk vMB cultures, with key midbrain differentiation markers such as FOXA2, LMX1A, OTX2, and NGN2 expressed in a similar temporal sequence (Figure 13C-F). Later on, the co-expression of TH and MAP2 underscored the emergence of midbrain DA neurons in silk vMB organoids (Figure 13G). Similar to forebrain-patterned organoids, the silk scaffold did not appear to impact the differentiation process, making this approach compatible with guided differentiation protocols as well.

Single-cell RNA sequencing further validated the presence of the expected cell populations at both early (day 30) and late (day 120) stages of differentiation, including FP progenitors, DA neurons, OPCs, astrocytes, and VLMCs (Figure 13H,I). Notably, comparisons across three biological replicates of silk vMB organoids revealed a remarkable consistency in cell type proportions, significantly reduc-

ing the inter-organoid variability typically observed in conventional cultures (Figure 13H,I). More importantly, the percentage of DA neurons in bioengineered vMB organoids was consistently higher than non-silk cultures, with limited organoid-to-organoid fluctuations (Figure 13J).

Similar to their non-silk counterparts, neurons in the outer layer of silk vMB organoids exhibited mature electrophysiological characteristics, including spontaneous and repetitive firing (Figure 14A-E). Notably, similar features were also observed in the inner regions of silk vMB organoids, with minimal differences between neurons located in different areas of the culture (Figure 14F-L). To further validate the DA identity of neurons in both culture conditions, we performed real-time chronoamperometry to measure DA exocytosis from axonal terminals (Figure 14M,N). Consistent with prior findings, the currents recorded in silk vMB organoids were consistently larger and with lower variability than conventional vMB samples (Figure 14M,N). These results suggest that while the overall neuronal maturation levels in silk and non-silk vMB organoids are comparable, the bioengineered cultures represent a more robust platform for generating functionally mature DA neurons *in vitro*.

Bioengineered organoids exhibit a reduced intra-organoid variability, oxidative stress and interior hypoxia.

The incorporation of silk scaffolds into organoid cultures significantly enhances functionality and homogeneity compared to non-silk counterparts following both guided and unguided differentiation protocols. These improvements suggest that silk scaffolding might provide more favorable culturing conditions. Indeed, colorimetric assays confirmed higher cell viability in silk-based brain organoids, even after extended culture periods of up to six months (Figure 15A). Furthermore, markers of apoptosis and DNA damage, which are commonly observed in the core regions of conventional organoids, were essentially absent in silk-based organoids (Figure 15B–E). Additionally, levels of hypoxia-inducible factor-1 alpha (HIF-1α), a protein upregulated in low-oxygen conditions, were significantly reduced in silk organoids (Figure 15F).

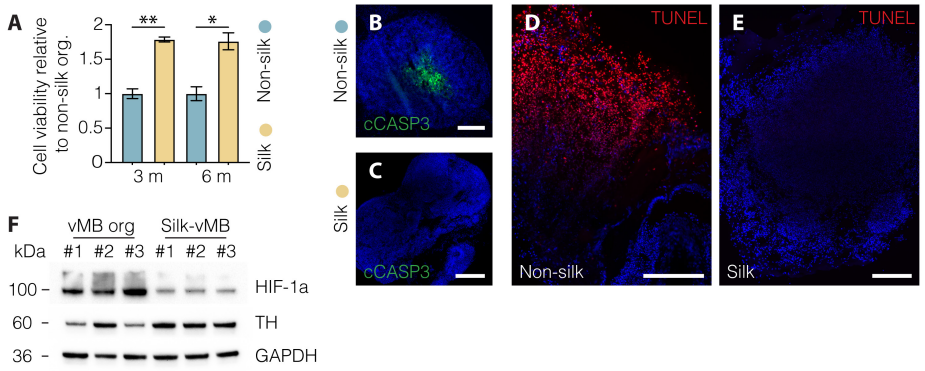

Figure 15 | Silk scaffolding reduces organoid necrotic core.

A) Cell viability assay in silk and non-silk brain organoids at 3 and 6 months of differentiation. B,C) Cryosections of brain organoids stained for cleaved caspase 3, a marker of apoptosis at day 120. Scale bars 200 μm (B) and 400 μm (C). D,E) DNA damage visualized via TUNEL staining in silk and non-silk cultures at day 120. Scale bars 200 μm. F) Western blot of HIF1-α protein, TH and GAPDH in vMB organoids with and without silk scaffolds in normoxia conditions (21% O_2).

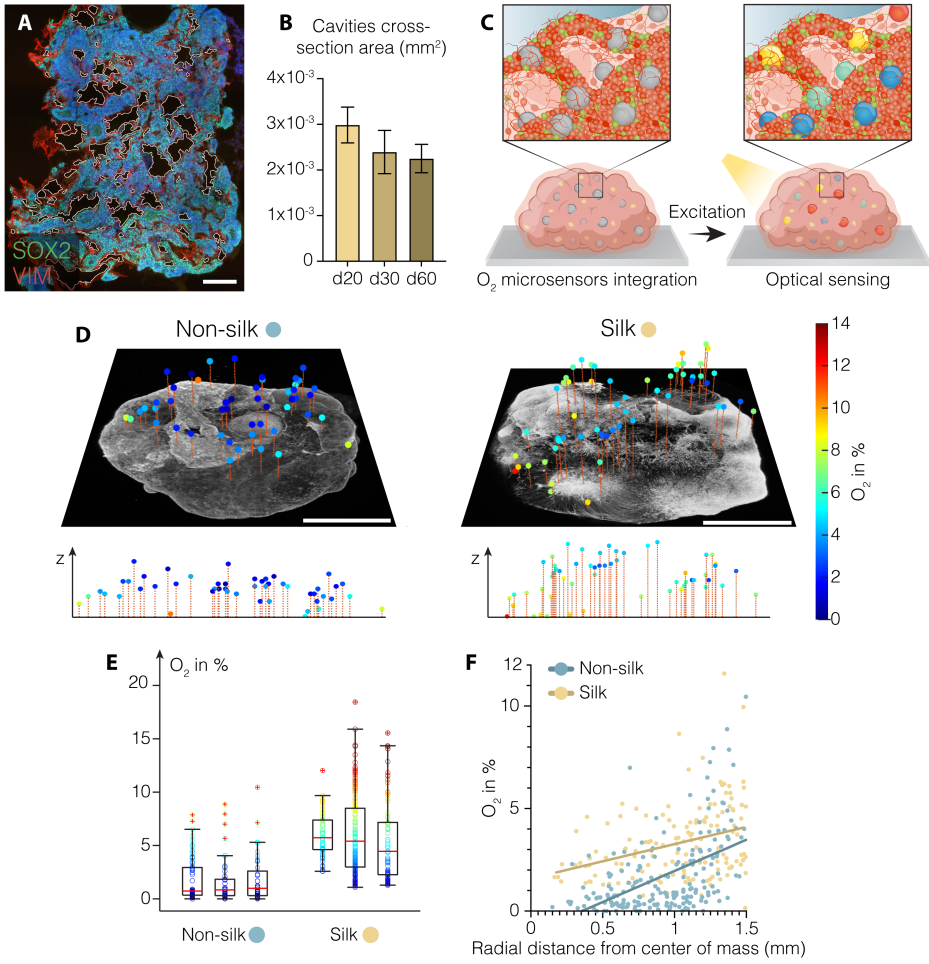

Figure 16 | Microcavities facilitate oxygen distribution in silk brain organoids.

A,B) Visualization of internal cavities and quantification of their cross-sectional area in silk brain organoids. Data represent mean ± SEM obtained from 3 individual organoids per time-point. Scale bar 250 µm. C) Illustration of oxygen microsensors integration in human brain organoids. D) Three-dimensional oxygen tension maps of silk and non-silk brain organoids overlayed with live cell imaging. Scale bars, 1mm. E) Quantification of oxygen distribution in 3 biological replicates per condition. Color represents the oxygen levels detected (%). F) Correlation between oxygen tension and distance from the organoid center of mass in silk and non-silk brain organoids at day 60.

These findings suggest that the microcavities created by the silk scaffolds facilitate oxygen and nutrient diffusion into the inner regions of the organoids, thus providing a more favourable environment for neuronal differentiation and maturation (Figure 16A,B). To investigate this hypothesis, we employed optical microsensors to map the 3D oxygen tension distribution in silk and non-silk organoids (Wesseler et al., 2022) (Figure 16C). As expected, the overall oxygen levels were significantly

higher in silk-scaffolded organoids, and in the physiological oxygenation range of human brain tissue (Figure 16D,E). Furthermore, the spatial distribution of oxygen tension from the core to the edges was more uniform in silk-based organoids compared to their non-silk counterparts (Figure 16F).

These results underscore the ability of the silk scaffold's microarchitecture to facilitate oxygenation throughout the organoid, promoting cell survival and creating an improved environment for neurogenesis. The reduced inter- and intra-organoid variability represents a significant advantage for many applications, such as developmental studies, disease modeling, and drug screening. Compared to previously published bioengineering approaches, silk scaffolding represents an simpler and easily adaptable three-dimentional approach (Lancaster et al., 2017; Rothenbucher et al., 2021). Furthermore, silk scaffolds are compatible with diverse differentiation protocols and both hESC and iPSC lines, making them a versatile tool for achieving uniform differentiations across patient-derived and healthy cell lines.

Defining molecular profile of human DA neuron subtypes by their target specificity (Paper IV)

As described so far, organoids have emerged as a powerful model for recapitulating key aspects of human brain development *in vitro*, including the specification and diversity of DA neurons. Incorporating silk scaffolds into organoids has further advanced these models, improving cell viability, oxygenation, and promoting neuronal differentiation and maturation. Nevertheless, organoids lack the anatomical landmarks defining neuronal subtypes residing in distinct brain nuclei . This limitation is particularly relevant for distinguishing DA subtypes in vitro, as no definitive set of markers reliably separate A9 and A10 subpopulations, and the few identified so far are not exclusive to one class or the other.

The advent of single-cell RNA sequencing enabled detailed profiling of human and mouse midbrain DA neurons, revealing a greater diversity than expected (Agarwal et al., 2020; Birtele et al., 2022; Kamath et al., 2022; La Manno et al., 2016; Poulin et al., 2020; Poulin et al., 2014; Tiklova et al., 2019). However, molecular classifications of DA neurons remain inconsistent across different studies, and often lack a direct correlation with the neurons' anatomical locations or projection patterns (Fiorenzano, Sozzi, et al., 2021; Poulin et al., 2020). Therefore, the relationship between DA neuron molecular identities and their topographical location remains unresolved.

hPSC- and fetal-derived progenitors give rise to similar cell type composition in homotopic grafts

To address this challenge, we homotopically transplanted fetal midbrain tissue and hPSC-derived vMB progenitors into a rat lesion model of PD, with the aim of generating a comprehensive map of human DA neuron diversity, linking their transcriptomic profiles to axonal target specificity (Figure 17A,B). Over the course of one year, both fetal and hPSC-derived cells matured into DA neurons able to mediate motor recovery, as assessed by amphetamine-induced rotations (Figure 17C). Grafted neurons from both groups exhibited similar projection patterns, extending axons from the midbrain

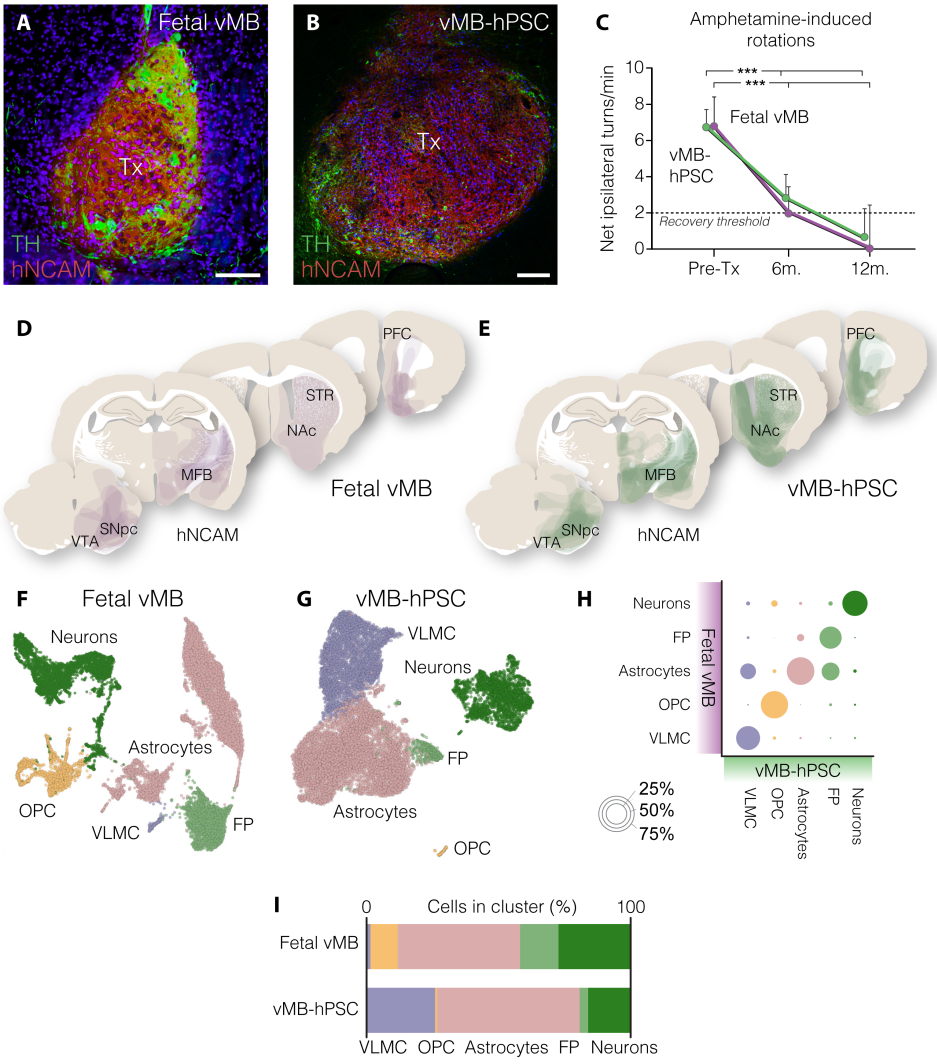

Figure 17 | Fetal and hPSC-derived vMB grafts show a high transcriptional similarity.

A,B) Immunohistochemistry for TH and human-specific NCAM (hNCAM) in human fetal midbrain (A) and hPSC-derived (B) intranigral grafts 12 months post transplantation. Scale bars, 200 µm. C) Motor rotation test demonstrating functional recovery in animals grafted with human fetal tissue or vMB-patterned hPSCs after 6- and 12-months post engraftment. D,E) Composite overlays of hNCAM$^+$ fibers innervating target regions in the host brain. F,G) UMAP plots showing the cellular composition of fetal and vMB-hPSC graft 12 months post transplantation. H) Dot plot demonstrating the transcriptional similarity of cell types in mature grafts derived from the two cell sources. I) Relative proportions of cell types in fetal and hPSC-derived grafts 12 months post-transplantation.

along the medial forebrain bundle (MFB) to key target areas, including the ventral and dorsal striatum, PFC, and amygdala (Figure 17D,E). Single-nucleus RNA sequencing (snRNAseq) of the mature grafts identified multiple cell types, including vMB FP cells, postmitotic DA neurons, astrocytes, OPCs, and VLMCs, resembling previously reported graft compositions (Tiklova et al., 2020) (Figure 17F,G). Interestingly, fetal and vMB-patterned hPSC grafts contained cell types with matching transcriptional profiles, confirming the authenticity of hPSC-derived vMB progenitors, and in line with prior studies demonstrating their equipotency to fetal tissue in preclinical models (Doi et al., 2014; Grealish et al., 2014; Grealish et al., 2015; Kirkeby et al., 2012; Kriks et al., 2011). However, while the proportion of astrocytes and neurons was comparable between the two groups, differences were observed for OPCs and VLMCs: fetal grafts contained more OPCs, while stem cell-derived grafts exhibited a higher VLMC content (Figure 17I).

Single nuclei RNA sequencing defines DA neuron subtypes based on molecular features

To perform a detailed assessment of DA neuron diversity in hPSC-derived grafts, we isolated *TH*$^+$ cells from the neuronal compartment for a high-resolution analysis (Figure 18A). Re-clustering of DA neurons in isolation revealed nine transcriptionally distinct subpopulations (DA-1 to DA-9). All subtypes shared a similar expression profile, including canonical DA markers such as *NURR1, SLC6A3* (DAT), *SLC18A2* (VMAT2), *FOXA2*, and *TH*, but were distinguished by a small subset of differentially expressed genes that defined their respective molecular signatures (Figure 18A). These included genes known to be enriched in A9 DA neurons (*ALDH1A1, KCNJ6* - GIRK2, *SNCA, GFRA1*) and A10 DA neurons (*LMO3, OTX2, NFIB, FOXP2*) as well as others reported in similar datasets (Agarwal et al., 2020; Kamath et al., 2022; La Manno et al., 2016; Poulin et al., 2014; Saunders et al., 2018; Tiklova et al., 2019).

Moreover, a force-directed graph was employed to infer the dynamics of DA neuron specification and the relationships between different populations (Figure 18B). This analysis aligned well with the graft dissection time points, allowing a reconstruction of DA developmental trajectories between

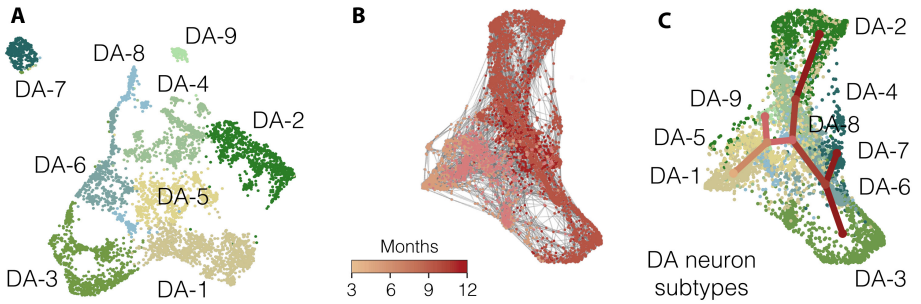

Figure 18 | Human DA neuron diversity in hPSC-derived grafts.

A) DA neuron subpopulations after *TH*$^+$ cells re-clustering. B,C) Slingshot trajectory reconstruction overlaid with a force-directed graph visualizing DA neuron subtypes in stem cell grafts. Pseudocells are color-coded by time point (B) or cell cluster (C).

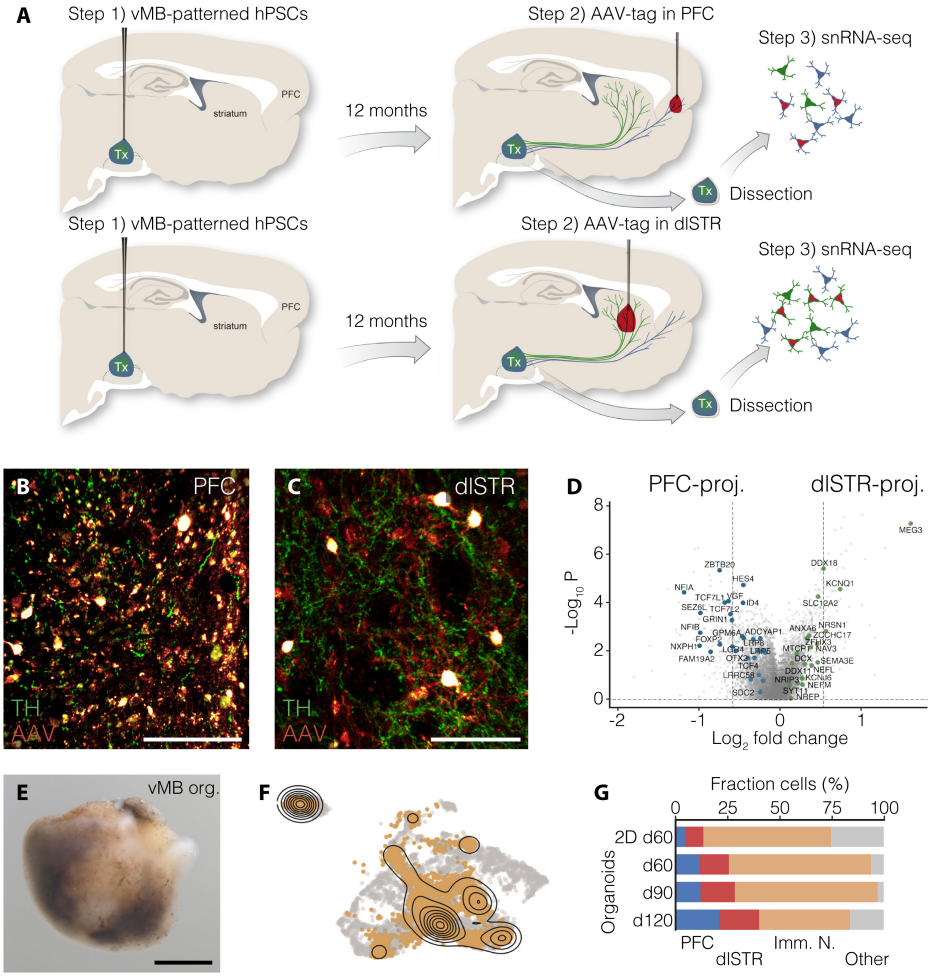

Figure 19 | Target-based snRNAseq profiling of human DA neurons.

A) Schematic illustration of the Target-Seq methodology. B,C) Detection of retrograde AAVs and TH staining in the PFC (B) and dlSTR (C) injection site. Scale bars, 100 µm. D) Volcano plot showing differentially expressed genes between dlSTR- and PFC-projecting DA neurons. E) Bright field picture of mature vMB organoid after 2 years in culture. Scale bar, 1 mm. F) Projection of vMB organoid-derived DA neurons dataset over the *in vivo* DA diversity map. G) Proportion of DA neurons in vMB organoids mapping with PFC- or dlSTR-projecting transcriptomes from hPSC-derived grafts.

3- and 12-months post-engraftment (Figure 18B,C). However, despite the high resolution achieved with snRNAseq, as in previous studies, it was not possible to directly correlate DA neuron molecular identities with their target specificity, functional roles, or vulnerability to diseases.

Target-Seq links the identities of DA neuron subtypes with their projection patterns

In order to link the molecular identities of human DA neuron subtypes with their projection patterns in the host brain, we utilized adeno-associated viruses (AAVs) engineered for retrograde transport in DA neurons (Figure 19A). These AAVs were designed to carry a fluorescent reporter gene (mCherry), effectively tagging the DA neurons in the graft that picked up the virus, and a barcode for identification upon sequencing (Figure 19A-C). In an homotopic transplantation setup, after human DA neuron fibers had extended to their forebrain targets (11 months post-tx), we injected AAVs into two specific regions: the dlSTR, the primary target of A9 DA neurons residing in the SNpc, and the PFC, a key target of A10 DA neurons (Figure 19A). The virus entered human DA fibers at these injection sites and was retrogradely transported back to the soma, effectively labeling the cells projecting to each target (Figure 19A-C). By snRNAseq, we were then able to distinguish dlSTR-projecting DA neurons from PFC-projecting ones, achieving, for the first time, a direct association between molecular identity and projection pattern in human DA neurons (Figure 19D).

The dlSTR-projecting DA neurons mainly corresponded to the DA-2 subtype, characterized by the expression of *KCNJ6, SLC18A2, VGLUT2,* and *SNCA*, together with activation of the MAPK pathway (Figure 19D). In contrast, DA-7 identity was enriched in PFC-projecting DA neurons, marked by transcription factors *OTX2, LMO3, NFIB*, and *FOXP2*, as well as genes involved in the WNT signaling pathway (Figure 19D). As previously mentioned, several of these markers were also identified in previous studies and were differentially expressed across DA subtypes in vMB organoids, as shown in **Paper I**. However, this dataset provides a comprehensive transcriptomic reference map that goes beyond a limited set of selected markers, allowing a precise identification of DA neuron identites also in human stem cell *in vitro* models, such as vMB organoids (Figure 19E,F). Indeed, this comparison revealed a gradual emergence of dlSTR-projecting and PFC-projecting DA neurons in vMB organoids, particularly from day 60 to day 120 (Figure 19E-G). This dataset serves as a valuable resource for linking projection patterns, transcriptional identities, and the functional organization of DA circuitry, with significant implications in refining the cell products used in cell replacement therapies for PD.

Extrinsic modulation of DA neuron maturation and specification in co-grafts (Paper V)

The identification of distinct cell types within hPSC-derived grafts raises questions about the factors driving lineage commitment (Tiklova et al., 2020). Given that vMB-patterned DA progenitors exhibit a homogeneous transcriptomic profile and are multipotent at the time of transplantation (Storm et al., 2024), it is likely that the cellular environment plays a significant role in influencing their fate commitment and differentiation. This is particularly relevant when considering the specification of DA neuron subtypes, as A9 and A10 neurons regulate different functions and display selective vulnerabilities to PD and other neurological disorders. In the context of cell replacement therapy, understanding how the graft microenvironment influences the differentiation, functionality, and integration of therapeutic DA neurons is essential. Such insights can not only help unravelling the mechanisms of specification process but also lead to the development of more effective grafting strategies.

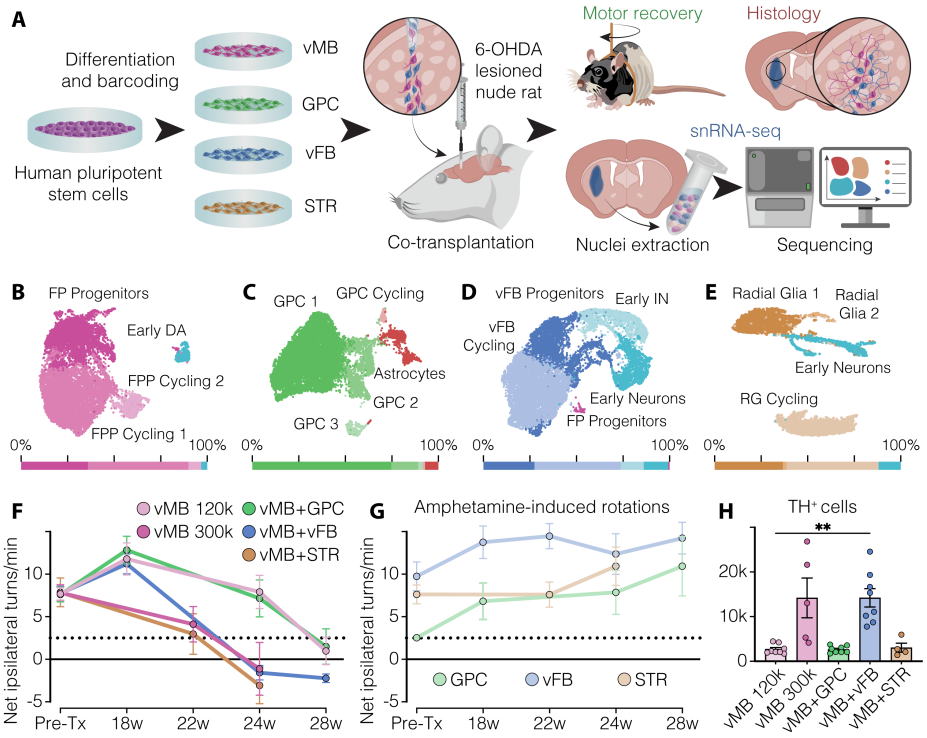

Figure 20 | Co-grafting of vMB and vFB progenitors increase the yield of TH⁺ neurons.

A) Schematic representation of the overall experimental design, including differentiation, co-transplantation and graft assessments. B-E) Single cell RNA sequencing confirming the distinct patterning of vMB (B), GPC (C), vFB (D) and STR (E) progenitors. Relative cluster proportions are displayed below each UMAP plots. F,G) Functional assessments of hPSC-derived grafts through amphetamine-induced rotation tests. H) Stereological quantification of DA neurons 7 months post-transplantation, highlighting a significant increase in TH⁺ cells in animals co-grafted with vMB and vFB progenitors.

Co-grafting vMB progenitors and support cells affects graft outcome

To evaluate the impact of different cell types on the survival, function, and maturation of DA neurons, we performed a series of co-grafting experiments in which vMB DA progenitors were transplanted together with different support cell types. These experiments aimed to explore how the graft environment influences the subtype-specific differentiation, maturation, and functionality of DA neurons (Figure 20A). Specifically, we examined the effects of three distinct cell populations: glial progenitor cells (GPCs), which are known for their neuroprotective and supportive roles in both *in vitro* and *in vivo* models (Mori et al., 2005; Song et al., 2018); ventral forebrain (vFB) patterned cells, which primarily give rise to interneurons and modulate neuronal activity and plasticity (Southwell et al., 2014); and striatal medium spiny neurons (STR), the principal axonal targets of A9 DA neurons (Figure 20A).

After confirming the correct patterning of all four cell preparations (Figure 20B-E), vMB progenitors were transplanted into the striatum of a rat lesion model of PD, either alone or in combination with the support cell types (Figure 20A). The design of the intrastriatal procedure was in line with the pre-clinical assessments performed prior to cell replacement therapy trials, such as STEM-PD (Kirkeby et al., 2023). As anticipated, the maturation of vMB progenitors into DA neurons induced a motor recovery in all groups receiving vMB cells, whether transplanted alone or in co-grafts (Figure 20F). In contrast, no motor recovery was observed in control animals transplanted only with support cells, as these cells did not differentiate into DA-producing neurons (Figure 20G). Notably, co-grafts of vMB progenitors with either vFB or STR cells led to earlier motor recovery compared to animals receiving the same number of vMB cells alone, suggesting that some support cells can positively influence the graft outcome by enhancing the functional integration and maturation of vMB-derived DA neurons (Figure 20F). Furthermore, quantification TH^+ cells revealed a significant increase in DA neuron yield specifically within the vMB+vFB co-graft group (Figure 20H).

Co-grafted cells influence the lineage commitment of vMB progenitors

Single nucleus transcriptomic profiling confirmed the cellular composition of vMB grafts previously described, including neurons, FP cells, astrocytes, OPCs and VLMCs (Storm et al., 2024; Tiklova et al., 2020) (**Paper IV**) (Figure 21A). VLMCs were exclusively observed in vMB-containing grafts and were absent in vFB, GPC, or STR transplants, suggesting a midbrain-specific origin for this cell

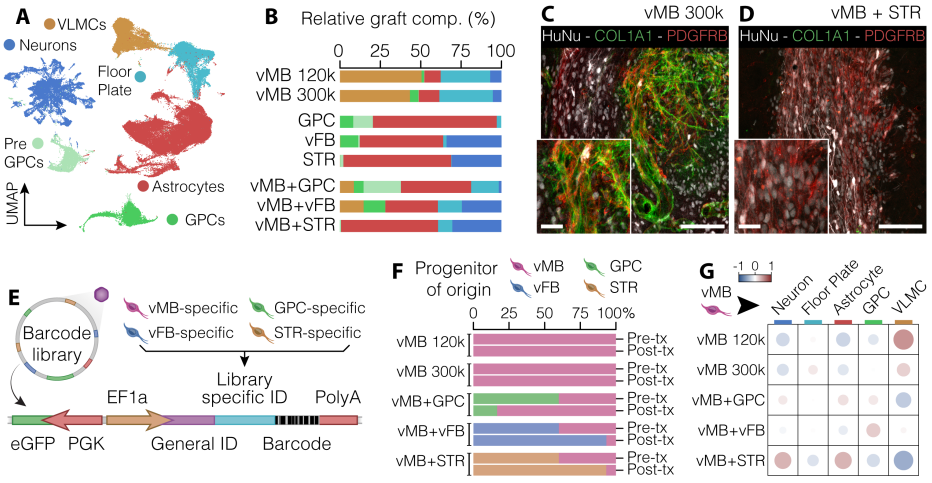

Figure 21 | Single-nuclei RNA profiling reveals co-grafts cellular composition.

A) UMAP plot showing the cellular composition of all grafts 7 months after transplantations. B) Bar plots showing the percentage of cells belonging to each cluster in the different transplantation groups. C,D) Immunohistochemistry for the VLMC markers COL1A1 and PDGFRB in vMB only (C) and vMB+STR co-grafts (D). Scale bars, 100 μm. E) Schematic representation of the barcode libraries used to distinguish the progenitor of origin in co-grafts. The PGK promoter drives the expression of eGFP, while the transcription of the library specific ID, specific for each progenitor population, is driven by the EF1a promoter. F) Proportion of human cells originated from vMB progenitors or support cells in each group. The top bar represents the composition before transplantation, while the bottom one refers to the mature grafts 7 months post transplantation. G) Dot plot showing the relative proportions of vMB-derived cell types in the different groups.

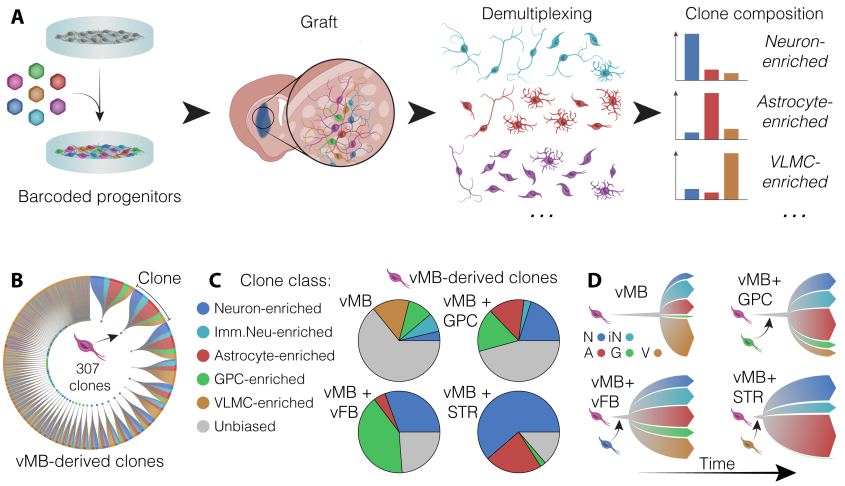

Figure 22 | Molecular barcoding highlights the impact of support cells on the lineage commitment of individual vMB progenitors.

A) Schematic representation of the lineage tracing strategy, illustrating how clones are classified depending on their cellular composition. B) Hierarchical plot of the 307 vMB-derived clones analyzed, arranged by clone size. C) Pie charts depicting the distribution of vMB-derived clone classes across different co-grafts. D) Diagram summarizing the influence of support cells on vMB progenitor lineage commitment. N, neurons; A, astrocytes; G, GPCs; V, VLMCs. The size of the arrows represents the relative proportion of that cell type within the vMB-derived component of the relative co-graft.

type (Figure 21A,B). The origin and developmental trajectory of VLMCs, as well as their functional role within the graft, is at the moment unknown. Previous lineage tracing studies, and the expression of some FP markers in VLMCs suggests a common progenitor population able to generate all components of the graft including DA neurons, astrocytes and VLMCs (Storm et al., 2024; Xu et al., 2022). Interestingly, VLMCs were also absent in vMB+STR co-grafts, despite the presence of vMB-derived cells (Figure 21A-D). Together with the increase of TH^+ cells in vFB co-grafts, these findings suggest an active role for support cells in influencing the lineage commitment of vMB progenitors.

To investigate this further, we first had to assign each cell within the co-grafts to its progenitor of origin - whether derived from vMB or GPC/vFB/STR-patterned cells. To achieve this, we took advantage of four molecular barcode libraries, one for each progenitor type, used to transduce the cells prior to transplantation (Figure 21E). The distinct sequences in the barcoded libraries allowed a precise identification of the progenitor of origin and revealed significant differences in the contribution of each progenitor type to the mature co-graft (Figure 21E,F). This barcode-based demultiplexing strategy also enabled us to examine how co-grafted cells influenced the differentiation potential of vMB-derived DA progenitors (Figure 21G). Differential abundance analysis of mature cell types originating only from vMB progenitors revealed a notable increase in neurons and astrocytes across all co-grafts, accompanied by a decrease in the VLMC population (Figure 21G).

The lentiviral libraries used to label progenitor cells prior to transplantation also included a unique, inheritable molecular identifier (ID), effectively tagging all mature *sister* cells derived from the same individual progenitor (Figure 22A). This molecular barcode system allowed retrospective lineage trac-

ing, where mature graft cells sharing the same barcode can be grouped in clones, originating from a unique transplanted progenitor (Storm et al., 2024) (Figure 22A). In this way, we analyzed 10.691 barcoded vMB-derived cells, constituting 307 clones of varying sizes (Figure 22A,B).

To assess lineage commitment bias, we evaluated the differentiation patterns of each vMB-derived clone into specific mature cell types. A *clone class* parameter was defined by comparing the composition of each clone with the expected distribution of cell types in vMB-derived grafts (Figure 22A). Clones with cell type proportions significantly deviating from the baseline were classified as "enriched", while they were named "unbiased" otherwise (Figure 22A). For example, a clone with a higher-than-expected proportion of neurons would be classified as "neuron-enriched," whereas a clone with a higher-than-expected proportion of astrocytes would be defined as "astrocyte-enriched", and so on. Interestingly, this analysis revealed an increase in neuron-enriched clones in co-grafts, particularly when vMB progenitors were co-transplanted with STR cells (Figure 22C). Taken together, these findings demonstrate that co-grafted cells significantly influence the differentiation trajectory of vMB progenitors, modulating their commitment toward neurons, astrocytes, or VLMCs (Figure 22D). In particular, STR co-grafting shifted the commitment of vMB progenitors toward the neuronal lineage, suppressing the VLMC fate.

Striatal target cells refine the specification of A9 DA neurons

To investigate the influence of co-grafted cells on DA neuron specification, we focused our analysis specifically on this cell population. Taking advantage of the Target-seq dataset (presented in **Paper IV**), we identified three distinct subtypes: A9-like DA neurons, closely matching the transcriptional profile of dlSTR-projecting cells; A10-like DA neurons, transcriptionally similar to PFC-projecting cells; and a more immature subpopulation, named *unspecified* (Figure 23A,B).

Interestingly, the relative proportions of these subtypes varied across groups, with an increased proportion of A9-like DA neurons in the STR co-graft (Figure 23C). High-throughput quantifications of cells co-expressing TH and the A9-enriched markers ALDH1A1 and GIRK2, or the A10-like gene OTX2, further validated these findings at the protein level (Figure 23D-I). These results suggest that human DA neuron identity can be refined by interactions with specific co-grafted cells, such as STR cells for the A9-like identity. If independently confirmed, this mechanism could shed some light on the *in vivo* specification of DA neurons, including how different identities, functions, and vulnerabilities to diseases are established. Furthermore, GSEA revealed an upregulation of genes associated with neuronal maturation in DA neurons co-grafted with STR or vFB cells, in line with the faster motor recovery observed in these groups (Figure 23J).

Identification of EBF3 and PBX3 as central transcription factors driving DA neuron maturation and A9 subtype specification

The distinct molecular profiles of A9 and A10 DA neurons suggest that their specification within the co-grafts may be orchestrated by specific TFs. To explore this hypothesis, we constructed the gene regulatory network (GRN) of DA neurons, focusing on differentially expressed genes between A9 and A10 clusters or involved in neuronal maturation (Figure 24A-D). While many of the identified genes overlapped with markers previously discussed in **Paper I** (from vMB organoids) and **Paper IV** (intranigral grafts), two TFs stood out: *EBF3* and *PBX3* (Figure 24A-D). These genes were upregu-

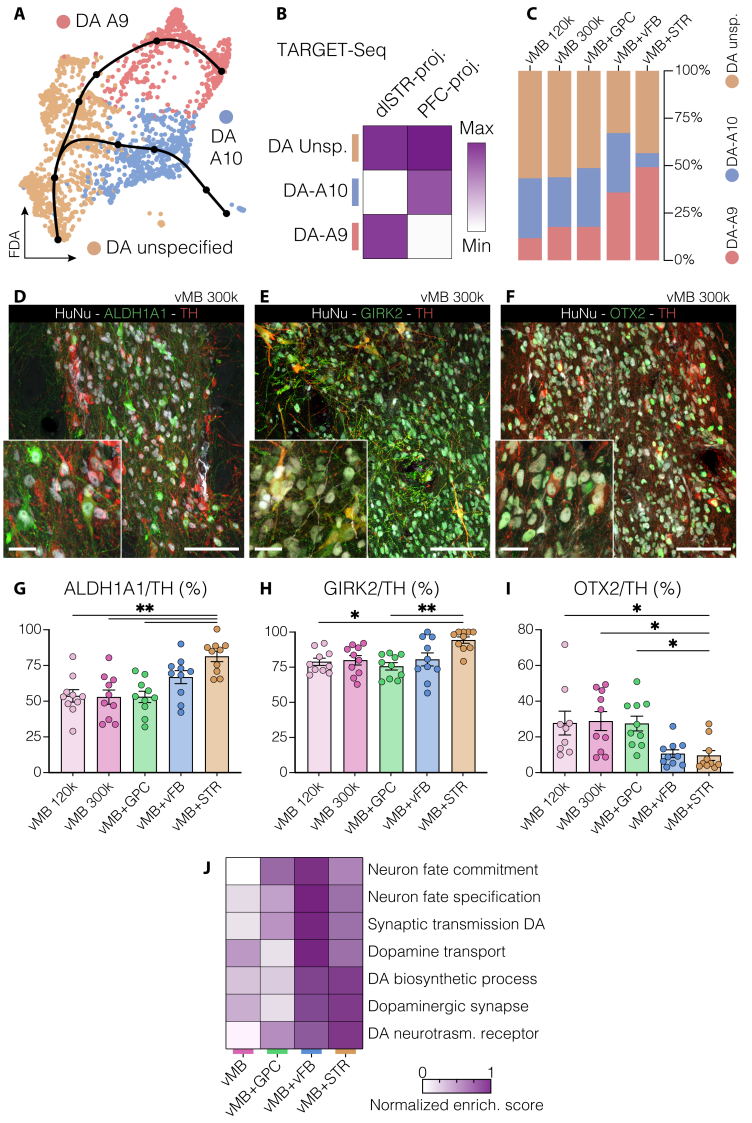

Figure 23 | Support cells influence DA neuron specification into A9- and A10-like subtypes.

A) Force-directed k-neighbor graph (SPRING) of computationally sorted DA neurons, with black lines indicating slingshot trajectories toward A9 and A10-like molecular profiles. B) Heatmap representing the correlation between the DA neuron subtypes and the transcriptome of dlSTR-projecting/PFC-projecting DA neurons described in Paper IV. C) Relative abundance of DA neuron subtypes in the different co-graft settings. D-F) Immunohistochemistry of ALDH1A1 D), GIRK2 E) and OTX2 F) coupled with TH and HuNu showing DA neuron diversity in vMB grafts. Scale bar 100 µm; inset, 25 µm. G-I) Percentage of ALDH1A1- H), GIRK2- I), OTX2-positive J) cells over TH in vMB alone grafts and co-grafts. J) Heatmap representing GSEA scores for GO terms related to DA neuron maturation across different groups.

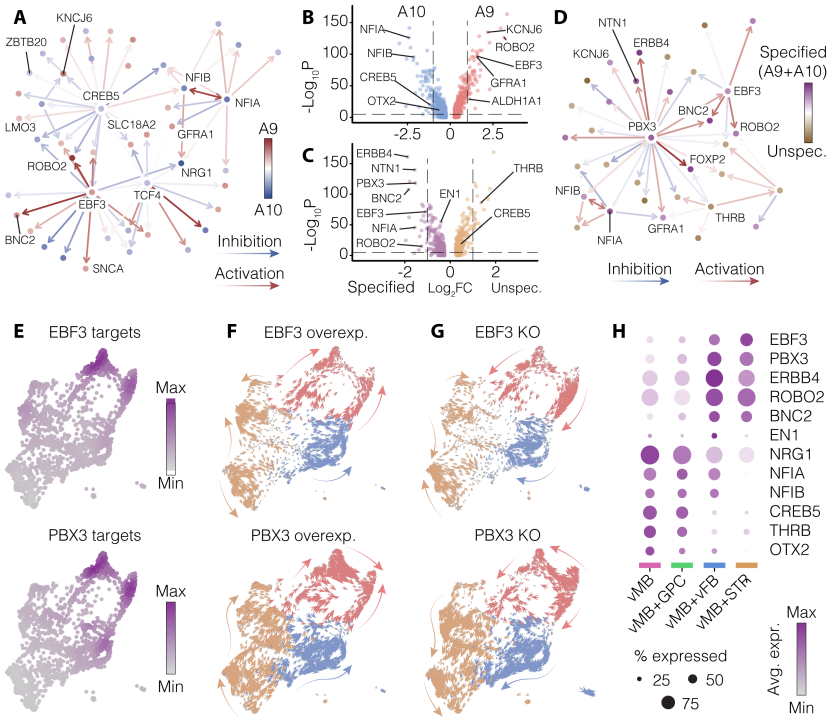

Figure 24 | The TFs *EBF3* and *PBX3* represent candidate drivers of human A9 DA neuron specification and maturation.

A) GRN of differentially expressed genes between A9-like and A10-like DA neuron clusters. Nodes represent genes and are colored based on the fold change (Log_2FC) value shown in the volcano plot in (B). B,C) Volcano plot of differentially expressed genes in A9 (red) versus A10 (blue) DA neurons (B) and specified (A9-like and A10-like together) and unspecified DA neuron clusters (C). The horizontal dashed line indicates the significance threshold (p-value < 0.05), and the vertical dashed lines represent the fold change thresholds ($Log_2FC = \pm 1$). D) GRN of differentially expressed genes between specified (A9-like and A10-like together) and unspecified DA neuron clusters. E) Feature plot depicting the cumulative expression pattern of *EBF3* (top) and *PBX3* (bottom) targets on the DA neuron SPRING plot. F,G) *In silico* simulation of *EBF3* and *PBX3* overexpression F) and knock-out (KO) G) obtained with CellOracle. The perturbation effect is shown as a vector overlayed over the DA neurons SPRING plot and colored based on the subtype assignment. H) Dot plot showing the differential expression of selected markers in vMB-derived DA neurons generated from vMB transplants alone or in the presence of support cells.

lated in A9-like DA neurons and seemed to act as central hubs for this fate, driving the expression of classical A9 markers such as *KCNJ6* (GIRK2) and *GFRA1* in the GRN (Figure 24A-D). Indeed, the combined expression of *EBF3* and *PBX3* targets revealed a distinct signature unique to A9-like DA neurons (Figure 24E). To further investigate their role, we performed in silico perturbations of *EBF3* and *PBX3* (knock-out and overexpression), supporting their involvement in the specification and maturation of human A9-like DA neurons (Figure 24F,G). Interestingly, the expression of *EBF3*, *PBX3*, and many of their downstream targets was also upregulated in DA neurons co-grafted with vFB or STR cells, compared to vMB transplants (Figure 24H). These findings suggest that *EBF3* and *PBX3* may play a central role in driving A9-like DA neuron identity by activating key downstream

genes. Furthermore, the upregulation of these TFs and their targets in vFB and STR co-grafts indicates once more the influence of the cellular microenvironment in shaping DA neuron specification and maturation.

In summary, this study highlights an active role of co-grafted cells in shaping the lineage commitment of vMB progenitors, affecting the cellular composition and the functional outcome of mature grafts. Single-cell analyses revealed that co-grafting vMB and STR progenitors resulted in the complete absence of VLMCs, a higher proportion of A9-like identity and an increased maturation. These changes corresponded with an earlier motor recovery in animals co-grafted with vMB and STR cells, with significant implications for cell replacement therapy for PD. Similarly, the increased number of TH^+ cells observed in vFB co-grafts might be explained by an enhanced survival of vMB progenitors within this supportive microenvironment. These findings emphasize the importance of identifying extrinsic factors that guide the survival, differentiation, maturation, and specification of grafted DA neurons. Ultimately, the acquisition of this knowledge can promote the development of better grafting strategies, leading to optimized therapeutic outcomes for stem cell-based therapies for PD. Finally, the identification of *EBF3* and *PBX3* in driving the molecular identity of A9-like DA neurons might shed some light on the specification process, and pave the way for more refined therapeutic cell products for PD.

Modelling vMB-STR neuron long range interactions in a multi-organoid system (ongoing study)

The analysis conducted so far indicated that the interaction between DA neurons and co-grafted STR cells induces transcriptional changes associated to both subtype specification and maturation. To validate these findings, we aimed to model the interaction between vMB and STR cells *in vitro* using brain organoids with appropriate patterning. The assembly of regionalized brain organoids, known as assembloids, has proven to be a powerful tool for studying the cellular communication between adjacent brain regions. These models effectively recreate region-specific axonal circuits and provide valuable insights into human-specific neurological disorders (Miura et al., 2022; Pasca, 2019).

However, current models still struggle to fully recapitulate long-range neuronal connections, as the topographical organization of human axonal networks requires precise spatial arrangements that can be difficult to achieve in current assembloid systems. This limitation is particularly relevant when attempting to model the physiological interactions between vMB and STR cells via the nigrostriatal pathway, where the spatial distance and topographical organization of the two regions can critically influence the extent and nature of the intercellular communication. To address these challenges, more advanced organoid-based models are required to accurately mimic long-range interactions between anatomically distinct and physically separated brain regions.

Generation of human vMB-STR connectoids.

To generate a fully humanized model of the nigrostriatal pathway *in vitro*, we adopted a multidisciplinary approach, integrating brain organoids with microfluidic devices. Regionalized organoids

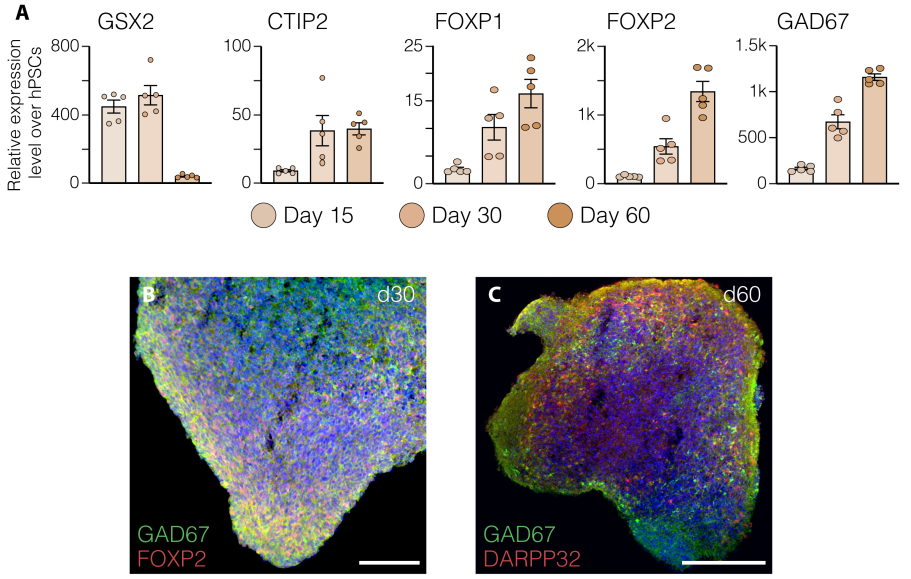

Figure 25 | Characterization of STR-patterned organoids.

A) Relative expression levels (qRT-PCR) of key STR markers. B,C) Immunohistochemistry of GAD67, FOXP2 and DARPP32 in STR-patterned organoids at day 30 (B) and day 60 (C) of differentiation. Scale bars, 100 μm (B), 200 μm (C).

were patterned toward vMB and STR fates following adaptations of established protocols (**Paper II**) (Miura et al., 2020), that accurately replicate the molecular, cellular, and cytoarchitectural features of the brain regions involved in this circuitry. Similar to the vMB organoids presented in **Paper I**, STR organoids were characterized using different techniques, confirming the expression of the forebrain marker FOXG1, along with GSX2 and FOXP1, which are characteristic of the lateral ganglionic eminence (LGE) (Figure 25A-C). By day 60, STR organoids exhibited markers of medium spiny neurons (MSNs), including the expression of GAD67, an enzyme essential for GABA synthesis, as well as DARPP-32 and CTIP2, indicative of a mature striatal neuronal identity (Figure 25B,C).

To facilitate axonal projections and establish a *connectoid* system, we designed a microfluidic device capable of spatially confining the organoids and guide the axonal growth between the two (Figure 26A). The device was constructed from a polydimethylsiloxane (PDMS) substrate with two distinct compartments, each 2 mm in diameter, designed to contain vMB and STR organoids based on their size (Figure 26B,C). These compartments were connected by a 9 mm-long channel with a height of 175 μm and a width of 250 μm, which allowed both axonal outgrowth and media exchange (Figure 26B). The vMB and STR organoids were placed into the microfluidic device on day 16, i.e. when they displayed distinct regional patterning, maintained a compact and spherical morphology, and early born neurons had not yet begun extending projections. By day 20 (4 days post-placement), the first pioneering axons were observed within the channel. Over time, the axonal projections increased in number and complexity, ultimately forming an interconnected bundle between the organoids after 90–100 days of differentiation (Figure 26D).

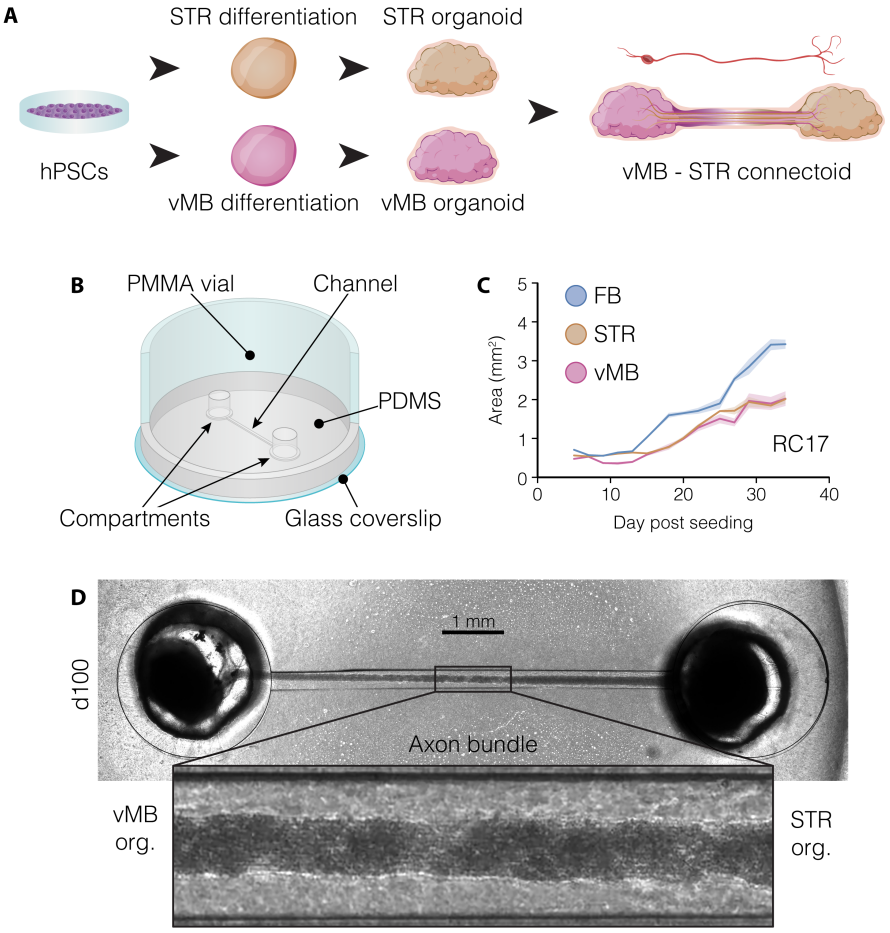

Figure 26 | Generation of human vMB-STR connectoids.

A) Illustration of nigrostriatal connectoid generation. B) Schematic representation of the microfluidic device. C) Measurements of cross-sectional area of vMB, STR and FB-patterned organoids over time. D) Representative bright-field picture of a mature vMB-STR connectoid after 100 days of differentiation.

DA neurons projects to STR target cells, recapitulating the nigrostriatal pathway in a microfluidic device.

To validate the generation of DA neuron projections within the connectoids, we took advantage of an engineered hPSC line in which the gene coding for the CRE recombinase was knocked into the TH locus (Fiorenzano, Birtele, et al., 2021) (Figure 27A). The integrated recombinase allowed specific visualization of TH-expressing DA neuron axons using Green Fluorescent Protein (GFP), delivered via a lentiviral vector containing a flex-GFP construct (Figure 27A). The dynamics of DA neuron ax-

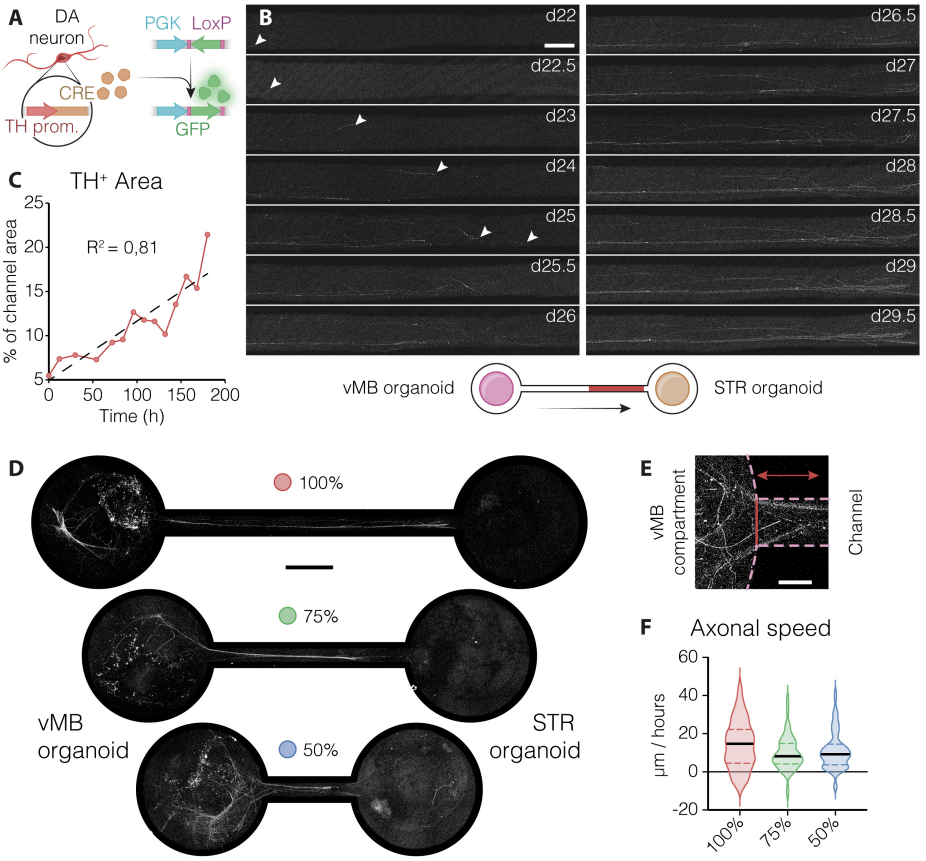

Figure 27 | Monitoring DA neuron axonal projections in vMB-STR connectoids.

A) Schematic illustration of the TH-Cre line system used for live imaging. B,C) Confocal pictures of GFP$^+$ DA neurons over time (B) and relative quantification of the channel area covered (C). Scale bar, 250 µm. D) Confocal images of vMB-STR connectoids with channels of various lengths. Scale bar, 1 mm. E) High magnification confocal picture of the interphase between the compartment housing vMB organoids and the channel, used as a starting point for axonal speed measurements. Scale bar, 200 µm. F) Violin plot showing the speed of single DA neurites in the different devices, reported as µm/hour.

onal growth were monitored using confocal live imaging over a 10-day period, revealing the progressive extension of DA neuron axons toward the STR compartment (Figure 27B,C). Additionally, by applying this approach to devices with varying channel lengths, we demonstrated that channel length did not influence axonal projection dynamics or neurite outgrowth speed (Figure 27D-F).

To complement the measurements of DA neuron fiber growth, we assessed the presence of axonal contacts between regionalized organoids. To this end, we employed a rabies-based tracing methodology to track the first-order vMB neurons connecting to the STR organoid (Figure 28A). Neurons in the STR organoids were transduced with a modified avian receptor (TVA), which is necessary for

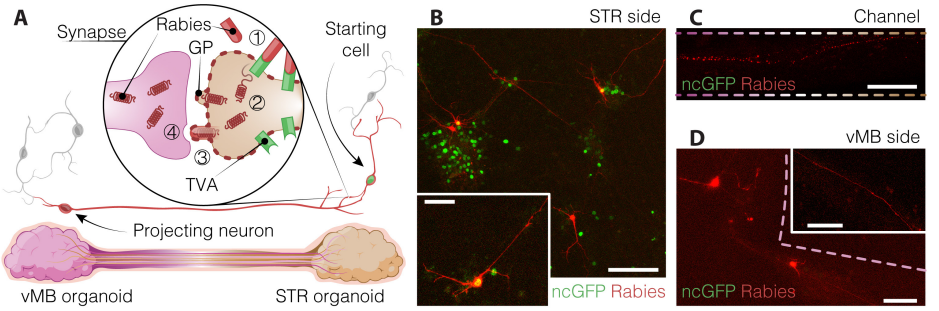

Figure 28 | Axonal connectivity in vMB-STR connectoids.

A) Schematic illustration of the rabies-based strategy utilized to trace neurons in synaptic contact. B-D) Confocal imaging of traced cells in the STR compartment (B), channel (C) and vMB side (D) of nigrostriatal connectoids. Scale bars, 100 μm (B), 200 μm (C), 50 μm (D).

the entry of the rabies virus into the cells (Figure 28A). This lentiviral construct was designed to co-express nuclear GFP alongside the transgene, effectively marking the initial cell population (Figure 28A,B). After adding the rabies vector, TVA/GFP-positive cells began to co-express the mCherry protein, which was then retrogradely transferred to neurons in contact with the initial cells (Figure 28B-D). Interestingly, we detected mCherry-positive fibers throughout the length of the channel, as well as somas on the vMB side, indicating axonal connections between the regionalized organoids (Figure 28C,D). Taken together, these data demonstrate that DA neurons in the connectoid not only extended fibers within the device but also formed contacts with STR target cells, effectively modeling the nigrostriatal pathway.

Interaction with STR organoids promotes DA neuron maturation in vitro.

To investigate transcriptional changes associated with STR-DA neurons extrinsic interactions, we compared vMB-patterned organoids in contact with STR cells to analogous vMB-vMB connectoids and vMB organoids cultured alone. Notably, *EBF3* and *PBX3* expression levels were significantly higher in vMB organoids in contact with STR cells compared to vMB organoids alone or vMB-vMB connectoids (Figure 29A). A similar trend was also observed for other key genes expressed in mature DA neurons, such as *DAT, PITX3, GIRK2*, or targets directly regulated by *EBF3* or *PBX3*, such as *ERBB4* and *ROBO2*, in line with the GRN inferred from the co-graft data (**Paper V**, Figure 29A). Protein expression of EBF3 and PBX3 in vMB organoids was further validated using immunofluorescence, which demonstrated their specific localization in the nuclei of TH^+ neurons (Figure 29B,C). Additionally, functional analysis of spontaneous DA release revealed an increased level of maturation in vMB-STR connectoids compared to vMB-vMB ones (Figure 29D).

Finally, to validate the hierarchical role of *EBF3* and *PBX3* in regulating transcriptional programs associated with DA neuron maturation, we induced the overexpression of these two TFs in vMB organoids (Figure 29E). This resulted in the upregulation of numerous genes critical for DA neuron development, including *TH, EN1*, and *PITX3*, in both groups carrying the overexpressing vectors

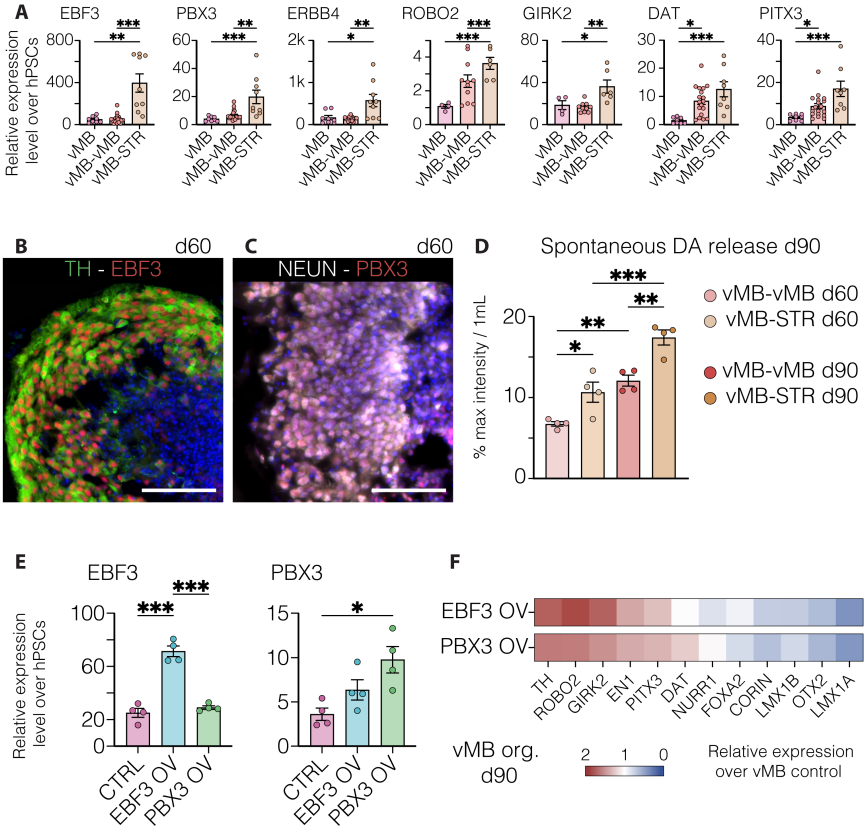

Figure 29 | Interaction with STR cells promotes transcriptional changes in DA neuron *in vitro*.

A) Expression levels of DA neuron markers identified in the co-graft GRN in vMB-STR connectoids and vMB-vMB / vMB organoid controls. B,C) Cryosections of vMB organoids at day 60 showing co-localization of EBF3/TH and PBX3/NEUN. Scale bar, 100 µm. D) Quantification of DA levels in vMB-STR and vMB-vMB connectoids measured via GRAB-DA2M sniffer cells at day 60 and day 90. E) Increase in *EBF3* and *PBX3* expression in transduced organoids at day 90. F) Upregulation of mature DA neuron markers in vMB organoids carrying the *EBF3* and *PBX3* overexpression vectors, and concurrent downregulation of early FP genes. Values are normalized over un-transduced vMB controls at the same time point.

(Figure 29F). Furthermore, markers enriched in A9-like DA neurons, such as *ROBO2* and *KCNJ6* (GIRK2), were also upregulated, at the expenses of early developmental markers such as *LMX1A*, *LMX1B, CORIN* and *OTX2* (Figure 29F). These results were in line with the in vivo findings, further supporting the role of *EBF3* and *PBX3* in driving DA neuron maturation and A9 specification.

CONCLUSIONS AND FUTURE PERSPECTIVES

Midbrain DA neurons are involved in many different functions, including motor control, cognition, and reward processing (Bjorklund & Dunnett, 2007). This functional heterogeneity is mirrored by distinct anatomical and molecular characteristics of the two primary classes of midbrain DA cells: A9 neurons, located in the SNpc and projecting to the dlSTR, and A10 neurons, residing in the VTA and innervating the PFC, *nucleus accumbens*, and amygdala (Garritsen et al., 2023). The focal and progressive degeneration of A9 DA neurons is a hallmark of PD and underscores the relevance of understanding their specification processes. Furthermore, insights into the differentiation and maturation of DA neurons are critical for producing authentic DA neurons *in vitro* for different applications, including stem cell-based therapies for PD. While cell differentiation protocols and manufacturing strategies are continuously being optimized, the refinement of cell replacement products can only progress as fast as our understanding of human DA neuron development.

In **Paper I**, we employed single-cell transcriptomics to dissect the cellular heterogeneity of vMB-patterned organoids over time. These three-dimensional cultures recapitulated key features of vMB development, including the characteristic apicobasal organization into distinct layers and the expression of FP markers. Through detailed characterization, we identified the emergence of various cell types constituting the vMB neurogenic niche, such as FP progenitors, astrocytes, OPCs, VLMCs, and, naturally, DA neurons. The temporal appearance of these cell types closely mirrored *in vivo* development, with FP progenitors undergoing gradual specification along distinct developmental trajectories. In particular, DA neurons exhibited a transcriptional profile that closely resembled their fetal counterpart, further confirming their authenticity. Importantly, this dataset represents the first attempt to comprehensively map DA neuron diversity in vMB organoids, providing insights into early markers and regulatory pathways involved in the differentiation of distinct human subtypes. The generation of vMB organoids also resulted in the development of an accessible and detailed protocol, presented in **Paper II**. To ensure wide adaptability, we tested the protocol with multiple hESC lines and optimized the culturing conditions for each of them. Furthermore, the procedure includes detailed steps for detecting neuromelanin granules within vMB organoids, a key feature of SNpc DA neurons. Overall, vMB organoids represent an accessible, scalable, and powerful platform for modeling the development and functional maturation of DA neurons, addressing some of the challenges associated with the limited accessibility of human brain tissue.

Despite these remarkable features, human brain organoids face significant issues, including low reproducibility and incomplete maturation in their inner core, often associated with cell death (Bhaduri et al., 2020; Vertesy et al., 2022). In a multidisciplinary effort to address these limitations, we introduced a biocompatible scaffold composed of spider silk fibers in 3D cell cultures. Over the work presented in this thesis, we successfully generated bioengineered silk organoids patterned toward the vMB (**Paper I**) or forebrain (FB), employing an unguided differentiation protocol (**Paper III**). In both approaches, the silk scaffolds preserved the developmental trajectories of the different progenitors, maintaining the biological characteristics of the respective differentiation protocols. However,

the microcavities within the silk network facilitated nutrient and oxygen diffusion, creating a more favorable microenvironment for neuroectodermal induction and neuronal maturation. While other attempts to integrate biomaterials with human brain organoids have been published, silk scaffolding represents a simple approach compatible with high-throughput applications, as it does not require specialized machinery (Rothenbucher et al., 2021) or the manual isolation of individual PLGA fibers (Lancaster et al., 2017). Moreover, silk is a molecularly defined material that can be further functionalized with bioactive molecules, broadening its potential applications. Through a detailed characterization, we demonstrated that silk scaffolds reduce both inter- and intra-organoid variability observed in conventional cultures, improving the functionality of neurons in the inner regions of organoids. The robust generation of human DA neurons in silk vMB organoids also underscores the potential of this approach for biomedical applications, including PD modeling and drug discovery.

The molecular profiles of distinct DA neuron subtypes identified in vMB organoids are not easily correlated with the classical A9/SNpc and A10/VTA subdivisions due to the lack of anatomical references *in vitro*. In **Paper IV**, we established a direct link between the molecular identities of specific DA neuron subpopulations and their target-specific connectivity. To achieve this, we transplanted stem cell-derived DA progenitors into the midbrain of a rat model of PD, from where they projected and innervated the host brain regions. We then combined snRNAseq and retrograde AAVs to identify the transcriptomic profiles of DA neurons projecting to the dlSTR or the PFC. While A10 DA neurons also project to other targets via the mesolimbic pathway, these areas were not included in this initial set of experiments, though they should be considered in future studies for a more detailed molecular map. This dataset represents a valuable resource for mapping and assessing the maturation of *in vitro*-derived or transplanted DA neurons, bridging between molecular features and target-specific innervation patterns. Moreover, this comprehensive profiling of human DA neuron subpopulations opens the way to investigate the pathways and TFs relevant to the acquisition of the different subtype identities.

In **Paper V**, the role of the cellular microenvironment on the specification, lineage commitment, and functionality of DA progenitors was investigated through a series of co-grafting experiments. This study demonstrated the extrinsic effects of GPC, vFB, and STR progenitors on the maturation of vMB-patterned cells, influencing both the cellular composition and functional outcome of the grafts. The earlier motor recovery and enhanced maturation of DA neurons observed in vFB and STR co-grafts indicate the potential to improve the efficacy of cell replacement therapies for PD. Importantly, the reported effects were cell-type specific, as they were not observed in GPC co-grafts. This suggests that rationally designed grafts, obtained through a mix of selected progenitor cells, could enhance not only the therapeutic outcome of DA neurons but also their survival post-transplantation (Park et al., 2023).

Furthermore, the observed increase in A9 neurons within vMB+STR co-grafts suggests a potential role of support cells in the acquisition or refinement of DA neuron molecular identity. Although the exact interactions and molecular pathways mediating this effect are not yet known, transcriptomic analysis has identified two TFs - EBF3 and PBX3 - as potential drivers of the A9 identity. To validate this observation, future studies should investigate the impact of perturbing the expression of these TFs in a homotopic transplantation setting, where both the molecular profile and target specificity of DA neurons can be examined. The ability to generate subtype-specific DA neurons *in vitro* paves

the way for the development of more advanced and precise cellular models that would consider the different vulnerabilities of A9 and A10 neurons in modeling PD and other disorders.

Finally, to further explore the interactions between vMB DA neurons and STR cells *in vitro*, we developed a novel multi-organoid system capable of recapitulating key elements of the human nigrostriatal pathway. These *connectoids* represent an innovative approach for generating multi-region organoid systems while maintaining the topographical organization of the human brain. Connectoids have the potential to expand the applicability of single organoids, potentially substituting or complementing animal models for specific experiments. Regarding DA neuron specification, connectoids provide a powerful platform for investigating and perturbing the mechanisms of DA neuron development, including the extrinsic effects of STR cells observed here.

In summary, the studies presented in this thesis represent an advancement in our understanding of human DA neuron development, integrating insights from brain organoid systems and xenograft models. While this knowledge remains still incomplete, the technological developments described here – vMB-patterned cell cultures, silk organoids, Target-seq, and connectoids - lay a strong foundation for further explorations of the complex molecular and cellular interactions shaping DA neuron fate. This is an exciting time for the study of human brain development, as the synergy between organoids, single-cell RNA sequencing, and xenograft models has the potential to unveil the mechanisms underlying the remarkable complexity and functional diversity of the human brain.

SUMMARY OF KEY METHODS

This section highlights the main methods utilized in the research presented in this thesis. For a comprehensive description of all the methodologies employed, please refer to the Materials and Methods sections of the relevant papers (see Appendix).

Human pluripotent stem cell culture

Most of the cell work presented in this thesis has been conducted using the GMP-grade hESC-line RC17 (sourced by Roslin Cells, cat. no. hPSCreg RCe021-A). In order to assess the robustness and reproducibility of the vMB-patterned organoid protocol, additional hESC-lines have been employed in **Paper I** and **II**, including: H9 (WiCell, cat. no. hPSCreg WAe009-A), HS983a, HS999, and HS1001 (from Karolinska Institute, Stockholm, Sweden). The TH-Cre knock-in line (clone B2), described in Fiorenzano et al. 2021, was also used for live imaging of growing DA neuron axons.

hESCs were maintained on plates (Sarstedt) coated with recombinant laminin-521 (Biolamina, 0.5 μg/cm² in DPBS+Mg^{2+}/Ca^{2+}) and cultured in iPS Brew XF medium (Miltenyi Biotec, GMP-grade). At 70-90% confluence, cells were passaged using EDTA (0.5 mM for 7 min at 37 °C) and reseeded at 5k-10k cells/cm² in iPS Brew supplemented with 10 μM ROCK inhibitor (Y-27632, Miltenyi, cat. no. 130-106-538) for the first 24 hours.

Monolayer differentiation of human pluripotent stem cells

vMB-patterned progenitors used in transplantation experiments in **Paper IV** and **V** were generated from RC17 hESCs following the detailed protocol outlined in Nolbrant et al. 2017. Briefly, neural induction involved dual SMAD inhibition (10 μM SB431542, Miltenyi, cat. no. 130-106-543 and 100 ng/mL Noggin, Miltenyi, cat. no. 130-103-456), followed by caudalization using a GSK3 inhibitor (0.9 μM CHIR99021, Miltenyi, cat. no. 130-106-539) and FGF8b (100 ng/mL, Miltenyi, cat. no. 130-095-740). To achieve a ventral fate, SHH-C24II (300 ng/mL, Miltenyi, cat. no. 130-095-727) was added. vFB progenitors used in co-grafting experiments (**Paper V**) were differentiated following a similar differentiation protocol but without caudalizing factors. GPCs were derived from RC17 following the Wang et al. 2013 protocol with the modifications outlined in Nolbrant et al. 2020. Finally, STR-patterned progenitors were derived from the H9 hESCs following Delli Carri et al. 2013. All cell preparations used for transplantations met the pre-defined quality criteria outlined in their respective published protocols. Prior to transplantation, differentiated progenitors were thawed, washed in DPBS, centrifuged for 5 min at 400 g, and resuspended in Hanks Balanced Salt Solution (HBSS, Thermo Fisher Scientific, cat. no. 14175095) supplemented with 0.1% DNAse (Sigma-Aldrich, cat.

no. DN25). The optimal differentiation time point selected for transplantation varied by cell type, depending on cell commitment and the proportion of cycling cells: 16 days of differentiation for vMB and vFB cells, 20 days for STR progenitors and 170 days for GPCs. For co-grafting experiments, each cell preparation was genetically tagged five days before transplantation using distinct lentiviral barcode libraries, as described by Storm et al. 2024. These libraries carried unique molecular identifiers, enabling lineage tracing within the graft. By retrieving the molecular IDs, it was possible to determine the progenitor cell of origin within the co-graft setting, distinguishing whether a mature graft cell originated from a vMB progenitor or a support cell.

Surgical procedures and cell transplantation

All surgical procedures described in **Paper IV** and **V** were performed on female athymic nude rats. Nigrostriatal pathway lesions were induced by unilateral injection of 6-hydroxydopamine (6-OHDA) into the right MFB, at a dose of 3.5 μg/μL (freebase) delivered in a 3 μL volume at a diffusion rate of 0.3 μL/min. The targeted brain region and the stereotactic surgery coordinates are summarized in table 1. Amphetamine-induced rotations (2.5 mg/kg, intraperitoneal; Apoteksbolaget, Sweden) were used to assess lesion severity and motor recovery at least 4 weeks after surgery. Behavioral rotational data were recorded over 90 min in automated rotor bowls (Omnitech Electronics) and reported as net turns per minute.

Intranigral cell transplantations (**Paper IV**) involved injecting 150k vMB progenitors across two sites (75k cells/deposit, 1 μL per site, 2 μL total per animal). In intrastriatal cell transplantations (**Paper V**), animals received a total of 300k progenitors via two tracts, each with two deposits (75k cells/deposit, 1μL per site, 4 μL total per animal). For both approaches, injections were performed at 1 μL/minute, with an additional 2-minute diffusion time. Co-grafting experiments (**Paper V**) utilized a cell mix of 40% vMB progenitors and 60% support cells (STR, GPCs or vFB progenitors), totaling 300k cells/rat.

At the terminal time point, animals were transcardially perfused under sodium pentobarbital anesthesia (60 mg/kg; Apoteksbolaget, Sweden) with 0.9% saline, followed by ice-cold 4% paraformaldehyde (PFA). All experimental procedures complied with the EU directive 2010/63 and Swedish animal welfare legislation and were approved by the Lund Animal Ethics Board and the Swedish Department of Agriculture (Jordbruksverket).

Human brain organoid culture

Regardless of the differentiation protocol, all 3D organoid cultures were started by detaching homogeneous hPSC cultures at 70-90% confluency using Accutase solution (50 μL/cm², Thermo Fisher Scientific, cat.no. A1110501) for 5 minutes at 37°C. Unlike EDTA based dissociation, used for hPSCs passaging, Accutase ensures a single cell suspension free of small cell clusters, making it pref-

Table 1 | Antero-posterior (A/P) and mediolateral (M/L) coordinates were taken from Bregma, while dorsoventral (D/V) coordinates were measured from dura (flat head), and expressed in mm. Medial forebrain bundle (MFB), Substantia Nigra (SN), Pre-frontal cortex (PFC), Striatum (STR).

Paper	Purpose	Target region	A/P	M/L	D/V
IV	Lesion	MFB	-4.4	-1.1	-7.8
	Cell transplant	SN	-4.9	-2.3	-5.5 / -6.0
	Target-Seq AAV injection	STR (dorso-lateral)	+1.0	-2.9	-3.9
		PFC	+2.5	-0.6	-3.5
V	Lesion	MFB	-3.9	-1.2	-7.3
	Cell transplant	STR (medial)	+1.4	-2.6	-4.0 / -5.0
		STR (lateral)	+0.9	-3.0	-4.0 / -5.0

erable for organoid generation. Further general details and tips on stem cell culture prior to organoid differentiation can be found in **Paper II**.

Ventral midbrain organoid differentiation

The protocol for generating vMB-patterned brain organoids is carefully described in **Paper II** and it is based on Nolbrant et al. 2017. Briefly, cell aggregates were generated by seeding 8k single cells per well in a 96-well U-bottom plate (Corning, cat. no. 7007) in iPS Brew medium supplemented with 10 μM ROCK inhibitor (Y-27632). Different starting hPSC amounts have also been tested, identifying a working range of 2.5k – 10k cells/well. The differentiation medium consisted of a 1:1 ratio of DMEM/F12 and Neurobasal medium (Thermo Fisher Scientific, cat. nos. 21331020 and A1371201) supplemented with N2 supplement (1:100, Thermo Fisher Scientific, cat. no. A1370701), SB431542 (10 μM, Miltenyi, cat. no. 130-106-543), recombinant human Noggin (rhNoggin, 100 ng/mL, Miltenyi, cat. no. 130-103-456), SHH-C24II (Miltenyi, 400 ng/mL, cat. no. 130-095-727), and CHIR99021 (Miltenyi, 0.9-1.5 μM, cat. no. 130-106-539). All differentiation media used for organoid culture also included L-Glutamine (2 mM, Thermo Fisher Scientific, cat. no. 25030081), minimum essential medium nonessential amino acids (MEM-NEAA, 1X, Sigma-Aldrich, cat. no. M7145), penicillin-streptomycin (20 U/ml, Thermo Fisher Scientific, cat. no. 15140122) and 2-Mercaptoethanol (50 μM, Thermo Fisher Scientific, cat. no. 31350010). From day 8 onwards, cell aggregates were exposed to FGF-8b (100 ng/mL, Miltenyi, cat. no. 130-095-740). On day 11, developing vMB organoids were incubated with a medium composed of Neurobasal with B27 supplement (without vitamin A, 1:50, Thermo Fisher Scientific, cat. no. 12587010), BDNF (20 ng/mL, Miltenyi, cat. no. 130-096-286), and L-ascorbic acid (200 μM, Sigma-Aldrich, cat. no. A4403-100MG). On day 14, vMB organoids were embedded in 30 μL droplets of Matrigel (Corning, cat. no. 354234). For terminal differentiation, the organoids were maintained in Neurobasal medium supplemented with 1:50 B27 without vitamin A,

20 ng/mL BDNF, 200 μM L-ascorbic acid, 500 μM db-cAMP (Sigma-Aldrich, cat. no. D0627-1G), and 1 μM DAPT (R&D Systems, cat. no. 2634) for up to four months.

Forebrain organoid differentiation

FB organoids used in **Paper III** were generated following the unguided differentiation protocol reported in Lancaster et al. 2017. This procedure is based on different principles than vMB and STR organoids, as it involves minimal guidance of the cell fate through external patterning factors. Organoids generated through this protocol primarily recapitulate FP regions, including the cortex, though limited and spatially restricted spontaneous differentiation towards other cell types can also occur, as mentioned in **Paper III** (Lancaster et al., 2017; Lancaster & Knoblich, 2014a). Therefore, while retaining self-organizing properties, organoids generated using unguided protocols tend to exhibit greater variability in spatial and cell type composition compared to those generated with regionalizing approaches (He et al., 2024; Pasca et al., 2015).

Single cells seeded in low-attachment 96-well plates (8k cells/well) were cultured in mTeSR1 for 5 days, with 10 μM ROCK inhibitor (Y-27632) added for the first 48 hours. Cell aggregates were then cultured in differentiation medium consisting of DMEM/F12 (Thermo Fisher Scientific, cat. no. 21331020), N2 supplement (1:100, Thermo Fisher Scientific, cat. no. 17502048) and heparin (2 μg/mL, Sigma-Aldrich, cat. no. H3149) until day 8. Knockout serum replacement (KSR, 3%, Thermo Fisher Scientific, cat. no. 10828010) was also added for the first 48 hours. Developing organoids were then embedded evenly in 30 μL of Matrigel (Corning, cat. no. 354234) at day 14 and transferred to ultra-low attachment 6 well-plates (Corning, cat. no. 3471) with 1:1 DMEM/F12:Neurobasal medium (4 mL/well), supplemented with N2 supplement (1:200), B27 supplement (1:100, Thermo Fisher Scientific, cat. no. 12587010) and insulin (2.5 μg/mL, Sigma-Aldrich, cat. no. I9278-5ML). From day 15, the differentiation medium was substituted to 1:1 DMEM/F12:Neurobasal, N2 supplement (1:200), B27+Vitamin A supplement (1:50, Thermo Fisher Scientific, cat. no. 17504044), insulin solution (2.5 μg/mL) and ascorbic acid (400 μM, Sigma- Aldrich, cat. no. A4403-100MG). Terminal differentiation from day 25 was achieved with adding BDNF (10 ng/mL, Miltenyi, cat. no. 130-096-286), GDNF (10 ng/mL, R&D Systems, cat. no. 212-GD-010) and cAMP (200 μM, Sigma-Aldrich, cat. no. D0627-1G).

Striatal organoid differentiation

STR organoids were generated following Pasca lab´s protocol (Miura et al., 2020), with modifications. Briefly, hPSCs were plated in 96-well U-bottom plates and exposed to SB431542 (10 μM) and rhNoggin (200 ng/mL) in N2 base medium (see vMB organoid protocol) for the first 6 days. From day 6, Neurobasal medium supplemented with IWP-2 (2.5 μM, Selleckchem, cat. no. S7085) and Activin A (100 ng/mL, Peprotech, cat. no. 120-14E) was used to induce rostral fate. From day 12, the retinoid X receptor agonist SR11237 (200 nM; Tocris, cat. no. 3411) was added. Terminal differentiation used the same medium as for vMB organoids, ensuring compatibility for either assembloids (**Paper IV**) or connectoids experiments. All direct comparisons between conditions were conducted in organoids within the same batch – defined as those generated simultaneously in the same dish.

Generation of bioengineered silk organoids

The generation of 3D silk scaffolds for bioengineered organoids (**Paper I** and **III**) involved additional preparatory steps before differentiation. Initially, 20 µL droplets of Biosilk protein solution (Biolamina, cat. no. BS-0101) were functionalized with 1 µL each of Lam-111 (5 µg/mL, Biolamina, cat. no. LN111) and ROCK inhibitor (10 µM). These droplets were then placed in the center of hydrophobic cell culture wells of 24-well plates (Sarstedt, cat. no. 833922500). To create a dense but porous scaffold, air bubbles were incorporated by 10-15 pipetting strokes, ensuring uniform foam shape and size across samples. hPSC cultures at 70% confluency were detached using Accutase (50 µL/cm^2) for 5 minutes at 37 °C and prepared as a single-cell suspension at 15k cells/µL in either iPS Brew or mTeSR1 medium, both supplemented with ROCK inhibitor (10 µM), depending on the differentiation protocol. A total of 75k cells was evenly dispersed into the silk foam, and the contact with silk fibers stabilized at 37 °C for 25 min. At this stage, silk scaffolds remained attached to the plate bottom, enabling precise control of cell-to-silk ratio. Each silk culture was then incubated with 2 mL of iPS Brew or mTeSR1 containing ROCK inhibitor (10 µM) and differentiated toward vMB (**Paper I**) or FB (**Paper III**) organoids following the protocols described above. After 8 (FB) or 10 days (vMB) of differentiation, developing silk organoids were detached from the bottom of the plate using a scalpel, transferred to low-attachment 6-well plates and cut into 2-3 pieces each, based on size. Each piece was embedded in 30 µL Matrigel and cultured individually in suspension.

Connectoid formation

Microfluidic devices were generated using a photolithographic and replica molding process. The master mold was created with a SU8 2075 epoxy-based photoresist, exposed to ultraviolet light (500 mJ/cm^2 for 15 seconds), and subjected to pre- and post-exposure baking steps of 6 and 10 hours, respectively, at 50 °C. The SU8 was developed in propylene glycol methyl ether acetate (PGMEA) for 10 minutes and baked for 15 additional hours at 90 °C, resulting in a master mold 175 µm thick. To

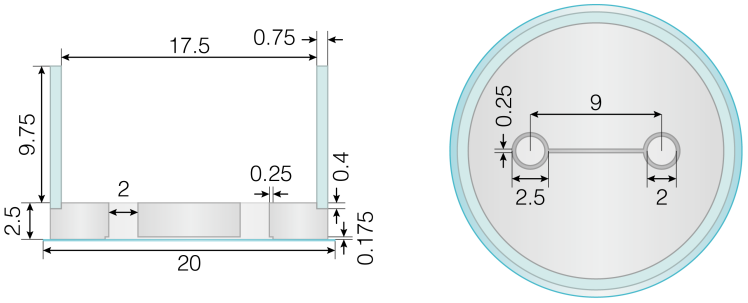

Figure 30 – Design of the connectoid microfluidic device. Measures are expressed in mm.

ensure easy detachment of PDMS replicas, the master mold underwent silanization treatment with a 1:10 solution of toluene and trichloromethyl silane. PMDS was then cast onto the master mold to replicate the microstructures. The final devices, consisting of multi-layer PDMS structures attached to polymethyl methacrylate (PMMA) vials designed to contain cell culture medium, featured two organoid compartments (2 mm in diameter) separated by a 9 mm-long channel measuring 250 μm x 175 μm (Figure 30).

To generate vMB-STR connectoids, day 16-regionalized organoids with appropriate patterning were placed in PDMS devices pre-coated with 2% Matrigel in DMEM for at least 24 hours. For long-term culture, connectoids were maintained in terminal differentiation medium containing Neurobasal, B27 (1:50, without vitamin A), BDNF (20 ng/mL), L-ascorbic acid (200 μM), db-cAMP (500 μM; Sigma-Aldrich, cat. no. D0627-1G), and DAPT (1 μM).

RNA extraction and qRT-PCR

To analyze the expression levels of selected genes, total RNAs was extracted from monolayer cell cultures or organoids using 350 μL of RTL lysis buffer and the RNeasy Microkit (Qiagen). RNA quantity and integrity was assessed with the NanoDrop 2000 spectrophotometer (Thermo Fisher), ensuring all samples had a 260 nm/280 nm ratio of 2 or higher to confirm RNA purity. Reverse transcription was conducted using the Maxima First Strand cDNA Synthesis Kit for qRT-PCR (Thermo Fisher Scientific). Each reaction incorporated 1 μL of synthesized cDNA, 4 μL of relevant primers (0.95 μM, Integrated DNA Technologies; primer sequences provided in Table 2) and 5 μL of Light Cycler 480 SYBR Green Master (Roche) in 384-well plates. Sample preparation was automated using a Bravo Automated Liquid Handling Platform (Agilent). Quantitative real-time PCR (qRT-PCR) was performed on a Light Cycler 480 II instrument (Roche) with a 40-cycle two-step protocol, consisting of a 1-minute annealing/elongation step at 60°C and a 30-second denaturation step at 95°C. Gene expression was calculated using the ΔΔCT method from three technical replicates per sample. *ACTB* and *GAPDH* were used as housekeeping genes for normalization. Relative expression values were normalized to undifferentiated RC17 hPSCs, unless stated otherwise, and expressed as average fold changes.

Isolation of xenografts from the host rat brain and nuclei extraction

The procedure for isolating xenografts from rat brains for single nuclei RNA sequencing, including nuclei extraction and isolation, has been the main analytical technique leading **Paper IV** and **V**. The procedure described below has been developed and perfectioned after observing that fragile cell types, such as mature DA neurons in grafts, can be underrepresented in single cell RNA sequencing (Tiklova et al., 2020), but better preserved in single nuclei RNA sequencing (**Paper IV**).

Rat brains were isolated in artificial cerebrospinal fluid (aCSF, containing 119 mM NaCl, 26 mM $NaHCO_3$, 2.5 mM KCl, 1.25 mM NaH_2PO_4, 2.5 mM $CaCl_2$, 1.3 mM $MgSO_4$, and 25mM glucose), and

Table 2 | Sequence of qPCR primers

Gene name	Primer sequence (fwd)	Primer sequence (rev)
ACTB	CCTTGCACATGCCGGAG	GCACAGAGCCTCGCCTT
ASCL1	CTAAAGATGCAGGTTGTGCG	GGAGCTTCTCGACTTCACCA
CORIN	CATATCTCCATCGCCTCAGTTG	GGCAGGAGTCCATGACTGT
BCL11B (CTIP2)	GAAGATGACCACCTGCTCTCAC	GCTCATCTTTACCTGCAATGTTCT
SLC6A3 (DAT)	CACTGCAACAACTCCTGGAA	AAGTACTCGGCAGCAGGTGT
EBF3	GACCATGAAGGAGGAGCCGCT	GCACATCTCCGGGTTCTTGTCCT
EN1	CGTGGCTTACTCCCCATTTA	TCTCGCTGTCTCTCCCTCTC
EN2	CCTCCTGCTCCTCCTTTCTT	GACGCAGACGATGTATGCAC
ERBB4	GGTAGTTCAGGATGTGGACGTT	GGCAATGATTTTCTGTGGGTCC
FOXA2	CCGTTCTCCATCAACAACCT	GGGGTAGTGCATCACCTGTT
FOXG1	TGGCCCATGTCGCCCTTCCT	GCCGACGTGGTGCCGTTGTA
FOXP1	AATACAACGTGCCCATTTCGTC	ATGGTGGTCTAACTTCTGCGTT
FOXP2	ATGAGCACTCTAAGCAGCCAAT	GTTGCAGATGCAGCAGTTCTAC
GAD67	CTCCTGGGGGCGCCATATCCAA	CCAGTTTAGGCACAGCCGCCAT
GAPDH	TTGAGGTCAATGAAGGGGTC	GAAGGTGAAGGTCGGAGTCA
KCNJ6 (GIRK2)	AGCTCACAGAATCCATGACTAACG	TTTCGACGTCCTGATCCATGG
GSX2	TCTCCGGGGACCCCTTTGTTCC	GACACGGGCAGTCAAGCCCTTG
HOXA2	CGTCGCTCGCTGAGTGCCTG	TGTCGAGTGTGAAAGCGTCGAGG
LMX1A	CGCATCGTTTCTTCTCCTCT	CAGACAGACTTGGGGCTCAC
LMX1B	CTTAACCAGCCTCAGCGACT	TCAGGAGGCGAAGTAGGAAC
MAP2	CCGTGTGGACCATGGGGCTG	GTCGTCGGGGTGATGCCACG
NANOG	TTGGGACTGGTGGAAGAATC	GATTTGTGGGCCTGAAGAAA
NEUROG2	ATCCGAGCAGCACTAACACG	GCACAGGCCAAAGTCACAG
NR4A2 (NURR1)	CAGGCGTTTTCGAGGAAAT	GAGACGCGGAGAACTCCTAA
POU5F1 (OCT4)	TCTCCAGGTTGCCTCTCACT	GTGGAGGAAGCTGACAACAA
OTX1	TATAAGGACCAAGCCTCATGGC	TTCTCCTCTTTCATTCCTGGGC
OTX2	ACAAGTGGCCAATTCACTCC	GAGGTGGACAAGGGATCTGA
PBX3	AGAATGGTGGGCATCATCCATCGA	GTTGGCTTCTTCCTGAAACTTGCCA
PITX3	GGAGGTGTACCCCGGCTACTCG	GAAGCCAGAGGCCCCACGTTGA
ROBO2	AATGGAAGCCTCTGCTACACTC	GAACCACAAACTGTGGGGGAG
SHH	CCAATTACAACCCCGACATC	AGTTTCACTCCTGGCCACTG
SOX17	CCAGACCGCGACAGGCCAGAAC	AGTGAGGCACTGAGATGCCCCGAG
EOMES (TBR2)	GCGAGAGAACCGTGCCACAGAC	GCCACCTCTTCGCTCTGTTGGG
TH	CGGGCTTCTCGGACCAGGTGTA	CTCCTCGGCGGTGTACTCCACA

Table 3 | Primary antibodies.

Antigen	Specie	Company	Cat. No.	Dilution
ALDH1A1	Goat	R&D	AF5869	1:1000
BRACHYURY	Goat	R&D	AF2085	1:300
CALBINDIN	Rabbit	Swant	CB38	1:500
cCASP3	Rabbit	Cell Signaling	9661	1:500
COL1A1	Sheep	R&D	AF6220	1:500
CORIN	Rat	R&D	MAB2209	1:200
DARPP32	Rabbit	Cell Signaling	2306	1:300
E-CADHERIN	Mouse	BD	610182	1:300
EBF3	Mouse	Abnova	381-480	1:800
FOXA2	Mouse	Santa Cruz	sc-101060	1:1000
FOXP2	Mouse	Merck Millipore	MAB-E415	1:300
GABA	Rabbit	Sigma-Aldrich	A2052	1:2000
GAD65/67	Rabbit	Abcam	AB49832	1:1000
GIRK2	Rabbit	Alamone Lab	APC006	1:500
HIF1A	Rabbit	GeneTex	127309	1:1000
KI67	Mouse	Novocastra	ACK02	1:500
KI67	Mouse	BD	550609	1:500
LMX1A	Rabbit	Merck Millipore	AB10533	1:1000
MAP2	Chicken	Abcam	AB5392	1:2000
NCAD	Mouse	BD	610920	1:500
NCAM	Mouse	Santa Cruz	sc-106	1:500
NEUN	Mouse	Merck Millipore	MAB377	1:1000
NEUROG2	Goat	Santa Cruz	19234	1:600
NKX2-1	Rabbit	Abcam	AB133737	1:500
OCT4	Mouse	Santa Cruz	sc-5279	1:500
OTX2	Goat	R&D	AF1979	1:2000
PAX6	Rabbit	Abcam	AB195045	1:300
PBX3	Rabbit	Proteintech	12571-1-AP	1:200
PDGFRA	Rabbit	Cell Signalling	5241S	1:300
PDGFRB	Rabbit	Invitrogen	MA5-15143	1:100
SOX17	Goat	R&D	AF1924	1:300
SOX2	Rabbit	Millipore	AB5603	1:400
SOX2	Mouse	R&D	MAB2018	1:500
TAU	Rabbit	DAKO	A0024	1:1000

Antigen	Specie	Company	Cat. No.	Dilution
TH	Rabbit	Merck Millipore	AB152	1:1000
TH	Mouse	Immunostar	22941	1:500
TH	Sheep	Millipore	AB1542	1:1000
TUBB3	Mouse	BioLegend	801202	1:1000
vGLUT1	Rabbit	Sysy	135303	1:500
VIM	Mouse	DAKO	M0725	1:50
ZO1	Mouse	Thermo Fisher	1A12	1:300
ZO1	Mouse	Invitro	339100	1:300

sectioned coronally using a vibratome (thickness 375 μm, amplitude 1.7 mm and speed 0.20 mm/sec). Grafted areas were isolated under a dissection microscope and placed in a glass Dounce homogenizer with 1 mL of nuclei lysis buffer (0.32 M sucrose; 5 mM $CaCl_2$; 3 mM MgAc; 0.1 mM Na_2EDTA; 10 mM Tris-HCl, pH 8.0, 1 mM DTT, 0.1% Triton X) on ice. The tissue was then homogenized into a nuclei suspension using a loose-fitting pestle (10 strokes), followed by a tight-fitting pestle (10 strokes). Samples were then centrifuged at 900g for 15 minutes at 4 °C. The resulting nuclei pellet was resuspended in 200-400 μL of cold wash buffer containing 0.1% BSA fraction V and 0.4 U/μL RNase inhibitors (Ambion™ and SUPERase In™, Invitrogen) in RNAse free-PBS, depending on the pellet size. Nuclei were purified using fluorescence-activated nuclei sorting (FANS) on a FACSAria III cell sorter (BD Biosciences) equipped with a 100 μm nozzle. Sorting was based on DRAQ7 staining and event size, collecting 7k – 10k nuclei per sample in BSA-precoated DNA LoBind tubes (Eppendorf) for snRNA-seq library preparation.

Organoid cryosectioning and immunofluorescence

Both conventional and silk brain organoids, regardless of the differentiation protocol, were fixed in 4% PFA for 5 hours at room temperature or overnight at 4°C. After fixation, organoids were then left to sink overnight in a mixture of 30% sucrose solution mixed and OCT cryomount (1:1 volume ratio) at 4°C. The following day, organoids were embedded in OCT cryomount in plastic molds, snap-frozen on dry ice, and stored at -80°C until needed. For sectioning, mounted organoids were cut in 20 μm slices using a cryostat, and the slides were stored at −20°C until further processing.

For immunofluorescence staining, organoid sections were first air-dried for 5 minutes at room temperature and washed three times with 1X KPBS. Sections were subsequently post-fixed in 4% PFA for 10 minutes at room temperature, followed by three additional washes. The slides were incubated in a blocking solution (0.3% Triton X-100, and 5% serum from the secondary antibody host species in 1X KPBS) for at least 1 hour. Primary antibodies (see Table 3) in blocking solution were added to the slides for an overnight incubation at 4°C. Sections were then washed and incubated with secondary antibodies conjugated to Alexa Fluor 488, 594, or 647 (1:400, Jackson ImmunoResearch

Laboratories) along with DAPI (1:1000) in the blocking solution for 1 hour at room temperature. Finally, the sections were mounted on glass coverslips using FluorSave Reagent and imaged at least 24 hours later.

Neuromelanin was detected using a silver-reducing technique, part of the Fontana-Masson method, to visualize melanin and cell granules in fixed tissue. Organoid sections, eventually stained with the DAB technique, were incubated in an ammoniacal silver solution (part of the Masson-Fontana Stain kit from Atom Scientific, cat. no. RRSK12-100) at 56 °C for 30 min. After three washes in distilled water, sections were dehydrated in a series of alcohols of ascending concentrations, cleared by immersion in fresh xylene three times and coverslipped with DPX mounting medium.

Histology and immunohistochemistry

While single nuclei RNA-seq represents a powerful technique for a comprehensive investigation of graft composition (**Paper IV**) and the effects of cell-cell interactions on lineage commitment (**Paper V**), histological assessments remain essential for validating findings at the protein level. Unlike sequencing techniques, which provide detailed insights into gene expression, immunohistochemistry preserves the spatial localization of proteins of interest in within tissues. This spatial context, which is often lost in most RNA sequencing techniques, is essential for understanding tissue architecture, adding further validation to molecular data.

After perfusion, brains were extracted and post-fixed overnight in 4% PFA at 4°C. Subsequently, they were transferred to 25% sucrose for 24 hours for cryoprotection and sectioned coronally at 35 μm thickness using a freezing microtome into 8 series of free-floating sections. The sections were incubated overnight in a 0.02 M K-PBS solution containing 0.25% Triton-X, 5% serum matching the species of the secondary antibody, and the appropriate primary antibody (details in Table 3). When necessary, antigen retrieval was performed using 0.5 M Tris-EDTA (pH 9.0) at 80°C for 15 minutes to unmask epitopes. Sections were then incubated with secondary antibodies - either fluorophore-conjugated for fluorescence detection or biotin-coupled, for DAB detection - for 1 hour and mounted on gelatin-coated microscope slides. For DAB staining, sections underwent dehydration through an ascending series of alcohol concentrations, were cleared with xylene, and finally cover-slipped using DPX mounting medium. For fluorescence immunostaining, sections were mounted using polyvinyl alcohol mounting medium containing DABCO (Sigma-Aldrich) to prevent photobleaching. All sections were left to dry overnight before imaging. Primary antibodies used for data presented in the Results section are listed in Table 3. For more detailed information, readers are directed to the Materials and Methods sections of the relevant paper (see Appendix).

Image acquisition and quantifications

Images presented in this thesis were acquired using various platforms, depending on the nature of samples and/or staining protocols. Brightfield images of developing organoids were taken using an Olympus CKX53 inverted microscope and acquired with the Olympus cellSens Standard software (v2.3). Fluorescent staining images were captured using either a Leica DMI6000B widefield microscope, or a Leica TCS SP8 laser scanning confocal microscope, both equipped with Leica LAS X image acquisition software. Axonal outgrowth of DA neurons in connectoids was monitored through the Leica TCS SP8 confocal microscope, with image acquisition every 12 hours over a span of 10 days, maintaining consistent acquisition settings.

Images of hNCAM- and TH-stained sections were acquired using an Olympus AX microscope, or an Epson Perfection V850 PRO scanner. The graft volume was estimated by measuring the area of the graft core in every eighth section throughout the entire graft using the ImageJ software (version 2.9.0). Area measurements were then multiplied by the distance between each sampled section (35 μm) and calibrated with a known measurement from a reference scale. Graft fiber innervation in each animal was assessed by hNCAM staining and measurements were overlayed on a nude rat brain reference based on anatomical landmarks. The number of TH^+ neurons in grafts were counted in all sections of a series under an Olympus microscope (BX53) equipped with an XYZ motorized stage using the Optical Fractionator probe of Stereo Investigator software (version 2023.2.3, MBF Bioscience). Stereological measurements were based on a region of interest traced with the 4x objective. Cell profiles were observed with a 100x oil objective, and a counting frame size of 100 μm x 100 μm was used. All images were processed using Adobe Photoshop CC2020, with any adjustments applied equally across the entire image.

Cell viability analysis

To assess cell viability in both silk and conventional organoids (**Paper I** and **III**), different strategies have been employed, including cell proliferation assays, immunofluorescence staining for cleaved caspase 3 and indirect measures of DNA damage. For colorimetric assays, mature organoids (with or without the silk scaffold) were dissociated at single cell level using papain, following the same procedure used for single-cell RNA sequencing sample preparation. Cell viability was then measured using either CyQuant (Invitrogen, cat. no. C35011) or MTT (Abcam, cat. no. ab211091) cell proliferation assay kits, according to manufacturer's instructions. The absorbance was measured with a Biochrom Asys Expert 96 microplate reader, using 50k cells/sample at 520 nm (CyQuant), or 100k cells/sample at 620nm (MTT). Samples were collected from 3 distinct organoids per condition and each organoid was analyzed in 3 to 6 replicates. DNA damage in conventional and silk organoid sections was detected using the Click-iT plus Tunel assay (Invitrogen, cat. no. C10617) according to manufacturer's protocol. Sections from the same organoid were also pre-treated with 1 U of DNAse I for 30 minutes at room temperature as an internal positive control. In **Paper I**, apoptosis was also assessed using flow cytometry with the Alexa Fluor 647 Annexin V conjugate (BD Pharmigen, cat. no. A23204).

Bioinformatic analysis of bulk sequencing data

Short read bulk RNA sequencing was employed in **Paper III** to compare the transcriptome of conventional and silk brain organoids at early stage of development. Although this technique does not provide single-cell resolution like single cell RNA sequencing, it allows in-depth assessments of global gene expression across samples. After RNA extraction, cDNA libraries were generated using the Illumina TruSeq Stranded library preparation kit with poly-A selection. Sequencing was performed as 2x150 bp paired-end reads on either a NextSeq 550 or NovaSeq 6000 machine (Illumina). Demultiplexing was achieved through the bcl2fastq software (Illumina, v2.19) and resulting fastq files were quantified using Salmon (v1.1) and the Gencode v.33 gene model. Differential expression analysis was performed in R using DESeq2 (v1.3) and Enhanced Volcano (v1.8) for visualization of volcano plots. Enriched gene ontology (GO) terms were retrieved using the g:Profiler webtool.

Single cell RNA sequencing sample preparation

While xenografts in **Paper IV** and **V** have been processed for single nuclei RNA sequencing as described above, progenitor and organoid samples have been instead prepared for single cell RNA sequencing. Cultured progenitors were manually detached using Accutase for 5 minutes at 37°C, then centrifuged at 400 g for 5 minutes and resuspended in BSA 0.1% (Fraction V) in HBSS (Thermo Fisher Scientific, cat. no. 14175095) at a concentration of 1k cells/µL. Organoids samples were collected between day 15 and 120 of differentiation and prepared as a single cell suspension using a papain and DNAseI solution in EBSS (Earle's Balanced Salt Solution) from the Papain Dissociation kit (Worthington, cat. no. LK003150). A total of 7k - 10k cells per sample were used as input for scRNAseq library preparation.

Library preparation, sequencing, and raw data processing

Single cells/nuclei were loaded onto Chromium Single Cell 3´ Chips (10X Genomics, cat. no. PN-120233, v3.1) along with the master mix and encapsulated with barcoded beads. After pooling and amplification, the quality of the resulting libraries was assessed by Bioanalyzer (DNA HS kit, Agilent). Sequencing was performed on Illumina NovaSeq 5000, NovaSeq 6000, NovaSeq X or NextSeq 500 in a 2x 100bp paired-end mode. For co-grafting experiments (**Paper V**), double barcode amplification was employed using half of the unfragmented library to distinguish between cells of origin in co-grafts, as described in Storm et al. 2024, introducing the TruSeq Read 2 sequence, an i7 index and the P7 sequence. Amplified barcodes were then sequenced with Illumina NovaSeq 6000 or Illumina NovaSeq X 2 x 50 bp reads. Demultiplexing was performed using bcl2fastq (v2.19) to separate the different samples. Raw transcriptome data was processed with the CellRanger pipeline (10X Genomics, v3.0 - 6.0). For graft samples, data were aligned to a custom reference that combined the human

GRCH38 (2020-A) and the rat Rnor 6.0 (v93 from Ensembl) genomes, allowing differentiation between graft and host cells. For organoid and progenitor data, alignment was performed only to the human genome.

Bioinformatic analysis of single cell/nuclei sequencing data

Downstream processing of resulting matrices was performed in R following the Seurat pipeline for all studies. In the quality control step, cells with a mitochondrial fraction greater than 10%, or nuclei with a fraction exceeding 1% were excluded from further analysis. Generally, the downstream pipeline included a log-transformation step, followed by variable genes identification and principal component analysis (PCA). The Harmony package was used for data integration across different datasets to correct for batch effects. Corrected coordinates were used for downstream projections (UMAP) and clustering. Clustering was performed using the Louvain algorithm, with the optimal resolution for clustering determined by the silhouette function from the cluster package (v2.1). Clusters were annotated based on both conventional marker and differentially expressed genes in each cluster, identified using the FindAllMarkers function in Seurat. Further details about the code and analysis of sequencing data can be found in the data availability section below and the Material and Methods sections of the respective publications.

Barcode library analysis and lineage tracing

Molecular barcode reads used in **Paper V** were first demultiplexed with bcl2fastq (v2.19), then processed using a custom Perl script (Storm et al., 2024) to identify and extract the library motifs from the fastq files. The Starcode software was employed for sequencing error correction, by collapsing viral barcodes that were one edit distance apart for each cell. The resulting matrix was filtered to include only viral barcodes found in the whitelist pool, and the cell barcodes derived from the CellRanger output. The specific library IDs were then used to assign cells

To their respective progenitor of origin (vMB, GPC, vFB or STR-patterned cells). Clones derived from vMB progenitors with five or more cells were retained for downstream analysis. For each clone, a "class" variable was assigned comparing the clone composition with the expected cell type distribution of vMB grafts. Clones showing a significant difference in cell composition, as determined by a chi-squared test (chisq.test in the R stats package), were considered enriched, as identified by the cell type with the highest residual value.

Data availability

With the exception of **Paper V**, currently in a manuscript format, all sequencing data and R code for downstream analysis included in this thesis are publicly available in the Gene Expression Omnibus or on github.com/ParmarLab. Accession numbers are summarized in Table 4.

Table 4 | Accession numbers and repositories for the sequencing data presented in this thesis.

Paper	Samples	Format	Accession number	Repository: github.com/ParmarLab/
I	vMB organoids	scRNAseq	GSE168323	scRNA-seq_silk_organoids
III	FB org. (d20)	RNAseq	GSE202992	Silk_organoids
III	FB org. (d120)	scRNAseq	GSE196423	Silk_organoids
IV	vMB grafts	snRNAseq	GSE233885	target-seq

ACKNOWLEDGMENTS

Congratulations! You've reached the end of this thesis and what is for me the most meaningful part of this book. This work would not exist without the countless interactions, collaborations, and moments of encouragement from the incredible people I've been fortunate to share this little giant adventure with. As I reflect on these past years, I am reminded that, just as neurons do not develop in isolation, no PhD can be completed alone. Both are influenced by the environment around them - by the dreams, hopes, expectations, and challenges brought by the people encountered along the way. These acknowledgments are my humble attempt to express gratitude to everyone who has contributed to this journey and helped shape it into what it has become. And in thanking you all, I hope to remind you of a few precious moments we shared - perhaps not the ones you expect, but the ones that left their mark on me.

Malin, I am grateful for all the opportunities you've given me over the years. Thank you for welcoming me into the lab five years ago, first as a Master's intern and later as a PhD student. The freedom you gave me and the challenges we faced together have helped me grow immensely, both personally and scientifically. I'm especially thankful for the chance to travel and share our research with the world, like at the ISSCR in Boston or at the CSHL organoid conference. Glad we did not miss that last ferry in Helsingør!

Ale, a long time has passed since that interview on the balcony of A11, little did I know about how everything would have evolved. For our late-night meetings, all the calls I interrupted, and the endless questions you answered – thanks. You taught me many things: in the hood, how to deal with stem cells, and beyond the bench, how science really works. Thanks for believing in me and for sharing with me this intense journey full of ups and downs – just like the streets of San Francisco, where you first shared the news about Leo. We are in this together, go big or go home!

Daniella, I am deeply grateful for all the support you've given me during these challenging final months of my PhD. Sometimes, the right word truly makes all the difference. You've always been available to listen, offer advice, and lend a hand whenever it was needed. Thank you for your invaluable input over the years, especially on functional experiments and electrophysiology.

Anders, I would like to thank you for being such a great inspiration and for always providing encouraging feedbacks during our lab meetings. Your knowledge, calm, humility, and great experience have made you a mentor I will always look up to. I may have never mentioned this before, but a conversation we had in *Stadshallen* some years ago was the spark defining what I want to focus on during my postdoc. Working with you has been the highest honor.

María, thank you for being the calmest person in the lab. Teacher of organoid technology and an eager student of my *in vivo* expertise, it's hard to capture your role in just a few lines. Thank you for being my supportive *ericito* during dark times - yes, I mean the blackout! I promise you one day you

will finally win a bet against me, as you will be able to get the first prize at John Bull´s quiz. Until then, signed with love, your dirty nurse.

Thank you, **Raquel** *ardilla*, for all the deep moments we've shared. From the mural of Maradona to Illustrator tutorials, from the PDP to the streets of Hamburg - where I found inspiration for this thesis cover - your presence has been unforgettable. Like the *mariposas*, I hope you'll fly high and gracefully over every challenge, landing gently on all the beautiful things that this life has to offer. Thank you for sprinkling my life with happiness - just like the glitter at *Shotluckan*.

Kerstin, I am so grateful for our chocolate drawer, an endless source of happiness and comfort during tough times. I promise I won't mention any other drawers here, as it would definitely be not appropriate. Everything I know about F1 (and most other sports) comes from you, along with the skill of starting a fire. Without you, I would have probably forgotten to write this thesis, and many other things along the way (taxes included).

Sara, thank you for hosting me in moments of need (and we understood each other) and for teaching me how to climb the fire escape stairs. You have always been the responsible adult in the room, never encouraging us to drink - definitely not *Brancamenta*. But perhaps what I should really thank you for is all the times we yelled and got mad at each other, for all the discussions - scientific and not - from our first day in the cell lab together (my first day as a PhD student) to our FaceTime calls. I owe you more than my pride will ever let me admit, I hope you know that. And not just for introducing me to the *Accabadora*.

Andreas, thank you for being by my side from my very first day in Sweden (when you were patching) to my last (when you'll probably still be patching). In this constantly mutating environment, you have been a lighthouse. A million thanks for all the Lebanese salads, the free translations, the endless supply of candies, and for revealing the secret passages beneath the BMC. You've been my go-to person for all the times I accidentally received 100 pairs of shoes from Spain. If I could, I'd bring you all the *Nascondini* in the world – and I know they won´t be enough.

Petter, without you I wouldn't know what *Robinson* is. Also, I wouldn't know what bioinformatics is - though I suppose that's been of secondary importance for my PhD. *ifelse(Petter == 1, "PhD", "noPhD")*. Thanks for listening to all my rants, I couldn't ask for a better conference companion - well, except maybe for those early morning runs! For all the care and attention to detail you put into every project, thank you.

Thank you, **Jana**, for your genuine enthusiasm - it's truly one of your best qualities, and it's so greatly contagious. Never change! Keep pushing the idea of a single-cell lab dog - you've got my full support. As for my payment, I'll gladly settle for *Captain* and *Campari*, as agreed! Wishing you the best of luck!

Ulla, first of all, thank you for sparing my life that first time I attempted to prepare the morning coffee! Your help in the histology lab has been invaluable, and your support throughout my PhD has meant so much to me. I hope you'll have a sip of limoncello for me - cheers to you!

Bengt, this thesis wouldn't exist without you, literally. Thank you for helping me move, for the countless discussions about figures and color palettes, and for sharing the same appreciation for a pleasing aesthetic in all aspects of our work. If you're reading these lines before anyone else, know

that I had the privilege of sharing your office for so many years, just a short stroll away from all your microscopy expertise. Have a sip of tea for me!

Thank you **Malin Å** for your endless patience in teaching me the basics of molecular biology, I wish I could clone all your knowledge too! It's impossible to see you without a smile, and your contagious happiness always brightens the lab. For all those times I sent you a picture of an empty dish or a faint electrophoresis band, thank you! Looking forward to having you back!

Paulina, thank you for all the administrative help, both big and small - from managing travels to timesheets and grants. You've truly been my prince charming, rescuing me from the fearsome Skatteverket dragon!

To the present and past members of the Parmar lab: **Mette, Julia, Linda, Jenny N, Micke, Yogita, Janko, Fredrik, Marcella, Jessica G,** and **Janitha** - thank you for your patience, support, countless laughs, and all the little adventures and trips we have shared. **Janko**, thank you for introducing me to Illustrator - I'm now addicted, and not planning to quit anytime soon. If you ever see him again, please thank "Bob" for me, for encouraging us to dive into mechanobiology. **Fredrik**, thank you for hosting the first *fresh pasta workshop* ever (even though it was without your consent). Maybe next time I'll ask for permission first - just maybe. "Sofa: 5/5 stars, would stay again". And teach me how to spin, great *flamingo*!

I am deeply grateful to the students I had the privilege of accompanying for a few steps along their journey. Not so long ago, I walked through the doors of this lab as an intern, and I still feel like I am that same person inside. So, you can imagine how inspiring it was to watch you discover this incredible world of research, just as I once did. And trust me, I'm not lying when I say you've taught me more than I could ever give you in return. **Tamina**, I can't think of a more unconventional way to start our time together - working from two different countries and in two different labs! As a neuroscientist, I have never imagined I'd witness beating cardiac organoids, but with you, there was a first time for everything. Thank you for being so meticulous, attentive, and independent - you made everything seem so easy. **Maria**, it's been amazing to see how much you've grown over the past few years, and I feel so lucky to still have you close. You know my door is always open to you - yes, even after 5 PM with one of your *impossible* questions. You'll always be welcome, little Panda. **Germán**, I see so much of myself in you - even when it's not necessarily a good thing! Unable to take a no for an answer, you have been an unstoppable force of nature, always determined to find your way and so damn curious. Working with you has been effortless, except when it came to convincing you to go home! Your help this past year has been invaluable - I couldn't have done it without you. To all of you, my warmest wishes as you continue on your PhD journeys. I am so proud of each of you, and the future is yours!

To **Lisa, Lotte, Georgia, Mike, Alice,** and the whole crew - thank you for all the laughs and unforgettable moments, whether at Ericsson's or beyond (even if I had to suffer Taylor Swift). **Alice**, never lose that inner childlike spirit, emerging every time we let our intrusive thoughts win while playing with the rat plushies! And don't worry… *this is fine*!

Anna and **Jenny J**, thank you for always being reachable, friendly, and professional, and for the enthusiasm with which you share your incredible technical skills. Of course, working with me has been a breeze - I'm never late, I never change my mind about the number of samples to sort or sequence, and I'm the picture of reliability! Despite all of that (or perhaps because of it?), you've always

managed to deal with me - no experiment was ever too complex, and no dataset was too big for this dream team.

I would like to express my gratitude to all the amazing people in A11 who made this working environment so active, supportive, and warm: **Johan, Anita, Nino, Raquel, Ofelia, Chris, Fereshteh, Laura, Cilla, Elin, Marie, Sol, Anna, Elias, Daniel,** and **Katja**. Thank you for all the nice conversations during fika and for your help with everyday matters. To the B10 crew - **Claudia, Christina, Costanza, Gigi, Efrain, Shayini, Sara, Niko, Oskar, Frenkie, Nadja, Enrico, Julie,** and **James** - your contributions and presence truly made a difference. I miss invading your kitchen for those rogue lunch breaks! A special thanks to all the people I met during these years with whom I shared this journey in the name of science: **Nic, Ugne, Fabio, Evelyn, Eliska, Tiago, Martino, Matilde, Jana, Isak, Marija, Ana, Markus, Roberta,** and **Edo**. Thank you for all the fun outside the lab - for the dinners, barbecues, parties, movie nights, and beers we shared. So many great memories!

Over these past years, I have been lucky to collaborate with incredible groups from around the world and to exchange ideas, techniques, data, and more with some truly outstanding scientists. **Jürgen, Daniel, Abel,** and the rest of the **Knoblich lab** - thank you for warmly welcoming me in Vienna and for making me feel like part of the team during my stay. **Elena, Dario, Linda, Christian,** and the **Cattaneo lab** - thank you for the long-standing collaboration, the wonderful environment within **NSC-R**, and the unforgettable time in Bellagio. **Jenny, Giorgio, Arto, Surangrat,** and all the members of the **Emnéus lab** and **OpenMind** - thank you for your patience in introducing me to the world of biomaterials and bioengineering. There was (is!) so much to learn, and I truly appreciated the chance to dip my toe into another field.

To all my friends in Italy and scattered around the world, thank you for standing by my side for so long, despite the kilometers that separate us. Far away, yet never distant! To **Elena, Chiara, Marco**, and **Blendi** - thank you for being the soundtrack to this incredible movie called life. But don't worry, the credits aren't rolling yet… *it's not over*! And remember, you are never gonna be alone. **Ire** and **Pol**, it's incredible to think how much time has passed since that first day in *Aula Savi* - the beginning of this amazing journey through science. I'm so grateful for all the *degrado*, the AdBlue, and the unforgettable moments with *Bello Figo Gu*. **Marta**, I never thought it was possible to find someone as *permaloso* as me, but you never fail to surprise me! For all the drama, thank you *neh*… I guess?! **Jessica L**, thank you for the wonderful time in Innsbruck and for rescuing me with your trusty pink phone! Wishing you the best of luck, and I hope we get to see each other again soon!

To **Mamma, Papá, Muci,** and my family – thank you for your continuous and invaluable support throughout the years. Thanks for cultivating my curiosity and creativity, shaping me into who I am today. To **Cassiopeia, Dany, Padme, Vi, Chani, Kimiko, Ermione, Cupcake, Pesto,** and **Evey** – from the deepest shadows to the flickering light of a single candle, only *ashes* can express how grateful I am to have had you by my side.

To all the post-its, tirelessly serving to complement my memory – your sacrifice will not be forgotten. To all the words, the hugs, and the ideas shared over these years, to everything I carry with me. And, finally, to you reading this line – because, in the end, we share the same sky.

Thank you.

Edo

REFERENCES

Adams, Y., Clausen, A. S., Jensen, P. O., Lager, M., Wilhelmsson, P., Henningson, A. J., Lindgren, P. E., Faurholt-Jepsen, D., Mens, H., Kraiczy, P., Kragh, K. N., Bjarnsholt, T., Kjaer, A., Lebech, A. M., & Jensen, A. R. (2023). 3D blood-brain barrier-organoids as a model for Lyme neuroborreliosis highlighting genospecies dependent organotropism. iScience, 26(1), 105838. https://doi.org/10.1016/j.isci.2022.105838

Adler, A. F., Cardoso, T., Nolbrant, S., Mattsson, B., Hoban, D. B., Jarl, U., Wahlestedt, J. N., Grealish, S., Bjorklund, A., & Parmar, M. (2019). hESC-Derived Dopaminergic Transplants Integrate into Basal Ganglia Circuitry in a Preclinical Model of Parkinson's Disease. Cell Rep, 28(13), 3462-3473 e3465. https://doi.org/10.1016/j.celrep.2019.08.058

Agarwal, D., Sandor, C., Volpato, V., Caffrey, T. M., Monzon-Sandoval, J., Bowden, R., Alegre-Abarrategui, J., Wade-Martins, R., & Webber, C. (2020). A single-cell atlas of the human substantia nigra reveals cell-specific pathways associated with neurological disorders. Nat Commun, 11(1), 4183. https://doi.org/10.1038/s41467-020-17876-0

AlDakheel, A., Kalia, L. V., & Lang, A. E. (2014). Pathogenesis-targeted, disease-modifying therapies in Parkinson disease. Neurotherapeutics, 11(1), 6-23. https://doi.org/10.1007/s13311-013-0218-1

Andersson, E., Jensen, J. B., Parmar, M., Guillemot, F., & Bjorklund, A. (2006). Development of the mesencephalic dopaminergic neuron system is compromised in the absence of neurogenin 2. Development, 133(3), 507-516. https://doi.org/10.1242/dev.02224

Andersson, E., Tryggvason, U., Deng, Q., Friling, S., Alekseenko, Z., Robert, B., Perlmann, T., & Ericson, J. (2006). Identification of intrinsic determinants of midbrain dopamine neurons. Cell, 124(2), 393-405. https://doi.org/10.1016/j.cell.2005.10.037

Ang, S. L. (2009). Foxa1 and Foxa2 transcription factors regulate differentiation of midbrain dopaminergic neurons. Adv Exp Med Biol, 651, 58-65. https://doi.org/10.1007/978-1-4419-0322-8_5

Arenas, E., Denham, M., & Villaescusa, J. C. (2015). How to make a midbrain dopaminergic neuron. Development, 142(11), 1918-1936. https://doi.org/10.1242/dev.097394

Asgrimsdottir, E. S., & Arenas, E. (2020). Midbrain Dopaminergic Neuron Development at the Single Cell Level: In vivo and in Stem Cells. Front Cell Dev Biol, 8, 463. https://doi.org/10.3389/fcell.2020.00463

Atamian, A., Birtele, M., Hosseini, N., Nguyen, T., Seth, A., Del Dosso, A., Paul, S., Tedeschi, N., Taylor, R., Coba, M. P., Samarasinghe, R., Lois, C., & Quadrato, G. (2024). Human cerebellar organoids with functional Purkinje cells. Cell Stem Cell, 31(1), 39-51 e36. https://doi.org/10.1016/j.stem.2023.11.013

Bagley, J. A., Reumann, D., Bian, S., Levi-Strauss, J., & Knoblich, J. A. (2017). Fused cerebral organoids model interactions between brain regions. Nat Methods, 14(7), 743-751. https://doi.org/10.1038/nmeth.4304

Barker, R. A., Barrett, J., Mason, S. L., & Bjorklund, A. (2013). Fetal dopaminergic transplantation trials and the future of neural grafting in Parkinson's disease. Lancet Neurol, 12(1), 84-91. https://doi.org/10.1016/S1474-4422(12)70295-8

Barker, R. A., Bjorklund, A., & Parmar, M. (2024). The history and status of dopamine cell therapies for Parkinson's disease. Bioessays, 46(12), e2400118. https://doi.org/10.1002/bies.202400118

Barker, R. A., & consortium, T. (2019). Designing stem-cell-based dopamine cell replacement trials for Parkinson's disease. Nat Med, 25(7), 1045-1053. https://doi.org/10.1038/s41591-019-0507-2

Barker, R. A., Drouin-Ouellet, J., & Parmar, M. (2015). Cell-based therapies for Parkinson disease-past insights and future potential. Nat Rev Neurol, 11(9), 492-503. https://doi.org/10.1038/nrneurol.2015.123

Barker, R. A., Parmar, M., Studer, L., & Takahashi, J. (2017). Human Trials of Stem Cell-Derived Dopamine Neurons for Parkinson's Disease: Dawn of a New Era. Cell Stem Cell, 21(5), 569-573. https://doi.org/10.1016/j.stem.2017.09.014

Barker, R. A., Studer, L., Cattaneo, E., Takahashi, J., & consortium, G. F. P. (2015). G-Force PD: a global initiative in coordinating stem cell-based dopamine treatments for Parkinson's disease. NPJ Parkinsons Dis, 1, 15017. https://doi.org/10.1038/npjparkd.2015.17

Bayer, S. A., Wills, K. V., Triarhou, L. C., Verina, T., Thomas, J. D., & Ghetti, B. (1995). Selective vulnerability of late-generated dopaminergic neurons of the substantia nigra in weaver mutant mice. Proc Natl Acad Sci U S A, 92(20), 9137-9140. https://doi.org/10.1073/pnas.92.20.9137

Beier, K. T., Gao, X. J., Xie, S., DeLoach, K. E., Malenka, R. C., & Luo, L. (2019). Topological Organization of Ventral Tegmental Area Connectivity Revealed by Viral-Genetic Dissection of Input-Output Relations. Cell Rep, 26(1), 159-167 e156. https://doi.org/10.1016/j.celrep.2018.12.040

Beier, K. T., Steinberg, E. E., DeLoach, K. E., Xie, S., Miyamichi, K., Schwarz, L., Gao, X. J., Kremer, E. J., Malenka, R. C., & Luo, L. (2015). Circuit Architecture of VTA Dopamine Neurons Revealed by Systematic Input-Output Mapping. Cell, 162(3), 622-634. https://doi.org/10.1016/j.cell.2015.07.015

Bergmann, S., Lawler, S. E., Qu, Y., Fadzen, C. M., Wolfe, J. M., Regan, M. S., Pentelute, B. L., Agar, N. Y. R., & Cho, C. F. (2018). Blood-brain-barrier organoids for investigating the permeability of CNS therapeutics. Nature Protocols, 13(12), 2827-2843. https://doi.org/10.1038/s41596-018-0066-x

Bernheimer, H., Birkmayer, W., Hornykiewicz, O., Jellinger, K., & Seitelberger, F. (1973). Brain dopamine and the syndromes of Parkinson and Huntington. Clinical, morphological and neurochemical correlations. J Neurol Sci, 20(4), 415-455. https://doi.org/10.1016/0022-510x(73)90175-5

Bhaduri, A., Andrews, M. G., Mancia Leon, W., Jung, D., Shin, D., Allen, D., Jung, D., Schmunk, G., Haeussler, M., Salma, J., Pollen, A. A., Nowakowski, T. J., & Kriegstein, A. R. (2020). Cell stress in cortical organoids impairs molecular subtype specification. Nature, 578(7793), 142-148. https://doi.org/10.1038/s41586-020-1962-0

Birey, F., Andersen, J., Makinson, C. D., Islam, S., Wei, W., Huber, N., Fan, H. C., Metzler, K. R. C., Panagiotakos, G., Thom, N., O'Rourke, N. A., Steinmetz, L. M., Bernstein, J. A., Hallmayer, J., Huguenard, J. R., & Pasca, S. P. (2017). Assembly of functionally integrated human forebrain spheroids. Nature, 545(7652), 54-59. https://doi.org/10.1038/nature22330

Birey, F., Li, M. Y., Gordon, A., Thete, M. V., Valencia, A. M., Revah, O., Pasca, A. M., Geschwind, D. H., & Pasca, S. P. (2022). Dissecting the molecular basis of human interneuron migration in forebrain assembloids from Timothy syndrome. Cell Stem Cell, 29(2), 248-264 e247. https://doi.org/10.1016/j.stem.2021.11.011

Birtele, M., Storm, P., Sharma, Y., Kajtez, J., Wahlestedt, J. N., Sozzi, E., Nilsson, F., Stott, S., He, X. L., Mattsson, B., Ottosson, D. R., Barker, R. A., Fiorenzano, A., & Parmar, M. (2022). Single-cell transcriptional and functional analysis of dopaminergic neurons in organoid-like cultures derived from human fetal midbrain. Development, 149(23). https://doi.org/10.1242/dev.200504

Bjorklund, A., & Barker, R. A. (2024). The basal forebrain cholinergic system as target for cell replacement therapy in Parkinson's disease. Brain, 147(6), 1937-1952. https://doi.org/10.1093/brain/awae026

Bjorklund, A., & Dunnett, S. B. (2007). Dopamine neuron systems in the brain: an update. Trends Neurosci, 30(5), 194-202. https://doi.org/10.1016/j.tins.2007.03.006

Bjorklund, A., Dunnett, S. B., Stenevi, U., Lewis, M. E., & Iversen, S. D. (1980). Reinnervation of the denervated striatum by substantia nigra transplants: functional consequences as revealed by pharmacological and sensorimotor testing. Brain Res, 199(2), 307-333. https://doi.org/10.1016/0006-8993(80)90692-7

Bjorklund, A., & Stenevi, U. (1979). Reconstruction of the nigrostriatal dopamine pathway by intracerebral nigral transplants. Brain Res, 177(3), 555-560. https://doi.org/10.1016/0006-8993(79)90472-4

Bjorklund, A., Stenevi, U., Dunnett, S. B., & Iversen, S. D. (1981). Functional reactivation of the deafferented neostriatum by nigral transplants. Nature, 289(5797), 497-499. https://doi.org/10.1038/289497a0

Blaess, S., Bodea, G. O., Kabanova, A., Chanet, S., Mugniery, E., Derouiche, A., Stephen, D., & Joyner, A. L. (2011). Temporal-spatial changes in Sonic Hedgehog expression and signaling reveal different potentials of ventral mesencephalic progenitors to populate distinct ventral midbrain nuclei. Neural Dev, 6, 29. https://doi.org/10.1186/1749-8104-6-29

Bodea, G. O., Spille, J. H., Abe, P., Andersson, A. S., Acker-Palmer, A., Stumm, R., Kubitscheck, U., & Blaess, S. (2014). Reelin and CXCL12 regulate distinct migratory behaviors during the development of the dopaminergic system. Development, 141(3), 661-673. https://doi.org/10.1242/dev.099937

Bonilla, S., Hall, A. C., Pinto, L., Attardo, A., Gotz, M., Huttner, W. B., & Arenas, E. (2008). Identification of midbrain floor plate radial glia-like cells as dopaminergic progenitors. Glia, 56(8), 809-820. https://doi.org/10.1002/glia.20654

Braak, H., Ghebremedhin, E., Rub, U., Bratzke, H., & Del Tredici, K. (2004). Stages in the development of Parkinson's disease-related pathology. Cell Tissue Res, 318(1), 121-134. https://doi.org/10.1007/s00441-004-0956-9

Braun, E., Danan-Gotthold, M., Borm, L. E., Lee, K. W., Vinsland, E., Lonnerberg, P., Hu, L., Li, X., He, X., Andrusivova, Z., Lundeberg, J., Barker, R. A., Arenas, E., Sundstrom, E., & Linnarsson, S. (2023). Comprehensive cell atlas of the first-trimester developing human brain. Science, 382(6667), eadf1226. https://doi.org/10.1126/science.adf1226

Brignani, S., & Pasterkamp, R. J. (2017). Neuronal Subset-Specific Migration and Axonal Wiring Mechanisms in the Developing Midbrain Dopamine System. Front Neuroanat, 11, 55. https://doi.org/10.3389/fnana.2017.00055

Brignani, S., Raj, D. D. A., Schmidt, E. R. E., Dudukcu, O., Adolfs, Y., De Ruiter, A. A., Rybiczka-Tesulov, M., Verhagen, M. G., van der Meer, C., Broekhoven, M. H., Moreno-Bravo, J. A., Grossouw, L. M., Dumontier, E., Cloutier, J. F., Chedotal, A., & Pasterkamp, R. J. (2020). Remotely Produced and Axon-Derived Netrin-1 Instructs GABAergic Neuron Migration and Dopaminergic Substantia Nigra Development. Neuron, 107(4), 684-702 e689. https://doi.org/10.1016/j.neuron.2020.05.037

Broccoli, V., Boncinelli, E., & Wurst, W. (1999). The caudal limit of Otx2 expression positions the isthmic organizer. Nature, 401(6749), 164-168. https://doi.org/10.1038/43670

Brochier, C., Gaillard, M. C., Diguet, E., Caudy, N., Dossat, C., Segurens, B., Wincker, P., Roze, E., Caboche, J., Hantraye, P., Brouillet, E., Elalouf, J. M., & de Chaldee, M. (2008). Quantitative gene expression profiling of mouse brain regions reveals differential transcripts conserved in human and affected in disease models. Physiol Genomics, 33(2), 170-179. https://doi.org/10.1152/physiolgenomics.00125.2007

Bronstein, J. M., Tagliati, M., Alterman, R. L., Lozano, A. M., Volkmann, J., Stefani, A., Horak, F. B., Okun, M. S., Foote, K. D., Krack, P., Pahwa, R., Henderson, J. M., Hariz, M. I., Bakay, R. A., Rezai, A., Marks, W. J., Jr., Moro, E., Vitek, J. L., Weaver, F. M., . . . DeLong, M. R. (2011). Deep brain stimulation for Parkinson disease: an expert consensus and review of key issues. Arch Neurol, 68(2), 165. https://doi.org/10.1001/archneurol.2010.260

Brundin, P., Karlsson, J., Emgard, M., Schierle, G. S., Hansson, O., Petersen, A., & Castilho, R. F. (2000). Improving the survival of grafted dopaminergic neurons: a review over current approaches. Cell Transplant, 9(2), 179-195. https://doi.org/10.1177/096368970000900205

Brundin, P., Nilsson, O. G., Strecker, R. E., Lindvall, O., Astedt, B., & Bjorklund, A. (1986). Behavioural effects of human fetal dopamine neurons grafted in a rat model of Parkinson's disease. Exp Brain Res, 65(1), 235-240. https://doi.org/10.1007/BF00243848

Brundin, P., Strecker, R. E., Widner, H., Clarke, D. J., Nilsson, O. G., Astedt, B., Lindvall, O., & Bjorklund, A. (1988). Human fetal dopamine neurons grafted in a rat model of Parkinson's disease: immunological aspects, spontaneous and drug-induced behaviour, and dopamine release. Exp Brain Res, 70(1), 192-208. https://doi.org/10.1007/BF00271860

Cardoso, T., Adler, A. F., Mattsson, B., Hoban, D. B., Nolbrant, S., Wahlestedt, J. N., Kirkeby, A., Grealish, S., Bjorklund, A., & Parmar, M. (2018). Target-specific forebrain projections and appropriate synaptic inputs of hESC-derived dopamine neurons grafted to the midbrain of parkinsonian rats. J Comp Neurol, 526(13), 2133-2146. https://doi.org/10.1002/cne.24500

Castrioto, A., Lhommee, E., Moro, E., & Krack, P. (2014). Mood and behavioural effects of subthalamic stimulation in Parkinson's disease. Lancet Neurol, 13(3), 287-305. https://doi.org/10.1016/S1474-4422(13)70294-1

Chabrat, A., Brisson, G., Doucet-Beaupre, H., Salesse, C., Schaan Profes, M., Dovonou, A., Akitegetse, C., Charest, J., Lemstra, S., Cote, D., Pasterkamp, R. J., Abrudan, M. I., Metzakopian, E., Ang, S. L., & Levesque, M. (2017). Transcriptional repression of Plxnc1 by Lmx1a and Lmx1b directs topographic dopaminergic circuit formation. Nat Commun, 8(1), 933. https://doi.org/10.1038/s41467-017-01042-0

Chakrabarty, K., Von Oerthel, L., Hellemons, A., Clotman, F., Espana, A., Groot Koerkamp, M., Holstege, F. C., Pasterkamp, R. J., & Smidt, M. P. (2012). Genome wide expression profiling of the mesodiencephalic region identifies novel factors involved in early and late dopaminergic development. Biol Open, 1(8), 693-704. https://doi.org/10.1242/bio.20121230

Chambers, S. M., Fasano, C. A., Papapetrou, E. P., Tomishima, M., Sadelain, M., & Studer, L. (2009). Highly efficient neural conversion of human ES and iPS cells by dual inhibition of SMAD signaling. Nat Biotechnol, 27(3), 275-280. https://doi.org/10.1038/nbt.1529

Chen, Y., Xiong, M., Dong, Y., Haberman, A., Cao, J., Liu, H., Zhou, W., & Zhang, S. C. (2016). Chemical Control of Grafted Human PSC-Derived Neurons in a Mouse Model of Parkinson's Disease. Cell Stem Cell, 18(6), 817-826. https://doi.org/10.1016/j.stem.2016.03.014

Cho, A. N., Jin, Y., An, Y., Kim, J., Choi, Y. S., Lee, J. S., Kim, J., Choi, W. Y., Koo, D. J., Yu, W., Chang, G. E., Kim, D. Y., Jo, S. H., Kim, J., Kim, S. Y., Kim, Y. G., Kim, J. Y., Choi, N., Cheong, E., . . . Cho, S. W. (2021). Microfluidic device with brain extracellular matrix promotes structural and functional maturation of human brain organoids. Nat Commun, 12(1), 4730. https://doi.org/10.1038/s41467-021-24775-5

Chung, C. Y., Seo, H., Sonntag, K. C., Brooks, A., Lin, L., & Isacson, O. (2005). Cell type-specific gene expression of midbrain dopaminergic neurons reveals molecules involved in their vulnerability and protection. Hum Mol Genet, 14(13), 1709-1725. https://doi.org/10.1093/hmg/ddi178

Colas, J. F., & Schoenwolf, G. C. (2001). Towards a cellular and molecular understanding of neurulation. Dev Dyn, 221(2), 117-145. https://doi.org/10.1002/dvdy.1144

Connolly, B. S., & Lang, A. E. (2014). Pharmacological treatment of Parkinson disease: a review. JAMA, 311(16), 1670-1683. https://doi.org/10.1001/jama.2014.3654

Cserep, C., Posfai, B., & Denes, A. (2021). Shaping Neuronal Fate: Functional Heterogeneity of Direct Microglia-Neuron Interactions. Neuron, 109(2), 222-240. https://doi.org/10.1016/j.neuron.2020.11.007

Dahlstrom, A., & Fuxe, K. (1964). Localization of monoamines in the lower brain stem. Experientia, 20(7), 398-399. https://doi.org/10.1007/BF02147990

Damier, P., Hirsch, E. C., Agid, Y., & Graybiel, A. M. (1999). The substantia nigra of the human brain. II. Patterns of loss of dopamine-containing neurons in Parkinson's disease. Brain, 122 (Pt 8), 1437-1448. https://doi.org/10.1093/brain/122.8.1437

Dawson, T. M., Ko, H. S., & Dawson, V. L. (2010). Genetic animal models of Parkinson's disease. Neuron, 66(5), 646-661. https://doi.org/10.1016/j.neuron.2010.04.034

de Lau, L. M., & Breteler, M. M. (2006). Epidemiology of Parkinson's disease. Lancet Neurol, 5(6), 525-535. https://doi.org/10.1016/S1474-4422(06)70471-9

Delli Carri, A., Onorati, M., Castiglioni, V., Faedo, A., Camnasio, S., Toselli, M., Biella, G., & Cattaneo, E. (2013). Human pluripotent stem cell differentiation into authentic striatal projection neurons. Stem Cell Rev Rep, 9(4), 461-474. https://doi.org/10.1007/s12015-013-9441-8

Denham, M., Bye, C., Leung, J., Conley, B. J., Thompson, L. H., & Dottori, M. (2012). Glycogen synthase kinase 3beta and activin/nodal inhibition in human embryonic stem cells induces a pre-neuroepithelial state that is required for specification to a floor plate cell lineage. Stem Cells, 30(11), 2400-2411. https://doi.org/10.1002/stem.1204

Di Salvio, M., Di Giovannantonio, L. G., Omodei, D., Acampora, D., & Simeone, A. (2010). Otx2 expression is restricted to dopaminergic neurons of the ventral tegmental area in the adult brain. Int J Dev Biol, 54(5), 939-945. https://doi.org/10.1387/ijdb.092974ms

Doi, D., Magotani, H., Kikuchi, T., Ikeda, M., Hiramatsu, S., Yoshida, K., Amano, N., Nomura, M., Umekage, M., Morizane, A., & Takahashi, J. (2020). Pre-clinical study of induced pluripotent stem cell-derived dopaminergic progenitor cells for Parkinson's disease. Nat Commun, 11(1), 3369. https://doi.org/10.1038/s41467-020-17165-w

Doi, D., Samata, B., Katsukawa, M., Kikuchi, T., Morizane, A., Ono, Y., Sekiguchi, K., Nakagawa, M., Parmar, M., & Takahashi, J. (2014). Isolation of human induced pluripotent stem cell-derived dopaminergic progenitors by cell sorting for successful transplantation. Stem Cell Reports, 2(3), 337-350. https://doi.org/10.1016/j.stemcr.2014.01.013

Duncan, G. W., Khoo, T. K., Yarnall, A. J., O'Brien, J. T., Coleman, S. Y., Brooks, D. J., Barker, R. A., & Burn, D. J. (2014). Health-related quality of life in early Parkinson's disease: the impact of nonmotor symptoms. Mov Disord, 29(2), 195-202. https://doi.org/10.1002/mds.25664

Dunnett, S. B., Bjorklund, A., Stenevi, U., & Iversen, S. D. (1981). Grafts of embryonic substantia nigra reinnervating the ventrolateral striatum ameliorate sensorimotor impairments and akinesia in rats with 6-OHDA lesions of the nigrostriatal pathway. Brain Res, 229(1), 209-217. https://doi.org/10.1016/0006-8993(81)90759-9

Echelard, Y., Epstein, D. J., St-Jacques, B., Shen, L., Mohler, J., McMahon, J. A., & McMahon, A. P. (1993). Sonic hedgehog, a member of a family of putative signaling molecules, is implicated in the regulation of CNS polarity. Cell, 75(7), 1417-1430. https://doi.org/10.1016/0092-8674(93)90627-3

Farassat, N., Costa, K. M., Stojanovic, S., Albert, S., Kovacheva, L., Shin, J., Egger, R., Somayaji, M., Duvarci, S., Schneider, G., & Roeper, J. (2019). In vivo functional diversity of midbrain dopamine neurons within identified axonal projections. Elife, 8. https://doi.org/10.7554/eLife.48408

Ferri, A. L., Lin, W., Mavromatakis, Y. E., Wang, J. C., Sasaki, H., Whitsett, J. A., & Ang, S. L. (2007). Foxa1 and Foxa2 regulate multiple phases of midbrain dopaminergic neuron development in a dosage-dependent manner. Development, 134(15), 2761-2769. https://doi.org/10.1242/dev.000141

Fiorenzano, A., Birtele, M., Wahlestedt, J. N., & Parmar, M. (2021). Evaluation of TH-Cre knock-in cell lines for detection and specific targeting of stem cell-derived dopaminergic neurons. Heliyon, 7(1), e06006. https://doi.org/10.1016/j.heliyon.2021.e06006

Fiorenzano, A., Sozzi, E., Parmar, M., & Storm, P. (2021). Dopamine Neuron Diversity: Recent Advances and Current Challenges in Human Stem Cell Models and Single Cell Sequencing. Cells, 10(6). https://doi.org/10.3390/cells10061366

Freund, T. F., Powell, J. F., & Smith, A. D. (1984). Tyrosine hydroxylase-immunoreactive boutons in synaptic contact with identified striatonigral neurons, with particular reference to dendritic spines. Neuroscience, 13(4), 1189-1215. https://doi.org/10.1016/0306-4522(84)90294-x

Fu, Y., Yuan, Y., Halliday, G., Rusznak, Z., Watson, C., & Paxinos, G. (2012). A cytoarchitectonic and chemoarchitectonic analysis of the dopamine cell groups in the substantia nigra, ventral tegmental area, and retrorubral field in the mouse. Brain Struct Funct, 217(2), 591-612. https://doi.org/10.1007/s00429-011-0349-2

Gantner, C. W., de Luzy, I. R., Kauhausen, J. A., Moriarty, N., Niclis, J. C., Bye, C. R., Penna, V., Hunt, C. P. J., Ermine, C. M., Pouton, C. W., Kirik, D., Thompson, L. H., & Parish, C. L. (2020). Viral Delivery of GDNF Promotes Functional Integration of Human Stem Cell Grafts in Parkinson's Disease. Cell Stem Cell, 26(4), 511-526 e515. https://doi.org/10.1016/j.stem.2020.01.010

Garritsen, O., van Battum, E. Y., Grossouw, L. M., & Pasterkamp, R. J. (2023). Development, wiring and function of dopamine neuron subtypes. Nat Rev Neurosci, 24(3), 134-152. https://doi.org/10.1038/s41583-022-00669-3

Grealish, S., Diguet, E., Kirkeby, A., Mattsson, B., Heuer, A., Bramoulle, Y., Van Camp, N., Perrier, A. L., Hantraye, P., Bjorklund, A., & Parmar, M. (2014). Human ESC-derived dopamine neurons show similar preclinical efficacy and potency to fetal neurons when grafted in a rat model of Parkinson's disease. Cell Stem Cell, 15(5), 653-665. https://doi.org/10.1016/j.stem.2014.09.017

Grealish, S., Heuer, A., Cardoso, T., Kirkeby, A., Jonsson, M., Johansson, J., Bjorklund, A., Jakobsson, J., & Parmar, M. (2015). Monosynaptic Tracing using Modified Rabies Virus Reveals Early and Extensive Circuit Integration of Human Embryonic Stem Cell-Derived Neurons. Stem Cell Reports, 4(6), 975-983. https://doi.org/10.1016/j.stemcr.2015.04.011

Greene, J. G., Dingledine, R., & Greenamyre, J. T. (2005). Gene expression profiling of rat midbrain dopamine neurons: implications for selective vulnerability in parkinsonism. Neurobiol Dis, 18(1), 19-31. https://doi.org/10.1016/j.nbd.2004.10.003

Grimm, J., Mueller, A., Hefti, F., & Rosenthal, A. (2004). Molecular basis for catecholaminergic neuron diversity. Proc Natl Acad Sci U S A, 101(38), 13891-13896. https://doi.org/10.1073/pnas.0405340101

Groves, P. M., Wilson, C. J., Young, S. J., & Rebec, G. V. (1975). Self-inhibition by dopaminergic neurons. Science, 190(4214), 522-528. https://doi.org/10.1126/science.242074

Hagell, P., Schrag, A., Piccini, P., Jahanshahi, M., Brown, R., Rehncrona, S., Widner, H., Brundin, P., Rothwell, J. C., Odin, P., Wenning, G. K., Morrish, P., Gustavii, B., Bjorklund, A., Brooks, D. J., Marsden, C. D., Quinn, N. P., & Lindvall, O. (1999). Sequential bilateral transplantation in Parkinson's disease: effects of the second graft. Brain, 122 (Pt 6), 1121-1132. https://doi.org/10.1093/brain/122.6.1121

Harland, R. (2000). Neural induction. Curr Opin Genet Dev, 10(4), 357-362. https://doi.org/10.1016/s0959-437x(00)00096-4

Hayes, L., Zhang, Z., Albert, P., Zervas, M., & Ahn, S. (2011). Timing of Sonic hedgehog and Gli1 expression segregates midbrain dopamine neurons. J Comp Neurol, 519(15), 3001-3018. https://doi.org/10.1002/cne.22711

He, Z., Dony, L., Fleck, J. S., Szalata, A., Li, K. X., Sliskovic, I., Lin, H. C., Santel, M., Atamian, A., Quadrato, G., Sun, J., Pasca, S. P., Human Cell Atlas Organoid Biological, N., Camp, J. G., Theis, F. J., & Treutlein, B. (2024). An integrated transcriptomic cell atlas of human neural organoids. Nature, 635(8039), 690-698. https://doi.org/10.1038/s41586-024-08172-8

Hebsgaard, J. B., Nelander, J., Sabelstrom, H., Jonsson, M. E., Stott, S., & Parmar, M. (2009). Dopamine neuron precursors within the developing human mesencephalon show radial glial characteristics. Glia, 57(15), 1648-1658. https://doi.org/10.1002/glia.20877

Hegarty, S. V., Sullivan, A. M., & O'Keeffe, G. W. (2013). Midbrain dopaminergic neurons: a review of the molecular circuitry that regulates their development. Dev Biol, 379(2), 123-138. https://doi.org/10.1016/j.ydbio.2013.04.014

Hiller, B. M., Marmion, D. J., Thompson, C. A., Elliott, N. A., Federoff, H., Brundin, P., Mattis, V. B., McMahon, C. W., & Kordower, J. H. (2022). Optimizing maturity and dose of iPSC-derived dopamine progenitor cell therapy for Parkinson's disease. NPJ Regen Med, 7(1), 24. https://doi.org/10.1038/s41536-022-00221-y

Hong, S., Chung, S., Leung, K., Hwang, I., Moon, J., & Kim, K. S. (2014). Functional roles of Nurr1, Pitx3, and Lmx1a in neurogenesis and phenotype specification of dopamine neurons during in vitro differentiation of embryonic stem cells. Stem Cells Dev, 23(5), 477-487. https://doi.org/10.1089/scd.2013.0406

Hook, P. W., McClymont, S. A., Cannon, G. H., Law, W. D., Morton, A. J., Goff, L. A., & McCallion, A. S. (2018). Single-Cell RNA-Seq of Mouse Dopaminergic Neurons Informs Candidate Gene Selection for Sporadic Parkinson Disease. Am J Hum Genet, 102(3), 427-446. https://doi.org/10.1016/j.ajhg.2018.02.001

Hu, Z., Cooper, M., Crockett, D. P., & Zhou, R. (2004). Differentiation of the midbrain dopaminergic pathways during mouse development. J Comp Neurol, 476(3), 301-311. https://doi.org/10.1002/cne.20230

Hyland, B. I., Reynolds, J. N., Hay, J., Perk, C. G., & Miller, R. (2002). Firing modes of midbrain dopamine cells in the freely moving rat. Neuroscience, 114(2), 475-492. https://doi.org/10.1016/s0306-4522(02)00267-1

Jacobs, F. M., van Erp, S., van der Linden, A. J., von Oerthel, L., Burbach, J. P., & Smidt, M. P. (2009). Pitx3 potentiates Nurr1 in dopamine neuron terminal differentiation through release of SMRT-mediated repression. Development, 136(4), 531-540. https://doi.org/10.1242/dev.029769

Jankovic, J. (2005). Motor fluctuations and dyskinesias in Parkinson's disease: clinical manifestations. Mov Disord, 20 Suppl 11, S11-16. https://doi.org/10.1002/mds.20458

Jo, J., Xiao, Y., Sun, A. X., Cukuroglu, E., Tran, H. D., Goke, J., Tan, Z. Y., Saw, T. Y., Tan, C. P., Lokman, H., Lee, Y., Kim, D., Ko, H. S., Kim, S. O., Park, J. H., Cho, N. J., Hyde, T. M., Kleinman, J. E., Shin, J. H., . . . Ng, H. H. (2016). Midbrain-like Organoids from Human Pluripotent Stem Cells Contain Functional Dopaminergic and Neuromelanin-Producing Neurons. Cell Stem Cell, 19(2), 248-257. https://doi.org/10.1016/j.stem.2016.07.005

Joksimovic, M., Yun, B. A., Kittappa, R., Anderegg, A. M., Chang, W. W., Taketo, M. M., McKay, R. D., & Awatramani, R. B. (2009). Wnt antagonism of Shh facilitates midbrain floor plate neurogenesis. Nat Neurosci, 12(2), 125-131. https://doi.org/10.1038/nn.2243

Kabanova, A., Pabst, M., Lorkowski, M., Braganza, O., Boehlen, A., Nikbakht, N., Pothmann, L., Vaswani, A. R., Musgrove, R., Di Monte, D. A., Sauvage, M., Beck, H., & Blaess, S. (2015). Function and developmental origin of a mesocortical inhibitory circuit. Nat Neurosci, 18(6), 872-882. https://doi.org/10.1038/nn.4020

Kadoshima, T., Sakaguchi, H., Nakano, T., Soen, M., Ando, S., Eiraku, M., & Sasai, Y. (2013). Self-organization of axial polarity, inside-out layer pattern, and species-specific progenitor dynamics in human ES cell-derived neocortex. Proc Natl Acad Sci U S A, 110(50), 20284-20289. https://doi.org/10.1073/pnas.1315710110

Kalia, L. V., & Lang, A. E. (2015). Parkinson's disease. Lancet, 386(9996), 896-912. https://doi.org/10.1016/S0140-6736(14)61393-3

Kamath, T., Abdulraouf, A., Burris, S. J., Langlieb, J., Gazestani, V., Nadaf, N. M., Balderrama, K., Vanderburg, C., & Macosko, E. Z. (2022). Single-cell genomic profiling of human dopamine neurons identifies a population that selectively degenerates in Parkinson's disease. Nat Neurosci, 25(5), 588-595. https://doi.org/10.1038/s41593-022-01061-1

Kanton, S., Boyle, M. J., He, Z., Santel, M., Weigert, A., Sanchis-Calleja, F., Guijarro, P., Sidow, L., Fleck, J. S., Han, D., Qian, Z., Heide, M., Huttner, W. B., Khaitovich, P., Paabo, S., Treutlein, B., & Camp, J. G. (2019). Organoid single-cell genomic atlas uncovers human-specific features of brain development. Nature, 574(7778), 418-422. https://doi.org/10.1038/s41586-019-1654-9

Kawano, H., Ohyama, K., Kawamura, K., & Nagatsu, I. (1995). Migration of dopaminergic neurons in the embryonic mesencephalon of mice. Brain Res Dev Brain Res, 86(1-2), 101-113. https://doi.org/10.1016/0165-3806(95)00018-9

Kee, N., Volakakis, N., Kirkeby, A., Dahl, L., Storvall, H., Nolbrant, S., Lahti, L., Bjorklund, A. K., Gillberg, L., Joodmardi, E., Sandberg, R., Parmar, M., & Perlmann, T. (2017). Single-Cell Analysis Reveals a Close Relationship between Differentiating Dopamine and Subthalamic Nucleus Neuronal Lineages. Cell Stem Cell, 20(1), 29-40. https://doi.org/10.1016/j.stem.2016.10.003

Kefalopoulou, Z., Politis, M., Piccini, P., Mencacci, N., Bhatia, K., Jahanshahi, M., Widner, H., Rehncrona, S., Brundin, P., Bjorklund, A., Lindvall, O., Limousin, P., Quinn, N., & Foltynie, T. (2014). Long-term clinical outcome of fetal cell transplantation for Parkinson disease: two case reports. JAMA Neurol, 71(1), 83-87. https://doi.org/10.1001/jamaneurol.2013.4749

Kele, J., Simplicio, N., Ferri, A. L., Mira, H., Guillemot, F., Arenas, E., & Ang, S. L. (2006). Neurogenin 2 is required for the development of ventral midbrain dopaminergic neurons. Development, 133(3), 495-505. https://doi.org/10.1242/dev.02223

Kelley, K. W., Revah, O., Gore, F., Kaganovsky, K., Chen, X., Deisseroth, K., & Pasca, S. P. (2024). Host circuit engagement of human cortical organoids transplanted in rodents. Nature Protocols, 19(12), 3542-3567. https://doi.org/10.1038/s41596-024-01029-4

Khan, I., Prabhakar, A., Delepine, C., Tsang, H., Pham, V., & Sur, M. (2021). A low-cost 3D printed microfluidic bioreactor and imaging chamber for live-organoid imaging. Biomicrofluidics, 15(2), 024105. https://doi.org/10.1063/5.0041027

Kiecker, C., & Lumsden, A. (2012). The role of organizers in patterning the nervous system. Annu Rev Neurosci, 35, 347-367. https://doi.org/10.1146/annurev-neuro-062111-150543

Kikuchi, T., Morizane, A., Doi, D., Magotani, H., Onoe, H., Hayashi, T., Mizuma, H., Takara, S., Takahashi, R., Inoue, H., Morita, S., Yamamoto, M., Okita, K., Nakagawa, M., Parmar, M., & Takahashi, J. (2017). Human iPS cell-derived dopaminergic neurons function in a primate Parkinson's disease model. Nature, 548(7669), 592-596. https://doi.org/10.1038/nature23664

Kim, H., Park, H. J., Choi, H., Chang, Y., Park, H., Shin, J., Kim, J., Lengner, C. J., Lee, Y. K., & Kim, J. (2019). Modeling G2019S-LRRK2 Sporadic Parkinson's Disease in 3D Midbrain Organoids. Stem Cell Reports, 12(3), 518-531. https://doi.org/10.1016/j.stemcr.2019.01.020

Kim, T. W., Piao, J., Koo, S. Y., Kriks, S., Chung, S. Y., Betel, D., Socci, N. D., Choi, S. J., Zabierowski, S., Dubose, B. N., Hill, E. J., Mosharov, E. V., Irion, S., Tomishima, M. J., Tabar, V., & Studer, L. (2021). Biphasic Activation of WNT Signaling Facilitates the Derivation of Midbrain Dopamine Neurons from hESCs for Translational Use. Cell Stem Cell, 28(2), 343-355 e345. https://doi.org/10.1016/j.stem.2021.01.005

Kirihara, T., Luo, Z., Chow, S. Y. A., Misawa, R., Kawada, J., Shibata, S., Khoyratee, F., Vollette, C. A., Volz, V., Levi, T., Fujii, T., & Ikeuchi, Y. (2019). A Human Induced Pluripotent Stem Cell-Derived Tissue Model of a Cerebral Tract Connecting Two Cortical Regions. iScience, 14, 301-311. https://doi.org/10.1016/j.isci.2019.03.012

Kirkeby, A., Grealish, S., Wolf, D. A., Nelander, J., Wood, J., Lundblad, M., Lindvall, O., & Parmar, M. (2012). Generation of regionally specified neural progenitors and functional neurons from human embryonic stem cells under defined conditions. Cell Rep, 1(6), 703-714. https://doi.org/10.1016/j.celrep.2012.04.009

Kirkeby, A., Nelander, J., Hoban, D. B., Rogelius, N., Bjartmarz, H., Novo Nordisk Cell Therapy, R., Storm, P., Fiorenzano, A., Adler, A. F., Vale, S., Mudannayake, J., Zhang, Y., Cardoso, T., Mattsson, B., Landau, A. M., Glud, A. N., Sorensen, J. C., Lillethorup, T. P., Lowdell, M., . . . Parmar, M. (2023). Preclinical quality, safety, and efficacy of a human embryonic stem cell-derived product for the treatment of Parkinson's disease, STEM-PD. Cell Stem Cell, 30(10), 1299-1314 e1299. https://doi.org/10.1016/j.stem.2023.08.014

Kirkeby, A., Nolbrant, S., Tiklova, K., Heuer, A., Kee, N., Cardoso, T., Ottosson, D. R., Lelos, M. J., Rifes, P., Dunnett, S. B., Grealish, S., Perlmann, T., & Parmar, M. (2017). Predictive Markers Guide Differentiation to Improve Graft Outcome in Clinical Translation of hESC-Based Therapy for Parkinson's Disease. Cell Stem Cell, 20(1), 135-148. https://doi.org/10.1016/j.stem.2016.09.004

Kouwenhoven, W. M., von Oerthel, L., & Smidt, M. P. (2017). Pitx3 and En1 determine the size and molecular programming of the dopaminergic neuronal pool. PLoS One, 12(8), e0182421. https://doi.org/10.1371/journal.pone.0182421

Kramer, D. J., Risso, D., Kosillo, P., Ngai, J., & Bateup, H. S. (2018). Combinatorial Expression of Grp and Neurod6 Defines Dopamine Neuron Populations with Distinct Projection Patterns and Disease Vulnerability. eNeuro, 5(3). https://doi.org/10.1523/ENEURO.0152-18.2018

Kriks, S., Shim, J. W., Piao, J., Ganat, Y. M., Wakeman, D. R., Xie, Z., Carrillo-Reid, L., Auyeung, G., Antonacci, C., Buch, A., Yang, L., Beal, M. F., Surmeier, D. J., Kordower, J. H., Tabar, V., & Studer, L. (2011). Dopamine neurons derived from human ES cells efficiently engraft in animal models of Parkinson's disease. Nature, 480(7378), 547-551. https://doi.org/10.1038/nature10648

Kwak, T. H., Kang, J. H., Hali, S., Kim, J., Kim, K. P., Park, C., Lee, J. H., Ryu, H. K., Na, J. E., Jo, J., Je, H. S., Ng, H. H., Kwon, J., Kim, N. H., Hong, K. H., Sun, W., Chung, C. H., Rhyu, I. J., & Han, D. W. (2020). Generation of homogeneous midbrain organoids with in vivo-like cellular composition facilitates neurotoxin-based Parkinson's disease modeling. Stem Cells, 38(6), 727-740. https://doi.org/10.1002/stem.3163

La Manno, G., Gyllborg, D., Codeluppi, S., Nishimura, K., Salto, C., Zeisel, A., Borm, L. E., Stott, S. R. W., Toledo, E. M., Villaescusa, J. C., Lonnerberg, P., Ryge, J., Barker, R. A., Arenas, E., & Linnarsson, S. (2016). Molecular Diversity of Midbrain Development in Mouse, Human, and Stem Cells. Cell, 167(2), 566-580 e519. https://doi.org/10.1016/j.cell.2016.09.027

Lammel, S., Hetzel, A., Hackel, O., Jones, I., Liss, B., & Roeper, J. (2008). Unique properties of mesoprefrontal neurons within a dual mesocorticolimbic dopamine system. Neuron, 57(5), 760-773. https://doi.org/10.1016/j.neuron.2008.01.022

Lancaster, M. A., Corsini, N. S., Wolfinger, S., Gustafson, E. H., Phillips, A. W., Burkard, T. R., Otani, T., Livesey, F. J., & Knoblich, J. A. (2017). Guided self-organization and cortical plate formation in human brain organoids. Nat Biotechnol, 35(7), 659-666. https://doi.org/10.1038/nbt.3906

Lancaster, M. A., & Knoblich, J. A. (2014a). Generation of cerebral organoids from human pluripotent stem cells. Nature Protocols, 9(10), 2329-2340. https://doi.org/10.1038/nprot.2014.158

Lancaster, M. A., & Knoblich, J. A. (2014b). Organogenesis in a dish: modeling development and disease using organoid technologies. Science, 345(6194), 1247125. https://doi.org/10.1126/science.1247125

Lancaster, M. A., Renner, M., Martin, C. A., Wenzel, D., Bicknell, L. S., Hurles, M. E., Homfray, T., Penninger, J. M., Jackson, A. P., & Knoblich, J. A. (2013). Cerebral organoids model human brain development and microcephaly. Nature, 501(7467), 373-379. https://doi.org/10.1038/nature12517

Laperle, A. H., Sances, S., Yucer, N., Dardov, V. J., Garcia, V. J., Ho, R., Fulton, A. N., Jones, M. R., Roxas, K. M., Avalos, P., West, D., Banuelos, M. G., Shu, Z., Murali, R., Maidment, N. T., Van Eyk, J. E., Tagliati, M., & Svendsen, C. N. (2020). iPSC modeling of young-onset Parkinson's disease reveals a molecular signature of disease and novel therapeutic candidates. Nat Med, 26(2), 289-299. https://doi.org/10.1038/s41591-019-0739-1

Lees, A. J., Hardy, J., & Revesz, T. (2009). Parkinson's disease. Lancet, 373(9680), 2055-2066. https://doi.org/10.1016/S0140-6736(09)60492-X

Leibovitz, Z., Lerman-Sagie, T., & Haddad, L. (2022). Fetal Brain Development: Regulating Processes and Related Malformations. Life (Basel), 12(6). https://doi.org/10.3390/life12060809

Li, J., Duarte, T., Kocabas, A., Works, M., McConnell, S. K., & Hynes, M. A. (2014). Evidence for topographic guidance of dopaminergic axons by differential Netrin-1 expression in the striatum. Mol Cell Neurosci, 61, 85-96. https://doi.org/10.1016/j.mcn.2014.05.003

Li, W., Englund, E., Widner, H., Mattsson, B., van Westen, D., Latt, J., Rehncrona, S., Brundin, P., Bjorklund, A., Lindvall, O., & Li, J. Y. (2016). Extensive graft-derived dopaminergic innervation is maintained 24 years after transplantation in the degenerating parkinsonian brain. Proc Natl Acad Sci U S A, 113(23), 6544-6549. https://doi.org/10.1073/pnas.1605245113

Lin, L., Rao, Y., & Isacson, O. (2005). Netrin-1 and slit-2 regulate and direct neurite growth of ventral midbrain dopaminergic neurons. Mol Cell Neurosci, 28(3), 547-555. https://doi.org/10.1016/j.mcn.2004.11.009

Lin, W., Metzakopian, E., Mavromatakis, Y. E., Gao, N., Balaskas, N., Sasaki, H., Briscoe, J., Whitsett, J. A., Goulding, M., Kaestner, K. H., & Ang, S. L. (2009). Foxa1 and Foxa2 function both upstream of and cooperatively with Lmx1a and Lmx1b in a feedforward loop promoting mesodiencephalic dopaminergic neuron development. Dev Biol, 333(2), 386-396. https://doi.org/10.1016/j.ydbio.2009.07.006

Lindvall, O., Brundin, P., Widner, H., Rehncrona, S., Gustavii, B., Frackowiak, R., Leenders, K. L., Sawle, G., Rothwell, J. C., Marsden, C. D., & et al. (1990). Grafts of fetal dopamine neurons survive and improve motor function in Parkinson's disease. Science, 247(4942), 574-577. https://doi.org/10.1126/science.2105529

Lindvall, O., & Kokaia, Z. (2010). Stem cells in human neurodegenerative disorders--time for clinical translation? J Clin Invest, 120(1), 29-40. https://doi.org/10.1172/JCI40543

Lindvall, O., Rehncrona, S., Brundin, P., Gustavii, B., Astedt, B., Widner, H., Lindholm, T., Bjorklund, A., Leenders, K. L., Rothwell, J. C., Frackowiak, R., Marsden, D., Johnels, B., Steg, G., Freedman, R., Hoffer, B. J., Seiger, A., Bygdeman, M., Stromberg, I., & Olson, L. (1989). Human fetal dopamine neurons grafted into the striatum in two patients with severe Parkinson's disease. A detailed account of methodology and a 6-month follow-up. Arch Neurol, 46(6), 615-631. https://doi.org/10.1001/archneur.1989.00520420033021

Lindvall, O., Sawle, G., Widner, H., Rothwell, J. C., Bjorklund, A., Brooks, D., Brundin, P., Frackowiak, R., Marsden, C. D., Odin, P., & et al. (1994). Evidence for long-term survival and function of dopaminergic grafts in progressive Parkinson's disease. Ann Neurol, 35(2), 172-180. https://doi.org/10.1002/ana.410350208

Liu, A., & Joyner, A. L. (2001). EN and GBX2 play essential roles downstream of FGF8 in patterning the mouse mid/hindbrain region. Development, 128(2), 181-191. https://doi.org/10.1242/dev.128.2.181

Lo, P. S., Rymar, V. V., Kennedy, T. E., & Sadikot, A. F. (2022). The netrin-1 receptor DCC promotes the survival of a subpopulation of midbrain dopaminergic neurons: Relevance for ageing and Parkinson's disease. J Neurochem, 161(3), 254-265. https://doi.org/10.1111/jnc.15579

Lumsden, A., & Krumlauf, R. (1996). Patterning the vertebrate neuraxis. Science, 274(5290), 1109-1115. https://doi.org/10.1126/science.274.5290.1109

Maimaitili, M., Chen, M., Febbraro, F., Ucuncu, E., Kelly, R., Niclis, J. C., Christiansen, J. R., Mermet-Joret, N., Niculescu, D., Lauritsen, J., Iannielli, A., Klaestrup, I. H., Jensen, U. B., Qvist, P., Nabavi, S., Broccoli, V., Nykjaer, A., Romero-Ramos, M., & Denham, M. (2023). Enhanced production of mesencephalic dopaminergic neurons from lineage-restricted human undifferentiated stem cells. Nat Commun, 14(1), 7871. https://doi.org/10.1038/s41467-023-43471-0

Maiti, P., Manna, J., & Dunbar, G. L. (2017). Current understanding of the molecular mechanisms in Parkinson's disease: Targets for potential treatments. Transl Neurodegener, 6, 28. https://doi.org/10.1186/s40035-017-0099-z

Mansour, A. A., Goncalves, J. T., Bloyd, C. W., Li, H., Fernandes, S., Quang, D., Johnston, S., Parylak, S. L., Jin, X., & Gage, F. H. (2018). An in vivo model of functional and vascularized human brain organoids. Nat Biotechnol, 36(5), 432-441. https://doi.org/10.1038/nbt.4127

Marikawa, Y., & Alarcon, V. B. (2009). Establishment of trophectoderm and inner cell mass lineages in the mouse embryo. Mol Reprod Dev, 76(11), 1019-1032. https://doi.org/10.1002/mrd.21057

Marklund, U., Alekseenko, Z., Andersson, E., Falci, S., Westgren, M., Perlmann, T., Graham, A., Sundstrom, E., & Ericson, J. (2014). Detailed expression analysis of regulatory genes in the early developing human neural tube. Stem Cells Dev, 23(1), 5-15. https://doi.org/10.1089/scd.2013.0309

Martinez-Barbera, J. P., Signore, M., Boyl, P. P., Puelles, E., Acampora, D., Gogoi, R., Schubert, F., Lumsden, A., & Simeone, A. (2001). Regionalisation of anterior neuroectoderm and its competence in responding to forebrain and midbrain inducing activities depend on mutual antagonism between OTX2 and GBX2. Development, 128(23), 4789-4800. https://doi.org/10.1242/dev.128.23.4789

Martins-Costa, C., Wiegers, A., Pham, V. A., Sidhaye, J., Doleschall, B., Novatchkova, M., Lendl, T., Piber, M., Peer, A., Moseneder, P., Stuempflen, M., Chow, S. Y. A., Seidl, R., Prayer, D., Hoftberger, R., Kasprian, G., Ikeuchi, Y., Corsini, N. S., & Knoblich, J. A. (2024). ARID1B controls transcriptional programs of axon projection in an organoid model of the human corpus callosum. Cell Stem Cell, 31(6), 866-885 e814. https://doi.org/10.1016/j.stem.2024.04.014

Menegas, W., Akiti, K., Amo, R., Uchida, N., & Watabe-Uchida, M. (2018). Dopamine neurons projecting to the posterior striatum reinforce avoidance of threatening stimuli. Nat Neurosci, 21(10), 1421-1430. https://doi.org/10.1038/s41593-018-0222-1

Meyer-Lindenberg, A., Miletich, R. S., Kohn, P. D., Esposito, G., Carson, R. E., Quarantelli, M., Weinberger, D. R., & Berman, K. F. (2002). Reduced prefrontal activity predicts exaggerated striatal dopaminergic function in schizophrenia. Nat Neurosci, 5(3), 267-271. https://doi.org/10.1038/nn804

Miller, G. W., Erickson, J. D., Perez, J. T., Penland, S. N., Mash, D. C., Rye, D. B., & Levey, A. I. (1999). Immunochemical analysis of vesicular monoamine transporter (VMAT2) protein in Parkinson's disease. Exp Neurol, 156(1), 138-148. https://doi.org/10.1006/exnr.1998.7008

Miller, G. W., Gainetdinov, R. R., Levey, A. I., & Caron, M. G. (1999). Dopamine transporters and neuronal injury. Trends Pharmacol Sci, 20(10), 424-429. https://doi.org/10.1016/s0165-6147(99)01379-6

Millet, S., Bloch-Gallego, E., Simeone, A., & Alvarado-Mallart, R. M. (1996). The caudal limit of Otx2 gene expression as a marker of the midbrain/hindbrain boundary: a study using in situ hybridisation and chick/quail homotopic grafts. Development, 122(12), 3785-3797. https://doi.org/10.1242/dev.122.12.3785

Milton, A. L., & Everitt, B. J. (2012). The persistence of maladaptive memory: addiction, drug memories and anti-relapse treatments. Neurosci Biobehav Rev, 36(4), 1119-1139. https://doi.org/10.1016/j.neubiorev.2012.01.002

Miura, Y., Li, M. Y., Birey, F., Ikeda, K., Revah, O., Thete, M. V., Park, J. Y., Puno, A., Lee, S. H., Porteus, M. H., & Pasca, S. P. (2020). Generation of human striatal organoids and cortico-striatal assembloids from human pluripotent stem cells. Nat Biotechnol, 38(12), 1421-1430. https://doi.org/10.1038/s41587-020-00763-w

Miura, Y., Li, M. Y., Revah, O., Yoon, S. J., Narazaki, G., & Pasca, S. P. (2022). Engineering brain assembloids to interrogate human neural circuits. Nature Protocols, 17(1), 15-35. https://doi.org/10.1038/s41596-021-00632-z

Molinoff, P. B., & Axelrod, J. (1971). Biochemistry of catecholamines. Annu Rev Biochem, 40, 465-500. https://doi.org/10.1146/annurev.bi.40.070171.002341

Morales, M., & Margolis, E. B. (2017). Ventral tegmental area: cellular heterogeneity, connectivity and behaviour. Nat Rev Neurosci, 18(2), 73-85. https://doi.org/10.1038/nrn.2016.165

Mori, T., Buffo, A., & Gotz, M. (2005). The novel roles of glial cells revisited: the contribution of radial glia and astrocytes to neurogenesis. Curr Top Dev Biol, 69, 67-99. https://doi.org/10.1016/S0070-2153(05)69004-7

Moriarty, N., Gantner, C. W., Hunt, C. P. J., Ermine, C. M., Frausin, S., Viventi, S., Ovchinnikov, D. A., Kirik, D., Parish, C. L., & Thompson, L. H. (2022). A combined cell and gene therapy approach for homotopic reconstruction of midbrain dopamine pathways using human pluripotent stem cells. Cell Stem Cell, 29(3), 434-448 e435. https://doi.org/10.1016/j.stem.2022.01.013

Moriarty, N., Kauhausen, J. A., Pavan, C., Hunt, C. P. J., de Luzy, I. R., Penna, V., Ermine, C. M., Thompson, L. H., & Parish, C. L. (2022). Understanding the Influence of Target Acquisition on Survival, Integration, and Phenotypic Maturation of Dopamine Neurons within Stem Cell-Derived Neural Grafts in a Parkinson's Disease Model. J Neurosci, 42(25), 4995-5006. https://doi.org/10.1523/JNEUROSCI.2431-21.2022

Nelander, J., Hebsgaard, J. B., & Parmar, M. (2009). Organization of the human embryonic ventral mesencephalon. Gene Expr Patterns, 9(8), 555-561. https://doi.org/10.1016/j.gep.2009.10.002

Nilsson, F., Storm, P., Sozzi, E., Hidalgo Gil, D., Birtele, M., Sharma, Y., Parmar, M., & Fiorenzano, A. (2021). Single-Cell Profiling of Coding and Noncoding Genes in Human Dopamine Neuron Differentiation. Cells, 10(1). https://doi.org/10.3390/cells10010137

Nolbrant, S., Giacomoni, J., Hoban, D. B., Bruzelius, A., Birtele, M., Chandler-Militello, D., Pereira, M., Ottosson, D. R., Goldman, S. A., & Parmar, M. (2020). Direct Reprogramming of Human Fetal- and Stem Cell-Derived Glial Progenitor Cells into Midbrain Dopaminergic Neurons. Stem Cell Reports, 15(4), 869-882. https://doi.org/10.1016/j.stemcr.2020.08.013

Nolbrant, S., Heuer, A., Parmar, M., & Kirkeby, A. (2017). Generation of high-purity human ventral midbrain dopaminergic progenitors for

maturation and intracerebral transplantation. Nature Protocols, 12(9), 1962-1979. https://doi.org/10.1038/nprot.2017.078

Nordstrom, U., Jessell, T. M., & Edlund, T. (2002). Progressive induction of caudal neural character by graded Wnt signaling. Nat Neurosci, 5(6), 525-532. https://doi.org/10.1038/nn0602-854

Nouri, P., Gotz, S., Rauser, B., Irmler, M., Peng, C., Trumbach, D., Kempny, C., Lechermeier, C. G., Bryniok, A., Dlugos, A., Euchner, E., Beckers, J., Brodski, C., Klumper, C., Wurst, W., & Prakash, N. (2020). Dose-Dependent and Subset-Specific Regulation of Midbrain Dopaminergic Neuron Differentiation by LEF1-Mediated WNT1/b-Catenin Signaling. Front Cell Dev Biol, 8, 587778. https://doi.org/10.3389/fcell.2020.587778

Nunes, I., Tovmasian, L. T., Silva, R. M., Burke, R. E., & Goff, S. P. (2003). Pitx3 is required for development of substantia nigra dopaminergic neurons. Proc Natl Acad Sci U S A, 100(7), 4245-4250. https://doi.org/10.1073/pnas.0230529100

Okun, M. S. (2012). Deep-brain stimulation for Parkinson's disease. N Engl J Med, 367(16), 1529-1538. https://doi.org/10.1056/NEJMct1208070

Ono, Y., Nakatani, T., Sakamoto, Y., Mizuhara, E., Minaki, Y., Kumai, M., Hamaguchi, A., Nishimura, M., Inoue, Y., Hayashi, H., Takahashi, J., & Imai, T. (2007). Differences in neurogenic potential in floor plate cells along an anteroposterior location: midbrain dopaminergic neurons originate from mesencephalic floor plate cells. Development, 134(17), 3213-3225. https://doi.org/10.1242/dev.02879

Panman, L., Papathanou, M., Laguna, A., Oosterveen, T., Volakakis, N., Acampora, D., Kurtsdotter, I., Yoshitake, T., Kehr, J., Joodmardi, E., Muhr, J., Simeone, A., Ericson, J., & Perlmann, T. (2014). Sox6 and Otx2 control the specification of substantia nigra and ventral tegmental area dopamine neurons. Cell Rep, 8(4), 1018-1025. https://doi.org/10.1016/j.celrep.2014.07.016

Park, C. H., Minn, Y. K., Lee, J. Y., Choi, D. H., Chang, M. Y., Shim, J. W., Ko, J. Y., Koh, H. C., Kang, M. J., Kang, J. S., Rhie, D. J., Lee, Y. S., Son, H., Moon, S. Y., Kim, K. S., & Lee, S. H. (2005). In vitro and in vivo analyses of human embryonic stem cell-derived dopamine neurons. J Neurochem, 92(5), 1265-1276. https://doi.org/10.1111/j.1471-4159.2004.03006.x

Park, T. Y., Jeon, J., Lee, N., Kim, J., Song, B., Kim, J. H., Lee, S. K., Liu, D., Cha, Y., Kim, M., Leblanc, P., Herrington, T. M., Carter, B. S., Schweitzer, J. S., & Kim, K. S. (2023). Co-transplantation of autologous T(reg) cells in a cell therapy for Parkinson's disease. Nature, 619(7970), 606-615. https://doi.org/10.1038/s41586-023-06300-4

Parkinson, J. (2002). An essay on the shaking palsy. 1817. J Neuropsychiatry Clin Neurosci, 14(2), 223-236; discussion 222. https://doi.org/10.1176/jnp.14.2.223

Parmar, M., Grealish, S., & Henchcliffe, C. (2020). The future of stem cell therapies for Parkinson disease. Nat Rev Neurosci, 21(2), 103-115. https://doi.org/10.1038/s41583-019-0257-7

Pasca, A. M., Sloan, S. A., Clarke, L. E., Tian, Y., Makinson, C. D., Huber, N., Kim, C. H., Park, J. Y., O'Rourke, N. A., Nguyen, K. D., Smith, S. J., Huguenard, J. R., Geschwind, D. H., Barres, B. A., & Pasca, S. P. (2015). Functional cortical neurons and astrocytes from human pluripotent stem cells in 3D culture. Nat Methods, 12(7), 671-678. https://doi.org/10.1038/nmeth.3415

Pasca, S. P. (2018). The rise of three-dimensional human brain cultures. Nature, 553(7689), 437-445. https://doi.org/10.1038/nature25032

Pasca, S. P. (2019). Assembling human brain organoids. Science, 363(6423), 126-127. https://doi.org/10.1126/science.aau5729

Pasca, S. P., Arlotta, P., Bateup, H. S., Camp, J. G., Cappello, S., Gage, F. H., Knoblich, J. A., Kriegstein, A. R., Lancaster, M. A., Ming, G. L., Muotri, A. R., Park, I. H., Reiner, O., Song, H., Studer, L., Temple, S., Testa, G., Treutlein, B., & Vaccarino, F. M. (2022). A nomenclature consensus for nervous system organoids and assembloids. Nature, 609(7929), 907-910. https://doi.org/10.1038/s41586-022-05219-6

Pereira Luppi, M., Azcorra, M., Caronia-Brown, G., Poulin, J. F., Gaertner, Z., Gatica, S., Moreno-Ramos, O. A., Nouri, N., Dubois, M., Ma, Y. C., Ramakrishnan, C., Fenno, L., Kim, Y. S., Deisseroth, K., Cicchetti, F., Dombeck, D. A., & Awatramani, R. (2021). Sox6 expression distinguishes dorsally and ventrally biased dopamine neurons in the substantia nigra with distinctive properties and embryonic origins. Cell Rep, 37(6), 109975. https://doi.org/10.1016/j.celrep.2021.109975

Perlow, M. J., Freed, W. J., Hoffer, B. J., Seiger, A., Olson, L., & Wyatt, R. J. (1979). Brain grafts reduce motor abnormalities produced by destruction of nigrostriatal dopamine system. Science, 204(4393), 643-647. https://doi.org/10.1126/science.571147

Perrier, A. L., Tabar, V., Barberi, T., Rubio, M. E., Bruses, J., Topf, N., Harrison, N. L., & Studer, L. (2004). Derivation of midbrain dopamine neurons from human embryonic stem cells. Proc Natl Acad Sci U S A, 101(34), 12543-12548. https://doi.org/10.1073/pnas.0404700101

Piao, J., Zabierowski, S., Dubose, B. N., Hill, E. J., Navare, M., Claros, N., Rosen, S., Ramnarine, K., Horn, C., Fredrickson, C., Wong, K., Safford, B., Kriks, S., El Maarouf, A., Rutishauser, U., Henchcliffe, C., Wang, Y., Riviere, I., Mann, S., . . . Tabar, V. (2021). Preclinical Efficacy and Safety of a Human Embryonic Stem Cell-Derived Midbrain Dopamine Progenitor Product, MSK-DA01. Cell Stem Cell, 28(2), 217-229 e217. https://doi.org/10.1016/j.stem.2021.01.004

Piccini, P., Brooks, D. J., Bjorklund, A., Gunn, R. N., Grasby, P. M., Rimoldi, O., Brundin, P., Hagell, P., Rehncrona, S., Widner, H., & Lindvall, O. (1999). Dopamine release from nigral transplants visualized in vivo in a Parkinson's patient. Nat Neurosci, 2(12), 1137-1140. https://doi.org/10.1038/16060

Piccini, P., Lindvall, O., Bjorklund, A., Brundin, P., Hagell, P., Ceravolo, R., Oertel, W., Quinn, N., Samuel, M., Rehncrona, S., Widner, H., & Brooks, D. J. (2000). Delayed recovery of movement-related cortical function in Parkinson's disease after striatal dopaminergic grafts. Ann Neurol, 48(5), 689-695. https://www.ncbi.nlm.nih.gov/pubmed/11079531

Poulin, J. F., Gaertner, Z., Moreno-Ramos, O. A., & Awatramani, R. (2020). Classification of Midbrain Dopamine Neurons Using Single-Cell Gene Expression Profiling Approaches. Trends Neurosci, 43(3), 155-169. https://doi.org/10.1016/j.tins.2020.01.004

Poulin, J. F., Zou, J., Drouin-Ouellet, J., Kim, K. Y., Cicchetti, F., & Awatramani, R. B. (2014). Defining midbrain dopaminergic neuron diversity by single-cell gene expression profiling. Cell Rep, 9(3), 930-943. https://doi.org/10.1016/j.celrep.2014.10.008

Puelles, E., Annino, A., Tuorto, F., Usiello, A., Acampora, D., Czerny, T., Brodski, C., Ang, S. L., Wurst, W., & Simeone, A. (2004). Otx2 regulates the extent, identity and fate of neuronal progenitor domains in the ventral midbrain. Development, 131(9), 2037-2048. https://doi.org/10.1242/dev.01107

Puopolo, M., Raviola, E., & Bean, B. P. (2007). Roles of subthreshold calcium current and sodium current in spontaneous firing of mouse midbrain dopamine neurons. J Neurosci, 27(3), 645-656. https://doi.org/10.1523/JNEUROSCI.4341-06.2007

Qian, X., Nguyen, H. N., Song, M. M., Hadiono, C., Ogden, S. C., Hammack, C., Yao, B., Hamersky, G. R., Jacob, F., Zhong, C., Yoon, K. J., Jeang, W., Lin, L., Li, Y., Thakor, J., Berg, D. A., Zhang, C., Kang, E., Chickering, M., . . . Ming, G. L. (2016). Brain-Region-Specific Organoids Using Mini-bioreactors for Modeling ZIKV Exposure. Cell, 165(5), 1238-1254. https://doi.org/10.1016/j.cell.2016.04.032

Quadrato, G., Nguyen, T., Macosko, E. Z., Sherwood, J. L., Min Yang, S., Berger, D. R., Maria, N., Scholvin, J., Goldman, M., Kinney, J. P., Boyden, E. S., Lichtman, J. W., Williams, Z. M., McCarroll, S. A., & Arlotta, P. (2017). Cell diversity and network dynamics in photosensitive human brain organoids. Nature, 545(7652), 48-53. https://doi.org/10.1038/nature22047

Renner, H., Grabos, M., Becker, K. J., Kagermeier, T. E., Wu, J., Otto, M., Peischard, S., Zeuschner, D., TsyTsyura, Y., Disse, P., Klingauf, J., Leidel, S. A., Seebohm, G., Scholer, H. R., & Bruder, J. M. (2020). A fully automated high-throughput workflow for 3D-based chemical screening in human midbrain organoids. Elife, 9. https://doi.org/10.7554/eLife.52904

Renner, M., Lancaster, M. A., Bian, S., Choi, H., Ku, T., Peer, A., Chung, K., & Knoblich, J. A. (2017). Self-organized developmental patterning and differentiation in cerebral organoids. EMBO J, 36(10), 1316-1329. https://doi.org/10.15252/embj.201694700

Reubinoff, B. E., Pera, M. F., Vajta, G., & Trounson, A. O. (2001). Effective cryopreservation of human embryonic stem cells by the open pulled straw vitrification method. Hum Reprod, 16(10), 2187-2194. https://doi.org/10.1093/humrep/16.10.2187

Reumann, D., Krauditsch, C., Novatchkova, M., Sozzi, E., Wong, S. N., Zabolocki, M., Priouret, M., Doleschall, B., Ritzau-Reid, K. I., Piber, M., Morassut, I., Fieseler, C., Fiorenzano, A., Stevens, M. M., Zimmer, M., Bardy, C., Parmar, M., & Knoblich, J. A. (2023). In vitro modeling of the human dopaminergic system using spatially arranged ventral midbrain-striatum-cortex assembloids. Nat Methods, 20(12), 2034-2047. https://doi.org/10.1038/s41592-023-02080-x

Revah, O., Gore, F., Kelley, K. W., Andersen, J., Sakai, N., Chen, X., Li, M. Y., Birey, F., Yang, X., Saw, N. L., Baker, S. W., Amin, N. D., Kulkarni, S., Mudipalli, R., Cui, B., Nishino, S., Grant, G. A., Knowles, J. K., Shamloo, M., . . . Pasca, S. P. (2022). Maturation and circuit integration of transplanted human cortical organoids. Nature, 610(7931), 319-326. https://doi.org/10.1038/s41586-022-05277-w

Rezaei, B., Giacomoni, J., Nilsson, F., Sozzi, E., Fiorenzano, A., Parmar, M., Keller, S. S., & Kajtez, J. (2023). Modular 3D printed platform for fluidically connected human brain organoid culture. Biofabrication, 16(1). https://doi.org/10.1088/1758-5090/ad0c2c

Rising, A., Widhe, M., Johansson, J., & Hedhammar, M. (2011). Spider silk proteins: recent advances in recombinant production, structure-function relationships and biomedical applications. Cell Mol Life Sci, 68(2), 169-184. https://doi.org/10.1007/s00018-010-0462-z

Rossi, M., Bruno, V., Arena, J., Cammarota, A., & Merello, M. (2018). Challenges in PD Patient Management After DBS: A Pragmatic Review. Mov Disord Clin Pract, 5(3), 246-254. https://doi.org/10.1002/mdc3.12592

Rothenbucher, T. S. P., Gurbuz, H., Pereira, M. P., Heiskanen, A., Emneus, J., & Martinez-Serrano, A. (2021). Next generation human brain models: engineered flat brain organoids featuring gyrification. Biofabrication, 13(1), 011001. https://doi.org/10.1088/1758-5090/abc95e

Sabate-Soler, S., Nickels, S. L., Saraiva, C., Berger, E., Dubonyte, U., Barmpa, K., Lan, Y. J., Kouno, T., Jarazo, J., Robertson, G., Sharif, J., Koseki, H., Thome, C., Shin, J. W., Cowley, S. A., & Schwamborn, J. C. (2022). Microglia integration into human midbrain organoids leads to increased neuronal maturation and functionality. Glia, 70(7), 1267-1288. https://doi.org/10.1002/glia.24167

Saucedo-Cardenas, O., Quintana-Hau, J. D., Le, W. D., Smidt, M. P., Cox, J. J., De Mayo, F., Burbach, J. P., & Conneely, O. M. (1998). Nurr1 is essential for the induction of the dopaminergic phenotype and the survival of ventral mesencephalic late dopaminergic precursor neurons. Proc Natl Acad Sci U S A, 95(7), 4013-4018. https://doi.org/10.1073/pnas.95.7.4013

Saunders, A., Macosko, E. Z., Wysoker, A., Goldman, M., Krienen, F. M., de Rivera, H., Bien, E., Baum, M., Bortolin, L., Wang, S., Goeva, A., Nemesh, J., Kamitaki, N., Brumbaugh, S., Kulp, D., & McCarroll, S. A. (2018). Molecular Diversity and Specializations among the Cells of the Adult Mouse Brain. Cell, 174(4), 1015-1030 e1016. https://doi.org/10.1016/j.cell.2018.07.028

Seiler, S. T., Mantalas, G. L., Selberg, J., Cordero, S., Torres-Montoya, S., Baudin, P. V., Ly, V. T., Amend, F., Tran, L., Hoffman, R. N., Rolandi, M., Green, R. E., Haussler, D., Salama, S. R., & Teodorescu, M. (2022). Modular automated microfluidic cell culture platform reduces glycolytic stress in cerebral cortex organoids. Sci Rep, 12(1), 20173. https://doi.org/10.1038/s41598-022-20096-9

Shults, C. W., Hashimoto, R., Brady, R. M., & Gage, F. H. (1990). Dopaminergic cells align along radial glia in the developing mesencephalon of the rat. Neuroscience, 38(2), 427-436. https://doi.org/10.1016/0306-4522(90)90039-7

Siletti, K., Hodge, R., Mossi Albiach, A., Lee, K. W., Ding, S. L., Hu, L., Lonnerberg, P., Bakken, T., Casper, T., Clark, M., Dee, N., Gloe, J., Hirschstein, D., Shapovalova, N. V., Keene, C. D., Nyhus, J., Tung, H., Yanny, A. M., Arenas, E., . . . Linnarsson, S. (2023). Transcriptomic diversity of cell types across the adult human brain. Science, 382(6667), eadd7046. https://doi.org/10.1126/science.add7046

Simon, H. H., Saueressig, H., Wurst, W., Goulding, M. D., & O'Leary, D. D. (2001). Fate of midbrain dopaminergic neurons controlled by the engrailed genes. J Neurosci, 21(9), 3126-3134. https://doi.org/10.1523/JNEUROSCI.21-09-03126.2001

Sloan, S. A., Andersen, J., Pasca, A. M., Birey, F., & Pasca, S. P. (2018). Generation and assembly of human brain region-specific three-dimensional cultures. Nature Protocols, 13(9), 2062-2085. https://doi.org/10.1038/s41596-018-0032-7

Smidt, M. P., Asbreuk, C. H., Cox, J. J., Chen, H., Johnson, R. L., & Burbach, J. P. (2000). A second independent pathway for development of mesencephalic dopaminergic neurons requires Lmx1b. Nat Neurosci, 3(4), 337-341. https://doi.org/10.1038/73902

Smits, L. M., Reinhardt, L., Reinhardt, P., Glatza, M., Monzel, A. S., Stanslowsky, N., Rosato-Siri, M. D., Zanon, A., Antony, P. M., Bellmann, J., Nicklas, S. M., Hemmer, K., Qing, X., Berger, E., Kalmbach, N., Ehrlich, M., Bolognin, S., Hicks, A. A., Wegner, F., . . . Schwamborn, J. C. (2019). Modeling Parkinson's disease in midbrain-like organoids. NPJ Parkinsons Dis, 5, 5. https://doi.org/10.1038/s41531-019-0078-4

Smits, S. M., Ponnio, T., Conneely, O. M., Burbach, J. P., & Smidt, M. P. (2003). Involvement of Nurr1 in specifying the neurotransmitter identity of ventral midbrain dopaminergic neurons. Eur J Neurosci, 18(7), 1731-1738. https://doi.org/10.1046/j.1460-9568.2003.02885.x

Solnica-Krezel, L., & Sepich, D. S. (2012). Gastrulation: making and shaping germ layers. Annu Rev Cell Dev Biol, 28, 687-717. https://doi.org/10.1146/annurev-cellbio-092910-154043

Song, J. J., Oh, S. M., Kwon, O. C., Wulansari, N., Lee, H. S., Chang, M. Y., Lee, E., Sun, W., Lee, S. E., Chang, S., An, H., Lee, C. J., & Lee, S. H. (2018). Cografting astrocytes improves cell therapeutic outcomes in a Parkinson's disease model. J Clin Invest, 128(1), 463-482. https://doi.org/10.1172/JCI93924

Sonntag, K. C., Pruszak, J., Yoshizaki, T., van Arensbergen, J., Sanchez-Pernaute, R., & Isacson, O. (2007). Enhanced yield of neuroepithelial precursors and midbrain-like dopaminergic neurons from human embryonic stem cells using the bone morphogenic protein antagonist noggin. Stem Cells, 25(2), 411-418. https://doi.org/10.1634/stemcells.2006-0380

Southwell, D. G., Nicholas, C. R., Basbaum, A. I., Stryker, M. P., Kriegstein, A. R., Rubenstein, J. L., & Alvarez-Buylla, A. (2014). Interneurons from embryonic development to cell-based therapy. Science, 344(6180), 1240622. https://doi.org/10.1126/science.1240622

Spitz, S., Ko, E., Ertl, P., & Kamm, R. D. (2023). How Organ-on-a-Chip Technology Can Assist in Studying the Role of the Glymphatic System in Neurodegenerative Diseases. Int J Mol Sci, 24(3). https://doi.org/10.3390/ijms24032171

Steinbeck, J. A., & Studer, L. (2015). Moving stem cells to the clinic: potential and limitations for brain repair. Neuron, 86(1), 187-206. https://doi.org/10.1016/j.neuron.2015.03.002

Steinkellner, T., Zell, V., Farino, Z. J., Sonders, M. S., Villeneuve, M., Freyberg, R. J., Przedborski, S., Lu, W., Freyberg, Z., & Hnasko, T. S. (2018). Role for VGLUT2 in selective vulnerability of midbrain dopamine neurons. J Clin Invest, 128(2), 774-788. https://doi.org/10.1172/JCI95795

Storm, P., Zhang, Y., Nilsson, F., Fiorenzano, A., Krausse, N., Akerblom, M., Davidsson, M., Yuan, J., Kirkeby, A., Bjorklund, T., & Parmar, M. (2024). Lineage tracing of stem cell-derived dopamine grafts in a Parkinson's model reveals shared origin of all graft-derived cells. Sci Adv, 10(42), eadn3057. https://doi.org/10.1126/sciadv.adn3057

Stott, S. R., Metzakopian, E., Lin, W., Kaestner, K. H., Hen, R., & Ang, S. L. (2013). Foxa1 and foxa2 are required for the maintenance of dopaminergic properties in ventral midbrain neurons at late embryonic stages. J Neurosci, 33(18), 8022-8034. https://doi.org/10.1523/JNEUROSCI.4774-12.2013

Sun, X. Y., Ju, X. C., Li, Y., Zeng, P. M., Wu, J., Zhou, Y. Y., Shen, L. B., Dong, J., Chen, Y. J., & Luo, Z. G. (2022). Generation of vascularized brain organoids to study neurovascular interactions. Elife, 11. https://doi.org/10.7554/eLife.76707

Tabar, V., & Studer, L. (2014). Pluripotent stem cells in regenerative medicine: challenges and recent progress. Nat Rev Genet, 15(2), 82-92. https://doi.org/10.1038/nrg3563

Takahashi, K., & Yamanaka, S. (2006). Induction of pluripotent stem cells from mouse embryonic and adult fibroblast cultures by defined factors. Cell, 126(4), 663-676. https://doi.org/10.1016/j.cell.2006.07.024

Taylor, K. S., Counsell, C. E., Harris, C. E., & Gordon, J. C. (2006). Screening for undiagnosed parkinsonism in people aged 65 years and over in the community. Parkinsonism Relat Disord, 12(2), 79-85. https://doi.org/10.1016/j.parkreldis.2005.08.005

Tejchman, A., Znoj, A., Chlebanowska, P., Fraczek-Szczypta, A., & Majka, M. (2020). Carbon Fibers as a New Type of Scaffold for Midbrain Organoid Development. Int J Mol Sci, 21(17). https://doi.org/10.3390/ijms21175959

Thanvi, B. R., & Lo, T. C. (2004). Long term motor complications of levodopa: clinical features, mechanisms, and management strategies. Postgrad Med J, 80(946), 452-458. https://doi.org/10.1136/pgmj.2003.013912

Thompson, L. H., Grealish, S., Kirik, D., & Bjorklund, A. (2009). Reconstruction of the nigrostriatal dopamine pathway in the adult mouse brain. Eur J Neurosci, 30(4), 625-638. https://doi.org/10.1111/j.1460-9568.2009.06878.x

Thomson, J. A., Itskovitz-Eldor, J., Shapiro, S. S., Waknitz, M. A., Swiergiel, J. J., Marshall, V. S., & Jones, J. M. (1998). Embryonic stem cell lines derived from human blastocysts. Science, 282(5391), 1145-1147. https://doi.org/10.1126/science.282.5391.1145

Tiklova, K., Bjorklund, A. K., Lahti, L., Fiorenzano, A., Nolbrant, S., Gillberg, L., Volakakis, N., Yokota, C., Hilscher, M. M., Hauling, T., Holmstrom, F., Joodmardi, E., Nilsson, M., Parmar, M., & Perlmann, T. (2019). Single-cell RNA sequencing reveals midbrain dopamine neuron diversity emerging during mouse brain development. Nat Commun, 10(1), 581. https://doi.org/10.1038/s41467-019-08453-1

Tiklova, K., Nolbrant, S., Fiorenzano, A., Bjorklund, A. K., Sharma, Y., Heuer, A., Gillberg, L., Hoban, D. B., Cardoso, T., Adler, A. F., Birtele, M., Lunden-Miguel, H., Volakakis, N., Kirkeby, A., Perlmann, T., & Parmar, M. (2020). Single cell transcriptomics identifies stem cell-derived graft composition in a model of Parkinson's disease. Nat Commun, 11(1), 2434. https://doi.org/10.1038/s41467-020-16225-5

Tolve, M., Ulusoy, A., Patikas, N., Islam, K. U. S., Bodea, G. O., Ozturk, E., Broske, B., Mentani, A., Wagener, A., van Loo, K. M. J., Britsch, S., Liu, P., Khaled, W. T., Metzakopian, E., Baader, S. L., Di Monte, D. A., & Blaess, S. (2021). The transcription factor BCL11A defines distinct subsets of midbrain dopaminergic neurons. Cell Rep, 36(11), 109697. https://doi.org/10.1016/j.celrep.2021.109697

Ungless, M. A., & Grace, A. A. (2012). Are you or aren't you? Challenges associated with physiologically identifying dopamine neurons. Trends Neurosci, 35(7), 422-430. https://doi.org/10.1016/j.tins.2012.02.003

Vadodaria, K. C., Jones, J. R., Linker, S., & Gage, F. H. (2020). Modeling Brain Disorders Using Induced Pluripotent Stem Cells. Cold Spring Harb Perspect Biol, 12(6). https://doi.org/10.1101/cshperspect.a035659

Van den Heuvel, D. M., & Pasterkamp, R. J. (2008). Getting connected in the dopamine system. Prog Neurobiol, 85(1), 75-93. https://doi.org/10.1016/j.pneurobio.2008.01.003

Velasco, S., Kedaigle, A. J., Simmons, S. K., Nash, A., Rocha, M., Quadrato, G., Paulsen, B., Nguyen, L., Adiconis, X., Regev, A., Levin, J. Z., & Arlotta, P. (2019). Individual brain organoids reproducibly form cell diversity of the human cerebral cortex. Nature, 570(7762), 523-527. https://doi.org/10.1038/s41586-019-1289-x

Vertesy, A., Eichmuller, O. L., Naas, J., Novatchkova, M., Esk, C., Balmana, M., Ladstaetter, S., Bock, C., von Haeseler, A., & Knoblich, J. A. (2022). Gruffi: an algorithm for computational removal of stressed cells from brain organoid transcriptomic datasets. EMBO J, 41(17), e111118. https://doi.org/10.15252/embj.2022111118

Wakeman, D. R., Hiller, B. M., Marmion, D. J., McMahon, C. W., Corbett, G. T., Mangan, K. P., Ma, J., Little, L. E., Xie, Z., Perez-Rosello, T., Guzman, J. N., Surmeier, D. J., & Kordower, J. H. (2017). Cryopreservation Maintains Functionality of Human iPSC Dopamine Neurons and Rescues Parkinsonian Phenotypes In Vivo. Stem Cell Reports, 9(1), 149-161. https://doi.org/10.1016/j.stemcr.2017.04.033

Wang, S., Bates, J., Li, X., Schanz, S., Chandler-Militello, D., Levine, C., Maherali, N., Studer, L., Hochedlinger, K., Windrem, M., & Goldman, S. A. (2013). Human iPSC-derived oligodendrocyte progenitor cells can myelinate and rescue a mouse model of congenital hypomyelination. Cell Stem Cell, 12(2), 252-264. https://doi.org/10.1016/j.stem.2012.12.002

Wenning, G. K., Odin, P., Morrish, P., Rehncrona, S., Widner, H., Brundin, P., Rothwell, J. C., Brown, R., Gustavii, B., Hagell, P., Jahanshahi, M., Sawle, G., Bjorklund, A., Brooks, D. J., Marsden, C. D., Quinn, N. P., & Lindvall, O. (1997). Short- and long-term survival and function of unilateral intrastriatal dopaminergic grafts in Parkinson's disease. Ann Neurol, 42(1), 95-107. https://doi.org/10.1002/ana.410420115

Wesseler, M. F., Johansen, M. N., Kiziltay, A., Mortensen, K. I., & Larsen, N. B. (2022). Optical 4D oxygen mapping of microperfused tissue models with tunable in vivo-like 3D oxygen microenvironments. Lab Chip, 22(21), 4167-4179. https://doi.org/10.1039/d2lc00063f

Widhe, M., Shalaly, N. D., & Hedhammar, M. (2016). A fibronectin mimetic motif improves integrin mediated cell biding to recombinant spider silk matrices. Biomaterials, 74, 256-266. https://doi.org/10.1016/j.biomaterials.2015.10.013

Widner, H., Tetrud, J., Rehncrona, S., Snow, B., Brundin, P., Gustavii, B., Bjorklund, A., Lindvall, O., & Langston, J. W. (1992). Bilateral fetal mesencephalic grafting in two patients with parkinsonism induced by 1-methyl-4-phenyl-1,2,3,6-tetrahydropyridine (MPTP). N Engl J Med, 327(22), 1556-1563. https://doi.org/10.1056/NEJM199211263272203

Wilson, C. J., & Callaway, J. C. (2000). Coupled oscillator model of the dopaminergic neuron of the substantia nigra. J Neurophysiol, 83(5), 3084-3100. https://doi.org/10.1152/jn.2000.83.5.3084

Xi, J., Liu, Y., Liu, H., Chen, H., Emborg, M. E., & Zhang, S. C. (2012). Specification of midbrain dopamine neurons from primate pluripotent stem cells. Stem Cells, 30(8), 1655-1663. https://doi.org/10.1002/stem.1152

Xu, P., He, H., Gao, Q., Zhou, Y., Wu, Z., Zhang, X., Sun, L., Hu, G., Guan, Q., You, Z., Zhang, X., Zheng, W., Xiong, M., & Chen, Y. (2022). Human midbrain dopaminergic neuronal differentiation markers predict cell therapy outcomes in a Parkinson's disease model. J Clin Invest, 132(14). https://doi.org/10.1172/JCI156768

Yaghmaeian Salmani, B., Lahti, L., Gillberg, L., Jacobsen, J. K., Mantas, I., Svenningsson, P., & Perlmann, T. (2024). Transcriptomic atlas of midbrain dopamine neurons uncovers differential vulnerability in a Parkinsonism lesion model. Elife, 12. https://doi.org/10.7554/eLife.89482

Yang, S., Edman, L. C., Sanchez-Alcaniz, J. A., Fritz, N., Bonilla, S., Hecht, J., Uhlen, P., Pleasure, S. J., Villaescusa, J. C., Marin, O., & Arenas, E. (2013). Cxcl12/Cxcr4 signaling controls the migration and process orientation of A9-A10 dopaminergic neurons. Development, 140(22), 4554-4564. https://doi.org/10.1242/dev.098145

Yu, J., Vodyanik, M. A., Smuga-Otto, K., Antosiewicz-Bourget, J., Frane, J. L., Tian, S., Nie, J., Jonsdottir, G. A., Ruotti, V., Stewart, R., Slukvin, II, & Thomson, J. A. (2007). Induced pluripotent stem cell lines derived from human somatic cells. Science, 318(5858), 1917-1920. https://doi.org/10.1126/science.1151526

Zeng, X., Cai, J., Chen, J., Luo, Y., You, Z. B., Fotter, E., Wang, Y., Harvey, B., Miura, T., Backman, C., Chen, G. J., Rao, M. S., & Freed, W. J. (2004). Dopaminergic differentiation of human embryonic stem cells. Stem Cells, 22(6), 925-940. https://doi.org/10.1634/stemcells.22-6-925

Zhang, S. C., Wernig, M., Duncan, I. D., Brustle, O., & Thomson, J. A. (2001). In vitro differentiation of transplantable neural precursors from human embryonic stem cells. Nat Biotechnol, 19(12), 1129-1133. https://doi.org/10.1038/nbt1201-1129

Zheng, X., Han, D., Liu, W., Wang, X., Pan, N., Wang, Y., & Chen, Z. (2023). Human iPSC-derived midbrain organoids functionally integrate into striatum circuits and restore motor function in a mouse model of Parkinson's disease. Theranostics, 13(8), 2673-2692. https://doi.org/10.7150/thno.80271

nature COMMUNICATIONS

ARTICLE

https://doi.org/10.1038/s41467-021-27464-5 OPEN

Paper I

Single-cell transcriptomics captures features of human midbrain development and dopamine neuron diversity in brain organoids

Alessandro Fiorenzano[1✉], Edoardo Sozzi[1], Marcella Birtele[1], Janko Kajtez[1], Jessica Giacomoni[1], Fredrik Nilsson[1], Andreas Bruzelius[2], Yogita Sharma[1], Yu Zhang[1], Bengt Mattsson[1], Jenny Emnéus[3], Daniella Rylander Ottosson[2], Petter Storm[1] & Malin Parmar[1]

Three-dimensional brain organoids have emerged as a valuable model system for studies of human brain development and pathology. Here we establish a midbrain organoid culture system to study the developmental trajectory from pluripotent stem cells to mature dopamine neurons. Using single cell RNA sequencing, we identify the presence of three molecularly distinct subtypes of human dopamine neurons with high similarity to those in developing and adult human midbrain. However, despite significant advancements in the field, the use of brain organoids can be limited by issues of reproducibility and incomplete maturation which was also observed in this study. We therefore designed bioengineered ventral midbrain organoids supported by recombinant spider-silk microfibers functionalized with full-length human laminin. We show that silk organoids reproduce key molecular aspects of dopamine neurogenesis and reduce inter-organoid variability in terms of cell type composition and dopamine neuron formation.

[1] Developmental and Regenerative Neurobiology, Wallenberg Neuroscience Center, and Lund Stem Cell Center, Department of Experimental Medical Science, Lund University, Lund, Sweden. [2] Regenerative Neurophysiology, Wallenberg Neuroscience Center, Lund Stem Cell Center, Department of Experimental Medical Science, Lund University, Lund, Sweden. [3] Department of Biotechnology and Biomedicine (DTU Bioengineering), Technical University of Denmark, Lyngby, Denmark. ✉email: alessandro.fiorenzano@med.lu.se

The ability to control cell-fate specification and drive differentiation of human pluripotent stem cells (hPSCs) into regionally specified neuronal subtypes has opened up new avenues of research into human-specific brain development, disease modeling, and cell-based therapies. hPSC differentiation is most routinely carried out in two-dimensional (2D) cultures, which poorly recapitulate the cellular composition and structural complexity of human brain. Although models of human neural development that better recreate the intricacy of different regions of the developing neural tube are being developed[1–3], it remains challenging to obtain mature cells in these systems. Three-dimensional (3D) human-brain organoids have rapidly become a widely adopted system to study the development and function/dysfunction of neuronal cells, as it provides a more physiologically relevant cellular context and allows for long-term maintenance of functionally mature neurons[4–6]. Recent advancements in single-cell sequencing technologies have increased the scope for dissecting organoid cultures to define cell-type composition and provide an opportunity to study brain development, cell diversity, and gene regulation of otherwise inaccessible human cells. To date, most studies of this sort have been conducted in cerebral organoids. For example, single-cell transcriptomics were used to map cell types and developmental states within organoids[7], to explore cortical development[8], and to define human-specific gene-regulatory changes[9]. However, the full potential of organoid models is still restricted by issues of reproducibility and variability in terms of morphology, cellular makeup, and activity[10–13].

In this study, we patterned hPSC-derived brain organoids into a ventral midbrain (VM) identity using a protocol that results in the formation of midbrain dopamine (DA) progenitors and of functionally mature DA neurons after transplantation in xenograft models of Parkinson's disease (PD)[14]. DA neurons in these organoids exhibited mature electrophysiological properties, neuromelanin production, and the ability to release DA, confirming the long-term maintenance of functionally mature human DA neurons in 3D culture as previously reported in both hPSC-derived[15–18] and neural progenitor-derived[19–21] midbrain organoids. A time-course transcriptional analysis of human VM development and DA neuron differentiation at single-cell level revealed four populations of cells with high transcriptional similarity to VM floor-plate cells, followed by the stepwise emergence of neurons, vascular leptomeningeal cells (VLMCs), astrocytes, and oligodendrocytes. Importantly, we found that mature neurons and glia formed within the organoids displayed high similarity to the corresponding cell types in adult human midbrain[22]. The large number of cells within the DA neuron cluster (14,606 cells) enabled us to perform a detailed molecular dissection of mature human DA neurons not previously possible. We identified several molecularly distinct human DA neuron subgroups, similarly to recent observations in developing and adult mouse brain[23–25].

These brain organoids showed a lower level of variability compared with self-organized 3D structures[4,7], and a similar level of variability as other protocols based on extrinsic patterning factors[15,26]. To further reduce variability in the organoids, we used recombinant spider silk microfibers functionalized with full-length human laminin. These bioengineered silk-VM organoids reproduced key molecular aspects of DA neurogenesis but with more precise patterning and less organoid-to-organoid as well as intra-organoid variation. Furthermore, detailed functional and molecular analyses showed that the silk scaffolds reduced necrosis and supported neuronal maturation in all regions of the organoid. In sum, silk-fiber scaffolding is an experimentally straightforward method that does not require specialized equipment or technical expertise and can thus be widely implemented in organoid culturing.

Results

Key features of human VM development can be recapitulated in 3D culture. We established VM organoids by adapting a commonly used protocol for the generation of forebrain organoids[27] with the addition of dual-SMAD inhibition combined with exposure to SHH, GSK3i, and FGF8 in the same temporal sequence used in 2D culture to promote neurogenic conversion of VM FP progenitors toward a DA neuron identity (Fig. 1a)[28,29]. We confirmed that in 3D cultures, this patterning regime also resulted in efficient neuralization and ventral midbrain differentiation as evaluated by expression of *CNPY1*, *LMX1a*, *LMX1b*, *OTX1*, *CORIN*, *SHH*, and *FOXA2* (Fig. 1b). The expression of midbrain genes was accompanied by complete downregulation of pluripotency-associated genes *OCT4* and *NANOG* (Fig. 1b). Expression of early neural marker NGN2 (Fig. 1c–e) as well as tight-junction protein ZO1 (Fig. 1d) and atypical protein kinase aPKC (Fig. 1e) was detected by immunocytochemistry at early stage of organoid formation. Although the architectural arrangements morphologically resembled the intermediate rosette stage typical of anterior neuroectoderm[30], they were PAX6-negative (Supplementary Fig. 1a–c) and expressed both CORIN and FOXA2 (Fig. 1f), in accordance with their VM identity. Successful 3D VM differentiation was reproduced using two additional cell lines, H9 and HS1001 (Supplementary Fig. 1d–k), demonstrating the robustness of the protocol.

Staining for the cell cycle marker Ki67 showed that cell proliferation was largely confined to the basal region, while postmitotic neurons detected by MAP2 were located in the apical regions (Fig. 1g, h). We further assessed the presence of different developmental zones as defined by expression of MASH1, FOXA2, and MAP2 (Fig. 1i–k) and found a layered-restricted organization (Fig. 1j). This was confirmed by quantification of cells in different anatomical locations of the organoids, showing that FOXA2- and MAP2-expressing cells were concentrated to the outer layer (Fig. 1k). By the second week, FOXA2-positive cells appeared in the organoids (Fig. 1l), and from day 30, TH-expressing neurons were detected (Fig. 1m). To directly compare our VM organoids with other hPSC-derived midbrain-patterned organoids generated using previously published protocols, we recreated midbrain-like organoids (MLO) according to Jo et al.[15] and dorsomorphin A82-01 midbrain organoids (DA-MO) according to Kwak et al.[17] as well as forebrain organoids (FBO) as reported in Lancaster et al.[27]. Quantifications revealed a similar number of cells expressing the key VM markers FOXA2, LMX1, and TH in all three midbrain patterned organoids (Supplementary Fig. 1l–p), while PAX6 was only expressed in FBO (Supplementary Fig. 1a, p).

After 60 days, expression of G-protein-regulated inwardly rectifying potassium channel 2 (GIRK2) (Fig. 1n and Supplementary Fig. 1q), calcium-binding protein 1 (CALB1) (Fig. 1o and Supplementary Fig. 1r), and DA transporter (DAT) (Fig. 1p) indicated that mature DA neuron subtypes had emerged within the organoids. Quantifications at day 60 confirmed comparable differentiation into mature DA neurons as from previously reported protocols (Supplementary Fig. 1q–w). Specification toward a mature and authentic A9-like DA population, which consists of pigmented neurons located in SNc in primate VM—and which is prevalently lost in PD—was corroborated by combined Fontana–Masson staining/TH immunohistochemistry revealing the presence of intracellular and extracellular neuromelanin, visible as dark granular pigmentation after long-term culture (Fig. 1q, r).

scRNAseq reveals cellular composition and developmental trajectory in VM organoids. We next performed a 10X genomics droplet-based single-cell time-course transcriptomic analysis of

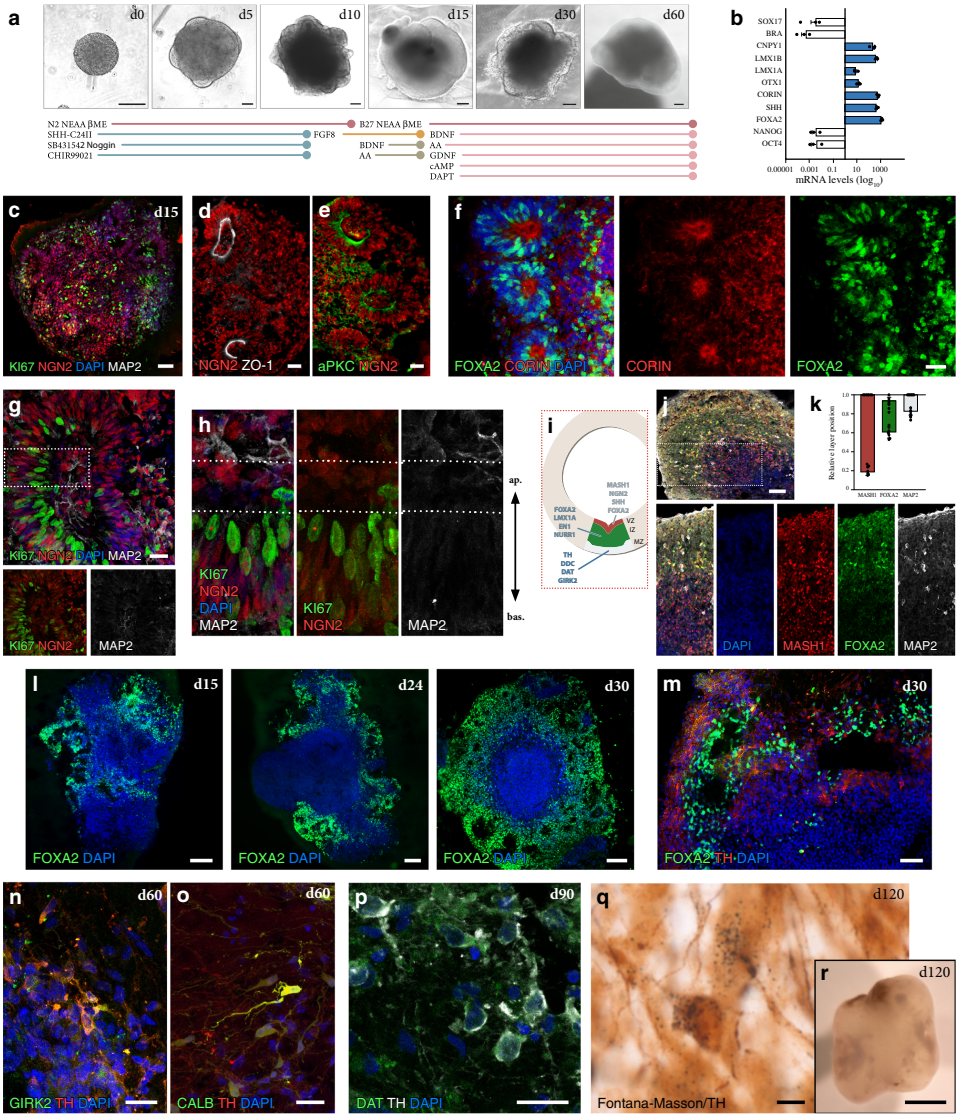

human VM organoid development (Fig. 2a) by profiling a total of 91,034 single cells isolated from organoids at days 15, 30, 60, 90, and 120 of VM organoid differentiation with several replicates per time point (day 15, $n = 2$; day30, $n = 4$; day 60, $n = 5$; day 90, $n = 2$; day 120, $n = 6$). After integration using the Harmony approach[31], uniform manifold approximation and projection (UMAP) and graph-based clustering visualized eight different clusters (Fig. 2b), all assigned a neuroectodermal identity (Fig. 2b–d and Supplementary Fig. 2c) with no remaining pluripotent cells (Supplementary Fig. 3a), mesodermal (*T*), or endodermal derivatives (*SOX17*) (Supplementary Fig. 3b). All identified clusters showed distinct separations with high average silhouette widths (Supplementary Fig. 2b).

The most highly differentially expressed genes were used together with canonical markers to manually annotate clusters with their respective cellular identities. The yellow cluster in the UMAP space was made up of cells expressing neural markers (*HES1*, *NES*, and SOX2) (Fig. 2d and Supplementary Fig. 3c) and cells with a highly proliferative signature (*TOP2A, CCNB2,* and *CENPF1*) (Fig. 2e, f), which we named FP-0. These cells display similar characteristics to cycling FP progenitors located in VM at early stages of embryonic development[32,33]. FP-0 population was

Fig. 1 Dopamine neurogenesis in VM organoids. a Representative bright-field images of ventral midbrain (VM) organoid differentiation at different time points (upper) and schematic overview of the experimental design (lower). Scale bars, 200 µm. **b** qRT-PCR of selected markers at day 15 of VM organoid differentiation. The results are given as fold change over undifferentiated hPSCs. Data represent mean ± SEM of 3 independent organoids. **c–e** Immunocytochemistry of (**c**) NGN2/Ki67/MAP2, (**d**) NGN2/ZO-1, and (**e**) NGN2/aPKC at day 15 during VM organoid differentiation. Scale bars, 50 µm. **f** Immunohistochemistry of FOXA2/CORIN and **g** NGN2/Ki67/MAP2 in VM organoid at day 15. Scale bars, 100 µm (**f**) and 50 µm (**g**). **h** High-power magnification of the inset in **g**. **i** Schematic representation of developing DA neurons in vivo showing genes expressed at different stages of development (MZ, mantle zone; IZ, intermediate zone; VZ, ventricular zone). **j** Immunohistochemistry of MASH1, FOXA2, and MAP2 showing layer-specific organization and **k** relative quantification of fluorescence staining in VM organoid at day 24. Data represent mean ± SEM of 7 independent VM organoids. Scale bar, 100 µm. **l** Immunohistochemistry of FOXA2 across a time course (day 15–30). Scale bars, 50 µm. **m** Cryosection of VM organoid at month 1 showing TH/FOXA2 double staining. Scale bars, 100 µm. **n**, **o** Immunohistochemistry of TH stained with GIRK2/CALB at day 60 and **p** with DAT at day 90. Scale bars, 50 µm (**n**, **o**) and 20 µm (**p**). **q** Fontana Masson/TH double-stained cryosection from long-term cultured VM organoid (month 4). Scale bars, 50 µm. **r** Representative bright-field image of VM organoid at month 4. Scale bars, 1 mm. Nuclei were stained with DAPI in **g**, **h**, **j**, **l–p**. Source data are provided as a Source Data file.

the prominent cluster at the early time points (Fig. 2c and Supplementary Fig. 4a, b), and based on pseudo-time-inference reconstruction analysis (Supplementary Fig. 4c) gave rise to all the other identified cell clusters (see later section). UMAP also visualized another large FP-like progenitor population that was further subdivided into three different clusters, referred to as FP-1 (light green), FP-2 (purple), and FP-3 (blue) (Fig. 2b). The concomitant expression of *HES5* and *SOX2* with *VIM* and *FABP7* (also known as *BLBP1*) (Fig. 2d and Supplementary Fig. 3c, d) indicated that FP-1 shares many features of radial glial cells and is also enriched in cell cycle genes (Fig. 2e). FP-2 was instead enriched in cells expressing *SHH* and *CORIN*, and also contained early DA progenitor markers, including *FOXA2*, *LMX1A*, *MSX1*, and *OTX2* (Fig. 2d and Supplementary Fig. 3e). The FP-3 cluster mainly differed from the FP-2 cluster in the additional expression of neuronal precursor markers *STMN2* and *SYT1*, and DA progenitor markers *EN1* and *DDC* (Fig. 2d and Supplementary Fig. 2c and Supplementary Fig. 3f, g), as well as its exit from cell cycle (Fig. 2e, f). Furthermore, scRNAseq analysis revealed the absence of forebrain (*FOXG1*) and only very few scattered hindbrain (*HOXA2*) cells, indicating efficient VM patterning (Supplementary Fig. 3d). In agreement, the neuronal cluster (orange in Fig. 2b) defined by expression of *DCX*, *SYT1*, and *STMN2*, primarily expressed genes associated with DA-fate identity (*PBX1, NR4A2*/NURR1*, EN1, TH*, and *DDC*) (Fig. 2d and Supplementary Fig. 2c and Supplementary Fig. 3f, g), with only few cells showing GABAergic (*VGAT*) and glutamatergic (*VGLUT1*) features (Supplementary Fig. 3k). VM organoids also contained a newly discovered class of perivascular-like cells termed vascular leptomeningeal cells (VLMCs) expressing *PDGFRa*, *COL1A1*, *COL1A2*, and *LUM*, astrocytes (*GFAP, AQP4,* and *EDNRB*) and a small cluster of oligodendrocyte progenitors (*OLIG1/2, PDGFRa*, and *SOX10*) (Fig. 2b, d and Supplementary Fig. 3h–j and l–n). Consistent with efficient VM patterning, the single-cell dataset generated here correlated well with published bulk and single-cell sequencing of midbrain 3D cultures derived from either hPSCs or neural progenitors (Supplementary Fig. 5a)[15,20,21] and, as expected, displayed a lower correlation to FBO (Supplementary Fig. 5a). We also performed scRNAseq of one-month-old MLOs generated using the protocol described by Jo et al. (29,112 cells analyzed from two replicates), which showed the presence of the same cell types at the same timepoints (Supplementary Fig. 5b).

Analysis of organoid composition over time revealed that the different cell types appeared in a temporal pattern: the yellow cluster was the first emerging progenitor population, while FP-2 and FP-3 appeared slightly later (Fig. 2g and Supplementary Fig. 4a, b). Unlike FP-0 and FP-1, FP-3 increased proportionally in frequency over time and FP-3 was the only population still present in high numbers at day 120 (Fig. 2g and Supplementary Fig. 4a, b). The DA cluster started to emerge from day 15 and was present in high numbers at all subsequent time points analyzed, although its relative proportion varied due to the increased presence of other cell types at later timepoints (Fig. 2g and Supplementary Fig. 4a, b). VLMCs, astrocytes, and oligodendrocyte progenitors appeared in a sequential manner (Fig. 2g and Supplementary Fig. 4a, b). When organizing cells—from pluripotent to mature differentiated states—according to transcriptional similarity along a temporal axis, force-directed *k*-nearest-neighbor graph-based pseudotime trajectory defined distinct branches segregating from the FP progenitor cells (Fig. 2h, i). At month 1, a first branch gave rise to DA progenitors, which by month 2 had started to mature into postmitotic DA neurons (Fig. 2h, i). A second branch trajected toward vascular stromal progenitors able to differentiate into VLMC progenitors after month 1, but into more mature cell types only from month 3 (Fig. 2h, i). These findings were corroborated by Slingshot analysis (Supplementary Fig. 4c), where lineages are identified by treating clusters of cells as nodes in a graph and drawing a minimum spanning tree between nodes[34].

Molecular diversity in human DA neuron cluster. We next investigated whether the mature cell types generated in VM-patterned organoids were transcriptionally similar to those present in a recently published snRNA-seq dataset from adult human midbrain containing ~6000 midbrain nuclei derived from five adult individuals[22]. This study identified distinct cell types in the adult midbrain: astrocytes, oligodendrocytes, oligodendrocyte progenitors (OPCs), microglia, endothelial cells, and neurons[22]. Merged clustering with our VM organoid dataset showed that the cell types present in organoids and human midbrain were transcriptionally similar, with the exception of microglia, which were not present in the organoids (Fig. 3a). Interestingly, all cell types in VM-patterned organoids displayed much higher transcriptional similarity to the corresponding cell types in human midbrain than to those in the cortex from the same dataset (~10,700 cortical cells from the middle frontal gyrus) (Fig. 3b).

Histological analysis (Fig. 1) indicated that DA neurons mature over time in the organoids, and that markers enriched in the two subtypes A9 and A10 neurons were present in long-term cultures (Fig. 1n–r). Several recent studies based on scRNAseq describe a greater-than-expected molecular DA neuron diversity, and at least five different molecular subtypes are reported in adult mouse VM[23–25,35]. However, similar datasets for mature human DA neurons do not yet exist. To determine if distinct molecular subtypes of human DA neurons appear in the organoids, we isolated the DA compartment (14,606 cells, all time points) and reran the integration (Harmony) and clustering. A SPRING plot visualized two major populations (Fig. 3c), one mostly present at

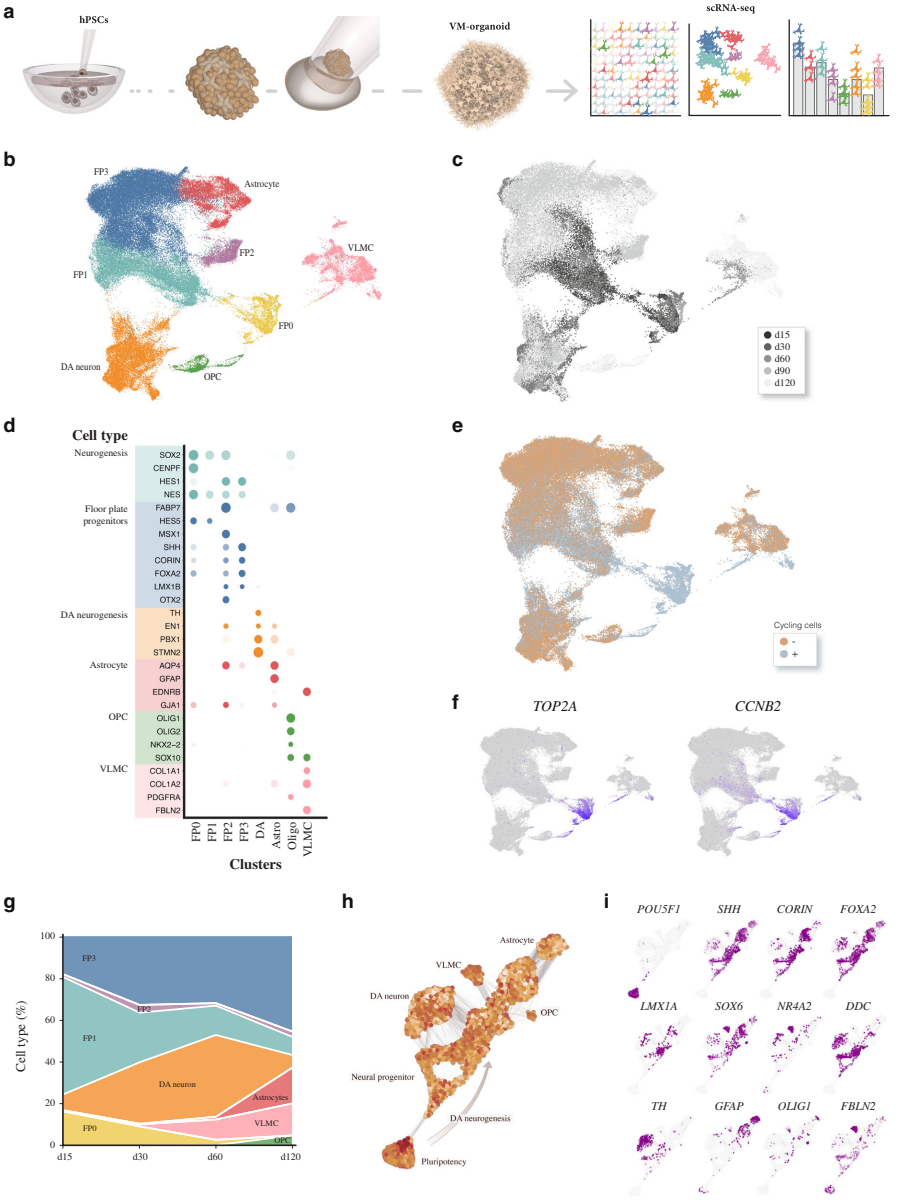

early time points and one present at late stages of VM organoid differentiation, which we termed DA^{Early} and DA^{Late}, respectively (Fig. 3c, d). Both DA^{Early} and DA^{Late} expressed TH (Fig. 3e). The expression of embryonic/early neural markers (*NES*, *SOX2*, and *RFX4*) in DA^{Early} confirmed their relatively immature neuronal state, whereas the expression of mature, postmitotic DA markers (NURR1/*NR4A2*, VMAT-2/*SLC18A2*) and voltage-gated potassium- and sodium-channel subfamily members (*KCNC2*, *SCN2A*) defined the more mature DA population (Fig. 3e).

The resulting network map (Fig. 3f) indicated transcriptional diversity within this cluster, prompting us to perform a higher-resolution analysis in order to detect the potential existence of human DA neuron molecular subtypes. The refined graph-based

Fig. 2 Single-cell transcriptomics identifying VM organoid cell types. a Schematic overview of the experimental design. hPSCs differentiated into regionalized VM organoids for up to 120 days, were analyzed at single-cell resolution. **b** 2D scatterplot of uniform manifold approximation and projection (UMAP) embeddings showing clustering of 91,034 analyzed cells from VM organoids at days 15, 30, 60, 90, and 120. Cell-type assignments are indicated. **c** UMAP plot of cells color-coded by organoid of origin. **d** Dot plot showing expression levels of indicated genes in each cluster. Indicated genes are established markers for neural progenitors, floor-plate progenitors, DA neurons, astrocytes, oligodendrocyte progenitors (OPCs), and vascular leptomeningeal cells. **e** UMAP plots showing cell cycle classification of analyzed cells (Seurat CellCycleScoring predictions). Cycling cells shown with gray dots. **f** Expression levels of indicated cell cycle genes visualized in the UMAP plots. **g** Proportion of each cell type along the temporal axis during VM organoid differentiation (day 15–120). **h** Developmental trajectory from pluripotency to terminally differentiated stages in VM organoid reconstructed using SPRING in VM organoid. Pseudocells are color-graded by total count. **i** SPRING plot colored (purple) by marker gene expression in emerging cellular clusters.

clustering segregated the early DA neurons into two distinct clusters (Fig. 3f): one with low TH (DA^{E-1}) and one with high TH (DA^{E-2}) (Fig. 3g). DA^{E-1} also showed increased expression of neural markers (*SOX2*), and reduced level of *SYT1* compared with DA^{E-2} (Fig. 3g). The late DA neurons segregated into three distinct molecular identities (named DA^{L-1}, DA^{L-2}, and DA^{L-3}) (Fig. 3f). Within the DA^{L-1} subcluster we found concomitant expression of *DLK1*, *KCNJ6* (also known as *GIRK2*), *SLC6A3* (*DAT*), and *DCC*. Interestingly, *SNCG* and *SNCA* (encoding members of the synuclein family of proteins), glycoprotein CD24, and transcription factors *ZDHHC2* and *NHLH2*, which were all observed in this subcluster, were also found enriched in SNc from mouse bulk and scRNAseq datasets[36] (Fig. 3h). Synapse-associated protein 1 (*SYAP1*) transcription factors and engrailed homeobox 2 (EN2) were significantly expressed in DA-$^{L-2}$. This subcluster also expressed *ANXA1*, encoding for a calcium-dependent phospholipid-binding protein, recently found associated with SNc at different developmental stages[25,37,38], and a large set of genes coding for components of respiratory electron-transport complexes (*COX17*, *NDUF,* and *ATP5ME*) as well as the brain mitochondrial receptor (*MPC1*) (Fig. 3h). The DA^{L-3} subcluster was molecularly defined by expression of *OTX2* and *CALB1*, markers of A10 DA neurons, while *DLK1* also appeared enriched in both DA^{L-3} and DA^{L-2} (Fig. 3h)[23,39]. Importantly, the DA^{L-3} cluster was also enriched in genes previously identified at single-cell level during mouse development up until adulthood, such as POU2F2 and ID4, as candidate regulators that may drive A10 subtype diversification (Fig. 3h). A set of genes associated with neuropsychiatric conditions, including Alzheimer's disease (*CLU*, *P4HA1*), schizophrenia (*CNIH2*, *DKK3*), and autism-spectrum disorders (*SEZ6L*, *SDC2*), was found particularly upregulated in this cluster (Fig. 3h)[40].

To assess to what extent the molecular identity of DA neurons in the organoids corresponds to that of authentic human DA neurons, we compared our single cell data with two scRNA-seq datasets of fetal VM DA populations, one previously reported by La Manno et al.[35] (Supplementary Fig. 5c, d) and the other obtained from 6 to 11-week post-conception human embryos and cultures thereof (Birtele et al., bioRxiv doi.org/10.1101/2020.10.01.322495) (Fig. 3i). In this latter fetal dataset, containing more mature neurons, 18,848 human fetal DA cells formed four molecularly distinct DA populations, two of which consisted of DA progenitors (gray) and the remaining two more mature populations (green) (Fig. 3j and Supplementary Fig. 5e). To confidently define organoid DA populations, we integrated fetal and hPSC-derived data, and normalized and clustered the gene expression matrix, identifying commonalities visualized via UMAP (Fig. 3k). We found a high similarity between developing and mature DA cell populations in hPSC-derived subclusters and their fetal DA neuronal counterparts (Fig. 3k), demonstrating that DA neurons in VM organoids have a similar molecular identity to authentic midbrain DA neurons sourced from human fetal brain. A detailed comparison between the four clusters of fetal VM-derived DA neurons with the five clusters of DA neurons detected in VM organoids revealed that DA progenitors from fetal brain showed high transcriptional similarity to DA^{E-1} in the organoids, unlike DA^{E-2} (Fig. 3k). Moreover, $DA^{L1,2,3}$ all showed high similarity to the mature fetal VM-sourced DA neurons (Fig. 3k).

Molecular and functional heterogeneity in VM organoids. scRNAseq followed by clustering of sample-to-sample correlations (Pearson) (Fig. 4a) and principal component analysis (PCA) (Supplementary Fig. 6a) revealed that organoids analyzed at the same developmental stage (days 30, 60, and 120) contained the same cell types (Fig. 4b), confirming the reproducibility of this protocol. However, relative frequency analysis quantifying changes in cell-type composition revealed high variability in the proportion of cell types within each cluster from organoid to organoid (Fig. 4b) even though the VM organoids were generated from a small number of hPSCs (2500 cells) following an optimized protocol reported to reduce organoid-to-organoid heterogeneity and increase long-term viability of 3D structures[7,41]. In addition to the variation between individual organoids, intra-organoid heterogeneity was observed in serial confocal TH-stained sections (Fig. 4c), showing that VM organoids exhibited a poorly developed core with sparse TH^+ neurons, suggesting that nonsynchronous differentiation and maturation takes place. To test this, we performed whole-cell patch-clamp recordings to assess functional maturation of neurons within organoids using a recently reported method based on embedding in low-melting-point agarose[42], allowing recordings in both the interior and exterior regions. We found that the cells at the surface of the organoids (Fig. 4d) exhibited more hyperpolarized resting-membrane potentials (Supplementary Fig. 6b, c) and rapidly inactivating inward sodium (Na^+) and outward delayed-rectifier potassium (K^+) currents (Fig. 4e) indicative of a mature neuronal state. In line with these findings, cells in the external part ($n = 16$) displayed the ability to fire induced action potentials (APs) upon current injections, indicating a neuronal function (Fig. 4f). These cells also showed spontaneous firing at resting-membrane potential (Fig. 4g) as well as a rebound depolarization (Fig. 4h) typical for DA neuron phenotype. In contrast, when recording from cells located in the inner region (Fig. 4i), no inward Na^+ and outward K^+ voltage-dependent currents or abortive APs were observed ($n = 20$ cells) (Fig. 4j–l). This distribution of functional cells located toward the edge of the organoids was confirmed using two additional protocols for PSC-derived midbrain organoids (Supplementary Fig. 6d–i).

Generation and characterization of silk-bioengineered VM organoids. In an attempt to create more homogeneous VM organoids and further reduce organoid-to-organoid variability, we evaluated a biomaterial made of recombinant spider-silk protein[43,44] that can self-assemble into a biocompatible cell scaffold. Silk scaffolds in the form of a network of microfiber

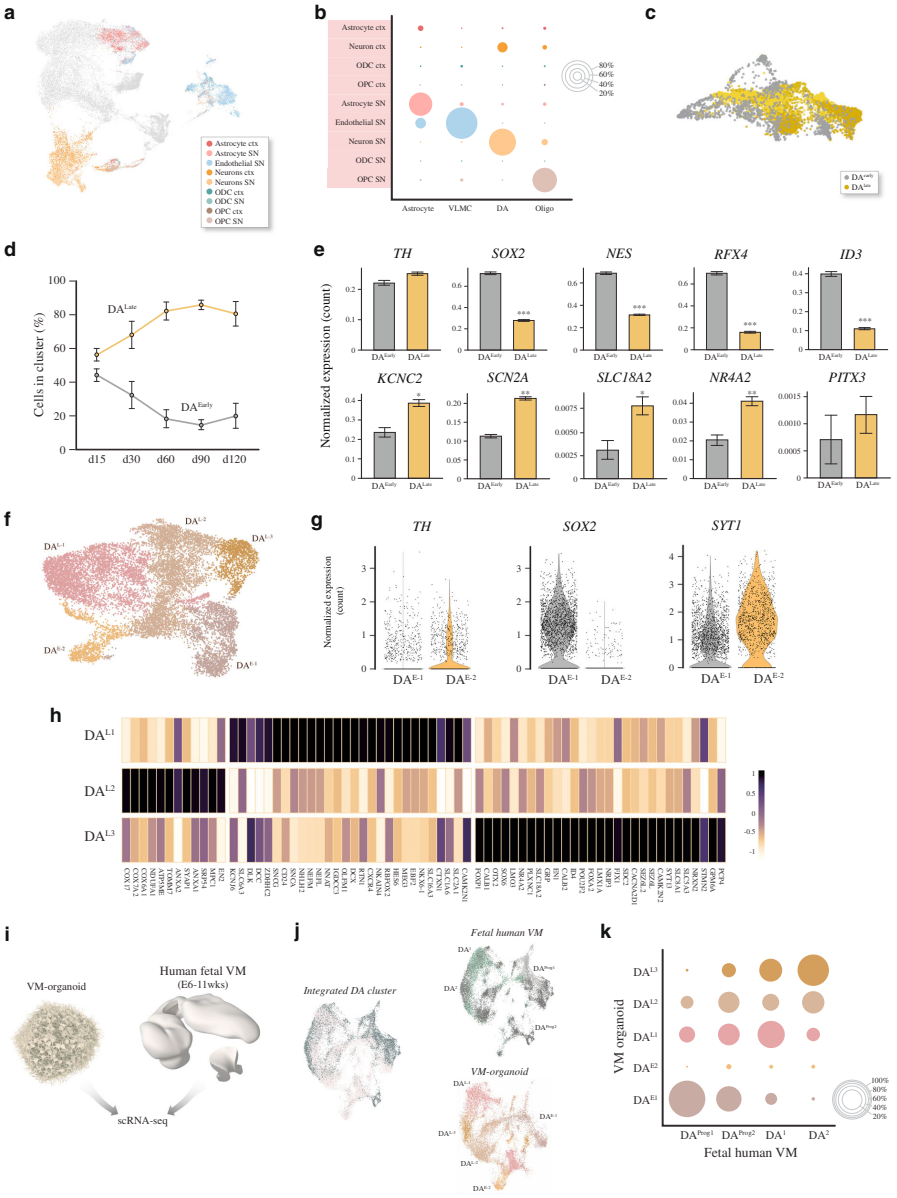

solution were obtained by placing a 20 µl droplet at the bottom center of a hydrophobic well and then introducing air bubbles by repeatedly pipetting air into the droplet (Fig. 5a and Supplementary Fig. 7a). Via self-assembly of the silk protein, a thin film was formed around each air bubble, producing a temporary foam (Fig. 5b and Supplementary Fig. 7a). hPSCs were then dispersed throughout the 3D silk scaffold to obtain the controlled cell distribution and adherence of cells within the network along the entire length of the microfibers (Fig. 5b and Supplementary Fig. 7b). Subsequently, during incubation in culture media, the foam collapses as the film around the air bubbles bursts, leaving a network of microfibers (Fig. 5c, d). Silk fibers were used either alone as an inert scaffold or functionalized with Lam-111, previously shown to promote DA patterning and support DA

Fig. 3 Single-cell transcriptomics mapping DA diversity in VM organoids. a UMAP cluster-integration analysis combining published scRNA-seq datasets of adult human midbrain[18] and the hPSC-derived VM organoids with **b**, relative overlapping quantification. **c** SPRING network plot showing the distribution of single cells in 2 dopamine (DA) clusters (DA^{Early}, gray, and DA^{Late}, yellow) within the VM organoids. **d** Percent distribution of DA^{Early} and DA^{Late} clusters across a time course during VM organoid differentiation (d15 $n = 2$; d30 $n = 5$; d60 $n = 5$; d90 $n = 2$; d120 $n = 6$). Data represent mean ± SD per 10X run. **e** Bar plot of normalized expression for DA^{Early} and DA^{Late} clusters of immature and mature neuronal marker genes (d15 $n = 2$; d30 $n = 5$; d60 $n = 5$; d90 $n = 2$; d120 $n = 6$). Data represent mean ± SEM, two-tailed Wilcoxon Rank Sum test, KCNC2 $p = 0.0045$; SCN2A $p = 0.0002$; SLC18A2 $p = 0.0269$; NR4A2 $p = 0.0013$, $^{***}p < 0.0001$. **f** UMAP plot showing DA subclusters after reintegration and clustering (DA^{E-1}, DA^{E-2}, DA^{L-1}, DA^{L-2}, and DA^{L-3}). **g** Violin plots showing differential expression levels of indicated genes in each DA^{Early} subclusters. **h** Heatmap showing differentially expressed genes and manually selected markers in 3 DA^{Late} neuron subclusters (DA^{L-1}, DA^{L-2}, and DA^{L-3}). **i** Schematic overview of experimental design where scRNAseq data from dissected human fetal VM (6–11-week embryos) and 3D primary cultures thereof (1 month) Birtele et al., bioRxiv doi.org/10.1101/2020.10.01.322495. **j** Overlapping and individual UMAP plots showing DA subcluster-integration analysis from scRNA-seq dataset of human fetal VM and hPSC-derived VM organoid. **k** Relative overlapping quantification of DA organoid subtypes vs human fetal DA neuron dataset after prediction of DA neuronal subtypes using fetal data as reference (Seurat).

differentiation in 2D cultures[14,28]. With time, the cells gradually occupied the surface and inner space of the scaffold (Fig. 5e, f), and at day 10, the resulting 3D structures were mechanically detached from the bottom of the plate (Fig. 5g, h and Supplementary Fig. 7c, d). We named the resulting bioengineered organoids *silk-VM organoids* (Fig. 5i, j and Supplementary Fig. 7g). Unlike VM-patterned organoids grown without a scaffold, *silk*-VM organoids was less round and more variable in shape (Fig. 5g, h and Supplementary Fig. 7d), yet displayed a less distinct boundary between outer and inner regions (Fig. 5g, i and Supplementary Fig. 7e, f). Cell-viability assay indicated that the self-arrangement of cells along silk fibers to enhance organoid generation did not affect their viability (Supplementary Fig. 7c). Immunocytochemistry after one month confirmed a robust expression of the VM FP progenitor cell markers ZO-1, SOX2, FOXA2, and LMX1A (Fig. 5k–m and Supplementary Fig. 7h–l, n, o), indicating a similar developmental progression to that observed in organoids without scaffolding. The establishment of midbrain DA neuronal fate was confirmed by FOXA2 (Fig. 5n, o), TH, and MAP2 expression (Fig. 5p, q and Supplementary Fig. 7m, p–v). Quantifications at day 50 revealed a similar patterning and higher number of TH-expressing neurons in silk organoids (Fig. 5q and Supplementary Fig. 7t–v), followed by expression of GIRK2 and CALB1, markers of A9 and A10 DA neuron subtypes, and DAT at month 3 (Fig. 5r–u).

Silk scaffolding reduces interorganoid variability in cell-type composition and DA neuron formation. We used scRNAseq to compare 1-month-old VM organoids grown without a scaffold, here defined as "conventional" organoids (12,830 cells analyzed), silk-VM organoids (16,740 cells analyzed), and silk-VM organoids functionalized with Lam-111 (silk-lam VM organoids) (15,520 cells analyzed) from three independent biological replicates and separate 10X runs. UMAP embedding and graph-based clustering resulted in six major clusters (Fig. 6a). To annotate the clusters, we exploited the cell types identified in conventionally generated organoids and projected these labels onto the new data using Seurat's v3 label transfer[45]. Frequency analysis quantifying the number of cells in each cluster showed a lower variability in both silk and silk-lam VM organoids than in organoids grown without a scaffold (Fig. 6b). UMAP plots (Fig. 6a) and chord diagram (Fig. 6c) visualizing cell-type interrelationships, revealed a larger DA cluster when the silk fibers were functionalized with Lam-111 (Fig. 6d, e and Supplementary Fig. 8a).

We next examined gene expression profiles of DA neurons and their progenitors in multiple independent batches of organoids generated with and without silk at month 2. Early and late DA markers were highly varied in inter- and intrabatches of conventionally generated VM brain organoids, as shown by RT-PCR, whereas self-arrangement into silk scaffolds alone or functionalized with Lam-111 significantly limited batch variability (Fig. 6f). To more precisely quantify the reproducibility of the silk methodology at protein level, we used a CRISPR/Cas9-mediated gene-edited transgenic hPSC line where *CRE* is knocked into the first exon of the *TH* gene[46]. When transduced with a flexed *GFP* lentiviral vector, this line serves as live reporter cell line where GFP is expressed specifically in DA neurons[46]. Also using this reporter system, the TH neurons appeared much more heterogeneously distributed in conventional vs silk organoids (Fig. 6g, h) Flow-based quantification in individual organoids established from this *TH*-Cre knock-in line revealed that *silk*-lam VM organoids displayed a higher percentage and more homogeneous formation of DA neurons (Fig. 6i and Supplementary Fig. 8b).

We further used scRNAseq to analyze three independent silk-lam VM organoid batches after four months. UMAP analysis of 18,375 cells visualized the same eight distinct major clusters (FP0–3, DA neurons, astrocytes, oligodendrocytes, and VLMCs) found in conventional organoids (Fig. 6j). However, frequency analysis quantifying the number of cells in each cluster revealed a lower variability in silk-lam VM organoids than in organoids grown without a scaffold also at this time point (Fig. 6k, l). To test this statistically, we utilized intraclass correlation (ICC), a correlation metric testing the proportions of each cell type in each 10X run where an ICC near 1.0 indicates high agreement. The sx batches produced using the standard protocol had an ICC of 0.51 (95% CI: 0.214–0.837) compared with 0.98 (0.96–0.99) for silk-lam VM organoids. Importantly, a high proportion of DA neurons was maintained long term in *silk*-lam organoids, indicating a precise and reproducible patterning (Fig. 6l). The FP2 population was also detected at this time point, suggesting that its absence at the early stage (Fig. 6a) reflects a slightly different developmental timing in silk organoids (Supplementary Fig. 8c). In addition, when analyzing the same number of cells and time points in both culture systems, DA neurons in silk-lam VM organoids showed a higher expression of TH and postmitotic DA neuron markers (Fig. 6m), indicating that a greater degree of maturation had been reached.

Silk scaffolding reduces intra-organoid variability. Immunolabeling-enabled imaging of solvent-cleared organs (iDISCO) (Fig. 7a, b) reconstructed a more complex and highly intricate DA region throughout the entire silk-engineered organoids (Supplementary Video 1), showing more extensive DA circuitry and more efficient generation of VM regions than in conventional 3D cultures (Fig. 7c–e). Quantification of TH, GIRK2, CALB, and DDC in the core vs edge of organoids confirmed that the distribution of DA cells was much more homogeneous in *silk*-lam VM organoids than in our conventional VM organoids (Fig. 7f), as well as in previously described midbrain-patterned organoids (Supplementary Fig. 9a–d)[15,17].

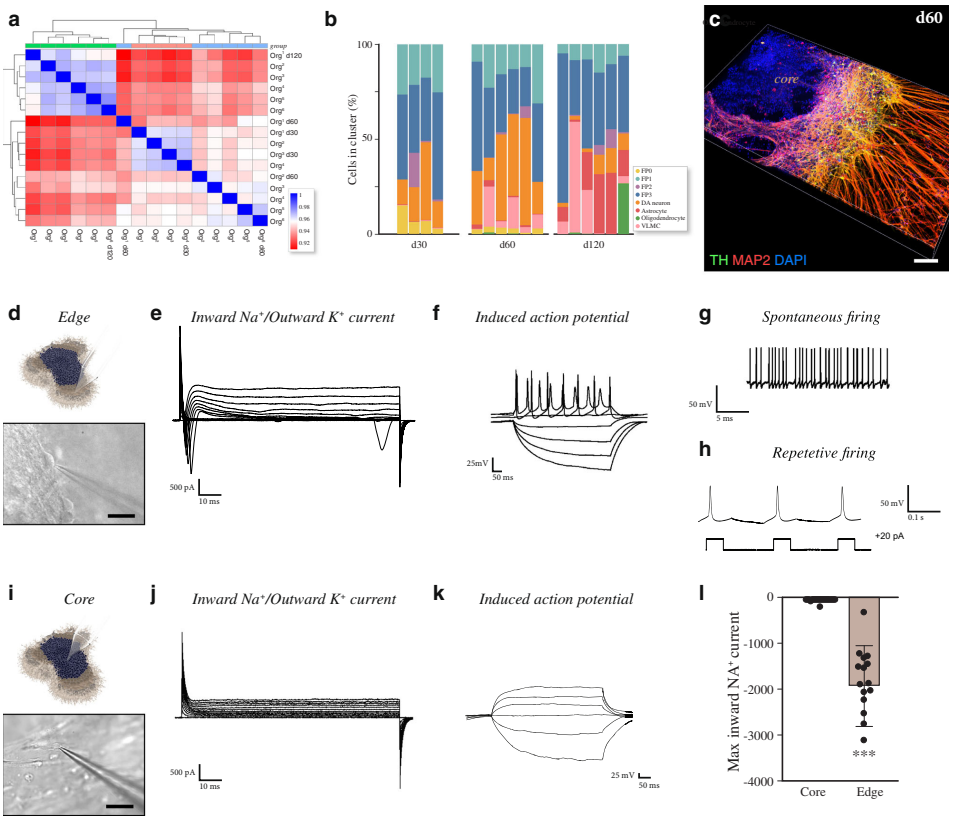

Fig. 4 Molecular and functional heterogeneity in human VM organoids. a Clustering of sample to sample correlations (Pearson) of organoids and different timepoints using Euclidean distance on normalized and log-transformed read counts. **b** Percentage of cells belonging to each cell cluster from individual organoids at days 30, 60, and 120. Intraclass correlation coefficient (correlation metric that considers group structure in the data) decreased from 0.717 at day 30 to 0.682 at day 60 and to 0.548 at day 120. **c** 3D reconstruction of an image stack from an 80 µm-thick optical section of TH and MAP2 immunohistochemistry at day 60. Scale bars, 100 µm. **d** Representative image of external functional recordings using whole-cell patch-clamp technique. Scale bars, 100 µm. **e** Representative trace from external patching showing inward sodium- and outward potassium-rectifying current traces of VM organoid at day 90 triggered by stepwise depolarization. **f** Patch-clamp recordings of external VM organoid cells depicting current-induced action potentials (APs) at day 90 (−85 pA to +165 pA with 20 pA steps). **g** External spontaneous firing at resting-membrane potential indicative of mature DA neuronal physiology in VM organoids at day 90. **h** Example trace of rebound depolarization after brief membrane depolarization (20pA) indicative of DA phenotype in externally located cells. **i** Representative image of internal functional recordings using whole-cell patch-clamp technique, Scale bars, 100 µm. **j** Representative inward sodium- and outward potassium-rectifying current traces of internally located cells at day 90 triggered by stepwise depolarization. **k** Patch-clamp recordings of internal VM organoid cells depicting the absence of current-induced APs at day 90 (−85 pA to +165 pA with 20 pA steps). **l** Inward sodium current quantifications in externally ($n = 20$) and internally ($n = 16$) localized cells within VM organoids at day 90. Data represent mean ± SD, unpaired two-tailed *t*-test, $p = 0.0007$. Source data are provided as a Source Data file.

Studies on current organoid methods report that the increasing size of organoids can limit access to oxygen and nutrients in the inner layers, thereby affecting cell function and lifespan[12,47,48]. We found that while conventional and *silk* organoids had a similar volume (Fig. 7c), the volume of the immature core was smaller in *silk* organoids (Fig. 7d, e). Even when larger silk organoids were generated by proportionally increasing the number of cells and silk fibers, the core volume in each organoid remained small independent of the size of the individual organoid (Fig. 7c–e). By analyzing 2D sequential imaging of DAPI-stained sections, we observed the presence of porous microarchitectures in silk-engineered 3D structures (Fig. 7g) with an average cavity size of 3957 ± 817 µm^2, likely to promote an increase in oxygen and nutrients in the inner regions and thus reducing cell death. To test this hypothesis, we performed whole-organoid Western blot analysis of hypoxia-inducible factor-1 alpha (HIF-1α), a key oxygen-labile protein. We found that silk scaffolding led to attenuation of hypoxic response pathway (Fig. 7h), which also persisted when *silk*-lam VM organoids were cultured for the first few hours under low oxygen tension (1%) in a gas-controlled chamber (Fig. 7i). Analysis based on scRNAseq showed that the global level of

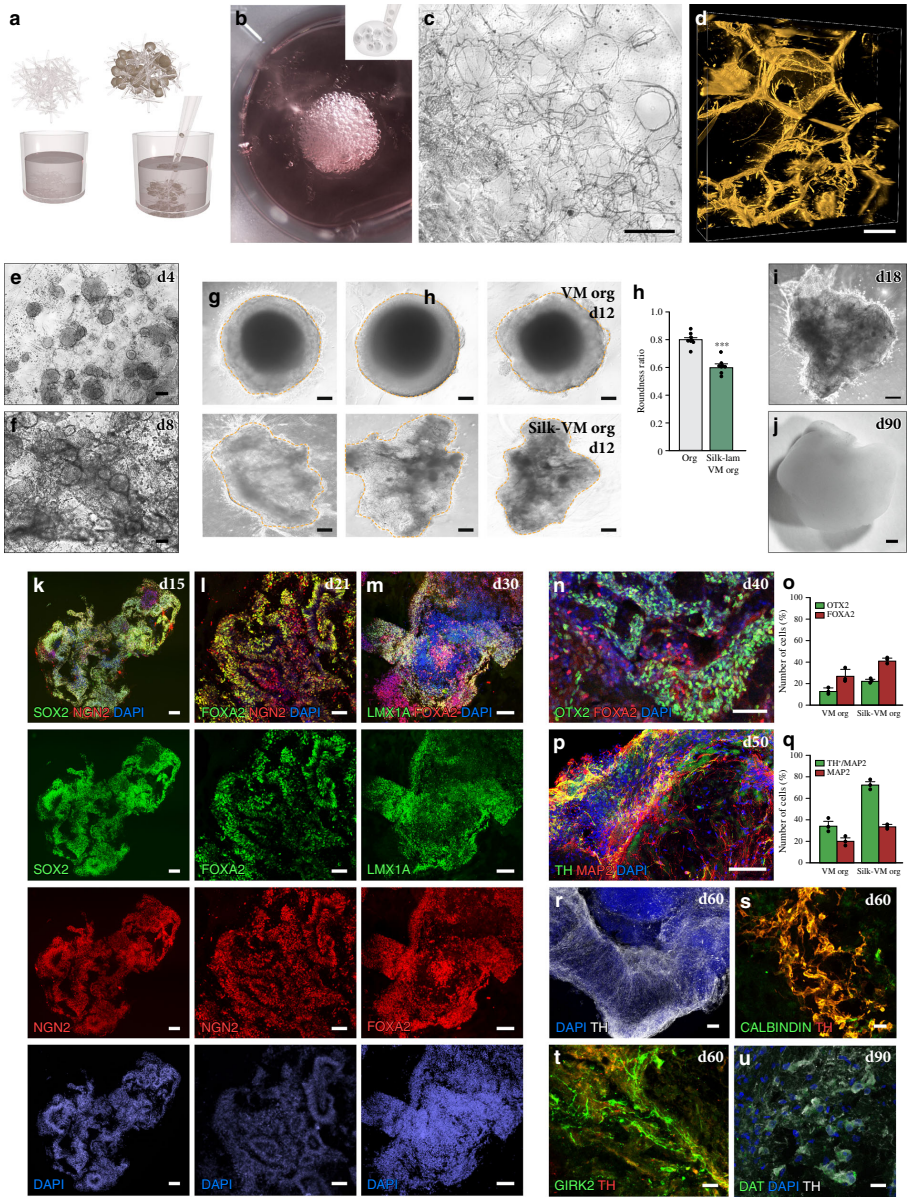

stress-response signaling in DA neurons is lower in silk than in conventionally generated VM organoids (Fig. 7j), as is the expression of individual genes associated with metabolic dysfunctions including glycolysis, oxidative stress and DNA damage (Fig. 7k). In agreement with this finding, decreased interior cell death was also observed in *silk*-lam VM organoids (Fig. 7l–q).

Furthermore, the increased homogeneity, decreased cell death, and increased oxygen diffusion within the silk organoids resulted in mature and functional DA neurons in all regions of the organoid as assessed using whole-cell patch-clamp recordings from the outer and inner regions of the *silk*-VM organoids. This analysis revealed that in contrast to conventionally generated VM organoids, cells in the inner core of silk 3D culture also exhibited

Fig. 5 Generation and characterization of *silk*-VM organoids. a Schematic representation of *silk*-VM organoid generation. **b** Representative image of cells dispersed throughout silk foam. **c** Bright-field and **d** confocal images of 3D silk scaffold after reabsorption of foam. Scale bars, 50 µm. **e**, **f** Bright-field images showing adherence and growth of cells along the length of silk microfibers at days 4 and 8. Scale bars, 200 µm. **g** Representative bright-field images, and **h**, roundness measurement of VM organoids grown with and without scaffold at day 12. Scale bars, 100 µm. Data represent mean ± SEM of 8 biologically independent organoids, two-tailed Mann–Whitney test, $^{***}p < 0.0001$. **i** Representative bright-field images of a short-term and, **j**, long-term *silk*-VM organoid culture. Scale bar, 200 µm. **k** Immunohistochemistry of SOX2/NGN2 from organoid at day 15 and **l–n** FOXA2 across a time course from day 21 to 40, stained with NGN2 (**l**), LMX1A (**m**), and OTX2 (**n**). Scale bars, 100 µm (**l**, **n**) and 50 µm (**k**, **m**). **o** Quantifications of $OTX2^+$ and $FOXA2^+$ cells in VM and *silk*-VM organoids. Data represent mean ± SEM obtained from 3 independent organoids. **p** Immunohistochemistry of TH and MAP2 and **q**, quantifications of MAP2 and TH/MAP2 in VM and *silk*-VM organoids at day 50. Data represent mean ± SEM obtained from 3 independent organoids per condition. Scale bars, 100 µm. **r** Immunohistochemistry of TH and **s, t** with CALB1/GIRK2 at day 60. Scale bars, 20 µm. **u** Immunohistochemistry of TH stained with DAT at day 90. Scale bars, 20 µm. Nuclei were stained with DAPI in **j–l**, **m**, **o**, **q** and **t**. Source data are provided as a Source Data file.

inward Na^+ and outward K^+ currents, confirming expression of voltage-gated sodium and potassium channels and a mature neuronal phenotype ($n = 20$ cells, inner; $n = 19$ cells, outer) (Fig. 8a–l and Supplementary Fig. 9e, f). Moreover, cells in both the core and outer layers of *silk*-lam VM organoids revealed mature electrophysiological properties of DA neurons with the presence of induced APs as well as spontaneous firing and rebound depolarization (Fig. 8b–e, h–k and Supplementary Fig. 9e, f). In addition, calcium imaging of MAP2–GcaMP5-labeled neurons indicated active neuronal signaling, confirming that mature and functional DA networks were present in silk-VM organoids (Fig. 8m, n). Finally, we performed real-time chronoamperometric measurements of DA exocytosis using a carbon-coated fiber (200 µm diameter) as a working electrode in a three-electrode electrochemical setup (Fig. 8o, p)[49]. Although DA release confirmed the high maturation and functionality of DA neurons in conventionally generated organoids, a lower proportion of the recordings showed a release of DA than in *silk*-lam VM organoids (Fig. 8q). Thus, although the quality of individual DA neurons generated in 3D organoids is comparable in conventional and silk organoids, the silk-based tissue engineering technology is more robust and results in better DA patterning with less variation within and between organoids.

Discussion

We used VM organoids derived from pluripotent stem cells to perform a time course transcriptional analysis of human VM development and human DA neuron differentiation at single-cell level. This allowed us to (i) determine cellular composition, (ii) deduce the timing of cell-type appearance during organoid maturation, and (iii) trace developmental trajectories. We also more closely dissected the DA neuron cluster (14,606 cells), which led to the identification of three molecularly distinct subgroups of mature human DA neurons.

We used ventralizing and caudalizing factors known to direct a VM identity in 2D culture[28,29] and to result in the formation of functional DA neurons after transplantation in preclinical rat models of PD[50,51]. A subset of these factors was previously used to generate similar midbrain-patterned organoids derived from hPSCs[15–17] and other studies report VM organoids derived from neural progenitors[19–21]. Together, these reports show that it is possible to form and maintain DA neurons with mature functional properties for extended periods in 3D culture, and midbrain-patterned organoids have now started to be used for developmental studies, disease modeling, and high-throughput screening[18,20].

In this study, we performed single cell transcriptional profiling of over 120,000 cells at different time points and produced a comprehensive map of cell type composition in VM organoids. This type of large-scale transcriptional mapping at single cell level has previously been performed in cerebral organoids, identifying a large diversity of neuronal cell types expressing both markers of multiple brain regions including forebrain, midbrain, hindbrain, and retina, as well as long-term excitatory/inhibitory neuronal identities[9,52]. Our analysis revealed that VM organoids have a more restricted repertoire of cell types, and that the composition is analogous to that observed in DAergic transplants from similarly patterned hPSCs, as previously described[53]. In addition, comparison of our single cell dataset with findings reported in adult human midbrain shows a high similarity between all mature cell types (neurons, astrocytes, and OPCS) within VM organoids and those present in human SNc, confirming the successful regionalization in vitro[22] and supporting the use of midbrain organoids in developmental studies and in the therapeutic development.

The clear temporal appearance of different cell types, with FP-like cells being the dominant cell type at early time points followed by generation of DA neurons and subsequently development of astrocytes, OPCs, and VLMCs, enabled us to perform a detailed analysis of cell lineage using force-directed *k*-nearest-neighbor graph-based pseudotime trajectory to predict the future cellular states in each cluster. The readout of this analysis points to the fact that cells with an FP-like transcriptional profile serve as a common progenitor for all mature cell types arising in VM organoids. Further, the expression in both DA neuron and VLMC clusters of NR4A2 and SOX6, known to exert a critical role in the specification and maturation of DA phenotype, suggests that lineage segregation is a relatively late event during DA neurogenesis.

DA neurons in adult VM are traditionally divided into two main subtypes based on anatomical landmarks: A9 neurons located in SNc with projections into the dorsolateral striatum, and A10 neurons located in the ventral tegmental area (VTA) with more widespread projections including nucleus accumbens, septum, and prefrontal cortex[54,55]. Recent investigations at single cell level in mouse VM revealed a greater-than-expected molecular diversity in midbrain DA neurons[23,24,35], but similar studies of human DA neurons are lacking. Previously, such a detailed analysis has not been possible using existing datasets from human midbrain[22,35] due to the low number of mature DA neurons captured. To date, no scRNAseq data set from midbrain organoids obtained from pluripotent stem cells exists, and only one scRNA-seq analysis into neural progenitor-derived VM organoids is available in the literature[21]. This dataset[21] describes a similar cell type composition to the one we identified in hPSC-derived VM organoids but did not analyze enough DA neurons or perform the late-stage profiling needed to define molecularly distinct DA neuron subtypes. The emergence of functionally mature DA neurons in high numbers within our VM patterned organoids derived using a protocol known to result in authentic and functional DA neurons capable of mediating functional recovery and circuitry reconstruction after transplantation in rat models of PD[28,50,51], thus uniquely enabled a molecular analysis at single cell level in order to map human DA neuron diversity. By

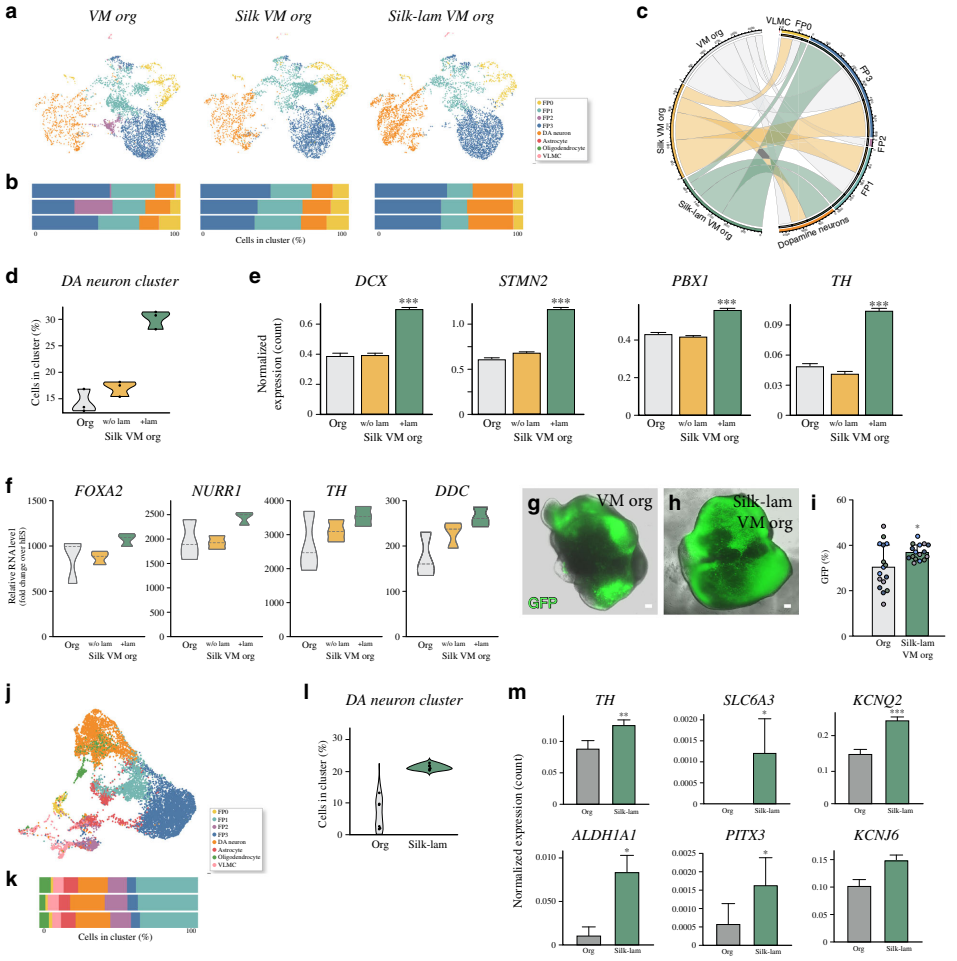

Fig. 6 Single-cell transcriptomics identifying *silk*-VM organoid cell composition. a UMAP plots showing cell clusters from conventional VM, *silk*-VM, and *silk*-lam VM organoids and **b**, percentage of cells belonging to each cell cluster from individual organoids at month 1. **c** Chord diagram visualizing cell-type interrelationships between conventional, *silk*-VM and *silk*-lam VM organoids. **d** Violin plot showing the percentage of cells belonging to DA neuron clusters from conventional, *silk*-VM, and *silk*-lam VM organoids at month 1 from three individual organoids per condition. **e** Expression of selected markers belonging to DA neuron cluster in conventional, *silk*-VM, and *silk*-lam VM organoids at 1 month. Data represent mean ± SEM of 3 biologically independent organoids, two-tailed Wilcoxon Rank Sum test, ***$p < 0.0001$. **f** qRT-PCR analysis of early and late DA neuron markers in conventional and *silk/silk*-lam VM individual organoids at month 2. Data represent mean ± SEM of 3 independent organoids per condition. **g**, **h** Representative images of GFP expression in conventional and *silk*-lam VM organoids differentiated from the CRISPR/Cas9-mediated gene-edited *TH*-Cre hPSC line. Scale bars, 100 µm. **i** FACS-based quantification of GFP expression in conventional and *silk*-lam VM organoids differentiated from a CRISPR/Cas9-mediated gene-edited *TH*-Cre hPSC line in 4 biologically independent experiments shown as color-coded dots (green, light blue, blue and purple). Data represent mean ± SD, two-tailed unpaired *t* test $p = 0.0162$. **j** UMAP plot showing cell clusters from *silk*-lam VM organoids and **k**, percentage of cells belonging to each cell cluster from individual organoids at month 4. **l** Violin plot of percentage of cells belonging to DA neuron cluster from conventional and *silk*-lam VM organoids at month 4 from three individual organoids. **m** Expression of selected markers belonging to DA neuron cluster in conventional and *silk*-lam VM organoids at month 4. Data represent mean ± SEM of 3 biologically independent organoids, two-tailed Wilcoxon Rank Sum test, TH $p = 0.0045$, SLC6A3 $p = 0.010462$, KCNQ2 $p = 0.0007$, ALDH1A1 $p = 0.046$. Source data are provided as a Source Data file.

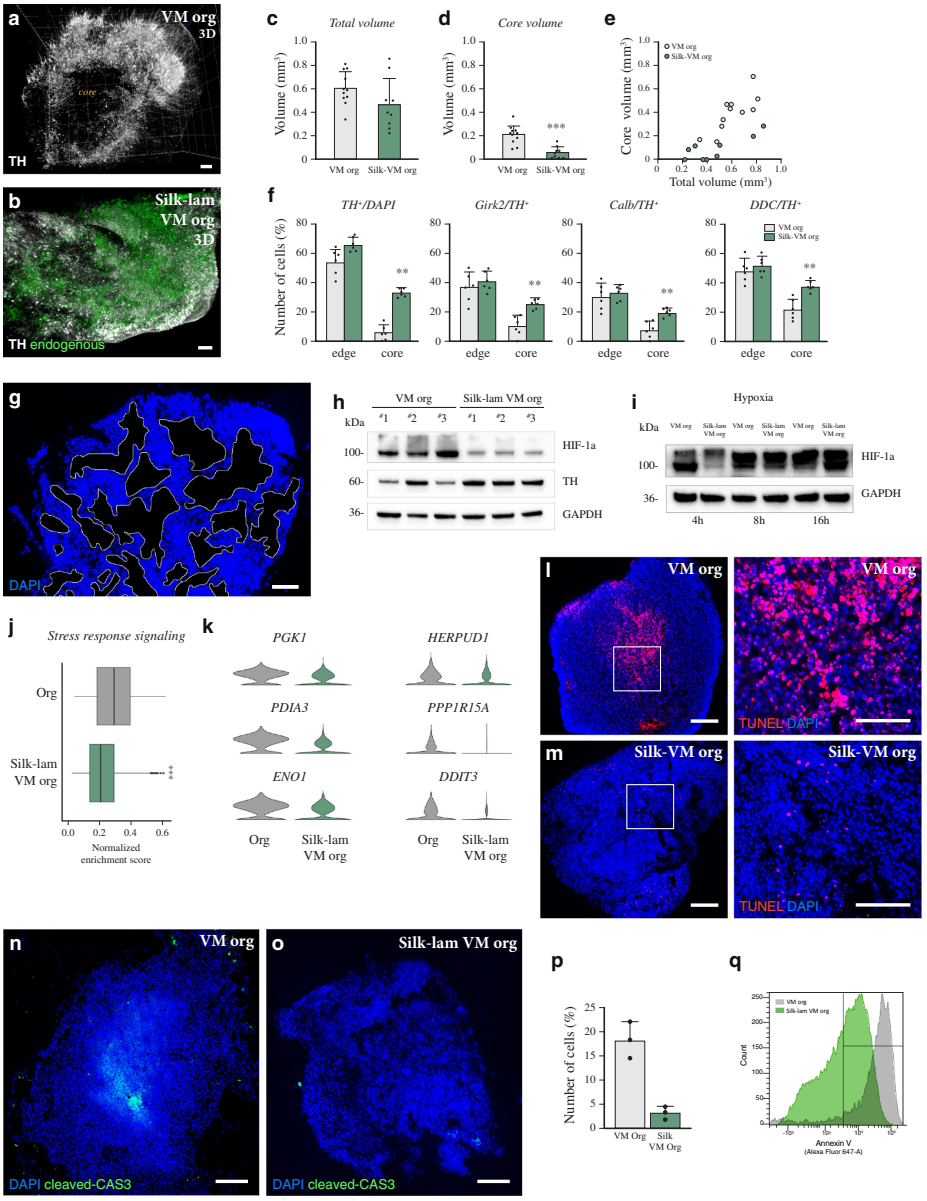

performing an unbiased and comprehensive characterization of the mature DA cluster we identified three molecularly distinct subtypes (DA^{L-1}, DA^{L-2}, and DA^{L-3}). These separate DA clusters showed several points of similarity with previously published datasets from bulk and single cell mouse VM DA neuron populations[36]. We also identified a set of genes in VM organoids which may define similar DA neuron subtypes in both mouse and human. Our data suggest that DA^{L-1}, which mainly expresses *SLC6A3*, *KCNJ6*, and *SNCG*, corresponds to two DA groups (T-Dat^{high} and AT-Dat^{high}) reported to express high levels of DAT by Tiklova et al. and to another DA cluster (DA^{1}) identified in adult mouse brain by Poulin and colleagues. *ANXA1*, which was found enriched together with *SLC6A3* and *MCP1* in our DA^{L-2} cluster, was used as a marker to distinguish SNc from VTA and

Fig. 7 *Silk* fibers result in more homogeneous VM organoids. a iDISCO circuitry reconstruction obtained by mapping TH in conventional and **b** *silk*-lam VM organoids at day 60. Scale bar, 100 µm. **c** iDISCO-based total volume quantification and **d**, **e** core quantification of conventionally and *silk*-lam-generated VM organoids. Data represent mean ± SEM obtained from 11 and 9 independent conventionally and *silk*-lam-generated VM organoids respectively, two-tailed Mann–Whitney test, $p = 0.0002$. **f** Percentages of TH^+, $GIRK2^+$, $CALB^+$, and DDC^+ expressing cells located in the outer and inner layers in conventionally and *silk*-lam-generated VM organoids. Data represent mean ± SEM obtained from 6 biologically independent organoids per condition, two-tailed Mann–Whitney test, $p = 0.002$. **g** Immunohistochemistry showing microporous dimension. Scale bars 100 µm. **h** Representative Western blots of HIF-1α protein and TH expression in conventional and *silk*-lam VM organoids in normoxia conditions (21% O2). GAPDH was used as loading control. **i** Representative Western blots of HIF-1α protein in conventional and *silk*-lam VM organoids across a time course of 4 h, 8 h and 16 h under hypoxia conditions (<1% O2). GAPDH was used as loading control. **j** Gene Set Enrichment Analysis of Stress response signaling. Lower and upper hinges correspond to the first and third quartiles and the whisker extends from the hinge to the largest value no further than |1.5 * IQR | from the hinge (where IQR is the interquartile range, or distance between the first and third quartiles); two-tailed Wilcoxon Rank Sum test, $^{***}p < 0.0001$. **k** Representative markers of metabolic stress of DA neurons in VM organoids grown with and without scaffold at 4 months. **l**, **m** TUNEL staining of VM organoids grown with and without scaffold at 6 months. Scale bars, 100 µm. **n**, **o** Immunohistochemistry of cleaved caspase-3 and, **p** quantification of cleaved CAS3 over DAPI performed on conventional and *silk*-lam VM organoids at 6 months. Scale bars 100 µm. Data represent mean ± SEM of 6 biologically independent VM organoids per condition, two-tailed unpaired *t*-test, $p = 0.0028$. **q** FACS analysis for fluorescence intensity of Annexin-V staining in conventionally and silk-lam-generated VM organoids. Representative FACS plots of biological triplicates are shown. Nuclei were stained with DAPI in **g**, **j**. Source data are provided as a Source Data file.

to identify different SNc subpopulations during mouse VM development[25,37,38]. D^{L-3}, characterized by *CALB*, *OTX2*, *LMO3*, and *SOX6* expression, seems to resemble other clusters, DA^{2B} and mDA2, previously described in two mouse studies by Poulin et al. and La Manno et al., respectively.

Our datasets provide insights into early fundamental regulators involved in molecular mechanisms that may play an important role in driving segregation of different mature DA neuron subtypes. A greater understanding of how subidentity is established could lead to the design of more targeted and effective DA neuron differentiation strategies, with implications for stem-cell-based therapies and disease modeling in PD. However, current organoid studies are often hampered by problems of reproducibility within and between organoids, as well as incomplete maturation resulting from interior hypoxia and the emergence of an immature or necrotic inner core[41]. Such issues were also observed in our study and in previous reports of VM organoids[15,19]. Inter-organoid variability can be partially reduced by more precise patterning[20], careful titration of the initial cell number[7], starting with neural progenitor cells rather than pluripotent cells[19], the adoption of scalable and automated culture systems[20, 16], or the use of scaffolds to guide self-organization[41].

Bioengineering efforts to generate more homogeneous organoids with viable and mature cells in all regions are actively being pursued. Recent findings describe two very different strategies, one based on the creation of a 2D scaffold using individual inert microfilaments to guide the self-organization of hPSCs into organoids with more reproducible neuroectoderm features[41] and the other using biomaterials such as hydrogels, which support bioengineered 3D neural cultures by mimicking the native brain extracellular matrix[56,57]. Exogenous vascularization in human organoids can also be achieved either by transplanting human organoids into a physiological environment in mouse brain[58] and ectopically expressing genes to induce a vascular-like structure[59], or by coculturing with endothelial cells[60]. These approaches at least partly address issues of reproducibility and maturation, but with limited experimental control. Moreover, the in vivo model of vascularized human brain organoids limits their use in large-scale biomedical applications such as drug screening, and the coculture or genetic induction of vessels may affect the directed differentiation of hPSCs necessary to obtain organoids of a specific brain region.

In this study, we used recombinant spider-silk microfibers that provide an easily accessible in vitro platform to generate bioengineered VM organoids, which we termed *silk*-VM organoids. These spider-silk microfibers present several advantages over existing methods using inert fibers. *First*, they are a recombinant chemically defined biomaterial that creates a strong, elastic, and biocompatible 3D scaffold able to guide the self-assembly of hPSCs into complex tissue-specific structures. *Second*, they can be easily functionalized with bioactive molecules that favor cell adhesion or control patterning. *Third*, they have the dual capacity to serve as both an anchored scaffold during early and a floating scaffold during late stages of organoid differentiation, allowing precise control of the ratio between cell density and number of fibers, thus decreasing variation between organoids. *Fourth*, silk scaffolds form porous microarchitectures, creating more favorable growth and differentiation conditions by allowing for the diffusion of oxygen and extrinsic patterning factors into the core, thereby reducing necrosis, reducing metabolic stress, and supporting neuronal maturation in all regions of the organoid.

Silk-VM organoids reproduce key molecular aspects of DA neurogenesis with a similar developmental progression pattern as conventionally generated organoids. The DAergic patterning in *silk*-VM organoids was further enhanced when functionalized with Lam-111. In addition, silk fibers sustain the homogeneous and functional generation of DA neurons throughout all compartments of the organoid in a highly efficient manner. Reduction of the necrotic core was previously achieved by mechanical cutting and generation of sliced human cortical organoid cultures to prevent hypoxia and cell death in the core[12], or by engineering smaller organoids[16,20,59]. Unlike mechanically sliced organoids[12], *silk*-VM organoids are preserved in size and shape, thereby more likely to maintain functional properties as well as the intricacy of neuronal networks. The remarkable properties of silk scaffolds combined with their straightforward use requiring no specialized equipment thus provide an easily accessible in vitro methodological platform able to generate organoids in a reproducible and functional manner.

Methods

hPSC culture and 2D differentiation. Undifferentiated RC17 (Roslin Cells, cat. no. hPSCreg RCe021-A), H9 (WiCell, cat. no. hPSCreg WAe009-A), HS999 and HS1001 (kindly provided by the Karolinska Institute), and *TH*-Cre hPSC cells were maintained on 0.5 µg/cm2 Lam-521 (BioLamina, #LN-521)-coated plates in iPS Brew medium (Miltenyi, #130-104-368) and were differentiated into 2D VM-patterned progenitors using our GMP-grade protocol[14]. All procedures were in accordance with the European Union directive and approved by the local ethical committee at Lund University.

Human brain organoid culture. To start 3D VM organoid differentiation, RC17, H9, HS999, HS1001, and *TH*-Cre hPSC cells were detached from the culture dish with 0.5 mM Accutase (Thermo Fisher Scientific, #A1110501) to yield a single cell

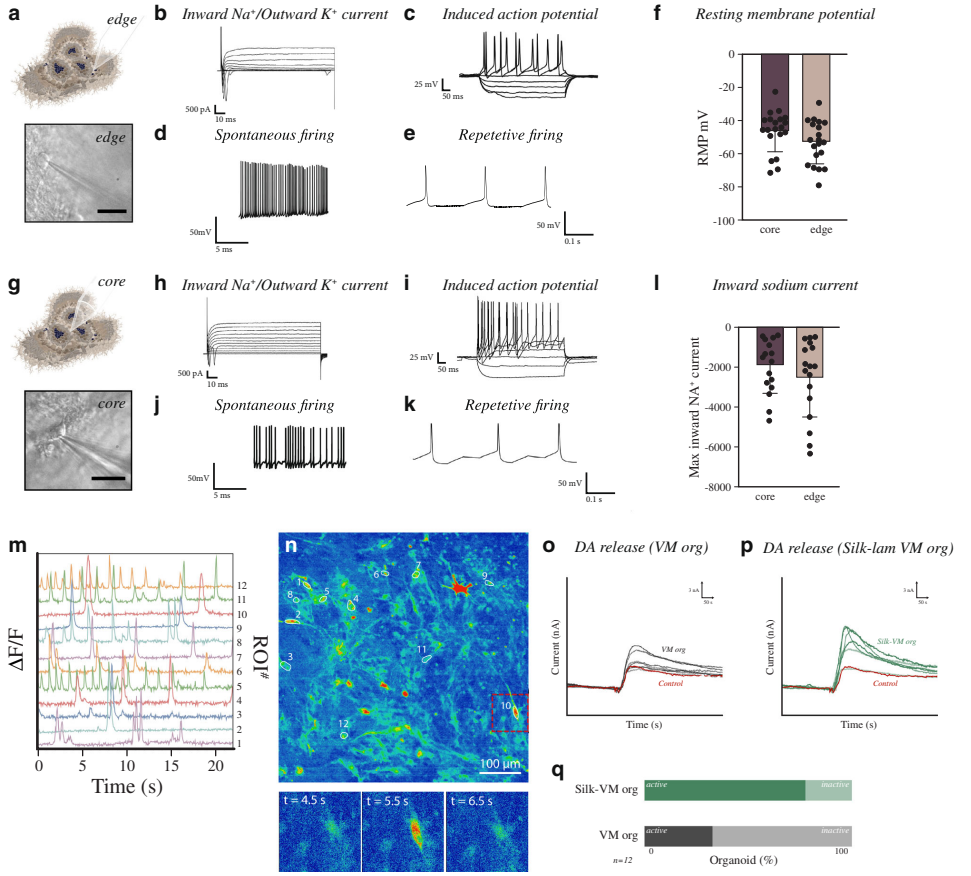

Fig. 8 *Silk*-VM organoids are functionally homogeneous. a Representative images of functional recordings from the external part using whole-cell patch-clamp technique. Scale bars, 100 µm. **b** Representative inward sodium- and outward potassium-rectifying current trace of external VM organoid at day 90 triggered by stepwise depolarization. **c** Whole-cell patch-clamp recordings of external VM organoid cells depicting current-induced APs at day 90 (−85 pA to +165 pA with 20 pA steps). **d** Spontaneous firings at resting membrane potential indicative of mature DA neuronal physiology in *silk*-lam VM organoids in the external part at day 90. **e** Example trace of rebound depolarization after brief membrane depolarization (20 pA) indicative of DA phenotype in externally located cells. **f** Resting-membrane quantifications between externally ($n = 20$) and internally localized cells ($n = 20$) in VM organoids at day 90. Data represent mean ± SD. **g** Representative images of functional recordings from the internal region of organoid using whole-cell patch-clamp technique. Scale bars, 100 µm. **h** Representative internal inward sodium- and outward potassium-rectifying current trace of VM organoid at day 90 triggered by stepwise depolarization **i**, Whole-cell patch-clamp recordings in internal region of VM organoid cells depicting current-induced APs at day 90 (−85 pA to +165 pA with 20 pA steps). **j** Spontaneous firings at resting-membrane potential indicative of mature DA neuronal physiology in the internal region of *silk*-lam VM organoids at day 90. **k** Example trace of rebound depolarization after brief membrane depolarization (20 pA) indicative of DA phenotype in internally located cells. **l** Quantification of maximum inward sodium current recorded in internal ($n = 16$ cells) and external ($n = 17$ cells) regions. Data represent mean ± SD. **m** Differential fluorescence-intensity profile of intracellular Ca^{+} levels as a function of time in neurons expressing MAP2-GCamP5 at day 90. **n** Fluorescence image with marked regions of interest corresponding to recorded cells and three timeframes displaying the change in intracellular fluorescence intensity. Scale bar, 100 µm. **o**, **p** Representative analysis of real-time DA release chronoamperometric measurements in conventional and *silk*-lam VM organoids and **q**, relative quantification ($n = 12$).

suspension. Differentiation was initiated by plating 2500 single cells in each well of a 96-well U-bottom plate (Corning, #CLS7007) in iPS Brew with 10 µM Y-27632 dihydrochloride (Miltenyi, #130-106-538), as previously described[27]. After three days in culture, embryoid bodies were transferred to differentiation medium consisting of 1:1 DMEM/F12:Neurobasal medium (Thermo Fisher Scientific, #21331020 and #A1371201), 1:100 N2 supplement (Thermo Fisher Scientific, #A1370701), 10 µM SB431542 (Miltenyi, #130-106-543), 150 ng/ml rhNoggin (Miltenyi, #130-103-456), 400 ng/ml SHH-C24II (Miltenyi, #130-095-727), and 1.5 µM CHIR99021 (Miltenyi, #130-106-539), and in the presence of 200 mM L-glutamine (Thermo Fisher Scientific, #25030081) and 10,000 U/mL penicillin-streptomycin (Thermo Fisher Scientific, #15140122). About 1% minimum essential medium nonessential amino acids (MEM-NEAA, Sigma-Aldrich, #M7145) and 0.1% 2-mercaptoethanol (Merck, #8057400005) were maintained for the entire differentiation period. On day 11, developing VM organoids were transferred to a

24-well plate containing 1:50 Neurobasal medium, B27 supplement without vitamin A (Thermo Fisher Scientific, #12587010), and 100 ng/mL FGF-8b (Miltenyi, #130-095-740). On day 14, 20 ng/mL BDNF (Miltenyi, #130-096-286) and 200 µM L-Ascorbic acid (Sigma-Aldrich, #A4403-100MG) were added. At this point, VM organoids were embedded in 30 µL droplets of Matrigel (BD Biosciences), as previously described[27]. From day 16 onward, 0.5 mM db-cAMP (Sigma-Aldrich, #D0627-1G) and 1 µM DAPT (R&D Systems, #2634) were added to the culture medium for terminal maturation for up to four months.

We define a batch of organoids as all organoids established at the same time and in the same dish.

Two additional midbrain-patterned organoids were also generated according to previously published protocols. Midbrain-like organoids (MLOs) were grown in tissue growth induction medium containing midbrain-patterning factors, as described in Jo et al.[15]. Midbrain organoids (MOs) were cultured with the addition of 2 µM dorsomorphin (Sigma), 2 µM A83-01 (Peprotech), 3 µM CHIR99021 (Miltenyi), and 1 µM IWP2 (Biogems), as reported by Kwak et al.[17]. Forebrain organoids were also generated using a whole organoid differentiation protocol[27].

Human embryonic tissue source. Human fetal tissue from legally terminated embryos was collected in accordance with existing guidelines with approval of the Swedish National Board of Health and Welfare and informed consent from women seeking elective abortions. To determine the gestational age of the embryos, the crown-to-rump length was measured and the embryo was staged according to week post conception.

Hypoxic conditions. Both conventional and *silk*-VM organoids were cultured at 37 °C in 21% O_2 and 5% CO_2 in normoxia conditions. For hypoxia analysis, VM organoids were transferred to the hypoxia chamber (Binder CB160), which was filled with 1% O_2 and 5% CO_2 and mixed with N_2, and collected after 4, 8, and 16 h.

Cell-viability analysis. Cell viability was measured using the colorimetric CyQuant cell proliferation assay (Invitrogen), following the manufacturer's instructions. Absorbance was analyzed at 480–520 nm, using 50,000 cells harvested from whole conventional and *silk*-VM organoids. Each organoid was analyzed in 6 replicates (i.e., 300 000 cells from each organoid) using Biochrom Asys Expert 96 Microplate Reader (Biochrom). Apoptosis was detected via flow cytometry after staining using the Alexa Fluor 647 Annexin V conjugate (BD Pharmingen, #A23204) and Click-iT plus Tunel assay (Invitrogen #C10617) according to the manufacturer's instructions.

Silk-scaffold preparation and hPSC integration. A 20 µL droplet of Biosilk protein solution (BioLamina, #BS-0101) either alone or functionalized with Lam-111 (BioLamina, #LN111), was placed in the center of hydrophobic culture wells in a 24-well plate (Sarstedt, #833922500). Recombinant human laminin-111 was purchased from Biolamina (Sweden) and added to the silk protein solution at a final concentration of 10 µg ml−1. The FN-silk/LN-111 mixture was incubated 10 min at RT before usage. About 10 µM Y-27632 dihydrochloride was added[44]. Air bubbles were introduced into the droplet by pipetting up and down (10–15 strokes), creating a dense foam. Multiple foams are generated in series with uniform shape and size (Supplementary Fig. 7b). Foam can also assume different dimension by increasing/reducing the volume of silk droplet giving rise to different organoid size in culture. RC17, H9, and HS1001 hPSCs were detached from the culture dish with 0.5 mM Accutase (Thermo Fisher Scientific, #A1110501) and prepared as a concentrated single cell suspension (20,000 cells/µL in iPS Brew medium). A total of 80,000 cells from the cell suspension were added to the silk foam and dispersed throughout by 6–8 additional pipette strokes[61]. The interaction between cells and silk microfibers was stabilized at 37 °C in an incubator for 20 min. Prewarmed iPS Brew medium containing 10 µM Y-27632 dihydrochloride was added to the foam-integrated cells.

Silk-bioengineered VM organoid generation and morphological characterization. After three days, differentiation medium consisting of 1:1 DMEM/F12:Neurobasal medium, 1:100 N2 supplement, 10 µM SB431542, 150 ng/mL rhNoggin, 400 ng/mL SHH-C24II, and 1.5 µM CHIR99021 was added from day 0 to 10, following the same protocol used for generating conventional VM organoids. At day 10, the resulting 3D structures were mechanically detached from the bottom of the plate with a spatula and transferred to a 6-well plate (Corning, #3471) and grown in suspension (free floating). *Silk*-VM organoids were embedded in 30 µL droplets of Matrigel and cultured following the VM organoid-differentiation protocol described in the subsection "hPSC VM organoid differentiation". Images were collected on phase-contrast inverted microscope (Olympus, #CKX31SF). Morphological classification (spherical/nonspherical) was performed in triplicate. Roundness measurements were based on bright-field images and calculated as the ratio between diameters of the largest inscribed and the smallest circumscribed circle of the organoid silhouettes (dotted line). Images were analyzed in ImageJ (NIH).

Library preparation, sequencing, and raw data processing. For 10x Genomics single-cell RNA sequencing, single-cell suspensions were loaded onto 10x Genomics Single Cell 3′ Chips along with the mastermix as per the manufacturer's protocol (https://support.10xgenomics.com/single-cell-gene-expression/index/doc/technical-note-chromium-single-cell-3-v3-reagent-workflow-and-software-updates) for the Chromium Single Cell 3′ Library to generate single cell gel beads in emulsion (GEMs, version 3 chemistry). The resulting libraries were sequenced on either a NextSeq500 or a NovaSeq 6000 with the following specifications Read1 28 cycles, Read2 98 cycles, and Index1 8 cycles using a 200-cycle kit. Raw base calls were demultiplexed and converted fastq files using cellranger mkfastq program (bcl2fastq 2.19/cellranger 3.0). Sequencing data were first preprocessed through the Cell Ranger pipeline (10x Genomics, Cellranger count v2) with default parameters (expect-cells set to the number of cells added to 10x system), aligned to GrCH38 (v 3.1.0), and the resulting matrix files were used for subsequent bioinformatic analysis.

Bioinformatics analysis of sequencing data. Seurat (v 3.1 and R version 3.6.1) was applied to the scRNA data for downstream analysis of matrix files. Cells with at least 600 but no more than 12000 genes detected were kept for analysis. In addition, cells with more than 20% mitochondrial reads were excluded. After log-transformation, 4000 highly variable genes were identified using vst and z-transformed expression values followed by dimensionality reduction (PCA). To integrate data from different 10x runs, Harmony was applied using the R-package "Harmony" using individual 10X runs as grouping variable. Harmony converged after 9 iterations and corrected coordinates were used for downstream analysis. To identify clusters, Louvain clustering (resolution 0.4, Seurat) was applied to harmony embeddings. Differential expression analysis between clusters was carried out using the Wilcoxon rank sum test (Seurat) with genes with a FDR-adjusted p-value < 0.05 considered significant. Gene ontology overrepresentation analysis was performed using the enrichGO function in the clusterProfiler package (3.13) using MSigDB as the database. Gene Set Enrichment Analysis was performed using the R package escape https://www.nature.com/articles/s42003-020-01625-6. For silhouette and tree analysis the cluster package (version 2.1) was used. Lineage inference and pseudotime reconstruction was performed using Slingshot (version 1.6.1). We first used the expression data from 4000top variable genes to generate the minimum spanning tree of cells in a reduced-dimensionality space (Harmony-corrected UMAP embeddings). Global lineage structure was identified with a cluster-based minimum spanning tree and fitting simultaneous principal curves describing each lineage using "slingshot" function. Pseudotime analysis was also performed using a force-directed layout of k-nearest-neighbor graphs (SPRING, http://pubmed.ncbi.nlm.nih.gov/29228172/) on normalized expression counts using default settings.

qRT-PCR. Total RNAs were isolated using the RNeasy Micro Kit (QIAGEN#74004) and reverse transcribed using random hexamer primers and Maxima Reverse Transcriptase (Thermo Fisher #K1642, Invitrogen). cDNA was prepared together with SYBR Green Master mix (Roche#04887352001) using the Bravo instrument (Agilent) and analyzed by quantitative PCR on a LightCycler 480 device using a 2-step protocol with a 60 °C annealing/elongation step. All quantitative RT-PCR (qRT-PCR) samples were run in technical triplicates and the results are given as fold change over undifferentiated hPSCs using each of the two housekeeping genes for normalization (ACTB and GAPDH). Details and list of primers are reported in Supplementary Table 1.

Organoid cryosectioning and immunofluorescence. Both conventional and *silk*-VM organoids were fixed in 4% paraformaldehyde for 5 h at 4 °C followed by washing in PBS three times for 10 min. Both conventional and *silk*-VM organoids were left to sink in 30% sucrose overnight. Sucrose solution was replaced with 1:1 OCT:30% sucrose mixture for 6 h and then transferred to a cryomold and filled with OCT. The embedded tissue was frozen on dry ice and either cryosectioned at 20 µM or stored at −80 °C. For immunohistochemistry, sections were washed in PBS1X for 10 min and then blocked and permeabilized in 0.3% Triton X-100 and 5% normal donkey serum in PBS1X. After incubation with primary antibodies, the sections were incubated for 1 h with the appropriate secondary antibodies (Alexa Fluor 488, 594, and 647 used at 1:400, Molecular Probes) and then mounted on gelatin-coated slides and coverslipped with PVA-DABCO containing DAPI (1:1000). A list of primary antibodies is reported in Supplementary Table 2.

Quantification of fluorescence for developmental layers identified was performed using Image J software (NIH, v1.49). Measurements were performed by taking a radial line-intensity profile (80 µm width) for each channel from the center of the organoid to the edge of the organoid, subtracting the background and recording the position where the positive signal begins and ends. Recordings were normalized to the length of the radial line and mean value with standard deviation plotted for each of three fluorescence channels.

Whole silk- and conventionally generated VM organoids were sequentially sectioned to obtain slices from edge to core. For quantifications, each section was quartered into 4 equal areas and then scanned using a confocal microscope under 20X magnification. The number of TH^+, $Calb^+$, $Girk2^+$, and DDC^+ cells was manually counted in each area using Image J software (NIH, v1.49), and summed

to give the total number of positive cells per slice. Counting was performed on every 3 sections and the final counts were corrected for the total number of sections per organoid.

Immunohistochemistry and neuromelanin staining. For diaminobenzidine (DAB) staining, the sections were incubated with secondary biotinylated horse antibodies diluted (1:200, Vector Laboratories) for 1 h at room temperature (RT), washed three times, and then incubated with avidin-biotin complex (ABC) for 1 h at RT for amplification. Peroxidase-driven precipitation of DAB was used to detect the primary antibody. In this step, the sections were incubated in 0.05% DAB for 1–2 min before addition of 0.01% H_2O_2 for a further 1–2 min. After development of DAB staining, the sections were placed in an ammoniacal silver solution to detect neuromelanin using a Masson Fontana Stain Kit (Atom Scientific, #RRSK12-100), according to the manufacturer's instructions. The sections were then mounted on gelatin-coated slides and dehydrated in an ascending series of alcohol concentrations cleared in xylene, and coverslipped with DPX mounting.

iDISCO. Both conventional and *silk*-VM organoids were fixed in 2% paraformaldehyde overnight at 4 °C and permeabilized in 0.2% Triton X-100 20% DMSO and then in 0.1% Triton X-100, 0.1% Tween20, 0.1% $C_{24}H_{39}NaO_4$, 0.1% NP40, and 20% DMSO overnight at 37 °C. After incubation with primary antibodies for 2 days at 37 °C, the organoids were incubated for 2 days with the appropriate secondary antibody, embedded in 1% agarose, and dehydrated in an ascending series of methanol concentrations and dichloromethane as previously described[62]. Samples were imaged in a chamber filled with DBE. The cleared brain organoids were imaged on an Ultra Microscope II (LaVision Biotec) equipped with an sCMOS camera (Andor Neo, model 5.5-CL3) and 12x objective lenses (LaVision LVMI-Fluor 4x/0.3 or 12x/0.53 MI Plan). We used two laser configurations with the following emission filters: 525/50 for endogenous background and AlexaFluor 488. Whole-organoid volumes were quantified based on endogenous background, and DA neuron number based on TH+ cell. Several stacks (mosaic acquisition) were taken with 10% overlap to cover the entire brain-organoid volume, including edge and core. Stacks were acquired with ImspectorPro64 (LaVision Biotec) using 3 µm z-steps to acquire the volume in 3D. These image stacks were stitched to visualize the brain organoid in 3D with Arivis Vision 4D 3.5.0 (Arivis AG). The high density of cells in the core volume, characterized by the absence of TH+ staining, was quantified based on 525/50 endogenous signal. Rendered movies were compiled in Final Cut Pro 10.4.3 (Apple Inc.).

Microscopy. Images were captured using an Epson Perfection V850 PRO flatbed scanner, a Leica DMI6000B widefield microscope, or a Leica TCS SP8 confocal laser-scanning microscope, or a Nikon inverted Ti2 microscope equipped with a CSU-W1 spinning-disk system. Image acquisition software was Leica LAS X and images were processed using Volocity 6.5.1 software (Quorum Technologies) and Adobe Photoshop. Any adjustments were applied equally across the entire image, and without the loss of any information.

Flow cytometry. *TH*-Cre hPSC-derived single-cell suspensions, differentiated either from conventional or *silk*-VM organoids, were obtained using the Papain Kit (Worthington, #LK003150). GFP^+ cells were analyzed with BD FACSAria III (BD Biosciences) and all data plots were generated using FlowJo software.

Western blotting. VM-organoid lysates were prepared with ice-cold immunoprecipitation assay (RIPA) lysis buffer. Whole-cell lysates were then separated on gels (Invitrogen, NuPAGE 4–12%) and transferred to a PVDF membrane (Millipore, Immobilon-P Membrane, 0.45 µM). Detection was performed with ECL reagents (Amersham Biosciences). Details and list of antibodies are reported in Supplementary Table 2.

Organoid-slice preparation and electrophysiology. About 3% low-melting-point agarose (Promega, #V2111) was dissolved and melted in Neurobasal medium at 37 °C and placed in a cubic PDMS mold (1 cm^2). At day 90, VM organoids were immersed and embedded in an agarose mold and left to solidify for 5–10 mins at RT. Sections of 400 µm thickness were prepared using a vibratome tissue slicer (Leica VT1000 S) at 0.1 mm/s speed and 1 mm vibration amplitude. Agarose blocks containing the VM-organoids were submerged in oxygenated artificial cerebrospinal fluid (ACSF) at 4 °C during the cutting procedure. VM organoid slices were equilibrated for 30 min in oxygenated ACSF at 37.5 °C prior to whole-cell patch clamp recordings [42].

Whole-cell patch-clamp electrophysiological recordings were performed at day 90 of VM organoid differentiation. Both conventional and *silk*-VM organoids were transferred to a recording chamber containing Krebs solution gassed with 95% O_2 and 5% CO_2 at RT and exchanged every 20 min during recordings. The standard solution was composed of (in mM) 119 NaCl, 2.5 KCl, 1.3 $MgSO_4$, 2.5 $CaCl_2$, 25 glucose, and 26 $NaHCO_3$. For recordings, a Multiclamp 700B Microelectrode Amplifier (Molecular Devices) was used together with borosilicate glass pipettes (3–7 MOhm) filled with the following intracellular solution (in mM): 122.5 potassium gluconate, 12.5 KCl, 0.2 EGTA, 10 HEPES, 2 MgATP, 0.3 Na_3GTP, and 8 NaCl adjusted to pH 7.3 with KOH, as previously described[29]. Data acquisition was performed with pCLAMP 10.2 software (Molecular Devices); current was filtered at 0.1 kHz and digitized at 2 kHz. Cells with neuronal morphology and round cell body were selected for recordings. Resting-membrane potentials were monitored immediately after breaking-in in current-clamp mode. Thereafter, cells were kept at a membrane potential of −60 mV to −80 mV, and 500 ms currents were injected from −85 pA to +165 pA with 20 pA increments to induce action potentials. For inward sodium and delayed rectifying potassium current measurements, cells were clamped at −70 mV and voltage-depolarizing steps were delivered for 100 ms at 10 mV increments. Spontaneous action potentials were recorded in current-clamp mode at resting membrane potentials.

Calcium imaging of MAP2-GCamP5-labeled neurons. Calcium imaging was performed at day 120 of VM cultures containing the MAP2-GCamP5 reporter. Imaging was performed on an inverted Ti2 microscope (Nikon) equipped with a CSU-W1 spinning-disc system (Yokogawa), a sCMOS camera (Teledyne Photometrics), and a 20 × objective. An environment control chamber was used to maintain the temperature at 37 °C and CO_2 level at 5% during imaging. Exposure time was set to 50 ms Spontaneous activity was recorded from 3 different silk-lam VM organoids. Images were analyzed in ImageJ (NIH).

Chronoamperometry. Three-electrode setup with a pyrolyzed carbon fiber as the working electrode was used to detect dopamine. Electrode fabrication, electrochemical characterization, and setup assembly were performed as previously described[49]. In short, to perform the measurements, an organoid was placed on the working electrode immersed in baseline buffer, a constant potential was applied, and the resulting current monitored. Dopamine release was chemically triggered through addition of stimulation buffer that elevated K+ concentration to 150 mM. Measured current was normalized to the baseline value and plotted with respect to time.

Statistics and reproducibility. Statistical analysis of qRT-PCR data and immunofluorescence-based quantifications was performed using two-tailed Student's *t*-test and *p*-values <0.05 were considered significant. For comparisons of electrophysiological properties, two-tailed Student's t-test and one-way analysis of variance (ANOVA) was used. Data were statistically analyzed with the GraphPad Prism 9 software and presented as mean ± SEM, except where stated otherwise. Statistical analysis of sequencing data was conducted using two-tailed Wilcoxon rank-sum test (Seurat v3.1) in R v3.6.1. Please refer to the bioinformatics analysis section above for more details. Immunohistochemical staining images are representative of 6–12 sections from at least 4 biologically independent organoids. Western blots are representative of 3 biological replicates.

Reporting summary. Further information on research design is available in the Nature Research Reporting Summary linked to this article.

Data availability

The scRNA-seq data generated in this study have been deposited in the Gene Expression Omnibus under accession code "GSE168323". A reporting summary for this article is available as Supplementary Information file. All other relevant data supporting the key findings of this study are available within the article and its Supplementary Information files or from the corresponding author upon reasonable request. Source data are provided with this paper.

Code availability

The code used for this paper is available on GitHub https://github.com/ParmarLab/scRNA-seq_silk_organoids with https://doi.org/10.5281/zenodo.5603294.

Received: 24 February 2021; Accepted: 9 November 2021;
Published online: 15 December 2021

References

1. Kelava, I. & Lancaster, M. A. Stem cell models of human brain development. *Cell Stem Cell* **18**, 736–748 (2016).
2. Rifes, P. et al. Publisher correction: modeling neural tube development by differentiation of human embryonic stem cells in a microfluidic WNT gradient. *Nat. Biotechnol.* **38**, 1357 (2020).
3. Demers, C. J. et al. Development-on-chip: in vitro neural tube patterning with a microfluidic device. *Development* **143**, 1884–1892 (2016).
4. Lancaster, M. A. et al. Cerebral organoids model human brain development and microcephaly. *Nature* **501**, 373–379 (2013).
5. Bagley, J. A. et al. Fused cerebral organoids model interactions between brain regions. *Nat. Methods* **14**, 743–751 (2017).

6. Fiorenzano, A. et al. Dopamine neuron diversity: recent advances and current challenges in human stem cell models and single cell sequencing. *Cells* **10**, 1366 (2021).
7. Quadrato, G. et al. Cell diversity and network dynamics in photosensitive human brain organoids. *Nature* **545**, 48–53 (2017).
8. Camp, J. G. et al. Human cerebral organoids recapitulate gene expression programs of fetal neocortex development. *Proc. Natl Acad. Sci. USA* **112**, 15672–15677 (2015).
9. Kanton, S. et al. Organoid single-cell genomic atlas uncovers human-specific features of brain development. *Nature* **574**, 418–422 (2019).
10. Qian, X., Song, H. & Ming, G. L. Brain organoids: advances, applications and challenges. *Development* **146**, dev166074 (2019).
11. Mansour, A. A., Schafer, S. T. & Gage, F. H. Cellular complexity in brain organoids: current progress and unsolved issues. *Semin Cell Dev. Biol.* **111**, 32–39 (2021).
12. Qian, X. et al. Sliced human cortical organoids for modeling distinct cortical layer formation. *Cell Stem Cell* **26**, 766–781 e9 (2020).
13. Bhaduri, A. et al. Cell stress in cortical organoids impairs molecular subtype specification. *Nature* **578**, 142–148 (2020).
14. Nolbrant, S. et al. Generation of high-purity human ventral midbrain dopaminergic progenitors for in vitro maturation and intracerebral transplantation. *Nat. Protoc.* **12**, 1962–1979 (2017).
15. Jo, J. et al. Midbrain-like organoids from human pluripotent stem cells contain functional dopaminergic and neuromelanin-producing neurons. *Cell Stem Cell* **19**, 248–257 (2016).
16. Qian, X. et al. Brain-region-specific organoids using mini-bioreactors for modeling ZIKV exposure. *Cell* **165**, 1238–1254 (2016).
17. Kwak, T. H. et al. Generation of homogeneous midbrain organoids with in vivo-like cellular composition facilitates neurotoxin-based Parkinson's disease modeling. *Stem Cells* **38**, 727–740 (2020).
18. Kim, H. et al. Modeling G2019S-LRRK2 sporadic Parkinson's disease in 3D midbrain organoids. *Stem Cell Rep.* **12**, 518–531 (2019).
19. Monzel, A. S. et al. Derivation of human midbrain-specific organoids from neuroepithelial stem cells. *Stem Cell Rep.* **8**, 1144–1154 (2017).
20. Renner, H. et al. A fully automated high-throughput workflow for 3D-based chemical screening in human midbrain organoids. *Elife* 2020. **9**.
21. Smits, L. M. et al. Single-cell transcriptomics reveals multiple neuronal cell types in human midbrain-specific organoids. *Cell Tissue Res.* **382**, 463–476 (2020).
22. Agarwal, D. et al. A single-cell atlas of the human substantia nigra reveals cell-specific pathways associated with neurological disorders. *Nat. Commun.* **11**, 4183 (2020).
23. Tiklova, K. et al. Single-cell RNA sequencing reveals midbrain dopamine neuron diversity emerging during mouse brain development. *Nat. Commun.* **10**, 1–12 (2019).
24. Poulin, J. F. et al. Defining midbrain dopaminergic neuron diversity by single-cell gene expression profiling. *Cell Rep.* **9**, 930–943 (2014).
25. Saunders, A. et al. Molecular diversity and specializations among the cells of the adult mouse brain. *Cell* **174**, 1015–1030 e16 (2018).
26. Birey, F. et al. Assembly of functionally integrated human forebrain spheroids. *Nature* **545**, 54–59 (2017).
27. Lancaster, M. A. & Knoblich, J. A. Generation of cerebral organoids from human pluripotent stem cells. *Nat. Protoc.* **9**, 2329–2340 (2014).
28. Kirkeby, A. et al. Predictive markers guide differentiation to improve graft outcome in clinical translation of hESC-based therapy for Parkinson's disease. *Cell Stem Cell* **20**, 135–148 (2017).
29. Nilsson, F. et al. Single-cell profiling of coding and noncoding genes in human dopamine neuron differentiation. *Cells* **10**, 137 (2021).
30. Elkabetz, Y. et al. Human ES cell-derived neural rosettes reveal a functionally distinct early neural stem cell stage. *Genes Dev.* **22**, 152–165 (2008).
31. Korsunsky, I. et al. Fast, sensitive and accurate integration of single-cell data with Harmony. *Nat. Methods* **16**, 1289–1296 (2019).
32. Ono, Y. et al. Differences in neurogenic potential in floor plate cells along an anteroposterior location: midbrain dopaminergic neurons originate from mesencephalic floor plate cells. *Development* **134**, 3213–3225 (2007).
33. Bonilla, S. et al. Identification of midbrain floor plate radial glia-like cells as dopaminergic progenitors. *Glia* **56**, 809–820 (2008).
34. Street, K. et al. Slingshot: cell lineage and pseudotime inference for single-cell transcriptomics. *BMC Genomics* **19**, 477 (2018).
35. La Manno, G. et al. Molecular diversity of midbrain development in mouse, human, and stem cells. *Cell* **167**, 566–580 e19 (2016).
36. Poulin, J. F. et al. Classification of midbrain dopamine neurons using single-cell gene expression profiling approaches. *Trends Neurosci.* **43**, 155–169 (2020).
37. Hook, P. W. et al. Single-Cell RNA-Seq of mouse dopaminergic neurons informs candidate gene selection for Sporadic Parkinson disease. *Am. J. Hum. Genet.* **102**, 427–446 (2018).
38. Kramer, D. J. et al. Combinatorial expression of Grp and Neurod6 defines dopamine neuron populations with distinct projection patterns and disease vulnerability. *eNeuro* 10.1523/ENEURO.0152-18.2018 (2018).
39. Panman, L. et al. Sox6 and Otx2 control the specification of substantia nigra and ventral tegmental area dopamine neurons. *Cell Rep.* **8**, 1018–1025 (2014).
40. Braskie, M. N. et al. Common Alzheimer's disease risk variant within the CLU gene affects white matter microstructure in young adults. *J. Neurosci.* **31**, 6764–6770 (2011).
41. Lancaster, M. A. et al. Guided self-organization and cortical plate formation in human brain organoids. *Nat. Biotechnol.* **35**, 659–666 (2017).
42. Wiley, L. A. et al. A method for sectioning and immunohistochemical analysis of stem cell-derived 3-D organoids. *Curr. Protoc. Stem Cell Biol.* **37**, 1C 19 1–1C 19 11 (2016).
43. Widhe, M., Shalaly, N. D. & Hedhammar, M. A fibronectin mimetic motif improves integrin mediated cell biding to recombinant spider silk matrices. *Biomaterials* **74**, 256–266 (2016).
44. Astrand, C. et al. Assembly of FN-silk with laminin-521 to integrate hPSCs into a three-dimensional culture for neural differentiation. *Biomater. Sci.* **8**, 2514–2525 (2020).
45. Stuart, T. et al. Comprehensive integration of single-cell data. *Cell* **177**, 1888–1902 e21 (2019).
46. Fiorenzano, A. et al. Evaluation of TH-Cre knock-in cell lines for detection and specific targeting of stem cell-derived dopaminergic neurons. *Heliyon* **7**, e06006 (2021).
47. Kadoshima, T. et al. Self-organization of axial polarity, inside-out layer pattern, and species-specific progenitor dynamics in human ES cell-derived neocortex. *Proc. Natl Acad. Sci. USA* **110**, 20284–20289 (2013).
48. Pasca, A. M. et al. Human 3D cellular model of hypoxic brain injury of prematurity. *Nat. Med.* **25**, 784–791 (2019).
49. Vasudevan, S. et al. Leaky optoelectrical fiber for optogenetic stimulation and electrochemical detection of dopamine exocytosis from human dopaminergic neurons. *Adv. Sci.* **6**, 1902011 (2019).
50. Grealish, S. et al. Human ESC-derived dopamine neurons show similar preclinical efficacy and potency to fetal neurons when grafted in a rat model of Parkinson's disease. *Cell Stem Cell* **15**, 653–665 (2014).
51. Hoban, D. B. et al. Impact of alpha-synuclein pathology on transplanted hESC-derived dopaminergic neurons in a humanized alpha-synuclein rat model of PD. *Proc. Natl Acad. Sci. USA* **117**, 15209–15220 (2020).
52. Velasco, S. et al. Individual brain organoids reproducibly form cell diversity of the human cerebral cortex. *Nature* **570**, 523–527 (2019).
53. Tiklova, K. et al. Single cell transcriptomics identifies stem cell-derived graft composition in a model of Parkinson's disease. (vol 11, 2434, 2020). *Nat. Commun.* **11**, 1–11 (2020).
54. Bjorklund, A. & Dunnett, S. B. Dopamine neuron systems in the brain: an update. *Trends Neurosci.* **30**, 194–202 (2007).
55. Brichta, L. & Greengard, P. Molecular determinants of selective dopaminergic vulnerability in Parkinson's disease: an update. *Front Neuroanat.* **8**, 152 (2014).
56. Kajtez, J. et al. 3D biomaterial models of human brain disease. *Neurochem. Int.* **147**, 105043 (2021).
57. Hofer, M. & Lutolf, M. P. Engineering organoids. *Nat. Rev. Mater.* 6, 402–420 (2021).
58. Mansour, A. A. et al. An in vivo model of functional and vascularized human brain organoids. *Nat. Biotechnol.* **36**, 432–441 (2018).
59. Cakir, B. et al. Engineering of human brain organoids with a functional vascular-like system. *Nat. Methods* **16**, 1169–1175 (2019).
60. Shi, Y. et al. Vascularized human cortical organoids (vOrganoids) model cortical development in vivo. *PLoS Biol.* **18**, e3000705 (2020).
61. Johansson, U. et al. Assembly of functionalized silk together with cells to obtain proliferative 3D cultures integrated in a network of ECM-like microfibers. *Sci. Rep.* **9**, 6291 (2019).
62. Renier, N. et al. iDISCO: a simple, rapid method to immunolabel large tissue samples for volume imaging. *Cell* **159**, 896–910 (2014).

Acknowledgements

We thank BioLamina and Spiber® for providing Biosilk. We thank Dr Therese Kallur, Prof. My Hedhammar, Prof. Anders Björklund for helpful comments and discussions, and Ulla Jarl, Sol Da Rocha Baez, and Marie Persson Vejgården for technical assistance. The research leading to these results has received funding from the New York Stem Cell Foundation, European Research Council (ERC) under ERC Grant Agreement 771427, European Union–funded project NSC-Reconstruct (European Union, H2020, GA no 874758, 2020-23), Swedish Research Council (2016-00873), Swedish Parkinson Foundation (Parkinsonfonden), Swedish Brain Foundation, Strategic Research Area at Lund University Multipark, and Knut and Alice Wallenberg Stiftelse (KAW 2018-0040). Alessandro Fiorenzano is the recipient of a Thorsten and Elsa Segerfalk Foundation grant, which was used to support this study. Malin Parmar is a New York Stem Cell Foundation Robertson Investigator.

Author contributions

M.P. and A.F. conceived the project, designed experiments, and interpreted computational analysis, analyzed all results in the project, and wrote the paper. A.F. and E.S.

generated organoids, performed experiments and interpreted histological data with help from J.K., F.N., J.G., B.M., and Y.Z. P.S. and Y.S. analyzed and interpreted the single-cell RNA data. D.R.O., M.B., and A.B. performed and interpreted electrophysiological experiments. J.E. and J.K. analyzed and interpreted amperometry experiments. All authors read and approved the final paper.

Funding
Open access funding provided by Lund University.

Competing interests
M.P. is the owner of Parmar Cells AB and co-inventor of the following patents WO2016162747A2, WO2018206798A1, and WO2019016113A1. The remaining authors declare no competing interests.

Additional information
Supplementary information The online version contains supplementary material available at https://doi.org/10.1038/s41467-021-27464-5.

Correspondence and requests for materials should be addressed to Alessandro Fiorenzano.

Peer review information *Nature Communications* thanks the anonymous reviewer(s) for their contribution to the peer review of this work.

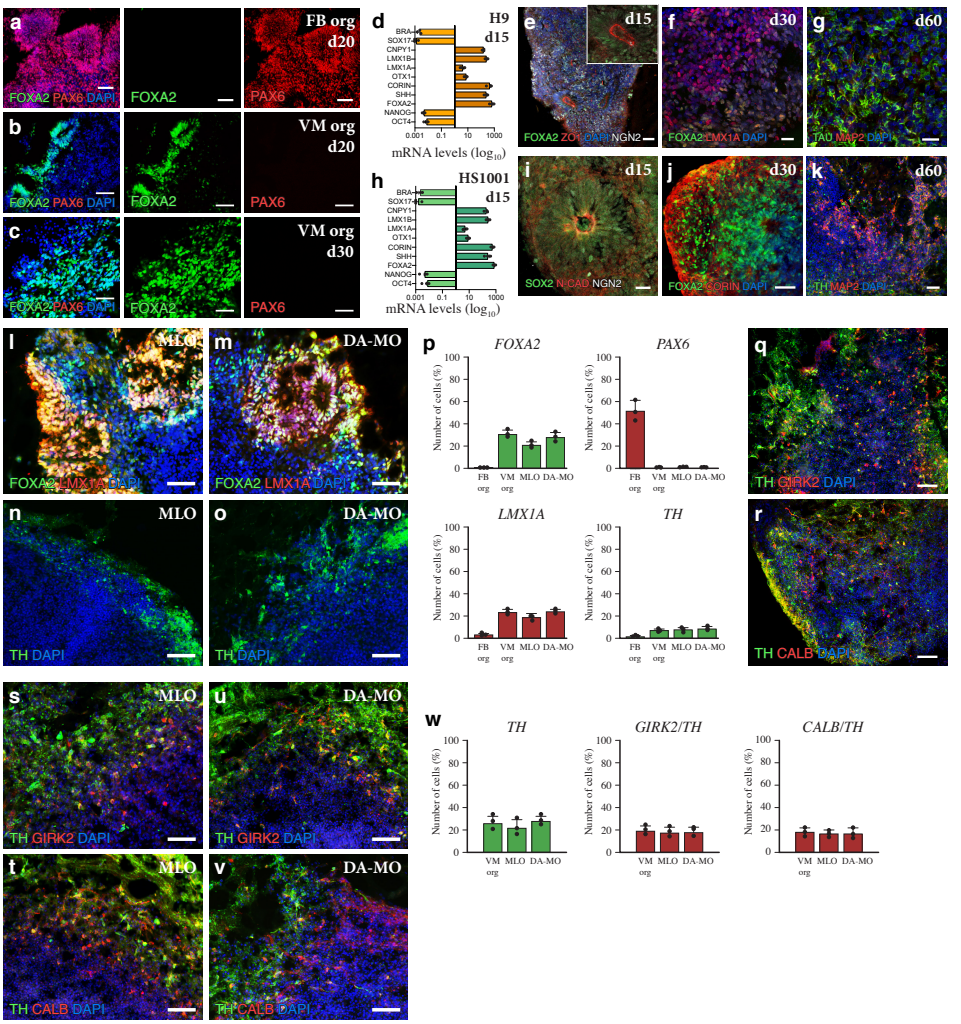

Supplementary Figure 1

a-c, Immunohistochemistry of FOXA2/PAX6 in **a,** forebrain organoids (FBO) at day 20 and **b, c,** in VM organoids across a time course (day 20- 30). Scale bars, 50 μm. **d,** qRT-PCR of selected markers at day 15 during H9-derived VM organoid differentiation. Results are given as fold change over undifferentiated hPSCs. Data represent mean ± SEM obtained from 3 individual organoids. **e,** Immunohistochemistry of FOXA2/ZO-1/NGN2 at day15, **f,** of LMX1A/FOXA2 at day 30, and **g,** of TAU/MAP2 at day 60 during H9 VM organoid differentiation. Scale bars, 50 μm (e) and 20 μm (f,g) **h,** qRT-PCR of selected markers at day 15 during H1001-derived VM organoid differentiation. Results are given as fold change over undifferentiated hPSCs. Data represent mean ± SEM obtained from 3 individual organoids. **i,** Immunohistochemistry of SOXA2/N-CAD at day15, **j,** FOXA2/CORIN at day 30, and **k,** of TH/MAP2 at day 60 during H1001 VM organoid differentiation. Scale bars, 20 μm (i), 50 μm (j) and 100 μm (k). **l, m,** Cryosection of VM organoids at month 1 showing FOXA2/LMX1A double staining in MLOs and DA-MOs. Scale bars, 100 μm. **n, o,** Immunohistochemistry of TH in MLO and DA-MO at month 1. Scale bars, 100 μm. **p,** Percentages of FOXA2$^+$, PAX6$^+$, LMX1A$^+$ and TH$^+$ cells at month 1 in our VM organoids and in MLOs, DA-MOs and FB organoids. Data represent mean ± SEM of 3 independent organoids. **q-v,** Immunohistochemistry of TH/GIRK2 (q) and TH/CALB (r) at day 60, in our VM organoids and, in **s-v,** MLOs (s,t) and DA-MOs (u,v). Scale bars, 100 μm (q,r) and 50 μm (s-v). **w,** Percentages of TH$^+$, GIRK2$^+$ and CALB$^+$ a at month 2 in our VM organoid and in MLOs and DA-MOs. Data represent mean ± SEM obtained from 3 individual organoids.

Nuclei were stained with DAPI.

Source data are provided as a Source Data file.

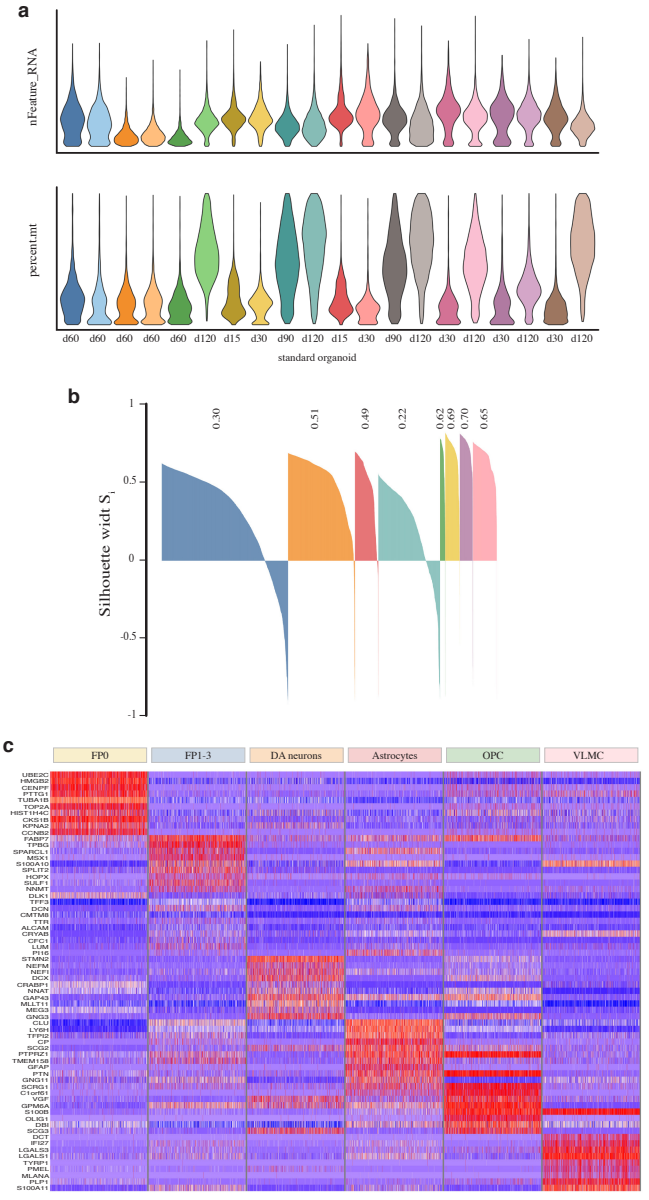

Supplementary Figure 2

a, Filtering of low quality cells based on and number of detected genes per cell and mitochondrial fraction. **b,** Silhouette plot and scores showing the difference between mean distance to cells within the same and nearest clusters. **c,** Heatmap visualizing normalized and scaled expression of top ten enriched genes in VM organoid for each cluster.

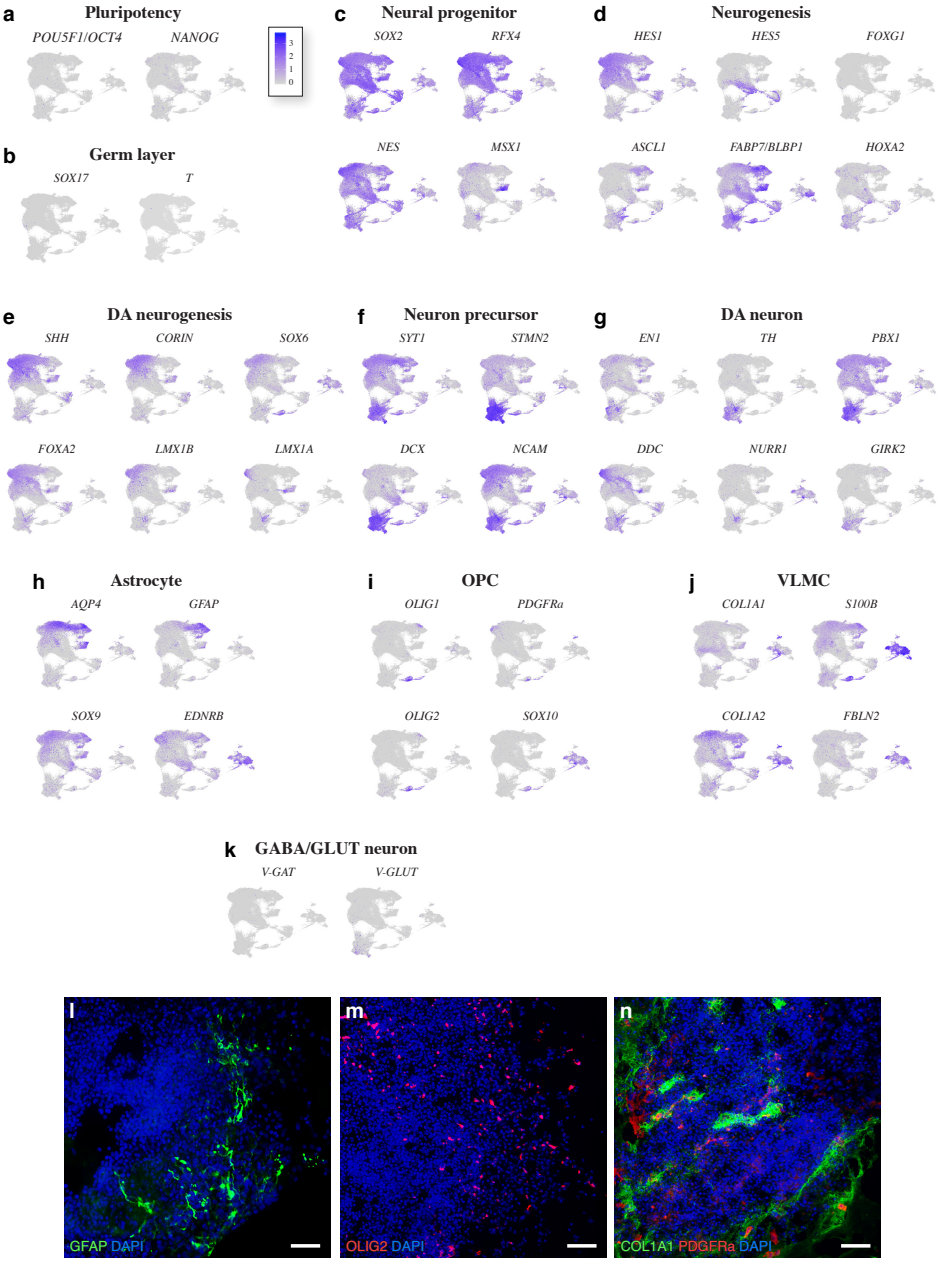

Supplementary Figure 3

a-k, Feature plots visualizing specific gene expression across clusters. Colors indicated expression level. **l-n,** Immunohistochemistry of GFAP, OLIG2 and COL1A1/PDGFRa at day 120 during H9 VM organoid differentiation. Scale bars, 100 μm.

Nuclei were stained with DAPI.

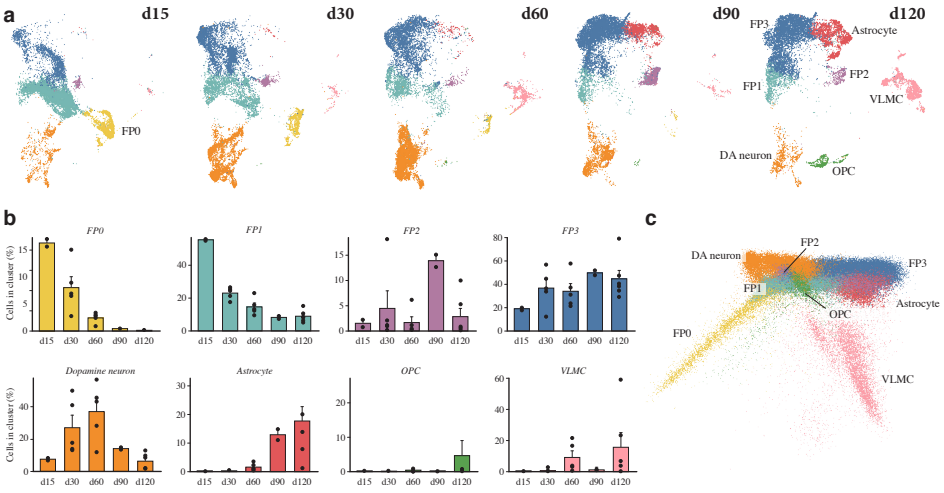

Supplementary Figure 4

a, UMAP plots of cell clusters for each time point (day 15, n=2; day30, n=4; day 60, n=5; day 90, n=2; day 120, n=6). **b,** Fraction of cells from each individual identified cluster from day 15 to day 120. Error bars indicates ± SEM of 2-6 replicates. **c,** Slingshot pseudotime developmental trajectory reconstruction during VM organoid differentiation (day 15–120).

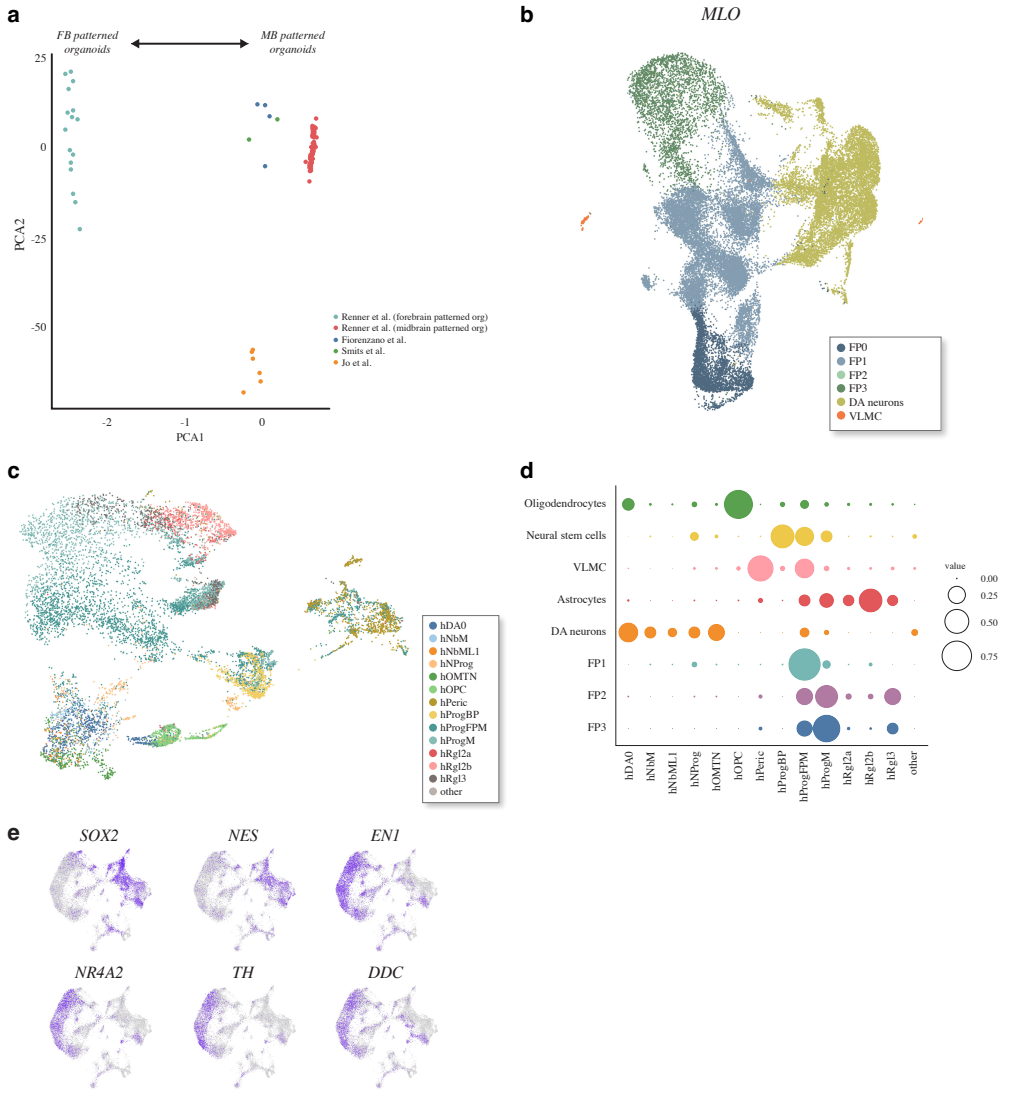

Supplementary Figure 5

a, Principal component (PC) analysis by merging published bulk and scRNAseq dataset from midbrain-patterned organoids from pluripotent stem cells (Jo et al [15]; Fiorenzano et al) and neural progenitors (Renner et al [20]; Smits et al [21]) generated and FBO (Renner et al [16]). **b,** UMAP plot showing clustering of 29,112 cells analyzed cells from MLO organoids at day 30. **c,** UMAP cluster integration analysis combining a published scRNAseq datasets of fetal human midbrain [34] and the hPSC-derived VM organoids with **d,** relative overlapping quantification. **e,** Feature plots visualizing specific gene expression across DA clusters from scRNAseq dataset of human fetal VM and human fetal VM 3D cultures. Colours indicated expression level.

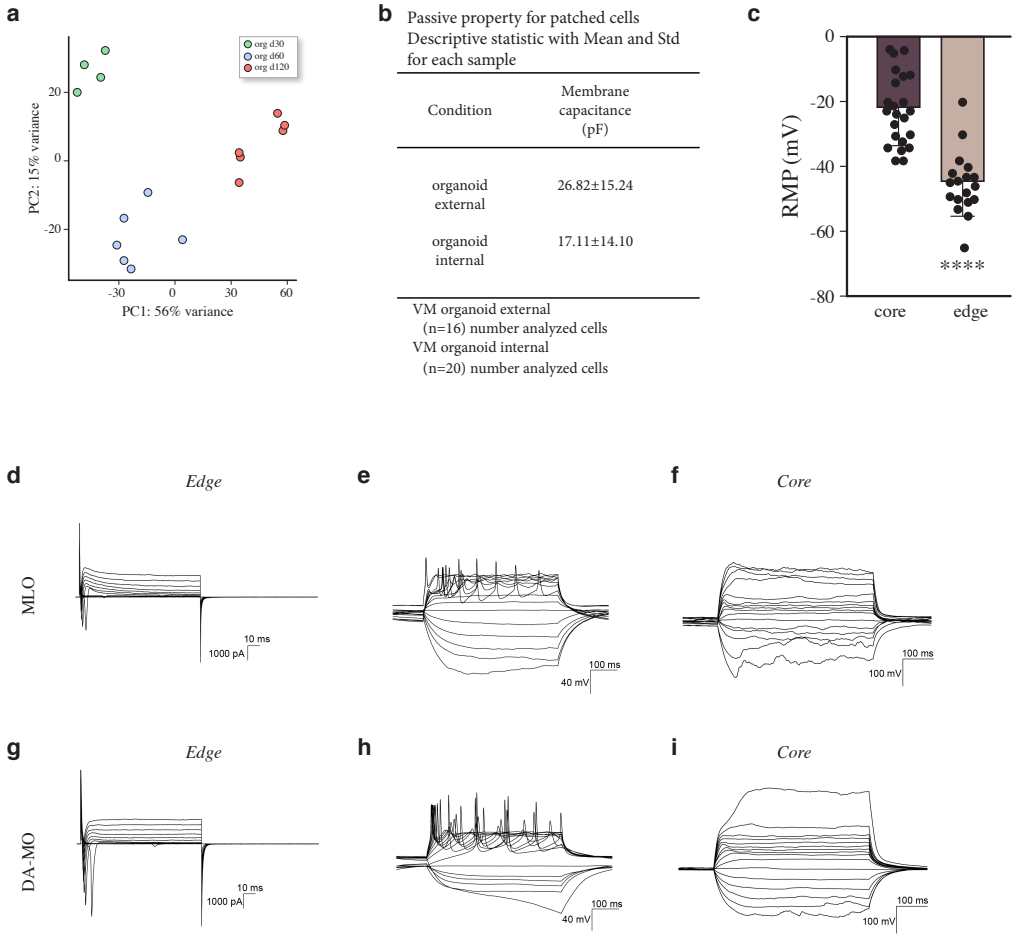

Supplementary Figure 6

a, Principal component (PC) analysis of averaged expression for all cells in VM organoids at day 30, 60, and 120. PC1 explaining 56% variance of organoid groups at different time points; PC2 accounting for 15% variance in biologically independent VM organoids. **b,** Schematic overview reporting passive electrical properties of VM organoid cell membranes from whole-cell patch-clamp recordings. **c,** Resting membrane potential (RMP)quantifications between externally (n=16) and internally (n=20) localized cells in VM organoids at day 90. Silk external (n=18 cells), silk internal (n=23 cells). Data represent mean ± SD. Unpaired two tailed t test, p= 0,0001. **d,** Representative trace from external patching showing inward sodium- and outward potassium-rectifying current traces of MLO at day 70 triggered by stepwise depolarization (n=8). **e,** Patch-clamp recordings of external MLO cells depicting current-induced action potentials (APs) (-85 pA to +165 pA with 20 pA steps) (n=8). **f,** Patch-clamp recordings of internal MLO cells depicting absence of current-induced APs at day 70 (-85 pA to +165 pA with 20 pA steps) (n=3). **g,** Representative trace from external patching showing inward sodium- and outward potassium-rectifying current traces of DA-MO at day 70 triggered by stepwise depolarization (n=3). **h,** Patch-clamp recordings of external DA-MO cells depicting current-induced action potentials (APs) (-85 pA to +165 pA with 20 pA steps) (n=3). **i,** Patch-clamp recordings of internal DA-MO cells depicting absence of current-induced APs at day 90 (-85 pA to +165 pA with 20 pA steps) (n=3).
Source data are provided as a Source Data file.

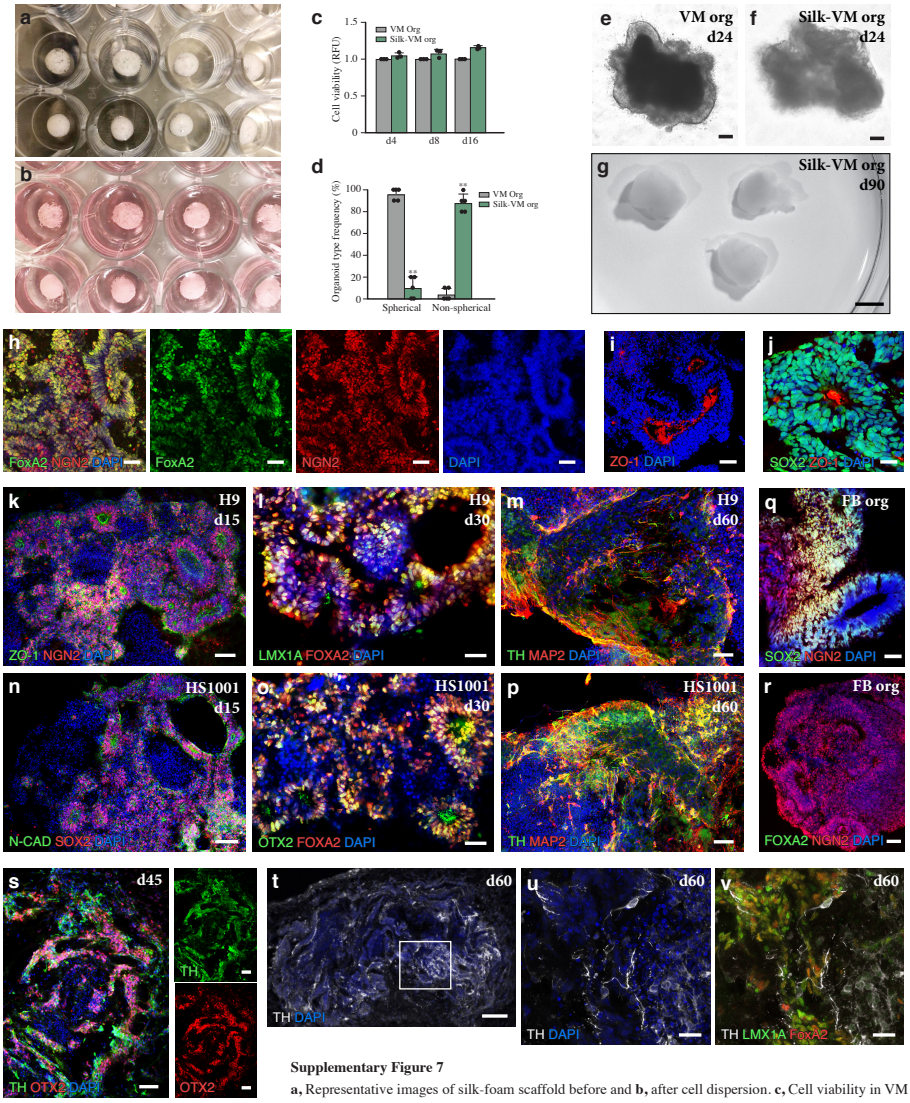

Supplementary Figure 7

a, Representative images of silk-foam scaffold before and **b,** after cell dispersion. **c,** Cell viability in VM organoid grown with and without scaffold measured by the CyQuant assay and expressed as relative fluorescence units (RFU). Data represent mean ± SEM obtained from 3 individual organoids per condition. **d,** Organoid-type frequency analysis (spherical vs non-spherical) of VM organoid grown with and without scaffold. Data represent mean ± SD of 5 biologically independent organoids; Mann-Whitney test, p= 0,0079. **e, f,** Representative bright field images of VM organoid grown with and without scaffold at day 24. Scale bars, 100 μm. **g,** Representative bright field images of a long-term silk-VM organoid culture. Scale bar, 1 mm. **h,** Immunohistochemistry of FOXA2/NGN2, **i,** ZO1, and **j,** SOX2/ZO1 from silk-VM organoids at day 21. Scale bars, 50 μm (g) and 20 μm (h,i). **k,** Immunohistochemistry of NGN2/ZO-1 at day 15, **l,** LMX1A/ FOXA2 at day 30, and **m,** TH/MAP2 at day 60 during H9 VM organoid differentiation. Scale bars, 100 μm. **n,** Immunohistochemistry of SOX2/NCAD at day 15, **o,** OTX2/FOXA2 at day 30, and **p,** TH/MAP2 at day 60 during HS1001 VM organoid differentiation. Scale bars, 100 μm. **q,** Immunohistochemistry of SOX2/NGN2 and **r,** FOXA2/NGN2 at day 20 in FBOs. Scale bars, 50 μm(q) and 100 μm(r). **s,** Immunohistochemistry of TH/OTX2 in silk-VM organoid at day 45. Scale bar, 100 μm. **t-v,** Immunohistochemistry of TH/LMX1A/FOXA2 in silk-VM organoid at day 60. Scale bars, 100 μm (t) and 20 μm (u,v). Nuclei were stained with DAPI.

Source data are provided as a Source Data file.

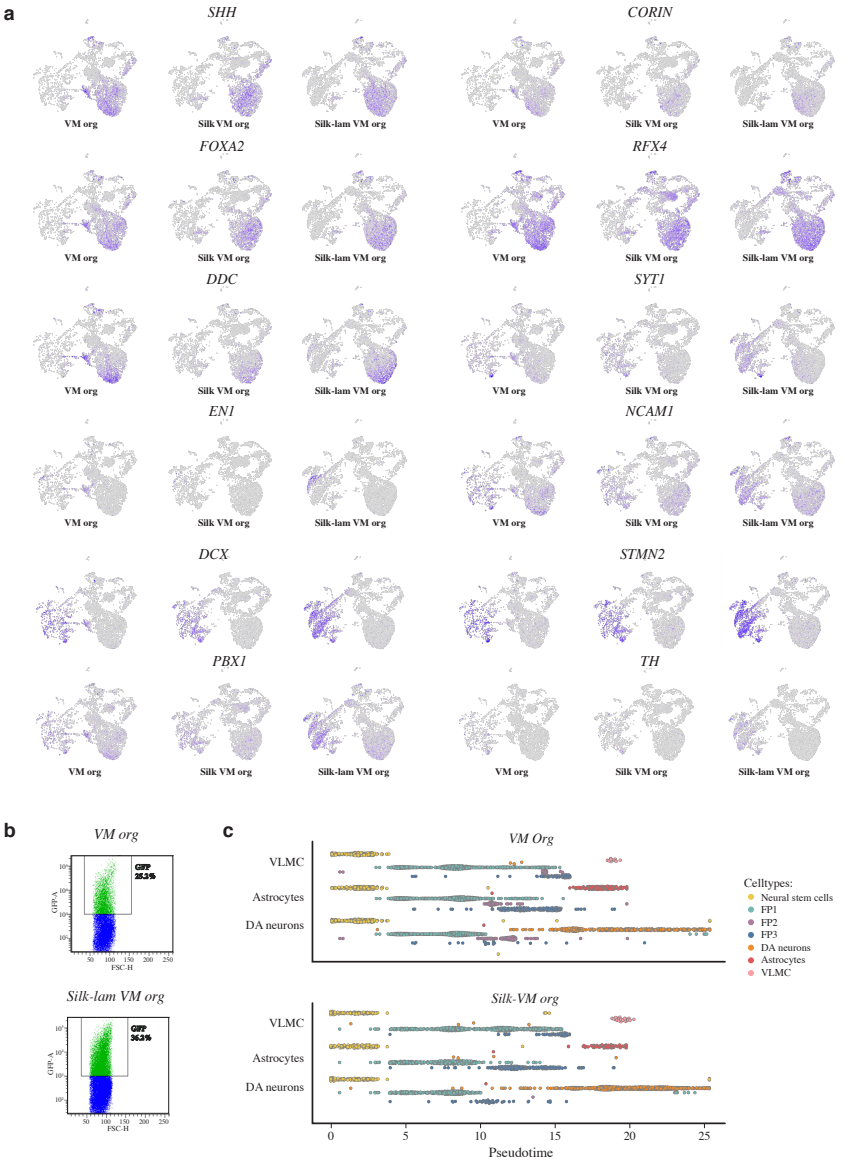

Supplementary Figure 8

a, Feature plots visualizing specific gene expression across identified clusters. Colours indicated expression level. **b,** Representative FACS-plots of GFP expression in conventional and silk-lam VM organoids differentiated from a CRISPR/Cas9-mediated gene-edited *TH*-Cre hPSC line. **c,** Pseudotime ordering of single cells using Slingshot from integrated data of VM and silk-VM organoids from day 30, 60, and 120 (total 5000 cells). Each data point represents a single cell color-coded by cell type. Pseudotimes were calculated by orthogonal projection of Slingshot derived MST.

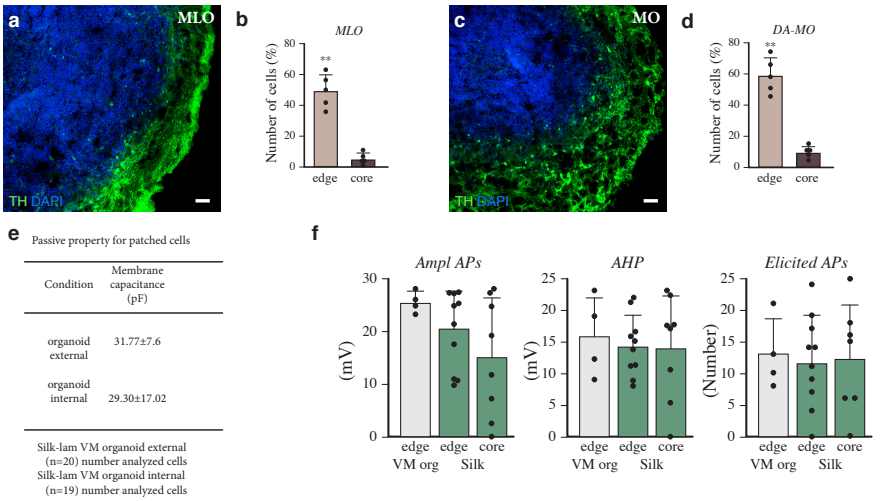

Supplementary Figure 9

a, Immunohistochemistry of TH at month 2 and **b,** its quantification in the outer and inner layers in MLOs. Data represent mean ± SEM obtained from 5 individual organoids; two-tailed Mann-Whitney test, p =0.0079. Scale bar, 100 μm. **c,** Immunohistochemistry of TH at month 2 and **d,** its quantification in the outer and inner layers in in DA-MOs. Data represent mean ± SEM obtained from 5 individual organoids; two-tailed Mann-Whitney test, p =0.0079. Scale bar, 100 μm. **e,** Schematic overview reporting passive electrical properties of silk-lam VM organoid cell membranes from whole-cell patch-clamp recordings. **f,** Amplitude (Ampl), Afterhyperpolarization (AHP) (afterhyperpolarization) and Elicited Action Potentials (APs) analysis of the edge in conventionally generated VM organoids (n= 4) and edge (n=10) and core (n=8) layers in silk-lam VM Organoids. Data represent mean ± SD. Ordinary one-way ANOVA.
Source data are provided as a Source Data file.

Supplementary Table1

Sequence of qPCR primers

GENE NAME	FORWARD PRIMER	REVERSE PRIMER
ACTB	CCTTGCACATGCCGGAG	GCACAGAGCCTCGCCTT
GAPDH	TTGAGGTCAATGAAGGGGTC	GAAGGTGAAGGTCGGAGTCA
CORIN	CATATCTCCATCGCCTCAGTTG	GGCAGGAGTCCATGACTGT
FOXA2	CCGTTCTCCATCAACAACCT	GGGGTAGTGCATCACCTGTT
OTX1	TATAAGGACCAAGCCTCATGGC	TTCTCCTCTTTCATTCCTGGGC
LMX1A	CGCATCGTTTCTTCTCCTCT	CAGACAGACTTGGGGCTCAC
LMX1B	CTTAACCAGCCTCAGCGACT	TCAGGAGGCGAAGTAGGAAC
CNPY1	TTGGCCTCTCAAACACCATTCT	GAGCGAAACAAAACGCAATCAC
EN1	CGTGGCTTACTCCCCATTTA	TCTCGCTGTCTCTCCCTCTC
TH	CGGGCTTCTCGGACCAGGTGTA	CTCCTCGGCGGTGTACTCCACA
BRACHYURY	ATGCAGTGACTTTTTGTCGTGG	ACTGAGGCTGCATTTCCTTCTT
SOX17	CCAGACCGCGACAGGCCAGAAC	AGTGAGGCACTGAGATGCCCCG
OCT4	TCTCCAGGTTGCCTCTCACT	GTGGAGGAAGCTGACAACAA
NANOG	TTGGGACTGGTGGAAGAATC	GATTTGTGGGCCTGAAGAAA

Supplementary Table2

List of antibodies used throughout the study

Antigen	Species	Company cat.no	Dilution
NGN2	Goat	Santa Cruz 19234	1:600
ZO-1	Mouse	Thermo Fisher 1A12	1:300
aPKC	Mouse	Santa Cruz 393219	1:1000
N-CAD	Mouse	BD610920	1:500
KI67	Mouse	BD 550609	1:500
CORIN	Rat	R&D MAB2209	1:200
bIII-Tubulin	Rabbit	Biosite PBR435P	1:1000
MASH1	Mouse	BD 556604	1:200
SOX2	Mouse	R&D MAB2018	1.500
FOXA2	Goat	Santa Cruz (sc-6554)	1:1000
FOXA2	Mouse	Santa Cruz-101060	1:1000
COLIA1	Sheep	R&D 6220	1:1000
LMX1A	Rabbit	Merck Millipore (AB10533)	1:1000
OTX2	Goat	R&D Systems (AF1979)	1:2000
TAU	Rabbit	DAKO A0024	1:1000
TH	Rabbit	Merck Millipore (AB152)	1:1000
TH	Mouse	Immunostar (22941)	1:500
MAP2	Chicken	AbCAM 5392	1.2000
GIRK2	Rabbit	Alamone Labs (APC006	1:500
CALB	Rabbit	Swant cb38	1:500
DDC	Rabbit	Millipore 1519	1:500
DAT	Rabbit	Santa Cruz 14002	1:300
GFAP	Mouse	BioLegend (SMI 21)	1:500
OLIG2	Rabbit	Neuromics RA 25081	1:500
PAX6	Rabbit	Biolegend 901301	1:300
HIF1alpha	Rabbit	GeneTex 127309	1:1000

Generation of Human Ventral Midbrain Organoids Derived from Pluripotent Stem Cells

Edoardo Sozzi,[1] Fredrik Nilsson,[1] Janko Kajtez,[1] Malin Parmar,[1] and Alessandro Fiorenzano[1,2]

[1]Developmental and Regenerative Neurobiology, Wallenberg Neuroscience Center, Lund Stem Cell Center, Department of Experimental Medical Science, Lund University, Sweden
[2]Corresponding author: *alessandro.fiorenzano@med.lu.se*

Published in the Toxicology section

Parkinson's disease (PD) is the second most common neurodegenerative disorder worldwide and is caused by the degeneration and loss of dopamine (DA) neurons in the ventral midbrain (VM). The focal and progressive degeneration of DA neurons in the VM makes PD a particularly attractive target for cell-based therapies. Human pluripotent stem cells (hPSCs) offer unprecedented opportunities to model the development and functional properties of human DA neurons in a dish. The use of human *in vitro* models based on hPSCs has empowered studies of VM development and provided access to neurons expressing a particular disease-specific phenotype. Currently, hPSC differentiation is most routinely carried out in monolayer cultures, which do not properly recapitulate cell-cell interactions and the structural complexity of the brain. Moreover, 2D cultures are challenging to maintain long term, as the cells tend to detach from the plate and lose their functional characteristics. This precludes the possibility of mimicking later phases of DA neurogenesis and recreating the complexity of functional neural circuitries. Here, we describe protocols showing how to maintain hPSCs in an undifferentiated state and how to then drive these hPSCs into 3D regionalized VM organoids. After long-term culture, these VM organoids exhibit mature and post-mitotic molecular features, including neuromelanin pigments similar to those released in primate VMs. We also report a protocol describing how to efficiently perform immunohistochemistry and how to detect neuromelanin-containing DA neurons in VM organoids. Together, these protocols provide a 3D *in vitro* platform that can be used to better understand the molecular mechanisms underlying DA neuron function and disease and may serve as a powerful tool for designing more targeted disease-modifying therapies. © 2022 The Authors. Current Protocols published by Wiley Periodicals LLC.

This article was corrected on 19 October 2024. See the end of the full text for details.

Basic Protocol 1: Human pluripotent stem cell culture
Basic Protocol 2: hPS cell differentiation for the generation of human ventral midbrain organoids
Basic Protocol 3: Characterization of ventral midbrain organoids

Keywords: dopamine neurons • human brain organoids • Parkinson's disease • pluripotent stem cells

CURRENT PROTOCOLS
A Wiley Brand

Current Protocols e555, Volume 2
Published in Wiley Online Library (wileyonlinelibrary.com).
doi: 10.1002/cpz1.555

How to cite this article:
Sozzi, E., Nilsson, F., Kajtez, J., Parmar, M., & Fiorenzano, A. (2022). Generation of human ventral midbrain organoids derived from pluripotent stem cells. *Current Protocols*, *2,* e555. doi: 10.1002/cpz1.555

INTRODUCTION

The brain is a complex organ composed of an enormous variety of architecturally organized cell types that give rise to intricate molecular, cellular, and biophysical processes that regulate its function and physiology (Arlotta & Pasca, 2019; Siddiqi, Kording, Parvizi, & Fox, 2022; Kelava & Lancaster, 2016). Although significant advances have been made to understand human brain development, the inaccessibility of pre- and postnatal human brain tissue severely restricts the scope of our knowledge, which, to date, has been derived mostly from studies using postmortem pathological specimens. While such studies yield data on the end-stage pathology of neurological diseases, their causes and consequences remain difficult to parse using such an approach (Krishnaswami et al., 2016; Agarwal et al., 2020). There is, therefore, a pressing need to develop novel experimental systems that can recapitulate key features of the developing and adult brain (Kim, Koo, & Knoblich, 2020; Pasca, 2018; Fiorenzano, Sozzi, Parmar, & Storm, 2021).

The ability to recreate functionally mature neurons from human pluripotent stem cells (hPSCs) holds the promise of mimicking key architectural and molecular features of brain tissue in a dish (Rifes et al., 2020; Demers et al., 2016). Currently, however, hPSC differentiation is routinely carried out in monolayer cultures, which fail to recapitulate the structural and molecular complexity of the brain. Moreover, 2D cultures are challenging to maintain long term, as the cells eventually detach from the plate and lose their functional properties. This precludes the possibility of mimicking later phases of DA neurogenesis and recreating the intricacy of neural circuitries. Recently, human brain organoids differentiated from hPSCs have emerged as an advanced human stem cell-based model capable of recapitulating the development and maturation of brain tissue in a 3D organ-like configuration in relevant physiological conditions (Lancaster et al., 2013; Quadrato et al., 2017; Kanton et al., 2019). New protocols based on extrinsic patterning factors have been developed to guide the differentiation of hPSCs toward regionalized brain organoids exhibiting a specific cell identity (Miura et al., 2020; Cederquist et al., 2019).

Dopamine (DA) neurons arise from the ventral midbrain (VM) following regionalization of the neural tube, and constitute the major source of dopamine in the mammalian central nervous system. DA neurons play a key role in the control of voluntary motor movement as well as in emotion-based behavior. The function (and dysfunction) of DA neurons has attracted great interest among the scientific community, as the degeneration of this cell population leads to motor deficits in Parkinson's disease (PD). Detailed protocols to generate human VM organoids, however, are still lacking. Moreover, modeling human VM *in vitro* requires the precise balance of patterning factors that lead to the generation of DA neurons exhibiting both mature molecular features and electrophysiological properties, which is not trivial (Nolbrant, Heuer, Parmar, & Kirkeby, 2017; Tiklova et al., 2020; Fiorenzano, Birtele, Wahlestedt, & Parmar, 2021; Fiorenzano et al., 2018).

Here, we report three protocols to generate and characterize human VM organoids (Fig. 1A and 1B). We first describe how to maintain hPSCs under undifferentiated conditions (Basic Protocol 1) and how to then efficiently drive these hPSCs into VM-patterned

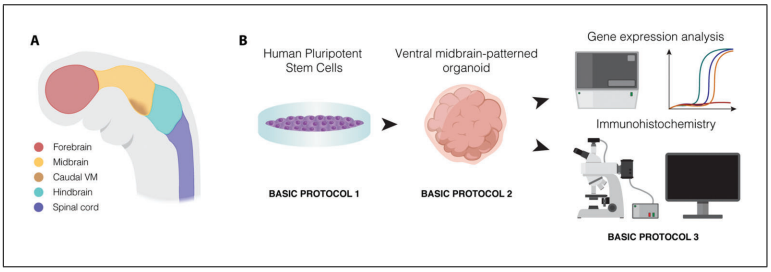

Figure 1 Protocol overview. (**A**) Anatomical patterning of the caudal ventral midbrain (VM) during development. (**B**) Overview of the protocols described in this article: Basic Protocol 1 describes hPSC cell culture, Basic Protocol 2 outlines the steps for differentiating the hPSC to generate human VM organoids, and Basic Protocol 3 describes the molecular characterization of VM organoids via immunohistochemistry. The resulting organoids are also suitable for gene expression analysis.

human brain organoids (Basic Protocol 2), which can give rise to mature and functional DA neurons (Fig. 1B). We then describe how to molecularly characterize these VM organoids, including the detection of DA neurons containing neuromelanin granules (Basic Protocol 3) (Fig. 1B) (Fiorenzano et al., 2021).

VM-patterned organoid differentiation exploits the intrinsic self-organization property of hPSCs via the addition of extrinsic patterning factors. Efficiently driving neural induction by exposing the cells to dual-SMAD inhibition factor, the neural tube ventralizing secreted factor sonic hedgehog (SHH), and glycogen synthase kinase 3 inhibitor (GSK3i) leads to finely tuned caudalized floor plate formation (Fig. 1A). This results in the efficient generation of DA progenitors within VM organoids, and their subsequent differentiation into mature DA neurons displaying electrophysiological properties and the ability to release dopamine (Fiorenzano et al., 2021). Importantly, we have previously shown that organoids patterned into a VM fate generated following this protocol give rise to mature DA neurons that are molecularly very similar to human DA neurons derived from human fetal VM (Fiorenzano et al., 2021). The recapitulation of VM patterning and the generation of mature and functional DA neurons within VM organoids offers a novel tool for molecular and functional studies of DA neuron maturation and diversity at a much greater level of detail.

Together, these protocols allow for the establishment of a valuable platform to study early phases of DA neurogenesis, but that can be maintained for a sufficiently long term to also recapitulate late stages of DA neuron differentiation, with potential implications for biomedical applications, including PD modeling and drug discovery.

HUMAN PLURIPOTENT STEM CELL CULTURE

BASIC PROTOCOL 1

The following protocol describes how to thaw, passage, and maintain hPSCs before inducing organoid differentiation. This step is necessary to ensure that the starting population is healthy, stable, and homogeneous, without spontaneously differentiated areas. hPSC cultures should also be routinely tested for mycoplasma contamination. We recommend performing one or two passages before organoid differentiation, which can take approximately 6 to 10 days depending on the chosen stem cell line and seeding density. The protocol presented here is based on culturing hPSCs on human recombinant Lam-521-coated plates and iPS-Brew medium, which results in a homogeneous cell culture while preserving pluripotency and self-renewal properties (Fig. 2A and 2B). The protocol could also be adapted to use Matrigel coating but, in that case, we recommend monitoring the quality of hPSC cultures to be alert to the presence of areas of spontaneous differentiation, which should be manually removed.

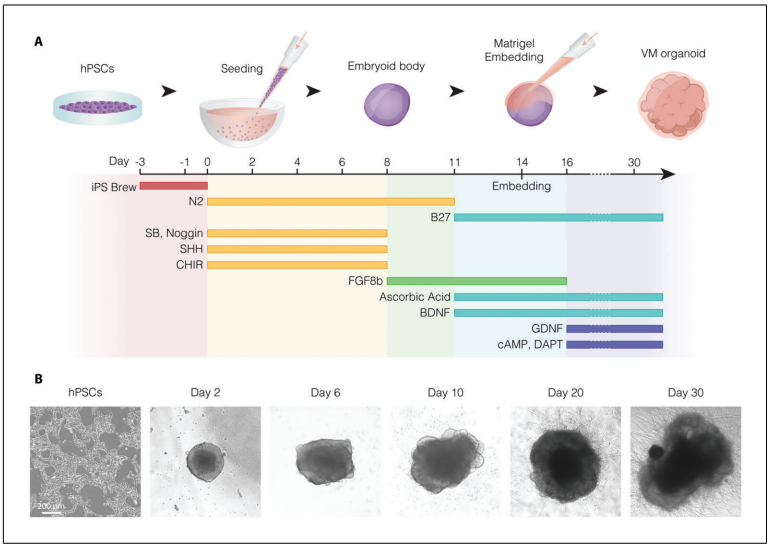

Figure 2 Ventral midbrain (VM) organoid differentiation protocol. (**A**) Schematic overview of the steps and timing of VM organoid differentiation achieved following Basic Protocols 1 and 2, showing hPSC culture and generation of mature VM organoids, respectively. (**B**) Representative bright-field images of hPSC culture and VM organoid differentiation at different time points (day 2-30). Scale bar 200 µm.

NOTE: Users should obtain all the necessary permissions and approvals for work with hPSC lines, and follow all institutional and national guidelines.

Materials

hPSC line of choice. For this study, the following human embryonic stem cell lines were used: RC17 (Roslin Cells, cat. no. hPSCreg RCe021-A), H9 (WiCell, cat. no. hPSCreg WAe009A), and HS983a, HS999, and HS1001 (all from Karolinska Institute, Stockholm, Sweden).

Laminin-521 (Lam-521; 100 µg/ml; Biolamina, cat. no. LN-521)

D-PBS $+Ca^{2+}/+Mg^{2+}$ (CTS, Thermo Fisher Scientific, cat. no. A1285801)

DMEM/F-12 (Thermo Fisher Scientific, cat. no. 31330038)

Knockout serum replacement (KOSR; Thermo Fisher Scientific, cat. no. 10828010)

iPS-Brew XF, Stem cell culture medium (StemMACS, Miltenyi, cat. no. 130-104-368)

Y-27632 dihydrochloride (Rho-associated kinase [ROCK] inhibitor; StemMACS, Miltenyi, cat. no. 130-106-538)

EDTA (0.5 M, pH 8.0; UltraPure, Thermo Fisher Scientific, cat. no. 15575020)

D-PBS $-Ca^{2+}/-Mg^{2+}$ (CTS, Thermo Fisher Scientific, cat. no. A1285601)

Trypan blue stain 0.4% (Invitrogen, cat. no. T10282)

Cell culture plastic 6-well plates (Sarstedt, cat. no. 83.3920)

Biological safety cabinet, class II (Thermo Scientific Holten LaminAir or similar)

Cell culture incubator set to 37°C and 5% CO_2 (Thermo Fisher Scientific, model no. 3541 DH or similar)

Cell culture centrifuge (for 1.5-, 15-, and 50-ml tubes; Beckman Coulter, model no. Allegra 21 or similar)

Countess automated cell counter (Thermo Fisher Scientific, cat. no. AMQAX1000 or AMQAX2000) or Bürker chamber (VWR, cat. no. 631-0921 or similar)

Pipette controller (for pipetting volumes of 1-25 ml; Corning Stripettor Ultra Pipet Controller, model no. 4099 or similar)

Sterile pipette tips (for pipetting volumes of 0.5-1000 µl; TipOne Pipette Tips: 1250 µl XL graduated tip, cat. no. S1112-1830; 200 µl beveled tip, cat. no. S1111-1716-C; 10 µl graduated tip, cat. no. S1111-3210 or similar)

Pipettes (for pipetting volumes of 0.5-1000 µl; Thermo Fisher Scientific, Finnpipette F2 variable-volume single-channel pipettes or similar)

Serological pipettes (sterile, non-pyrogenic; Sarstedt, 5 ml, cat. no. 86.1253.001; 10 ml, cat. no. 86.1254.001; 25 ml, cat. no. 86.1685.001)

Tubes (Sarstedt; 15 ml, cat. no. 62.554.502; 50 ml, cat. no. 62.547.254 or similar)

Freezers operating at −20°C and −80°C (Thermo Fisher Scientific, ES Series Combination Lab Refrigerator/Freezer; Thermo Fisher Scientific TSE Series −86°C, model no. 936; Panasonic Cryogenic ULT Freezer, model no. MDF-C2156VAN-PE or similar)

Refrigerator operating at 4°C

Phase-contrast inverted microscope (Olympus, model no. CKX53 or similar)

Automated thawing system (optional; Biocision ThawSTAR CFT2, cat. no. BCS-601)

Thawing and maintaining an hPSC line

1. Prepare a solution of Lam-521 (0.5 µg/cm^2) in PBS (+Ca^{2+}/+Mg^{2+}) (coating solution).

2. Coat one well of a 6-well plate with 2 ml/well of the coating solution. Then, gently shake the plate to ensure a homogeneous distribution of the solution and incubate for at least 2 hr (overnight preferred) at 37°C.

   Following this protocol, one well of a 6-well plate yields enough hPSCs to generate 100 organoids. In case a different amount is needed, adjust the number of wells accordingly.

   Plates can be prepared in advance: wrap in Parafilm and store for up to a week at 4°C. If the plates are to be stored for more than 48 hr at 4°C, increase the volume of the coating solution to 3 ml to make sure the wells do not dry out. Before use, incubate the plate at 37°C for at least 2 hr.

3. Before starting the procedure, prepare 5 ml of wash medium (5% KOSR [v/v] in DMEM/F-12) in a 15-ml tube.

4. Thaw the cells in the automated thawing system or in a water bath at 37°C until approximately half of the medium has thawed.

   Take care not to submerge the tube.

5. Add 1 ml wash medium to the cryovial dropwise, making sure to collect all the cells from the walls of the vial.

   This and all following steps should be performed in sterile conditions in the cell hood.

6. Transfer the cells to the remaining 4 ml of wash medium (step 3) and centrifuge the tube at 400 × *g* for 5 min at room temperature (RT).

7. Remove the supernatant and gently knock the tube to detach the pellet from the bottom.

8. Resuspend the cells in 1 ml iPS-Brew medium supplemented with Y-27632 (ROCK inhibitor, 10 µM final concentration).

9. Count the cells with an automated counter (e.g., Countess II) or a Bürker chamber.

10. Plate cells homogeneously onto Lam-521-coated plates at a density of 15,000 cells/cm^2 (approx. 144,000 cells/well for a 6-well plate). Add iPS-Brew medium

supplemented with Y-27632 (ROCK inhibitor, 10 μM final concentration), to reach a final volume of 2 ml/well.

11. After 24 hr, replace the stem cell medium with 2 ml/well fresh iPS-Brew medium without the Y-27632 supplement.

12. For culture maintenance, replace the stem cell medium every day with fresh iPS-Brew medium.

    During the weekend, twice the amount of medium can be added to the cells to avoid having to change the medium for one extra day.

Passaging of hPSC line

13. Prepare 5 ml of wash medium (5% KOSR [v/v] in DMEM/F-12) in a 15-ml tube and Lam-521-coated plates before starting, as described in steps 1-3.

14. Aspirate hPSC medium and wash the cells from step 11 once in 2 ml/well D-PBS $-Ca^{2+}/-Mg^{2+}$, to remove dead cells and debris.

15. Add 0.5 mM EDTA (50 μl/cm^2, e.g., 500 μl/well for a 6-well plate) directly to the cells and incubate at 37°C for 7 min.

16. Remove the EDTA, then detach the cells by adding 1.5 ml/well wash medium. Using a 1000-μl pipette, quickly but gently triturate the colony into small clumps, without introducing bubbles.

17. Transfer all cells to the tube containing the remaining wash medium and centrifuge at 400 × *g* for 5 min at RT.

18. Aspirate the supernatant and detach the pellet from the bottom by gently knocking the tube.

19. Resuspend the cells in 1 ml of iPS-Brew medium supplemented with 10 μM Y-27632.

20. Count the cells with an automated counter (e.g., Countess II) or a Bürker chamber.

21. Plate cells homogeneously onto Lam-521-coated wells on iPS-Brew supplemented with 10 μM Y-27632 with the aim of having 70% confluency on the day of hPSC differentiation.

    For the hPSC line RC17, approximate recommended seeding densities are: 3 days before seeding, 25k cells/cm^2; 4 days before seeding, 15k cells/cm^2; 5 days before seeding, 10k cells/cm^2.

    Note that different cell lines might have different growth rates and seeding densities might need to be adjusted accordingly.

22. After 24 hr, replace the stem cell medium with fresh iPS-Brew without the Y-27632 supplement.

23. For culture maintenance, replace the stem cell medium every 1-2 days with iPS-Brew, as described above.

24. Proceed to Basic Protocol 2 when cells have reached 70% to 75% confluency.

BASIC PROTOCOL 2

hPS CELL DIFFERENTIATION FOR THE GENERATION OF HUMAN VENTRAL MIDBRAIN ORGANOIDS

This protocol describes how to guide the self-organization of the hPSCs in Basic Protocol 1 into VM-patterned organoids. The cells are first plated in conical wells to favor cell aggregation leading to the formation of embryonic bodies. Cells are then cultured under

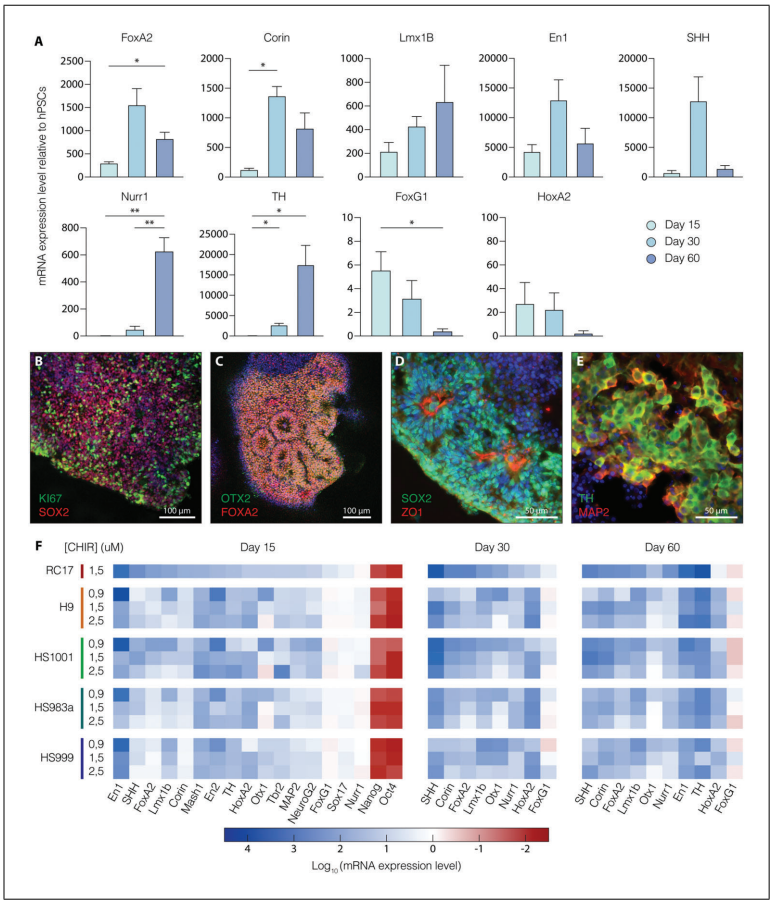

Figure 3 Molecular characterization of VM organoids. (**A**) RT-qPCR analysis of selected VM, forebrain, and hindbrain markers during VM organoid differentiation (days 15 to 60). Values are given as fold change relative to undifferentiated hPSCs. * $p < 0.05$, ** $p < 0.01$; statistical analysis was performed using two-tailed unpaired *t*-test with Welch´s correction (n = 3). Data are presented as mean ± standard error. (**B-E**) Immunohistochemistry of (**B**) KI67/SOX2 at day 15, (**C**) OTX2/FOXA2, (**D**) SOX2/ZO1 at day 30, and (**E**) TH/MAP2 at day 60. Scale bars 100 µm B-C, 50 µm D-E. Nuclei were stained with DAPI. (**F**) Heat map showing global mRNA expression levels of selected VM, forebrain, and hindbrain markers generated from four additional hPSC lines (H9, HS1001, HS983a, HS999) during VM organoid differentiation. Three different concentrations (0.9 µM, 1.5 µM, and 2.5 µM) of CHIR99021 were tested for each cell line. RC17-derived VM organoids treated with 1.5 µM CHIR99021 were reported as the internal control. Expression values were obtained from RT-qPCR analysis and presented as fold change over undifferentiated hPSCs (Log_{10}) normalized over ACTB and GAPDH expression levels.

undifferentiated conditions for 3 days (day -3 to day 0). At day 0, once the cells have aggregated, the culture medium is switched to differentiation medium, which includes the addition of the following extrinsic patterning factors to efficiently drive hPSCs into VM organoids: dual-SMAD inhibitors, ventralizing agent SHH-C24II, GSK3 inhibitor (CHIR99021), and fibroblast growth factor 8b (FGF8b) (Fig. 2A and 2B and Fig. 3A-E). The proper balancing and timing of the different patterning factors used during differentiation is crucial.

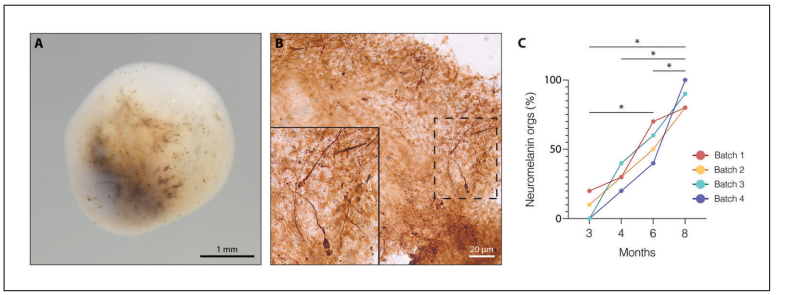

Figure 4 Analysis of neuromelanin production during VM organoid differentiation. (**A**) Representative bright-field image of neuromelanin-pigmented VM organoid at month 8. Scale bar, 1 mm. (**B**) Fontana-Masson/TH double staining of VM organoid at month 4 showing intracellular and extracellular neuromelanin release. Inset shows high magnification. Scale bar, 20 µm. (**C**) Time-course analysis showing the percentage (%) of pigmented VM organoids from different batches for up to 8 months. n = 10 organoids for each time point analyzed. *$p < 0.05$; Mann-Whitney test.

This protocol has been tested on multiple hPSC and induced PSC (iPSC) lines with similar results. However, the concentration of CHIR99021 may need to be optimized, as different cell lines exhibit slightly different sensitivities to this patterning factor. CHIR99021 titration is required to identify the optimal condition for efficient VM patterning (Fig. 3F). During differentiation, when the VM organoids have grown in size, they require scaffolding to support the 3D structure. Matrigel, a natural matrix material resembling the extracellular matrix, strengthens the organization of the organoids in a 3D culture space. The organoids are embedded in Matrigel droplets at day 14 of VM differentiation to enhance organoid architecture and obtain high-order brain functions. Basic Protocol 2 can be followed to generate VM organoids containing functionally mature and pigmented DA neurons (Fig. 4), which can then be used for biomedical applications as well as for PD disease modeling.

Materials

Homogeneous, compact, and flat culture of hPSCs at ~70% confluency (from Basic Protocol 1)
Y-27632 dihydrochloride (Rho-associated kinase [ROCK] inhibitor; StemMACS, Miltenyi, cat. no. 130-106-538)
D-PBS $-Ca^{2+}/-Mg^{2+}$ (CTS, Thermo Fisher Scientific, cat. no. A1285601)
iPS-Brew XF (StemMACS, Miltenyi, cat. no. 130-104-368)
DMEM/F-12 (Thermo Fisher Scientific, cat. no. 31330038)
Knockout serum replacement (KOSR; Thermo Fisher Scientific, cat. no. 10828010)
N2 base medium (see recipe)
B27 base medium (see recipe)
Accutase cell dissociation reagent (StemPro, Thermo Fisher Scientific, cat. no. A1110501)
SB431542 (TGF-β pathway inhibitor; StemMACS, Miltenyi, cat. no. 130-106-543)
Noggin (BMP inhibitor, recombinant human; Miltenyi, cat. no. 130-103-456)
SHH-C24II (sonic hedgehog, recombinant human; Miltenyi, cat. no. 130-095-727)
CHIR99021 (GSK3 inhibitor; StemMACS, Miltenyi cat. no. 130-106-539)
BDNF (brain-derived neurotrophic factor, recombinant human; Miltenyi, cat. no. 130-096-286)
GDNF (glia-derived neurotrophic factor, recombinant human; R&D Systems, cat. no. 212-GD-010)
FGF8b (fibroblast growth factor 8b, recombinant human; Miltenyi, cat. no. 130-095-740)
cAMP (dibutyryl-cyclic AMP; Sigma-Aldrich, cat. no. D0627)

DAPT (Tocris Bioscience, cat. no. 2634)
L-ascorbic acid (vitamin C; Sigma-Aldrich, cat. no. A4403)
Matrigel matrix basement membrane (Corning, cat. no. 354234)
Trypan blue stain 0.4% (if an automated cell counter is used; Invitrogen, cat. no. T10282)

Biological safety cabinet, class II (Thermo Scientific Holten LaminAir or similar)
Cell culture centrifuge (for 1.5-, 15-, and 50-ml tubes; Beckman Coulter, model no. Allegra 21 or similar)
Cell culture incubator set to 37°C and 5% CO_2 (Thermo Fisher Scientific, model no. 3541 DH or similar)
Countess automated cell counter (Thermo Fisher Scientific, cat. no. AMQAX1000 or AMQAX2000) or Bürker chamber (VWR, cat. no. 631-0921 or similar)
Pipette controller (for pipetting volumes of 1-25 ml; Corning Stripettor Ultra Pipet Controller, model no. 4099 or similar)
Sterile pipette tips (for pipetting volumes of 0.5-1000 µl; TipOne Pipette Tips: 1250 µl XL graduated tip, cat. no. S1112-1830; 200 µl beveled tip, cat. no. S1111-1716-C; 10 µl graduated tip, cat. no. S1111-3210 or similar)
Pipettes (for pipetting volumes of 0.5-1000 µl; Thermo Fisher Scientific, Finnpipette F2 variable-volume single-channel pipettes or similar)
Electronic Multi-Dispenser Pipette (Multipette® E3×, Eppendorf)
Serological pipettes (sterile, non-pyrogenic; Sarstedt, 5 ml, cat. no. 86.1253.001; 10 ml, cat. no. 86.1254.001; 25 ml, cat. no. 86.1685.001)
Tubes (Sarstedt; 15 ml, cat. no. 62.554.502; 50 ml, cat. no. 62.547.254 or similar)
Freezers operating at −20°C and −80°C (Thermo Fisher Scientific, ES Series Combination Lab Refrigerator/Freezer; Thermo Fisher Scientific TSE Series −86°C, model no. 936; Panasonic Cryogenic ULT Freezer, model no. MDF-C2156VAN-PE or similar)
Refrigerator operating at 4°C
Phase-contrast inverted microscope (Olympus, model no. CKX53 or similar)
Ultra-low attachment 96-well plate (round bottom; Corning Costar, cat. no. 7007)
Ultra-low attachment 6-well plate (Corning Costar, cat. no. 3471)
Parafilm (Sigma-Aldrich, cat. no. P7793 or similar)

Cell seeding (day –3)

1. Before differentiation, make sure that the hPSC culture from Basic Protocol 1 looks homogeneous and flat, without areas undergoing spontaneous differentiation.
2. Prepare 5 ml wash medium (5% KOSR [v/v] in DMEM/F-12) in a 15-ml tube.
3. Aspirate hPSC medium and wash the cells once in 2 ml/well of D-PBS $-Ca^{2+}/-Mg^{2+}$.
4. Incubate the cell culture with Accutase solution (50 µl/cm^2, e.g., 500 µl/well for a 6-well plate) at 37°C for 5 min.
5. Without removing the Accutase solution, gently add 1.5 ml wash medium to each well to detach the cells, using a 1000 µl pipette to mechanically obtain small cell clumps and single cells.
6. Transfer cell suspensions to the tube from step 2 and spin down at 400 × *g* for 5 min at RT.
7. Aspirate the supernatant and resuspend the pellet in 1 ml iPS-Brew supplemented with Y-27632 (ROCK inhibitor, 10 µM).
8. Count the cells with an automated counter (e.g., Countess II) or a Bürker chamber.

9. Dilute the cell suspension to a concentration of 160,000 cells/ml in the same medium.
10. Plate 8000 cells/well (e.g., 50 µl/well) in all wells of one ultra-low attachment 96-well plate, mixing the suspension from time to time to ensure an equal distribution of cells in all wells.
11. Gently add 200 µl/well of iPS-Brew supplemented with 10 µM Y-27632 (total volume 250 µl/well) and leave the plate undisturbed in the incubator.
12. After 48 hr (day –1), replace 150 µl of medium with 200 µl of fresh iPS-Brew without the Y-27632 supplement.

    This step should be performed carefully to avoid aspirating the cells.

13. Wait 24 hr before proceeding to the next step.

Embryoid body formation and patterning (days 0 to 14)

14. Prepare N2 base medium supplemented with 10 µM SB431542, 150 ng/ml Noggin, 1.5 µM CHIR99021, and 400 ng/ml SHH-C24II.
15. Gently replace 200 µl/well medium with the N2 medium.

    The culture can be very fragile at this stage as the embryoid bodies are forming. Make sure to remove the medium gently. All supplement factors should be freshly added at every medium exchange. The CHIR99021 concentration indicated here is optimal for differentiation of the hPSC RC17 line and has been previously tested through titration. The optimal concentrations among those tested with other hPSC lines are indicated in Figure 3F.

16. Replace 250 µl/well with N2 medium and fresh supplements (as above) on days 2, 4, and 6.
17. On day 8, replace 250 µl/well with N2 medium supplemented with fresh 100 ng/ml FGF8b.
18. On day 11, replace 250 µl/well with B27 medium supplemented with fresh 100 ng/ml FGF8b, 20 ng/ml BDNF, and 200 µM ascorbic acid.

Matrigel embedding (days 13 and 14) and terminal differentiation (day 16 onwards)

19. On day 13, before starting the embedding procedure, let the Matrigel thaw undisturbed overnight at 2°-8°C in a bucket of ice.

    It is crucial that the temperature of the Matrigel remains low (around 4°C), as Matrigel proteins start to polymerize at higher temperatures, and, under those conditions, the reagent will not be suitable for the embedding procedure.

20. On day 14, take a support surface with holes arranged horizontally and vertically (e.g., a 96-well plate), coat the surface with a Parafilm layer, and apply finger pressure to generate dimples. Sterilize the dimples with UV/ethanol.
21. Using a cut P1000 tip, transfer the embryoid bodies from the corresponding well to individual dimples in a small drop of medium.

    Embryoid bodies at this stage are visible to the naked eye and should appear as round spheres when observed under a microscope.

22. With a P200 tip, remove as much medium as possible from the surroundings of each 3D culture.

    If a large number of organoids are embedded at the same time, work quickly to ensure they do not dry out.

23. Evenly cover each embryoid body with a droplet of Matrigel (~30 µl/organoid).

    Work quickly during the procedure and keep the Matrigel on ice to avoid polymerization.

24. Incubate the plate at 37°C for 30 min.

25. After embedding, transfer the organoids to an ultra-low attachment 6-well plate, at approximately 10 organoids/well. To facilitate the transfer, detach the Parafilm from the support and wash out the embedded organoids with 300 µl/dimple of B27 base medium supplemented with fresh 20 ng/ml BDNF, 10 ng/ml GDNF, 200 µM ascorbic acid, 500 µM cAMP, and 1 µM DAPT. Once all organoids are transferred to the corresponding wells, add medium to reach a final volume of 4 ml/well.

26. For terminal differentiation of the culture, replace 4 ml/well of the medium 2 to 3 times a week for 2 to 4 months (depending on the experimental design) with B27 base medium supplemented with fresh 20 ng/ml BDNF, 10 ng/ml GDNF, 200 µM ascorbic acid, 500 µM cAMP, and 1 µM DAPT. Depending on the experimental design, the organoids can now be analyzed at different time points with the technique of choice. To perform IHF/IHC, proceed to Basic Protocol 3.

    Be aware that the morphology and size of the brain organoids will change over time, reflecting different stages of VM differentiation.

    RT-qPCR is one technique that is routinely used to determine progenitor cell identity during VM organoid differentiation. Specifically, for gene expression studies, 1 µg of extracted RNA and random primers were used here for cDNA synthesis (RNeasy Micro kit, Qiagen, cat. no. 74004; Maxima First Strand cDNA Synthesis Kit, Thermo Fisher, cat. No. K1642), following the manufacturer's instructions. In the example shown here, RT-qPCR was performed as described by Nilsson et al. (Nilsson et al., 2021) using the list of primers reported in Table 1. For sample data, see Figure 3A.

CHARACTERIZATION OF VENTRAL MIDBRAIN ORGANOIDS

BASIC PROTOCOL 3

During the differentiation of human VM organoids, cells in 3D space start exhibiting distinct molecular and architectural features. The presence of characteristic cell structures with apical-basal polarity and the formation of distinct cell layers is commonly analyzed by immunofluorescence staining using specific antibodies for marker proteins. The expression of immature and post-mitotic DA neuronal markers, including FOXA2, LMX1A, OTX2, and TH, detected by immunohistochemistry, is also specifically used to analyze VM differentiation efficiency. Specifically, maturation to A9-like DA neurons, which consist of pigmented neurons located in substantia nigra pars compacta (SNpc) in primate VM (Bjorklund & Dunnett, 2007), can be detected using Fontana-Masson staining in combination with tyrosine hydroxylase (TH) immunohistochemistry, which reveals the presence of dark neuromelanin granules (Figs. 3E and 4B).

Here, we describe how to molecularly characterize VM organoids generated from Basic Protocol 2 at the protein level. We report a step-by-step protocol for embedding and sectioning VM organoids to guarantee an efficient immunohistochemical analysis, including detection of neuromelanin pigmented DA neurons after long-term culture. This protocol is based on Fiorenzano et al. (2021).

Materials

Ventral midbrain patterned organoids generated from Basic Protocol 2, at the desired time point.
Paraformaldehyde (PFA; Merck Millipore, cat. no. 1040051000)
Sucrose (Fisher Chemical, cat. no. S/8600/60)
OCT cryo embedding compound (HistoLab, cat no 45830)
D-PBS $-Ca^{2+}/-Mg^{2+}$ (CTS, Thermo Fisher Scientific, cat. no. A1285601)

Table 1 qPCR Primers

Gene name	Full gene name	Primer sequence (fwd/rev, 5′-3′)
ACTB	Actin beta	CCTTGCACATGCCGGAGGCACAGAGCCTCGCCTT
GAPDH	Glyceraldehyde-3-phosphate dehydrogenase	TTGAGGTCAATGAAGGGGTCGAAGGTGAAGGTCGGAGTCA
NANOG	Homeobox Transcription Factor Nanog	TTGGGACTGGTGGAAGAATCGATTTGTGGGCCTGAAGAAA
OCT4 (POU5F1)	Octamer-Binding Protein 4	TCTCCAGGTTGCCTCTCACTGTGGAGGAAGCTGACAACAA
SOX17	SRY-Box Transcription Factor 17	CCAGACCGCGACAGGCCAGAACAGTGAGGCACTGAGATGCCCCGAG
FOXA2	Forkhead box A2	CCGTTCTCCATCAACAACCTGGGGTAGTGCATCACCTGTT
CORIN	Corin, serine peptidase	CATATCTCCATCGCCTCAGTTGGGCAGGAGTCCATGACTGT
LMX1B	LIM homeobox transcription factor beta	CTTAACCAGCCTCAGCGACTTCAGGAGGCGAAGTAGGAAC
EN1	Engrailed homeobox 1	CGTGGCTTACTCCCCATTTATCTCGCTGTCTCTCCCTCTC
NURR1 (NR4A2)	Nuclear Receptor Subfamily 4 Group A Member 2	CAGGCGTTTTCGAGGAAATGAGACGCGGAGAACTCCTAA
TH	Tyrosine Hydroxylase	CGGGCTTCTCGGACCAGGTGTACTCCTCGGCGGTGTACTCCACA
FOXG1	Forkhead box G1	TGGCCCATGTCGCCCTTCCTGCCGACGTGGTGCCGTTGTA
HOXA2	Homeobox A2	CGTCGCTCGCTGAGTGCCTGTGTCGAGTGTGAAAGCGTCGAGG
SHH	Sonic Hedgehog Signaling Molecule	CCAATTACAACCCCGACATCAGTTTCACTCCTGGCCACTG
MASH1 (ASCL1)	Achaete-Scute Family BHLH Transcription Factor 1	CTAAAGATGCAGGTTGTGCGGGAGCTTCTCGACTTCACCA
EN2	Engrailed Homeobox 2	CCTCCTGCTCCTCCTTTCTTGACGCAGACGATGTATGCAC
OTX1	Orthodenticle homeobox 1	TATAAGGACCAAGCCTCATGGCTTCTCCTCTTTCATTCCTGGGC
TBR2 (EOMES)	Eomesodermin	GCGAGAGAACCGTGCCACAGACGCCACCTCTTCGCTCTGTTGGG
MAP2	Microtubule Associated Protein 2	CCGTGTGGACCATGGGGCTGGTCGTCGGGGTGATGCCACG
NEUROG2	Neurogenin 2	ATCCGAGCAGCACTAACACGGCACAGGCCAAAGTCACAG

Table 2 Primary Antibodies

Antigen	Species	Brand (cat. no)	Dilution
KI67	Mouse	Novocastra (ACK02)	1:500
SOX2	Rabbit	Millipore (AB5603)	1:400
FOXA2	Mouse	Santa Cruz (sc-101060)	1:1000
OTX2	Goat	R&D Systems (AF1979)	1:2000
TH	Rabbit	Merck Millipore (AB152)	1:1000
MAP2	Chicken	Abcam (ab5392)	1:2000
ZO1	Mouse	Invitro (339100)	1:300

Donkey serum (Merck Millipore, cat. no. S30-100ML)
Triton X-100 (Fisher Scientific, cat. no. 10254640)
Primary antibodies (Table 2)
DAPI (Sigma-Aldrich, cat. no. D9542)
Secondary conjugated antibodies:
- Alexa Fluor 488 AffiniPure Donkey Anti-Rabbit IgG (H+L) (Jackson ImmunoResearch Laboratories, cat. no. 711-545-152)
- Alexa Fluor 488 AffiniPure Donkey Anti-Goat IgG (H+L) (Jackson ImmunoResearch Laboratories, cat. no. 705-545-003)
- Cy2 AffiniPure Donkey Anti-Rabbit IgG (H+L) (Jackson ImmunoResearch Laboratories, cat. no. 711-225-152)
- Cy2 AffiniPure Donkey Anti-Mouse IgG (H+L) (Jackson ImmunoResearch Laboratories, cat. no. 715-545-150)
- Cy3 AffiniPure Donkey Anti-Rabbit IgG (H+L) (Jackson ImmunoResearch Laboratories, cat. no. 711-165-152)
- Cy3 AffiniPure Donkey Anti-Chicken IgG (H+L) (Jackson ImmunoResearch Laboratories, cat. no. 703-165-155)
- Cy3 AffiniPure Donkey Anti-Mouse IgG (H+L) (Jackson ImmunoResearch Laboratories, cat. no. 715-165-150)

Neuromelanin staining
- Staining jars (Epredia E94 or similar)
- Fontana-Masson kit (Atom Scientific, cat. no. RRSK 12-100)

Cell culture plastic 24-well plates (Sarstedt, cat. no. 83.3922 or similar)
Cryostat (Fisher Scientific CryoStar NX70, or similar)
Fluorescence microscope (Leica, model no. DMI6000 B or similar)
Confocal laser scanning microscope (Leica, model no. TCS SP8 or similar)
High-resolution bright-field microscope (Olympus, model no. AX70 or similar)
Disposable base molds (Fisherbrand, Fisher Scientific, cat. no. 93019849)
Microscope slides (Epredia SuperFrost Plus, Fisher Scientific, cat. no. J1800AMNZ or similar)

Organoid cryosectioning and immunofluorescence

1. Transfer 3 to 6 VM organoids at the desired time point (from Basic Protocol 2) to a single well of a 24-well plate, remove any residual medium, and fix them with 500 µl/well of 4% v/v paraformaldehyde for 5 hr at RT.
2. Perform three 5-min washes with 1 ml/well of 1× PBS.
3. Remove the PBS and add 2 ml of 30% w/v sucrose to each well and leave overnight at 4°C on a shaker.
4. Replace sucrose solution with 2 ml of 1:1 (by volume) OCT:30% w/v sucrose mixture for 6 hr at 4°C on an orbital shaker.

5. Use a 5-ml pipette to transfer VM organoids to a cryomold and fill with OCT.
6. Immediately transfer the cryomold to dry ice and leave it to freeze for 5 min.

   Frozen cryomolds can be stored at −80°C until needed.

7. Using a cryostat, section the organoids embedded in OCT at 20 μm and then transfer the sections onto glass slides with the help of a brush.

   Sections can be stored at −20°C until needed. To perform immunofluorescence, continue to step 8. If neuromelanin detection is desired, please proceed to step 16.

8. Wash the slides in 1× PBS three times for 5 min each.
9. Fix the slides in 4% v/v paraformaldehyde for 10 min at RT and wash again three times with 1× PBS, as in step 8.
10. Incubate each slide with 500 μl of 0.3% v/v Triton X-100 and 5% v/v donkey serum in 1× PBS for at least 1 hr at RT.
11. Prepare primary antibodies solutions by diluting them in the same solution as step 10.

    Combinations of two or three antibodies, including DAPI, can be used on different VM organoids simultaneously. A list of primary antibodies and relative dilutions is reported in Table 2.

12. Incubate each slide with 300 μl of primary antibody solution overnight at 4°C.

    A humidified chamber is recommended, to avoid drying of the sections.

13. The next day, wash the sections in 1× PBS three times, for 5 min each.
14. After incubation with primary antibodies, incubate the sections for at least 1 hr with 300 μl/slide of the appropriate secondary antibodies (Alexa Fluor 488, 594, and 647 used at 1:400 in the same solution as in step 10) and then mount with coverslip and 500 μl PVA-DABCO containing DAPI (1:1000).
15. Analyze the immunocytochemically stained VM organoid sections using a fluorescence microscope or a confocal laser scanning microscope to estimate the expression pattern of early and late DA neuron markers. See Figure 3B-E.

Immunohistochemistry for neuromelanin detection

The following protocol is based on the Fontana-Masson method to visualize melanin in cells, as well as argentaffin cell granules and lipofuscins, which takes advantage of a silver-reducing technique. All reagents are included in the Fontana-Masson staining kit listed in Materials. This protocol is also compatible with DAB pre-stained tissue. All steps are performed in staining jars; make sure that all sections are completely covered with solution.

16. Prepare the ammoniacal silver solution by adding 33% ammonia solution drop by drop to 20 ml of 10% aqueous silver nitrate solution in a glass flask. Constantly agitate the flask to favor the dissolution of the formed precipitate. Stop adding the ammonia solution once a faint opalescence is obtained and the precipitate is dissolved.
17. After titration, add 20 ml distilled water.

    The solution can be stored at 4°C for up to a month. For optimal performance, store the bottle in the dark. Note that ammoniacal silver solutions are potentially explosive if stored incorrectly.

18. Hydrate the sections by rinsing them in tap water.
19. Wash the sections three times for 1 min each in distilled water.

20. Transfer the slides to a clean jar filled with the ammoniacal silver solution from step 17, cover with aluminum foil, and incubate in an oven at 56°C for 30 to 40 min.

    After 30 min, check the slides on the microscope until optimal staining is observed. Do not over-incubate, to avoid the formation of deposits over the sections. Make sure that the staining jar is clean, as the ammoniacal silver solution will react with any contaminant that might be present in the jar.

21. Gently wash the slides at least three times for 1 min each in distilled water.

22. Immerse the slides in 5% aqueous sodium thiosulphate solution for 1 min.

23. Wash well in running tap water for 3 min and rinse in distilled water.

24. Counterstain with 0.1% neutral red solution for 1 min.

25. Rinse in distilled water.

26. Rapidly dehydrate the sections by rinsing them in absolute ethanol three times, for 1 min each.

    Alternatively, dehydration can be achieved through a series of alcohols of ascending concentrations.

27. Clear the sections by immersion in fresh xylene three times, for 1 min each, and place under a coverslip with DPX mountant.

28. Analyze the immunohistochemically stained VM organoid section using a bright-field microscope to quantify the number of neuromelanin$^+$ organoids (Fig. 4).

    At the end of the procedure, melanin granules should be visible as black, while nuclei will be red. Users should expect to see between 40% and 60% neuromelanin$^+$ organoids at 5 months.

REAGENTS AND SOLUTIONS

N2 base medium

	Dilution	Final conc.	Amount	Vendor	Cat. no.
DMEM/F-12 (no glutamine)	1:2	0.5×	19.4 ml	Thermo Fisher	21331020
Neurobasal Plus	1:2	0.5×	19.4 ml	Thermo Fisher	A3582901
N2 supplement	1:100	1×	400 µl	Thermo Fisher	17502048
L-Glutamine	1:100	2 mM	400 µl	Thermo Fisher	25030081
Penicillin-Streptomycin	1:500	20 U/ml	80 µl	Thermo Fisher	15140122
MEM Non-essential amino acids solution	1:100	1×	400 µl	Thermo Fisher	11140050
2-Mercaptoethanol	1:1000	50 µM	40 µl	Thermo Fisher	31350010
Total			**40 ml**		

Filter and store at 2° to 8°C for up to 2 weeks.

B27 base medium

	Dilution	Final conc.	Amount	Vendor	Cat. no.
Neurobasal Plus	–	1×	38.4 ml	Thermo Fisher	A3582901
B27 supplement (without vitamin A)	1:50	1×	800 µl	Thermo Fisher	12587010
L-Glutamine	1:100	2 mM	400 µl	Thermo Fisher	25030081
Penicillin-Streptomycin	1:500	20 U/ml	80 µl	Thermo Fisher	15140122
MEM Non-essential amino acids solution	1:100	1×	400 µl	Thermo Fisher	11140050
2-Mercaptoethanol	1:1000	50 µM	40 µl	Thermo Fisher	31350010
Total			**40 ml**		

Filter and store at 2° to 8°C for up to 2 weeks.

COMMENTARY

Background information

Monolayer 2D culture systems laid the foundation for understanding the early developmental stages of DA neurons, enabling the development and optimization of more efficient differentiation protocols. This knowledge has now been transferred to 3D models, which are able to mimic the architectural organization and functional properties of DA neurons in a more physiologically relevant condition. Indeed, in the last decade, human brain organoids have emerged as a useful tool for recapitulating key aspects of mature DA neuron tissue. By exploiting specific extrinsic patterning factors, hPSCs can now be differentiated, in a 3D space, toward a VM fate, resulting in regionalized human VM organoids. These VM 3D structures reproduce later stages of midbrain development in a dish and can result in the generation of functionally mature DA neurons with post-mitotic molecular features as well as electrophysiological activity. Additionally, distinct DA neuron subtypes also emerge within these VM organoids, mimicking human dopamine diversity *in vitro*. Neuromelanin-pigmented DA neurons, similar to A9 populations in SNpc in VM primates, can be detected in long-term 3D culture (Jo et al., 2016; Fiorenzano et al., 2021). Given their ability to generate functionally mature DA neurons releasing neuromelanin, VM organoids also represent a valid tool for PD modeling using iPSCs from PD patients. PD is considered one of the most complex neurological disorders, as it results from the intricate interaction of genetic, epigenetic, and environmental factors that make the study of this disease extremely challenging in both animal models and 2D culture.

Here, we describe a set of protocols from hPSC culture to the generation and characterization of VM organoids that can then be used to study the mechanisms underlying the development and maturation of DA neurons and to model pathological phenotypes by recapitulating the molecular hallmarks observed in PD patients.

Critical Parameters

The protocol described here can be adopted in different laboratories to differentiate VM organoids using different hPSC as well as iPSC lines. High-quality hPSC culture prior to differentiation is critical. For this, i) hPSC colonies should be maintained at around 70% to 80% confluence; ii) no areas undergoing spontaneous differentiation should be present; and iii) hPSCs should be routinely tested to ensure they are free from mycoplasma infection, using a mycoplasma PCR detection kit (Thermo Fisher Scientific, cat. no. 4460626 or similar).

Accurate titration of patterning factors during the differentiation of VM organoids is also crucial. To avoid repeated freeze-thawing that could alter the efficiency of differentiation, growth factors should be stored in working aliquots at −20°C. It is also important to bear in mind that different hPSCs may require different concentrations of patterning factors during differentiation. For example, the concentration of CHIR99021 proved to be particularly critical in our assays. For this reason, we suggest adapting our protocol to differentiate different cell lines by testing different CHIR99021 concentrations, to avoid contamination of non-VM progenitors. In that case, we suggest including two negative controls: i) differentiation without patterning factors and ii) cerebral organoid differentiation as a negative control of neuromelanin release (Table 3).

During VM organoid generation, we recommend using the same batch of Matrigel during embedding of the organoids to avoid variability in differentiation efficiency and in cellular composition. An automatic pipette should be used to obtain droplets of Matrigel for embedding in order to attenuate organoid-to-organoid morphological differences.

As a quality control, we recommend testing FOXA2/OTX2/LMX1A marker expression on day 20 to day 30 before performing the analysis on adult organoids, through RT-qPCR and immunofluorescence (Tables 1 and 2).

Troubleshooting

Please see Table 3 for a list of common problems with the protocols, their causes, and potential solutions.

Understanding Results

This protocol generates VM organoids that can be used to model both early and late phases of DA differentiation in a dish, from the formation of the mesencephalic floor plate to the generation of mature DA neurons capable of producing neuromelanin.

The morphological analysis of VM organoids at different developmental stages under a bright-field microscope is the first step in understanding the efficiency of differentiation. In fact, VM organoids change in size, shape, and cellular composition during dif-

Table 3 Troubleshooting

Problem	Possible cause	Solution
No embryoid bodies are formed by day 2	Number of cells too low	Check cell counting Make sure Y-27632 (ROCK inhibitor) was added
Different-sized organoids at day 2	Plating a variable of cell number in each microwell	Use automatic pipetting
Yellow medium at day 15	High organoid growth at this stage	Add larger volume of medium (6 ml/well)
Poor expression of *LMX1*$^{+}$/*FOXA2*$^{+}$ as assessed by RT-qPCR	Organoids have assumed a too rostral identity expressing *FOXG1*	Increase CHIR99021 concentration to 2.5 μM in order to achieve a more caudal patterning of VM organoids
Absence of bright buds and layer generation on days 10-20	Medium composition Working aliquot was subjected to multiple freeze/thaw cycles	Thaw new reagents and prepare fresh CHIR99021 aliquots
TH expression is restricted to the outer region of VM organoids.	The collected sections were derived from the organoid inner core	Collect internal and external organoid sections on the same slide during cryosectioning
Weak immunohistochemical expression of DA neuron markers	Organoids not properly fixed in 4% paraformaldehyde (Basic Protocol 3 step 1)	Increase paraformaldehyde concentration to 6% in Basic Protocol 3 step 9
Absence of neuromelanin release	Medium composition	Organoids may show either a too rostral (forebrain) or a too caudal (hindbrain) patterning

ferentiation. The formation of buds between days 8 and 12 in the outer organoid regions indicates that the floor plate is forming, and is a sign of correct differentiation (Fig. 2B and Fig. 3B-D). After morphological analysis, RT-qPCR is the most straightforward method to monitor the progress of VM organoid differentiation at a molecular level. We recommend analyzing the expression of early and late DA markers on days 15, 30, and 60 of differentiation to trace a reliable expression profile of VM organoid cultures.

FOXA2, *CORIN*, *EN1,* and *SHH* peak at day 30 and indicate the proper formation of DA neuron progenitors, which will go on to acquire mature molecular features and express markers such as NURR1 and TH at day 60 (Figs. 3A and 3F). Immunohistochemical analysis enables a more detailed evaluation of marker expression at the protein level and allows monitoring for the presence of specific cytoarchitecture within organoids. In fact, radially organized cell structures resembling rosettes are an important architectural element showing the correct formation of the mesencephalic floor plate (Fig. 3B-D). In line with RT-qPCR analysis, robust TH expression can only be detected at month 2 (Fig. 3E), indicating that cells are acquiring post-mitotic molecular characteristics. The detection of neuromelanin starting from month 3 using a bright-field microscope can further help characterize developing VM organoids and monitor differentiation efficiency. The release of neuromelanin is considered one of the last events in the maturation of human DA neurons. Morphological observations, combined with immunohistochemical analysis that can more precisely determine the release of neuromelanin, show that mature and pigmented DA neurons emerge within VM organoids (Fig. 4A-C).

Time Considerations

The preparation of hPSCs to start VM organoid differentiation (Basic Protocol 1) takes at least 10 days (including thawing, culturing, and one passage before beginning differentiation). The time required to generate VM organoids following Basic Protocol 2 can vary depending on the differentiation phase of interest. If the research question is focused on floor plate progenitor cells, the highest expression of FOXA2/OTX2/LMX1A occurs between days 20 and 30. If, instead, the research focus is on the maturation of DA neurons and cell-cell interaction studies with glial cells, 3 to 4 months are sufficient. For DA diversity studies or PD modeling using

patient-derived iPSCs, at least 6 months are needed to obtain fully mature DA neurons with robust neuromelanin release. For VM organoid characterization at a molecular level (Basic Protocol 3), gene expression analysis to determine progenitor cell identity requires 1 to 2 days. Immunocytochemical analysis to determine progenitor cell identity requires 2 days.

Acknowledgments

The authors thank Ulla Jarl and Bengt Mattsson for their technical assistance. The research leading to these results was supported by funding from the New York Stem Cell Foundation, European Research Council (ERC) under ERC Grant Agreement 771427, European Union–funded project NSC-Reconstruct (European Union, H2O20, GA no 874758, 2020-23), Swedish Research Council (2016-00873), Swedish Parkinson Foundation (Parkinsonfonden), Swedish Brain Foundation, Strategic Research Area at Lund University Multipark, and Knut and Alice Wallenberg Stiftelse (KAW 2018-0040). Malin Parmar is a New York Stem Cell Foundation Robertson Investigator. Alessandro Fiorenzano is the recipient of grants from the Thorsten and Elsa Segerfalk Foundation, the Swedish Parkinson Foundation (Parkinsonfonden 1347/21) and the Anna-Lisa Rosenberg Foundation, which used to support this study.

Author Contributions

Edoardo Sozzi: Conceptualization, Data curation, Formal analysis, Investigation, Methodology, Visualization, Original draft; **Fredrik Nilsson**: Formal analysis, Investigation, Draft review and editing; **Janko Kajtez**: Visualization, Draft review and editing; **Malin Parmar**: Conceptualization, Funding acquisition, Resources, Supervision, Draft review and editing; **Alessandro Fiorenzano**: Conceptualization, Data curation, Funding acquisition, Methodology, Resources, Supervision, Original draft.

Conflict of Interest

MP is the owner of Parmar Cells AB and co-inventor of the following patents WO2016162747A2, WO2018206798A1, and WO2019016113A1. MP is a paid consultant, steering group member, and performs commissioned research for Novo Nordisk AS Cell Therapy Research and Development unit, and is a member of Arbor Bio SAB. The remaining authors declare no competing interests.

Data Availability Statement

The data, tools, and materials (or their source) that support the protocol are available from the corresponding author upon reasonable request.

Literature Cited

Agarwal, D., Sandor, C., Volpato, V., Caffrey, T. M., Monzon-Sandoval, J., Bowden, R., … Webber, C. (2020). A single-cell atlas of the human substantia nigra reveals cell-specific pathways associated with neurological disorders. *Nature Communication*, *11*(1), 4183. doi: 10.1038/s41467-020-17876-0

Arlotta, P., & Paşca, S. P. (2019). Cell diversity in the human cerebral cortex: From the embryo to brain organoids. *Current Opinion in Neurobiology*, *56*, 194–198. doi: 10.1016/j.conb.2019.03.001

Bjorklund, A., & Dunnett, S. B. (2007). Dopamine neuron systems in the brain: An update. *Trends in Neuroscience (Tins)*, *30*(5), 194–202. doi: 10.1016/j.tins.2007.03.006

Cederquist, G. Y., Asciolla, J. J., Tchieu, J., Walsh, R. M., Cornacchia, D., Resh, M. D., & Studer, L. (2019). Specification of positional identity in forebrain organoids. *Nature Biotechnology*, *37*(4), 436–444. doi: 10.1038/s41587-019-0085-3

Demers, C. J., Soundararajan, P., Chennampally, P., Cox, G. A., Briscoe, J., Collins, S. D., & Smith, R. L. (2016). Development-on-chip: In vitro neural tube patterning with a microfluidic device. *Development*, *143*(11), 1884–1892. doi: 10.1242/dev.126847

Fiorenzano, A., Birtele, M., Wahlestedt, J. N., & Parmar, M. (2021). Evaluation of TH-Cre knock-in cell lines for detection and specific targeting of stem cell-derived dopaminergic neurons. *Heliyon*, *7*(1), e06006. doi: 10.1016/j.heliyon.2021.e06006

Fiorenzano, A., Pascale, E., Gagliardi, M., Terreri, S., Papa, M., Andolfi, G., … Fico, A. (2018). An ultraconserved element containing lncRNA preserves transcriptional dynamics and maintains ESC self-renewal. *Stem Cell Reports*, *10*(3), 1102–1114. doi: 10.1016/j.stemcr.2018.01.014

Fiorenzano, A., Sozzi, E., Birtele, M., Kajtez, J., Giacomoni, J., Nilsson, F., … Parmar, M. (2021). Single-cell transcriptomics captures features of human midbrain development and dopamine neuron diversity in brain organoids. *Nature Communication*, *12*(1), 7302. doi: 10.1038/s41467-021-27464-5

Fiorenzano, A., Sozzi, E., Parmar, M., & Storm, P. (2021). Dopamine neuron diversity: Recent advances and current challenges in human stem cell models and single cell sequencing. *Cells*, *10*(6), 1366. doi: 10.3390/cells10061366

Jo, J., Xiao, Y. X., Sun, A. X., Cukuroglu, E., Tran, H. D., Goke, J., … Ng, H. H. (2016). Midbrain-like organoids from human pluripotent stem cells contain functional dopaminergic and neuromelanin-producing neurons. *Cell*

Stem Cell, *19*(2), 248–257. doi: 10.1016/j.stem.2016.07.005

Kanton, S., Boyle, M. J., He, Z., Santel, M., Weigert, A., Sanchis-Calleja, F., … Camp, J. G. (2019). Organoid single-cell genomic atlas uncovers human-specific features of brain development. *Nature*, *574*(7778), 418–422. doi: 10.1038/s41586-019-1654-9

Kelava, I., & Lancaster, M. A. (2016). Stem cell models of human brain development. *Cell Stem Cell*, *18*(6), 736–748. doi: 10.1016/j.stem.2016.05.022

Kim, J., Koo, B. K., & Knoblich, J. A. (2020). Human organoids: Model systems for human biology and medicine. *Nature Reviews Molecular Cell Biology*, *21*(10), 571–584. doi: 10.1038/s41580-020-0259-3

Krishnaswami, S. R., Grindberg, R. V., Novotny, M., Venepally, P., Lacar, B., Bhutani, K., … Lasken, R. S. (2016). Using single nuclei for RNA-seq to capture the transcriptome of postmortem neurons. *Nature Protocols*, *11*(3), 499–524. doi: 10.1038/nprot.2016.015

Lancaster, M. A., Renner, M., Martin, C. A., Wenzel, D., Bicknell, L. S., Hurles, M. E., … Knoblich, J. A. (2013). Cerebral organoids model human brain development and microcephaly. *Nature*, *501*(7467), 373–379. doi: 10.1038/nature12517

Miura, Y., Li, M. Y., Birey, F., Ikeda, K., Revah, O., Thete, M. V., … Pasca, S. P. (2020). Generation of human striatal organoids and cortico-striatal assembloids from human pluripotent stem cells. *Nature Biotechnology*, *38*(12), 1421–1430. doi: 10.1038/s41587-020-00763-w

Nilsson, F., Storm, P., Sozzi, E., Hidalgo Gil, D., Birtele, M., Sharma, Y., … Fiorenzano, A. (2021). Single-cell profiling of coding and noncoding genes in human dopamine neuron differentiation. *Cells*, *10*(1), 137. doi: 10.3390/cells10010137

Nolbrant, S., Heuer, A., Parmar, M., & Kirkeby, A. (2017). Generation of high-purity human ventral midbrain dopaminergic progenitors for in vitro maturation and intracerebral transplantation. *Nature Protocols*, *12*(9), 1962–1979. doi: 10.1038/nprot.2017.078

Pasca, S. P. (2018). The rise of three-dimensional human brain cultures. *Nature*, *553*(7689), 437–445. doi: 10.1038/nature25032

Quadrato, G., Nguyen, T., Macosko, E. Z., Sherwood, J. L., Min Yang, S., Berger, D. R., … Arlotta, P. (2017). Cell diversity and network dynamics in photosensitive human brain organoids. *Nature*, *545*(7652), 48–53. doi: 10.1038/nature22047

Rifes, P., Isaksson, M., Rathore, G. S., Aldrin-Kirk, P., Moller, O. K., Barzaghi, G., … Kirkeby, A. (2020). Publisher correction: Modeling neural tube development by differentiation of human embryonic stem cells in a microfluidic WNT gradient. *Nature Biotechnology*, *38*(11), 1357. doi: 10.1038/s41587-020-0590-4

Siddiqi, S. H., Kording, K. P., Parvizi, J., & Fox, M. D. (2022). Causal mapping of human brain function. *Nature Reviews Neuroscience*, *23*(6), 361–375. doi: 10.1038/s41583-022-00583-8

Tiklova, K., Nolbrant, S., Fiorenzano, A., Bjorklund, A. K., Sharma, Y., Heuer, A., … Parmar, M. (2020). Single cell transcriptomics identifies stem cell-derived graft composition in a model of Parkinson's disease. *Nature Communications*, *11*(1), 2434. doi: 10.1038/s41467-020-17421-z

Corrections

In this publication, the following correction has been made:

In step 14 of Basic Protocol 2, the concentration of SB431542 has been changed to 10 μM.

The current version online now includes this correction and may be considered the authoritative version of record.

frontiers | Frontiers in Cell and Developmental Biology

TYPE Original Research
PUBLISHED 14 October 2022
DOI 10.3389/fcell.2022.1023279

OPEN ACCESS

EDITED BY
Mark Denham,
Danish Research Institute of Translational Neuroscience (DANDRITE), Denmark

REVIEWED BY
Massimiliano Caiazzo,
Utrecht University, Netherlands
Cheen Euong Ang,
Harvard University, United States

*CORRESPONDENCE
Alessandro Fiorenzano,
alessandro.fiorenzano@med.lu.se

SPECIALTY SECTION
This article was submitted to Stem Cell Research, a section of the journal Frontiers in Cell and Developmental Biology

RECEIVED 19 August 2022
ACCEPTED 28 September 2022
PUBLISHED 14 October 2022

CITATION
Sozzi E, Kajtez J, Bruzelius A, Wesseler MF, Nilsson F, Birtele M, Larsen NB, Ottosson DR, Storm P, Parmar M and Fiorenzano A (2022), Silk scaffolding drives self-assembly of functional and mature human brain organoids.
Front. Cell Dev. Biol. 10:1023279.
doi: 10.3389/fcell.2022.1023279

Silk scaffolding drives self-assembly of functional and mature human brain organoids

Edoardo Sozzi[1], Janko Kajtez[1], Andreas Bruzelius[2], Milan Finn Wesseler[3], Fredrik Nilsson[1], Marcella Birtele[1], Niels B. Larsen[3], Daniella Rylander Ottosson[2], Petter Storm[1], Malin Parmar[1] and Alessandro Fiorenzano[1]*

[1]Department of Experimental Medical Science, Developmental and Regenerative Neurobiology, Wallenberg Neuroscience Center, Lund Stem Cell Center, Lund University, Lund, Sweden, [2]Department of Experimental Medical Science, Regenerative Neurophysiology, Wallenberg Neuroscience Center, Lund Stem Cell Center, Lund University, Lund, Sweden, [3]Department of Health Technology (DTU Health Tech), Technical University of Denmark, Kongens Lyngby, Denmark

Human pluripotent stem cells (hPSCs) are intrinsically able to self-organize into cerebral organoids that mimic features of developing human brain tissue. These three-dimensional structures provide a unique opportunity to generate cytoarchitecture and cell-cell interactions reminiscent of human brain complexity in a dish. However, current *in vitro* brain organoid methodologies often result in intra-organoid variability, limiting their use in recapitulating later developmental stages as well as in disease modeling and drug discovery. In addition, cell stress and hypoxia resulting from long-term culture lead to incomplete maturation and cell death within the inner core. Here, we used a recombinant silk microfiber network as a scaffold to drive hPSCs to self-arrange into engineered cerebral organoids. Silk scaffolding promoted neuroectoderm formation and reduced heterogeneity of cellular organization within individual organoids. Bulk and single cell transcriptomics confirmed that silk cerebral organoids display more homogeneous and functionally mature neuronal properties than organoids grown in the absence of silk scaffold. Furthermore, oxygen sensing analysis showed that silk scaffolds create more favorable growth and differentiation conditions by facilitating the delivery of oxygen and nutrients. The silk scaffolding strategy appears to reduce intra-organoid variability and enhances self-organization into functionally mature human brain organoids.

KEYWORDS

human pluripotent stem cells, cerebral organoid, silk scaffolding, tissue engineering, oxygen sensing

Introduction

The inaccessibility of human brain and the limited availability of human fetal tissue make studies on brain development, function and disease extremely challenging (Kelava and Lancaster, 2016; Di Lullo and Kriegstein, 2017; Fiorenzano et al., 2021c). In recent years, the emergence of brain organoids has brought about a major advancement in overcoming such issues. These three-dimensional (3D) tissue models have equipped researchers with a powerful *in vitro* platform that relies on the remarkable property of human pluripotent stem cells (hPSCs) to self-organize into complex 3D tissue structures that recapitulate architectural, functional, and transcriptional aspects of healthy and diseased human brain (Lancaster et al., 2013; Quadrato et al., 2017; Kanton et al., 2019; Bennett et al., 2021; Kelava et al., 2022). Current methodologies for the generation of human brain organoids can be broadly divided into two groups that follow either unguided or guided differentiation protocols (Arlotta and Pasca, 2019; Kim et al., 2020). The unguided approach leverages the intrinsic developmental potential of hPSCs and maximizes their inherent propensity to undergo spontaneous morphogenesis and self-driven differentiation. Consequently, the unguided route gives rise to brain organoids, commonly referred to as *cerebral* organoids, with complex structural patterning and cytoarchitecture akin to the native tissue of different brain regions. As such, these protocols provide an invaluable means to study cell-cell interactions and cellular diversity *in vitro* (Lancaster and Knoblich, 2014; Quadrato et al., 2017; Renner et al., 2017).

However, unguided protocols are susceptible to low reproducibility and unpredictable tissue heterogeneity both within and between individual organoids and batches. Brain organoids generated in this manner may also contain relatively large numbers of unwanted non-neuronal cells including derivatives of mesoderm and endoderm lineages. On the other hand, brain organoid protocols based on guided differentiation reduce cellular heterogeneity through the use of extrinsic patterning factors that induce hPSC toward the acquisition of cytoarchitectural identities mimicking individual brain regions such as dorsal and ventral forebrain, midbrain, and spinal cord (Bagley et al., 2017; Cederquist et al., 2019; Faustino Martins et al., 2020; Miura et al., 2020; Fiorenzano et al., 2021b). While guided brain organoid protocols provide an excellent platform to study region-specific features, the patterning factors used may reduce cell diversity and mask important developmental processes and refined phenotypes controlled by cell-cell interaction or finely controlled molecular gradients (Makrygianni and Chrousos, 2021; Nilsson et al., 2021; Sozzi et al., 2022). Furthermore, guided approaches do not fully address the limitations commonly encountered in the field of brain organoids such as inter-organoid variability, incomplete neuronal maturation, and the detrimental effects of insufficient tissue oxygenation leading to a hypoxic inner core (Pasca et al., 2019; Velasco et al., 2019; Bhaduri et al., 2020; Qian et al., 2020; Mansour et al., 2021). Therefore, there is an urgent need for novel solutions that are able to overcome these limitations while providing robust support for unguided hPSC differentiation.

To this end, bioengineering strategies aimed at generating homogeneous, mature, and healthy organoids are actively being pursued. Major efforts are being directed toward promoting more uniform tissue oxygenation as well as increased nutrient supply to and waste removal from cells throughout the organoid—tasks performed by the vascular network in native tissue. While ectopic vascularization in brain organoids has been achieved after transplantation into mouse cortex (Mansour et al., 2018), approaches to create vascular networks *in vitro* are still in the early phase of development and require advanced bioengineering systems (Cakir et al., 2019). As an alternative, researchers have resorted to cutting organoids mechanically into slice cultures (Qian et al., 2020) or have developed rotational mini-bioreactors and microfluidic chambers to enhance oxygen/nutrient diffusion *via* active flow of culture media leading to reduced hypoxia and enhanced functional maturation (Qian et al., 2016; Ao et al., 2020; Cho et al., 2021). It has also been hypothesized that biomaterial scaffolding (used in addition to the embedding hydrogel such as matrigel) could enhance cerebral organoid formation both structurally and functionally by templating hPSC aggregation, expansion, and differentiation along their backbones. To our knowledge, only two studies have tested this hypothesis (Lancaster et al., 2017; Rothenbucher et al., 2021). While these investigations confirmed that secondary biomaterial can direct hPSC self-organization into more homogeneous and reproducible neuroepithelial structures with enhanced gyrification by increasing the surface-to-volume ratio of the organoid (Lancaster et al., 2017; Rothenbucher et al., 2021), the use of synthetic scaffolding that is pseudo-3D at microscale, functionally inert, and without the ability to create microchannels limits the wider application of this approach (Lancaster et al., 2017; Rothenbucher et al., 2021).

Spider silk, a natural biomaterial with excellent biocompatibility and unique mechanical properties (Rising et al., 2011), holds great promise for unleashing the full potential of bioengineered scaffolding in organoid generation. Compared to silk fibroin, a protein obtained from *Bombyx mori* cocoons that has been extensively used in tissue engineering and shown to support 3D neuronal cultures (but not brain organoid formation) (Tang-Schomer et al., 2014; Sood et al., 2019; Rouleau et al., 2020), recombinant spider silk provides a highly reproducible and well-defined natural 3D scaffolding that is easy to handle and readily amenable (Johansson et al., 2019). We recently established that spider silk supports the successful generation of regionalized ventral midbrain organoids (Fiorenzano et al., 2021b). However, the effect of spider silk scaffolding on spontaneous morphogenesis and unguided hPSC self-patterning in cerebral organoids remains unexplored.

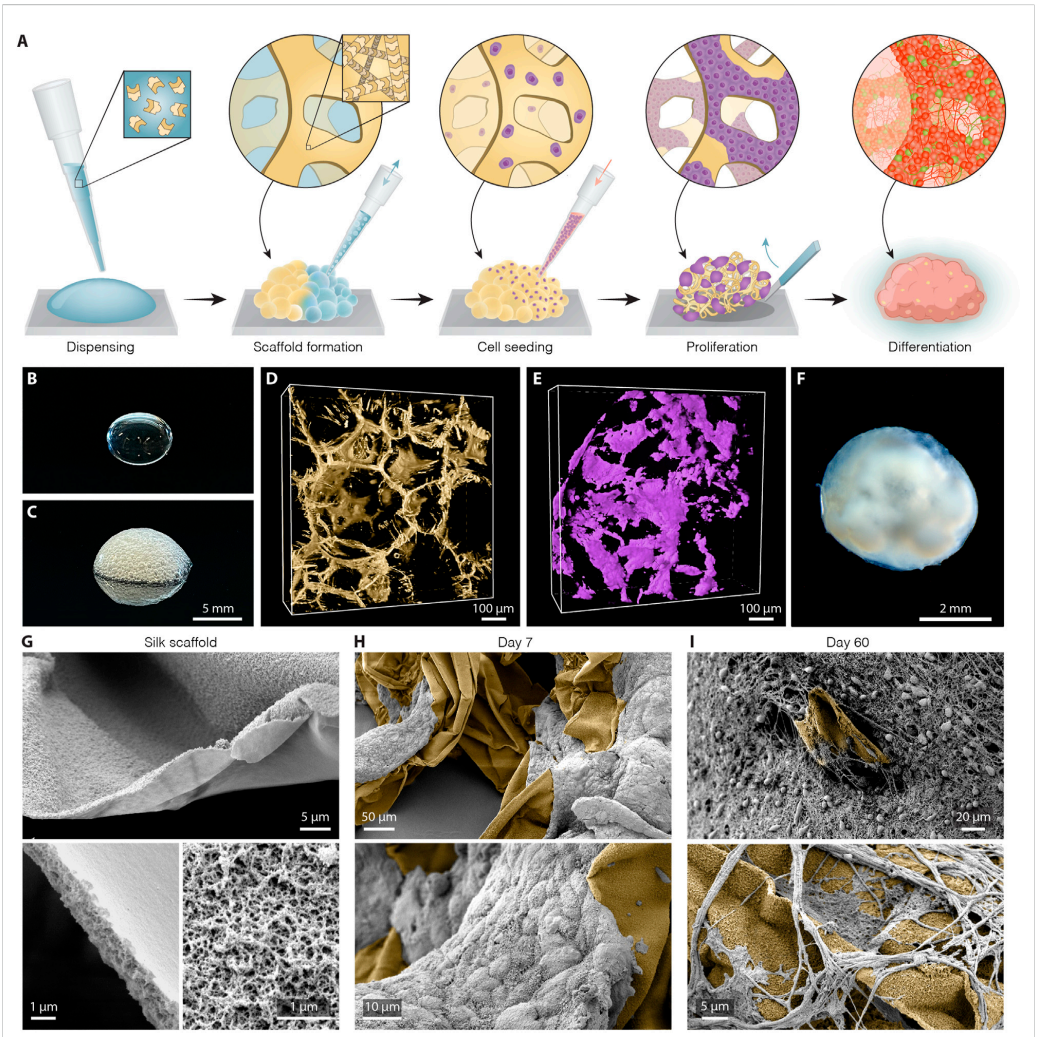

FIGURE 1
Generation of silk human cerebral organoids. **(A)** Schematic overview of silk scaffolding strategy for generation of silk human brain organoid. **(B,C)** Representative image of silk **(B)** in a liquid form as a droplet and **(C)** as a foam after introduction of air bubbles. Scale bar 5 mm. **(D)** Representative view of confocal fluorescence image stack of the polymerized silk scaffold (yellow) on day 5 of differentiation. Scale bar 100 µm. **(E)** Confocal image reconstructing in 3D live hPSCs (lilac) seeded along the silk fiber network. Scale bar 100 µm. **(F)** Representative bright-field image of long-term silk cerebral organoid culture (120 days). Scale bar 2 mm. **(G)** Scanning electron images (SEM) of silk scaffold without cells showing polymerized silk microfibers built up of nanofibrils. Scale bars 5 µm (top), 1 µm (bottom). **(H)** SEM images showing adherence and growth of hPSCs (grey) along the length of silk microfibers (yellow) at day 7. Scale bars 50 µm (top), 10 µm (bottom). **(I)** SEM images showing silk scaffold (yellow) with adherent neuronal cells and formation of intricate axon projections within silk engineered human cerebral organoids at day 60. Scale bars 20 µm (top), 5 µm (bottom).

In this work, we showed that spider silk microfibers biofunctionalized with recombinant full-length human laminin assembled into a hierarchical 3D scaffold are able to instruct hPSCs to self-arrange into cerebral organoids. Importantly, the silk scaffolding assumes a delicate 3D structure at both the macro- and microscale that not only templates cellular

seeding at the initial stages of organoid formation but also promotes the formation of interconnected microcavities as a form of passive vasculature. The presence of a silk scaffold enhanced neuroectoderm formation while reducing intra-organoid variability. Single cell transcriptomics revealed that a greater number of neurons are formed and that mature molecular features of human corticogenesis are better recapitulated within silk organoids cultured long term. This is furthermore accompanied by reduced activation of cellular stress pathways. Importantly, optical 3D mapping of tissue oxygenation revealed that the oxygen supply was increased in silk organoids, thus minimizing the formation of an inner necrotic core. Our silk scaffolding approach therefore provides a novel and reproducible solution for the generation of healthy cerebral organoids.

Results

Generation of silk cerebral organoids

To establish the bioengineered human brain organoid platform, we used a silk scaffold generated *via* a simple, easily adaptable, and reproducible approach (overall methodological concept presented in Figure 1A). The recombinant spider silk (Widhe et al., 2016) scaffold was biofunctionalized with full length human laminin 111, an important extracellular matrix protein that provides cell-adhesion motifs for stable neuronal adhesion, expansion, and maturation (Kirkeby et al., 2017; Fiorenzano et al., 2021a; Fiorenzano et al., 2021b). To form the scaffolding, air bubbles were introduced into droplets of ice-cold silk protein solution *via* repeated pipetting (Figures 1B,C). Restricted to thin layers between air pockets, soluble silk proteins polymerize at 37 °C into a 3D network of fibers formed around the wall of each air bubble, thereby producing a temporary foam in which undifferentiated hPSCs were dispersed. Attachment of cells to the scaffold is accompanied by the evacuation of air from the bubbles by diffusion into the surrounding cell culture media and by cellular consumption. This process results in a creation of a self-supported 3D network of fibers riddled with microcavities that successfully serves as a substrate for hPSC differentiation (Figure 1D). As can be seen by 3D fluorescence confocal microscopy, the cells propagated progressively along the surface of the formed scaffold and filled the inner space between silk fibers (Figure 1E). During this phase, the silk scaffold was attached to the bottom of an ultra-low attachment plate, generating a stationary engineered 3D culture. After 5 days, the culture was switched to neural induction media able to generate extensive cellular diversity, following a well-established and widely used protocol for the generation of cerebral organoids (Lancaster and Knoblich, 2014). Eight days after the start of differentiation, once the cells had filled the entire scaffold and the anchored organoid had grown in size, it was lifted from the bottom of the well to continue culturing in floating conditions, facilitating more efficient exchange of nutrients and oxygen (Figure 1F). Scanning electron microscope (SEM) imaging of the generated scaffold and subsequent organoid formation showed that silk, templated by air bubbles, polymerizes into flat microfibers with thickness of ~1 μm and composed of defined nanofibrils (Figure 1G). Notably, nano-topography could play an important role by facilitating and enhancing cell adhesion and neuronal growth even on cell-inert substrates (Asif et al., 2020). SEM images further show that both neuronal progenitors interact directly with the silk surface and successfully attached along the length of the silk microfibers in the engineered organoids (Figure 1H) while differentiating into mature neurons with projections extending along the silk scaffold (Figure 1I, Supplementary Figure S1A,B).

Compared to cerebral organoids conventionally generated using the same protocol (termed "non-silk") as a control, silk organoids displayed a less clear boundary between outer and inner regions, as well as the absence of a distinct core (Supplementary Figure S1C,D). Noteworthy, when the silk bubbles burst during silk organoid differentiation, they leave an empty space that will only be partially filled by cells (Figures 1G–I). This generates micropore structures that become smaller and smaller during stem cell differentiation (Supplementary Figure S1E,F).

Silk scaffolding enhances neural induction in cerebral organoids

Whole transcriptome expression analysis was performed using RNA-seq to directly compare silk and non-silk organoids at day 20 of differentiation, analyzing three biological replicates of each culture condition. We found a total of ~900 differentially expressed protein-coding genes (≥2-fold, adjusted p-value < 0.05) in the two different organoid culture conditions (Supplementary Figure S1G). In comparison to cerebral organoids grown without silk microfibers, silk organoids showed more robust upregulation of neuroectodermal markers (*FABP7*, *GBX2*, *FOXG1*, *NCAM1*) and complete downregulation of pluripotency-associated genes (*DPPA3*, *NANOG*, *LEF1*, *CLDN1*) (Figure 2A). In contrast, a different set of genes was found uniquely upregulated in non-silk organoids (Figure 2A), indicating the presence of non-neural identities at an early stage of brain organoid differentiation as revealed by mesodermal- and endodermal-related genes (*NODAL*, *SOX17*, *FOXA2*, *GATA4*) (Figure 2A and Supplementary Figure S1G). These findings were further validated by quantitative PCR (qPCR) (Supplementary Figure S1H–J). Additionally, Gene Ontology analysis of brain organoids grown with silk microfibers revealed a significant enrichment of terms all related to neurodevelopment including *Nervous System,* and *Sensory* and *Synaptic pathways* (Figures 2B,C).

Consistent with RNAseq data, silk organoids established an internally uniform cell organization with the formation of

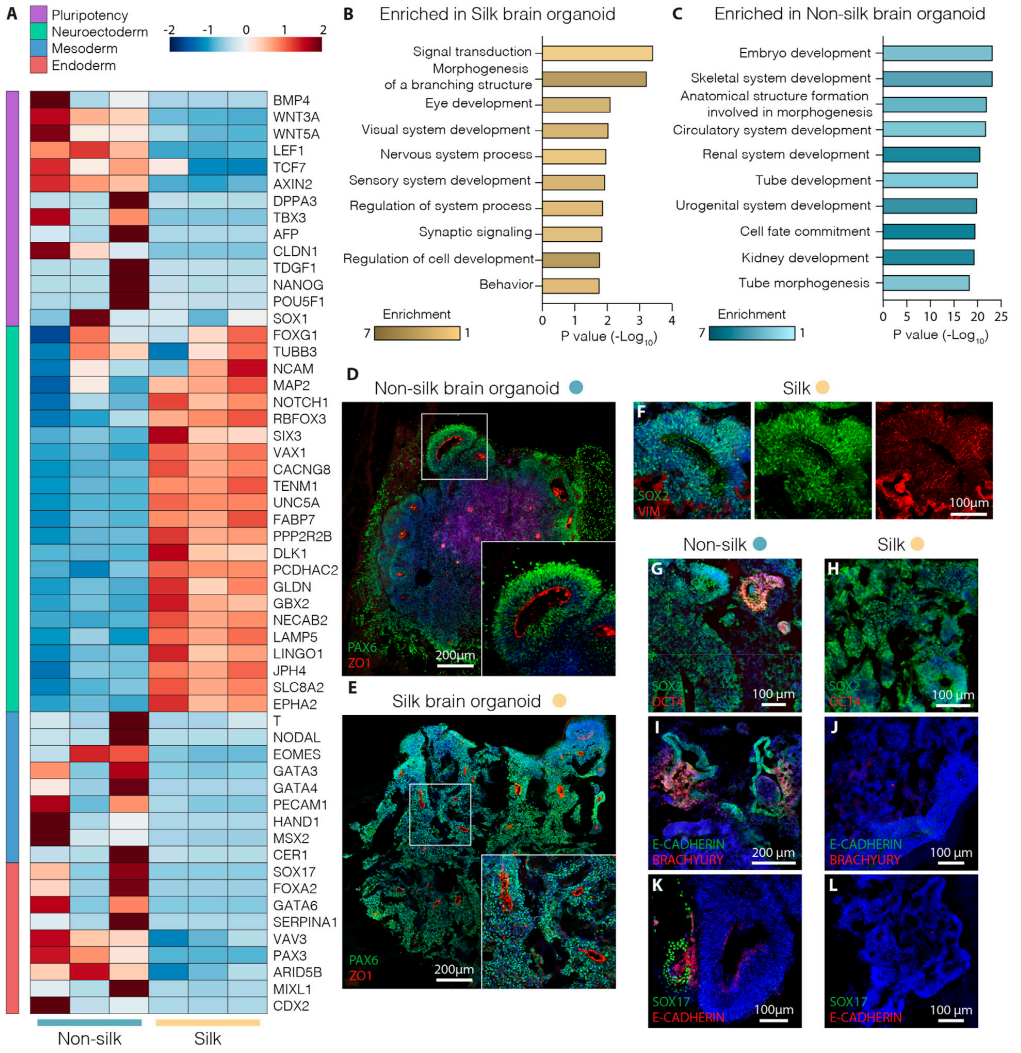

FIGURE 2
Silk cerebral organoids display enhanced neurogenesis. **(A)** Heat map showing expression levels of selected differentially expressed genes (DEG) considered markers of pluripotency and neuroectoderm, meso-endoderm differentiation in three biological replicates of silk and non-silk human brain organoids at day 20. **(B,C)** Enrichment of top ten biological process gene ontology terms ordered by *p*-value of upregulated genes in **(B)** silk and **(C)** non-silk brain organoids at day 20. **(D,E)** Immunohistochemistry of PAX6 and ZO1 showing *neural rosettes* in non-silk **(D)** and silk brain organoid **(E)** at day 20. Scale bars 200 µm. **(F)** Cryosection of silk brain organoid at day 20 showing SOX2/VIM double staining. Scale bar 100 µm. **(G,H)** Immunohistochemistry of SOX2/OCT4 in **(G)** non-silk and **(H)** silk organoid at day 20. Scale bars 100 µm. **(I–L)** Immunohistochemistry of **(I,J)** E-CAD/BRA and K,L) E-CAD/SOX17 in organoids grown with or without silk scaffold at day 20. Scale bars 200 µm **(I)** and 100 µm **(J–L)**. Nuclei were stained with DAPI.

radially organized cell structures resembling the neuroepithelial rosettes commonly described in cerebral organoids (Figures 2D,E and Supplementary Figure S1H). After 20 days of differentiation, intra-organoid variability was reduced in the silk organoids, shown by the emergence of homogeneous rosette-like structures expressing PAX6/SOX2/ZO1 (Figures 2D–F)

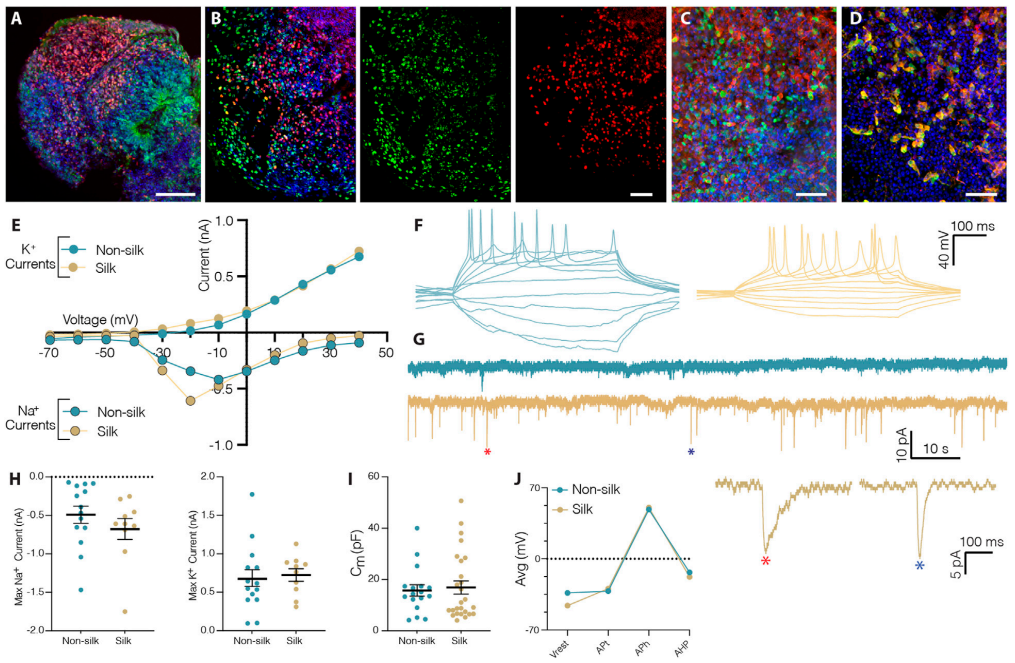

FIGURE 3

Silk scaffolding sustains functionally mature neurons generation. **(A)** Immunohistochemistry of FOXG1/CTIP2 showing cortical plate layer formation in silk brain organoid at day 60. Scale bar 100 µm. **(B)** Cryosection of silk brain organoid at day 120 showing SATB2/CTIP2 double staining. Scale bar 50 µm. **(C,D)** Immunohistochemistry of **(C)** VGLUT1/MAP2, **(D)** GABA/MAP2 showing distinct neuronal identities within silk brain organoids at day 120. Scale bars 50 µm. **(E)** Inward Na^+ and outward K^+ currents plotted as a function of stepwise voltage induction of cells in non-silk (n = 14) and silk (n = 10) organoids at 3 months. **(F)** Representative trace of evoked action potentials under rheobase current injection steps of cells in non-silk and silk organoids after 3 months in culture. **(G)** Sample traces of spontaneous activity recorded in voltage clamp, including magnification of selected postsynaptic events. **(H)** Quantification of maximum inward sodium current and maximum outward potassium current in silk (n = 14) and non-silk (n = 10) organoids after 3 months in culture. **(I)** Quantification of membrane capacitance in silk (n = 26) and non-silk (n = 17) organoids after 3 months in culture **(J)** Average value of action potential (AP) properties, resting membrane potential (V_{rest}), AP threshold (AP_t), AP amplitude (AP_h), and afterhyperpolarization (AHP). n = 5 silk, n = 5 non-silk, 3 months. Nuclei were stained with DAPI.

throughout both the core and the edge. By contrast, non-silk organoids exhibited ectopic expression of BRA and SOX17 (Figure 2I–L and Supplementary Figure S1J) as well as retaining OCT4 levels in spatially restricted areas (Figures 2G,H and Supplementary Figure S1I). These findings show that the presence of silk scaffolds guides hPSCs to more precisely self-pattern toward neuroectodermal identity during cerebral organoid differentiation.

scRNAseq reveals mature neuronal molecular features in silk-engineered cerebral organoids

Histological analysis revealed that silk cerebral organoids self-organized into different forebrain regions including those with ventral and dorsal forebrain cellular identities (Supplementary Figure S2A–D). As previously reported for conventional 3D cultures, silk brain organoids also presented a mature cortical layer organization (Figures 3A,B and Supplementary Figure S2E,F) (Lancaster et al., 2013; Quadrato et al., 2017). At month 2, cortical plate layer formation was defined by the presence of $FOXG1^+$ and $CTIP2^+$ neuronal cells enriched in the internal and external layer respectively (Figure 3A and Supplementary Figure S2E). At month 4, further segregation into early-born $CTIP2^+$ neurons in the inner and late-born $SATB2^+$ neurons in the outer layer defined a more mature degree of cortical organization (Figure 3B and Supplementary Figure S2F). The expression of glutamatergic (Vglut1) and GABAergic (GABA, GAD65/67) markers pointed to the generation of mature neuronal cells within silk cerebral organoids (Figures 3C,D and Supplementary Figure S2G–L).

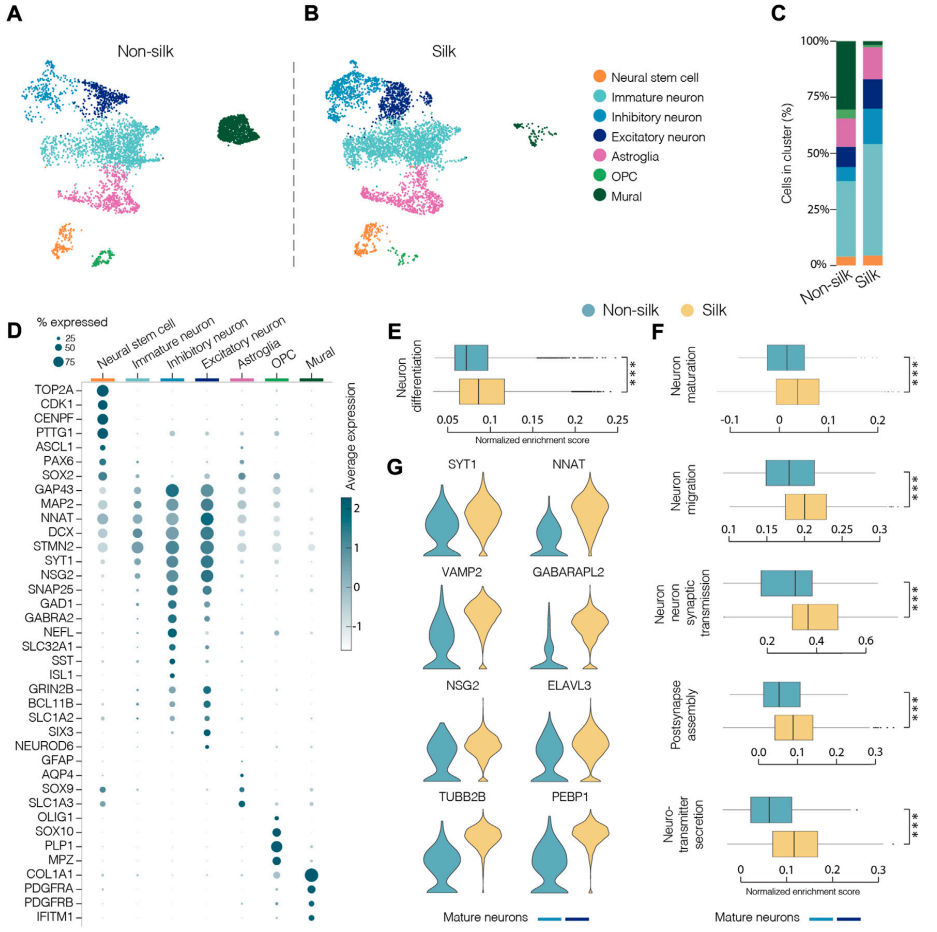

FIGURE 4

Single-cell transcriptomics reveals mature neuronal features in silk cerebral organoids. **(A and B)** 2D scatter plot of uniform manifold approximation and projection (UMAP) embeddings of non-silk H) and silk I) organoids at day 120 each showing clustering of ~4,500 randomly selected cells. Colors indicate different cell type assignments. OPC, oligodendrocyte progenitor cells. **(C)** Bar plot showing the percentage of cells belonging to each cluster from silk and non-silk organoids. **(D)** Dot plot showing expression levels of indicated genes in each cluster. Indicated genes are established markers for neural stem cells, inhibitory and excitatory neuronal subtypes, astroglia, OPC, and mural cells. **(E)** Gene set enrichment analysis (GSEA) showing a statistically significant different score in *Neuron differentiation* term in non-silk and silk brain organoids. ***$p <$ 0.001, two-tailed Wilcoxon rank sum test. **(F)** GSEA of *Neuron maturation, Neuron migration, Synaptic transmission, Post-synapse assembly and Neurotransmitter secretion* terms in mature neuronal clusters. ***$p < 0.001$, two-tailed Wilcoxon rank sum test. **(G)** Expression of representative mature neuronal markers in non-silk and silk brain organoid neuronal clusters after 4 months in culture.

Patch-clamp electrophysiological recordings performed at 3 months confirmed the functional maturation of neurons (Figures 3E–J). As in non-silk organoids, voltage-gated sodium (Na^+) and potassium (K^+) currents indicated the active neuronal state within silk organoids (Figures 3E,H). In line with these findings, we also found that neurons in both silk and non-silk organoids were able to elicit current-induced action potentials (APs). However, while neurons in the conventional 3D culture fired single APs, neurons within silk brain organoids were able to fire multiple APs (Figure 3F) revealing a more mature neuronal profile. Examining the AP discharge pattern and cell-intrinsic properties, we found that threshold (APt), amplitude (APh), afterhyperpolarization (AHp) and resting membrane potential (Vrest) all remained similar across these two 3D

culture conditions despite the difference in AP frequency (Figures 3I,J). We next evaluated the synaptic network by analyzing post-synaptic currents. While neurons in the non-silk cerebral organoids did not display any post-synaptic currents, multiple neurons (n = 7/20) in silk organoids exhibited post-synaptic currents indicative of a functional neuronal network, suggesting that silk 3D cultures facilitate formation of functional neuronal circuitries (Figure 3G).

To comprehensively characterize and compare cellular composition and neuronal identities within cerebral silk and non-silk organoids, we performed droplet-based single cell sequencing (10x) after 4 months in culture. Uniform manifold approximation and projection (UMAP) and graph-based clustering visualized seven major clusters after single cell data integration using Harmony (https://www.nature.com/articles/s41592-019-0619-0). We manually annotated the identified cell clusters by analyzing genes with highest differential expression, which were then used together with canonical cell type markers (Figures 4A,B). We also used previously published single cell datasets of cerebral organoids (Kanton et al., 2019) to confirm our cell type annotation by projecting the reference labels onto our data using Seurat's v4 label transfer (Supplementary Figure S3A–C). UMAP revealed that similar cell types were formed in both non-silk and silk-bioengineered cerebral organoids (Figures 4A–C). After 4 months, a small cluster of *Neural stem cells* (orange) could still be detected in the UMAP space and was made up of cells expressing neural markers (*ASCL1*, *PAX6*, *SOX2*) with a proliferative signature (*TOP2A*, *CDK1*, *CENPF*) (Figures 4A,B,D and Supplementary Figure S3D,E). Cells in the turquoise cluster mainly differed from *Neural stem cells* in that they exited from cell cycle while retaining the expression of neural progenitor markers (*SOX2*, *PAX6*) (Figures 4A,B,D and Supplementary Figure S3D,E). We named this cluster *Immature neurons*, as these cells also acquired the expression of early neuronal markers (*STMN2*, *DCX*, *MAP2*) but lacked a clear mature neuronal signature (Figure 4D and Supplementary Figure S3E). A large fraction of cells was assigned to neuronal identity at this developmental stage, and they were enriched for markers of cerebral cortex neurons (*NEUROD6*, *BCL11b*, also known as *CTIP2*) (Figures 4A–C). Both excitatory (*SLC1A2*, *GRIN2B*, *SLC17A7* also known as *VGLUT1*) (dark blue) and inhibitory (*GAD1*, *GABRA2*, *SST*) (light blue) neuronal cell types emerged in both cerebral organoids grown with and without scaffolding (Figures 4A–D and Supplementary Figure S3E). Within the excitatory neuronal cluster, molecular features related to neural retina (*SIX3*, *GBN1*) were also detected (Supplementary Figure S3E). Alongside neuroectodermal-derived cell types, we were able to detect astroglia (*GFAP, AQP4, RFX4*) as well as a small group of oligodendrocyte progenitors (OPC, *OLIG1, OLIG2, SOX10*) (Figure 4D and Supplementary Figure S3E–G). We also detected a cluster of cells expressing markers of mural cells (*COL1A1, IFITM1, S100A11*) as well as genes involved in mesoderm commitment pathway (*FOXP1, FOXC1, CD248*) (Figures 4A–D and Supplementary Figure S3E,H–K) similar to Kanton et al. (Kanton et al., 2019). These mural cells are distinct from a newly identified class of cells termed VLMCs (Zeisel et al., 2018), that have been detected in dopaminergic progenitor grafts (Tiklova et al., 2020) as well as in midbrain organoids (Fiorenzano et al., 2021b). While these midbrain-derived VLMCs also express collagen and *PDGFRa*, they lack mesodermal markers and instead express neuronal markers such as *SOX6*, *FABP7*, *SOX2* (Tiklova et al., 2020; Fiorenzano et al., 2021b) (Supplementary Figure S3J,K).

Additionally, we projected our scRNAseq dataset onto a four-dimensional (4D) reference atlas of a mouse brain (Fleck et al., 2021) in order to spatially and temporally annotate the emerging cell types within silk and non-silk cerebral organoid cultures during development. Interestingly, we found a high correlation of both organoid datasets with the transcriptome of E13.5 mouse forebrain, suggesting a regional identity of our 3D cultures along the rostro-caudal axis. (Supplementary Figure S3L).

We next determined the relative proportion of the identified cell types in silk and non-silk organoids. Consistent with immunohistochemical and functional assessments, scRNAseq revealed a greater percentage of neuronal cells in silk organoids than in non-silk cultures after 4 months, accompanied by an enrichment of the Gene Ontology (GO) term *Neuron differentiation* in silk organoids (Figures 4C,E). This difference in cell-type ratio was also evident when we analyzed the overall expression level of neuronal (*MAP2, SYT1, NCAM1*) and non-neuronal (*COL1A1, DCN, FBLN1*) markers in both 3D culture condition (Supplementary Figure S3M). Interestingly, the cells with fibroblast-like signature and mesoderm origin were almost completely absent in the silk-cerebral organoids (Figures 4A–C).

Importantly, high-resolution analysis investigating only the neuronal compartment (light and dark blue clusters) in both 3D culture systems revealed a higher enrichment score in silk organoids for the following GO terms: *neuron maturation*, *neuron-neuron synaptic transmission*, *neuron migration*, *post-synapse assembly*, and *neurotransmitter secretion* (Figure 4F). In line with electrophysiology data, the increased expression of mature and post-mitotic neuronal markers (*SYT1, NNAT, VAMP2*) as well as voltage-gated potassium, sodium, and calcium channel subfamily members (*KCNB1, SCN3A, CACNG4*) (Figure 4G and Supplementary Figure S3N) also showed that a greater degree of neuronal maturation had been reached within silk-engineered cerebral organoids.

Silk scaffolding attenuates oxidative stress and interior hypoxia in human brain organoids

The reduced intra-organoid variability accompanied by a higher proportion of functionally mature neurons observed in silk-engineered culture suggested that more favorable growth

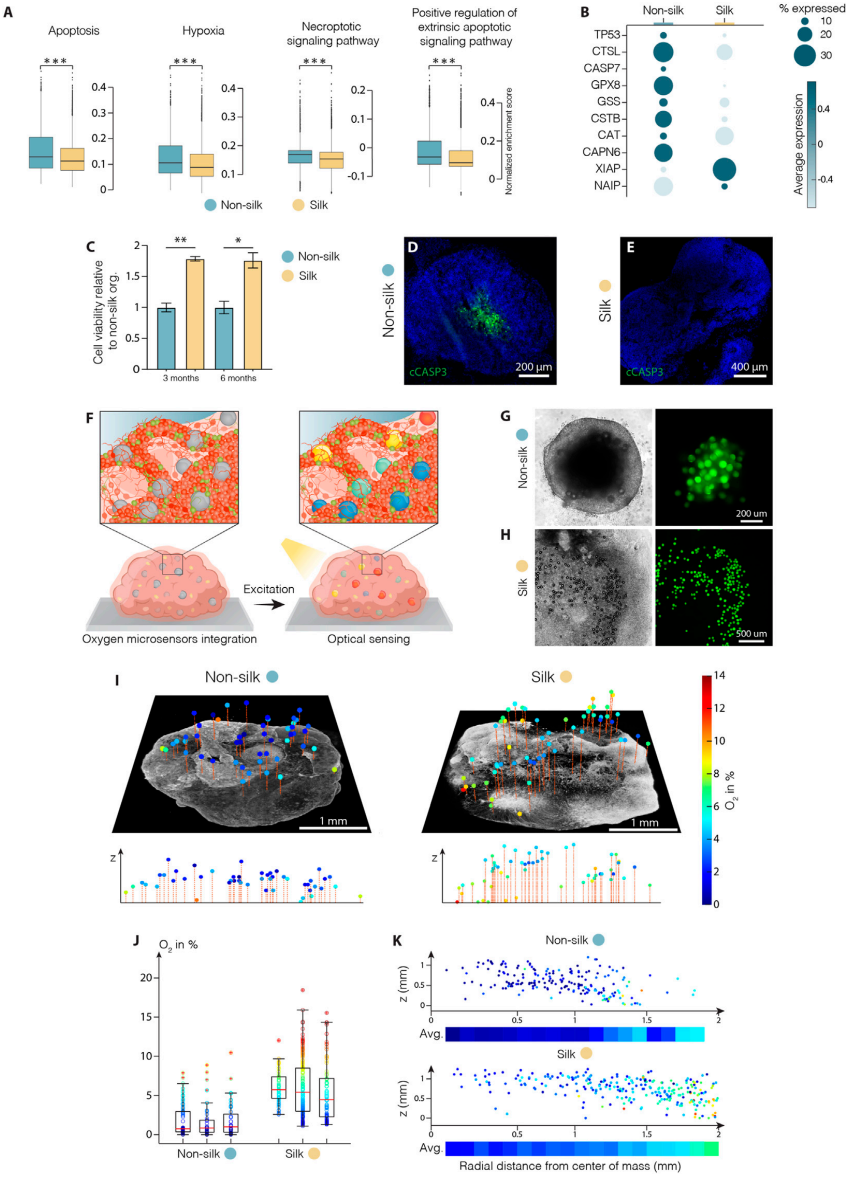

FIGURE 5
Silk scaffolding increases intra-organoid cell survival. **(A)** Apoptosis, hypoxia, necrosis signalling pathway analysis and **(B)** representative markers of cell death regulation in cerebral organoids grown with and without silk scaffold at 4 months ***$p < 0.001$, two-tailed Wilcoxon rank sum test. **(C)** Cell viability in cerebral organoids grown with and without scaffold measured by MTT assay and expressed as relative fluorescence units (RFU). Data represent mean ± SEM, normalized over non-silk organoids (n = 3). *$p < 0.05$, **$p < 0.01$, two-tailed Mann Whitney test. **(D,E)** Immunohistochemistry of cleaved caspase 3 in non-silk **(D)** and silk **(E)** organoids at day 120. Scale bars 200 µm **(D)** and 400 µm E). **(F)** Schematic illustration of oxygen tension measurements in human brain organoid. **(G,H)** Representative bright-field images of non-silk **(G)** and silk **(H)** brain organoids with integrated CPOx-50-Ptp oxygen sensor beads 8 days after seeding. Scale bars 200 µm G) and 500 µm H). **(I)** 3D oxygen maps of non-silk and silk organoids with simultaneously acquired co-localized live cell images and their cross-sectional oxygen distribution. Scale bars 1 mm. **(J)** Oxygen distribution in 3 silk and non-silk organoids at day 60 showing average oxygenation (red line) and 25th and 75th percentile (box). **(K)** Ratio of oxygen tension to height and distance from organoid center axis in silk and non-silk organoids, and heatmap of average oxygen level for every 100 µm step (n = 3). Nuclei were stained with DAPI.

culture conditions were recreated enabling 3D organoid differentiation and mature cell-type specification. We exploited the scRNAseq dataset to analyze the metabolic profiles and compare cell stress response pathways in silk and non-silk organoids. We found ectopic activation of cell stress response signaling only in non-silk generated organoids, highlighting a substantial alteration of metabolic activities (Figure 5A and Supplementary Figure S4A). Specifically, in non-silk organoids, we observed a larger number of cells enriched in hypoxia- and oxidative stress-associated genes, as well as the deregulated expression of enzymatic and molecular cues relating to apoptosis, DNA damage (*TP53*, *CASP7*) and repair (*XIAP, NAIP*) (Figure 5B). These findings suggested insufficient oxygen and nutrient supply within non-silk organoids, leading to several deleterious effects including necrosis. Additionally, ectopic expression of regulatory genes in DNA damage and repair pathways were also found in non-silk organoids (Figures 5A,B and Supplementary Figure S4A). Cell viability analyses (Figure 5C and Supplementary Figure S4B,C) and cleaved-Cas3 immunohistochemistry analysis at month four confirmed the presence of an evident necrotic inner core in conventionally generated organoids, not present in silk bioengineered cultures. (Figures 5D,E).

These findings led us to speculate whether reduced interior cell death was due to the fact that oxygen were uniformly delivered throughout the 3D silk scaffolds. Further, the presence of interconnected micropores structures may improve oxygen diffusion within organoids, thus increasing cell survival and sustaining differentiation. To test this hypothesis, we used phosphorescent microbeads as optical sensors to obtain 3D maps of oxygen tension distribution in silk and non-silk organoids (Figure 5F). The method allows non-invasive microscopy-based sensing of oxygen levels in 3D space by measuring oxygen-mediated quenching of phosphorescence (Wesseler et al., 2022). Oxygen sensitive microbeads were incorporated within human brain organoids at early stages of cell culture in order to achieve homogeneous distribution of microsensors throughout the body of the organoid and prevent their aggregation in the superficial layers during organoid expansions (Figures 5G,H). After 2 months in culture, oxygen tension levels were successfully extracted from beads distributed throughout the volume of both 3D culture systems (Figure 5I). Presence of gradual increase in oxygen levels (~5%) in the outward radial direction confirmed the competing effects of inward diffusion and cellular consumption within brain organoids. (Figures 5I,K and Supplementary Figure S4D). The overall mean oxygen level was significantly higher in silk than in non-silk organoids: non-silk organoids exhibited oxygen tensions of approximately 1.9 ± 0.7% dissolved O_2 (DO) compared to 5.8 ± 1.6% DO in silk brain organoids (mean ± S.E.M., Figure 5J). Importantly, comparison of spatial distribution of oxygen tension also showed that the silk scaffolding strategy resulted in higher, more homogeneous, and physiological tissue oxygenation in all areas of the organoid (Figure 5K and Supplementary Figure S4D). These results indicate that microarchitecture facilitated by silk scaffolding significantly improves organoid oxygenation, therefore increasing cell survival and leading to uniform cellular and functional intra-organoid composition.

Discussion

Pioneering studies in the last decade (Eiraku et al., 2011; Lancaster et al., 2013) revealed the remarkable ability of hPSCs to self-pattern and self-organize *in vitro*, generating complex neural tissue structures that contain a broad range of cell types mimicking several brain regions. Since then, unguided brain organoid differentiation protocols have been used extensively to model neurodevelopmental processes and neurodegenerative diseases in more physiologically relevant conditions than previously possible (Lancaster et al., 2013; Quadrato et al., 2017; Madhavan et al., 2018; Pellegrini et al., 2020). However, the organoid field is still riddled with issues of reproducibility and variability in terms of internal organization and cellular composition (Bhaduri et al., 2020; Qian et al., 2020; Fiorenzano et al., 2021c). Despite the obvious necessity to alleviate these issues, adequate multidisciplinary routes remain largely unexplored. To address this need, we developed a bioengineering approach based on silk scaffolds for the generation of cerebral organoids with reduced intra-organoid variability and enhanced functional maturation. We demonstrated that a recombinant spider silk microfiber network supports unguided hPSC differentiation and spontaneous self-patterning and morphogenesis into more oxygenated and healthier brain organoids.

In contrast to previously presented bioengineering methodologies for the establishment of brain organoid scaffolding, the formation of a silk fiber network does not require the laborious manual isolation of individual fibers (Lancaster et al., 2017) or specialized equipment such as a 3D printer (Rothenbucher et al., 2021). Our simple scaffold generation approach is easily executable by other research groups and is compatible with potential high-throughput applications. Spider silk fiber technology present several advantages over other scaffold-based methods. Spider silk fibers 1) form a strong and elastic 3D structure to guide the arrangement of hPSCs into an organ-like configuration; 2) can be functionalized with specific bioactive molecules to help drive the differentiation of hPSCs into specific human tissues; 3) act as an anchored scaffold at the initial stage of differentiation, thus facilitating hPSC seeding and adhesion to the microfibers; and 4) create a microporous structure promoting the intraorganoid delivery of growth factors.

Furthermore, recombinant spider silk protein provides a natural, highly biocompatible, and molecularly defined

material source. Importantly, the silk scaffold polymerized around air bubbles forms a stable structure with an intricate hierarchical architecture. On the macroscale, the scaffold takes the shape of a robust framework that allows reproducible cell seeding and expansion in the 3D space; on the microscale, silk polymerizes into flat microfibers with a nanoscale grass-like texture that provides cell-interactive topological cues further enhanced by the presence of human recombinant laminin. Easily obtainable and structurally defined across multiple length scales, the engineered silk scaffold presents a unique biomaterial support for cerebral organoid formation.

One of the main issues with the conventional brain organoid methodologies is the lack of a vascular network, resulting in incomplete and heterogeneous differentiation caused by the restricted diffusion of oxygen and nutrients as well as the accumulation of metabolic waste in interior layers (Pasca et al., 2019). Silk scaffolding mitigates detrimental hypoxic effects by facilitating the formation of an interconnected microcavity network within the organoid that not only increases surface-to-volume ratio (by exposing a larger fraction of cells to nutrients and oxygen) but also creates an interpenetrating system for metabolic waste removal. As such, the silk bioengineering approach reduces spontaneous differentiation toward non-neuroectodermal populations and prevents the emergence of resilient stem cell niches at early stages of organoid formation. In comparison to the conventional methodologies, our silk scaffolding strategy leads to more homogeneous differentiation both temporally (cells synchronously exit pluripotency and enhance neuroectoderm formation) and spatially (absence of localized populations with undesirable cell types), underscoring the supportive role of the scaffold during hPSC self-patterning (Xu et al., 2015; Fiorenzano et al., 2016). At early stages of silk organoid differentiation, neural stem cells are enclosed in rosette niches, as in conventionally generated organoids. However, a difference in $PAX6^{+}$ cell organization surrounding the central lumen is detected, possibly reflecting a greater level of maturation in silk organoids. At later stages, silk organoids exhibit the layering organization of cortical tissue, including the formation of a polarized cortical plate. Neurons show rudimental spatial separation into an early-born inner layer ($CTIP2^{+}$) and a late-born outer layer ($SATB2^{+}$). However, this layering organization remains limited, suggesting that additional cues and growth factors are needed to generate the complex stereotypical organization of layers II–VI *in vitro*. By combining silk scaffolding with the most recent and sophisticated guided differentiation protocols, it may be possible to recapitulate a similar degree of spatial organization of the mature layer as *in vivo*.

scRNAseq revealed a larger fraction of neuronal cells in silk than in non-silk organoids at the expense of populations of meso-endodermal origin, in particular those with endothelial identities. In line with functional assessments, neurons in silk organoids exhibited more mature molecular features with a higher expression of post-mitotic synaptic markers and ion channel subfamily members at single cell resolution. Importantly, the silk-bioengineered approach does not alter organoid differentiation trajectories but instead gives rise to a more robust and reproducible neuroectodermal signature than that of non-silk organoids, with the absence of pluripotent and meso-endodermal cell type contaminants.

This work presents multiple technological advantages associated with the use of silk scaffolding. Firstly, because the silk scaffolds are initially anchored at the bottom of the plate, cell distribution along the fibers can be finely controlled to overcome cell seeding discrepancies associated with free-floating scaffolds. The amenable nature of the silk technology could also allow the generation of brain organoids with specific size and shape by introducing molding and varying cellular density as well as silk fiber volume fraction. The optical oxygen sensing technique presented here provides a powerful approach for both temporal and spatial oxygen mapping in brain organoids that could be applied to other organoid protocols with the aim of determining and enhancing tissue oxygenation in these model systems or tuning them to mimic native tissue oxygen levels (Kajtez et al., 2021).

It is important to note that our approach is compatible with bioengineering solutions that seek to advance other aspects of organoid formation. For example, silk-based organoids would be compatible with microfluidic systems or engineered bioreactors. Furthermore, since silk scaffolding forms a secondary polymer network (in addition to the embedding hydrogel network), our platform is adaptable to other bioengineering strategies based on introducing matrigel substitutes with specific components that mimic the native brain extracellular matrix more closely. These efforts have yielded several studies where brain organoids were embedded in collagen, hyaluronic acid, or decellularized brain extracellular matrix, which could all be combined with silk (Lindborg et al., 2016; Zafeiriou et al., 2020; Cho et al., 2021; Simsa et al., 2021). Merging multiple bioengineering solutions together could lead to hybrid approaches that provide much needed advancements in the field of brain organoids. In this regard, silk scaffolding provides a versatile approach that can also be applied to guided differentiation of organoids into other brain regions, such as ventral midbrain (Fiorenzano et al., 2021b).

In summary, the silk bioengineering methodology presented here gives rise to cerebral organoids characterized by homogeneous 3D differentiation, a reduction in both metabolic stress and the formation of a necrotic core, more complex cytoarchitectural features, and improved functional maturation. Our approach therefore provides a novel platform based on spontaneous hPSC differentiation that can be used to better study key aspects of human brain physiology in a dish and, ultimately, in drug discovery and regenerative medicine.

Materials and methods

Human pluripotent stem cell culture

Undifferentiated human pluripotent stem cells (hPSCs) RC17 (Roslin Cells, hPSCreg RCe021-A) were cultured on 0.5 μg/cm^2 Lam-521 (BioLamina, LN-521)-coated plates in iPS-Brew XF medium (Miltenyi, 130-104-368). Once they reach confluence, the cells were passaged with 0.5 mM EDTA (for 7 min at 37°C, Thermo fisher Scientific, 15575020) and seeded at a density of 2,500-10,000 cells/cm^2 in iPS Brew medium with the addition of 10 μM Y-27632 (Miltenyi, 130-106-538) for the first 24 h after passaging.

Human cerebral organoid differentiation

To start 3D organoid formation, homogeneous hPSC culture at 75-90% confluency of the well area was washed with DPBS (-Mg^{2+}/-Ca^{2+}, Thermo Fisher Scientific, 14200075) and incubated with Accutase solution (50 μL/cm^2, Thermo Fisher Scientific, A1110501) for 5 min at 37°C. The cells were then centrifuged, resuspended in mTeSR1 (Stem Cell Technologies, 05850) with 10 μM Y-27632 and counted. To generate non-silk organoids, single cell suspension was then seeded at a density of 8,000 cells/well in an ultra-low attachment 96-well plate (Costar, round bottom, REF 7007) and supplemented with mTeSR1 with 10 μM Y-27632 to reach a final volume of 25 μl/well as reported in Lanc et al. (Lancaster and Knoblich, 2014). After 2 days of culture, 50% of media was replaced with mTesR1 without the Y-27632 supplement. After three additional days, differentiation medium consisting of DMEM/F12 (Thermo Fisher Scientific, 21331020), 1:100 N2 supplement (Thermo Fisher Scientific, 17502048) and 2 μg/ml Heparin (Sigma-Aldrich, H3149) was added from day 0-6 and replaced every second day. 1% minimum essential medium non-essential amino acids (MEM-NEAA; Sigma-Aldrich, M7145), 0.1% 2-mercaptoethanol (Merck, 8057400005), 1:500 penicillin-streptomycin (Thermo Fisher Scientific, 15140122), and 200 mM L-glutamine (Thermo Fisher Scientific, 25030081) were maintained for the entire differentiation period, as reported in Lancaster et al. (Lancaster and Knoblich, 2014). For the first 48 h the medium was also supplemented with 3% Knockout Serum Replacement (KSR, Thermo Fisher Scientific, 10828010). At day 8 each organoid was transferred in a sterile dimple, embedded evenly in 30 uL of matrigel (Corning, 354234) and incubated at 37°C for 25 min. After the polymerisation of matrigel was complete, the organoids were transferred in an ultra-low attachment six well plate (Corning, flat bottom, REF 3471) with 4 ml/well of 1:1 DMEM/F12:Neurobasal medium (Thermo Fisher Scientific, 21331020 and A3582901), 1:200 N2 supplement, 1:100 B27 supplement (Thermo Fisher Scientific, 12587010) and 2.5 μg/ml insulin (Sigma-Aldrich, I9278-5 ML), as reported in Lancaster et al. (Lancaster and Knoblich, 2014). The medium was replaced every second day. At day 15, the medium was substituted with 1:1 DMEM/F12:Neurobasal, 1:200 N2 supplement, 1:50 B27 + Vitamin A supplement (Thermo Fisher Scientific, 17504044) and 2.5 μg/ml insulin solution supplemented with 400 μM Ascorbic Acid (Sigma-Aldrich, A4403-100 MG). For terminal differentiation after day 25, the previously described medium was supplemented with 400 μM Ascorbic Acid, 10 ng/ml BDNF (Miltenyi, 130-096-286), 10 ng/ml GDNF (R&D Systems, 212-GD-010) and 200 μM cAMP (Sigma-Aldrich, D0627-1G).

Generation of bioengineered silk cerebral organoids

A 20 μL droplet of prepared Biosilk solution (BioLamina, BS-0101) functionalized with 5 μg/ml Lam-111 (BioLamina, LN111) and 10 μM Y-27632 was placed in the centre of hydrophobic cell culture wells of a 24-well plate (Sarstedt, REF 833922500) (Fiorenzano et al., 2021b). Air bubbles were introduced into the droplets by pipetting up and down (10-15 strokes) creating a dense foam. Human pluripotent stem cells were detached using Accutase solution (50 μl/cm^2) and prepared as a single cell suspension at high concentration (15,000 cells/μl in mTeSR1 with 10 μM Y-27632). A total of 75,000 cells was then added to the silk foam, dispersed homogeneously, and stabilized at 37°C for 25 min. Silk bioengineered culture was then incubated with 2 ml of mTeSR1 with 10 μM Y-27632 for 5 days and then cultured following the cerebral differentiation protocol as described in Lancaster et al. (Lancaster and Knoblich, 2014). 8 days after the start of differentiation, silk organoids were lift up with a scalper and detached from the bottom. Silk cultures were then embedded in matrigel as described above and grown in suspension (free floating) in a 6-well plate (Corning, 3,471) thereafter.

Silk and live-cell staining and microscopy

To prepare it for fluorescence imaging, silk scaffold was polymerized in a well with glass bottom compatible with high resolution imaging. The scaffold was then incubated for 30 min in 0.5% w/w Rhodamine B solution (Sigma Aldrich, 83689) in PBS and rinsed thoroughly to remove the excess dye. On separate samples, in order to visualize live cell distribution on the silk scaffold 10 days after cell seeding, cell-laden scaffolds were incubated with 2 μM Calcein AM (ThermoFisher Scientific, C3100MP) for 30 min at 37°C and then rinsed thoroughly with cell culture medium. Imaging was performed on a Nikon A1RHD confocal microscope equipped with a 20x objective. Image processing was performed in NIS-elements software (Nikon).

Scanning electron microscopy

Samples were fixed in 2% buffered glutaraldehyde (Sigma-Aldrich, G6257-10 ML) overnight and then rinsed in 0.1% HEPES buffer. Postfixation was performed for 1 h in 2% osmium tetroxide (TedPellaInc, n°18450, 18451, 18456). Samples were dehydrated in ethanol dilution series, then exposed to dilution series of hexamethyldisilazane (HMDS; TedPellaInc, n°18605) and left to dry in a fume hood overnight. Samples were mounted on 25 mm aluminum stubs, sputter coated with 10 nm Platinum/Palladium (80:20) and imaged in a Jeol JSM-7800F scanning electron microscope.

Organoid cryosectioning and immunofluorescence

Organoids were fixed with 4% PFA for 5 h at room temperature and then left to sink in sucrose 30% solution + OCT cryomount (volume ratio 1:1) overnight at 4°C. Organoids were then transferred to a cryomold filled with OCT, frozen in dry ice and stored at −80°C. After at least 24 h at −80°C, mounted organoids were cut in 20 µm slices using a cryostat and the slides were stored at −20°C until needed.

For the immunofluorescence, sections were dried for 5 min at room temperature, then washed with KPBS 1X three times and fixed again with PFA for 10 min at room temperature. After washing other three times, the slides were then incubated in blocking solution containing KPBS 1X +0.3% Triton solution+ 5% serum of secondary antibody host species for at least 1 h at room temperature. Primary antibodies (see Supplementary Table S1) in blocking solution were added to the slides for an overnight incubation at 4°C. Sections were then washed, incubated with appropriate secondary fluorophore-conjugated antibodies (Alexa Fluor 488, 594, 647 used at 1:400, Jackson ImmunoResearch Laboratories) + DAPI (1:1,000) in blocking solution for 1 h at room temperature and mounted on glass coverslips using FluorSave Reagent.

Microscopy

Brightfield images were taken using an Olympus CKX53 inverted microscope with a 4x objective (UPlanFL N 4x/0.13 NA) and acquired with the OLYMPUS cell Sens Standard v2.3 software. Fluorescent images were captured within a week from staining using a Leica DMI6000B widefield microscope or a Leica TCS SP8 laser scanning confocal microscope. The image acquisition software was Leica LAS X and images were processed using Adobe Photoshop CC 2020. In comparison experiments, all the images were taken with the same software settings and any adjustments were applied equally across the entire image, without the loss of any information.

qRT-PCR

Total RNAs were isolated on day of analysis from three individual organoids/sample using the RNeasy Micro Kit (Qiagen, 74004), according to manufacturer instructions. Reverse transcription was performed using Maxima First Strand cDNA Synthesis kit for qRT-PCR (Thermo Fisher, K1641). cDNA was then mixed with the relevant primers (0.95 µM; Integrated DNA Technologies, see Supplementary Table S2) and SYBR Green Master mix (Roche) using a Bravo pipetting robot instrument (Agilent). The analysis was performed with a LightCycler 480 II instrument (Roche) using a 40x cycle two-step protocol with a 60°C, 1 min annealing/ elongation step and a 95°C, 30 s denaturation step. The average CT values were calculated from three technical replicates and were used to determine the relative gene expression using the ΔΔCT method. The average fold change was normalized against two different housekeeping genes (ACTB and GAPDH) and the results were given as relative gene expression over undifferentiated hPSCs.

Cell viability analysis

Cell viability was measured using the MTT cell proliferation assay kit (Abcam, ab211091), following manufacturer instructions on organoids dissociated with papain after 3 and 6 months of culture. Absorbance was analyzed at 620 nm, using 100,000 cells/sample harvested from three organoids per condition. Each organoid was analyzed in three to six replicates in a 96 well plates using Biochrom Asys Expert 96 Microplate reader (Biochrom). DNA damage was detected *via* Click-iT plus Tunel assay (Invitrogen C10617) according to the manufacturer´s instructions and a positive control incubated with 1 unit of DNAse I for 30 min at RT, was included.

Bioinformatics analysis of bulk RNA sequencing data

cDNA libraries were prepared using the Illumina TruSeq library preparation kit and sequenced with 2 × 150 bp paired end reads on an Illumina NextSeq 500 High Output kit. Raw base calls were demultiplexed and converted into sample specific fastq format files using default parameters of the bcl2fastq program provided by Illumina (v. 2.19). Resulting fastq files were quantified using Salmon (1.1) using Gencode version 33 as the gene model. Downstream analysis was performed in R using DESeq2 (1.3) for differential expression analysis and EnhancedVolcano (1.8) for plotting volcano plots. Gene ontology analysis was performed using the gProfiler web tool (database updated on 07/05/2021).

Library preparation, and raw data processing for single cell RNA sequencing

For 10x Genomics single-cell RNA sequencing (scRNAseq), organoids at day 120 were prepared as a single cell suspension with the Papain kit (Worthington, #LK003150). Single cells were loaded onto 10x Genomics Single Cell 3′Chips along with the master mix following the manufacturer´s instruction for the Chromium Single Cell 3′ Library to generate single cell gel beads in emulsion (GEMs, version three chemistry). The resulting libraries were sequenced on a NovaSeq in a 2 × 100 bp paired end mode. Pre-processing of sequencing data was conducted with the Cell Ranger pipeline (10x Genomics, Cell Ranger version 6.0) with alignment to GrCh38 (2020-A) in order to generate the matrix files used for bioinformatic analysis.

Bioinformatics analysis of single cell RNA sequencing data

Downstream analysis of scRNAseq matrix files was conducted with Seurat (v 4.0.6 and R version 4.1.0). Single cell expression values were normalized, and the top 2000 highly variable genes were identified using *vst*. Data were then scaled, and principal component analysis (PCA) was performed using 30 dimensions. Cells with less than 200 or more than 5,000 genes detected were filtered out from further analyses, as well as cells with more than 10% mitochondrial reads. Data integration between different samples was performed with Harmony algorithm, which converged after seven iterations. The top 25 principal components were used for clustering using Seurat´s FindNeighbors and FindClusters functions (Louvain algorithm, resolution 0.1). Clusters identities were assigned based on cluster gene markers as determined by Seurat´s FindAllMarkers function (minimum percentage of cells expressed = 0.25 and log fold change threshold = 0.25) together with gene expression values of known markers. Differential gene expression analysis between samples was carried out using the Wilcoxon rank sum test and genes with an FDR-corrected p-value < 0.05 were considered significant. Density plots were generated using the plot_density function from the "Nebulosa" package (v 1.2.0). Comparison with published dataset was performed by projecting reference labels onto scRNAseq data using Seurat's v4 label transfer functions. Spatial similarity maps of silk and non-silk brain organoids with E13.5 mouse embryos (Allen Brain Atlas) were generated using VoxHunt package (v1.0.1; 300 genes). Gene Set Enrichement Analysis was performed using the "escape" package (v1.2) and gene sets obtained from MSigDB collections.

Electrophysiology

Whole cell patch-clamp electrophysiological recordings were performed on matrigel embedded organoids maintained in a Krebs solution gassed 95% O_2—5% CO_2 at room temperature that was changed every 20 min. The composition of the standard solution was (in mM): 119 NaCl, 2.5 KCl, 1.3 $MgSO_4$, 2.5 $CaCl_2$, 25 Glucose and 26 $NaHCO_3$. For recordings Multiclamp 700B amplifier (Molecular Devices) was used together with borosilicate glass pipettes (3-7 MOhm) filled with the following intracellular solution (in mM): 122.5 potassium gluconate, 12.5 KCl, 0.2 EGTA, 10 Hepes, two MgATP, 0.3 Na_3GTP and eight NaCl adjusted to pH 7.3 with KOH as reported in Fiorenzano et al. (Fiorenzano et al., 2021b). Data acquisition was performed with pClamp 10.2 (Molecular Devices, San Jose, CA, United States); current was filtered at 0.1 kHz and digitized at 2 kHz. Cells with neuronal morphology and round cell body were selected for recordings. Resting membrane potential was monitored immediately after breaking-in in current-clamp mode. Thereafter, cells were kept at a membrane potential of −65 to −70 mV, and 500 ms currents were injected from −20 pA to +35 pA with 5 pA increments to induce action potentials. For inward sodium and delayed rectifying potassium current measurements cells were clamped at −70 mV and voltage-depolarizing steps were delivered for 100 ms at 10 mV increments. Spontaneous activity was recorded in voltage clamp mode at −70 mV. Data were analysed using the software Clampfit 10.3 (Molecular Devices, San Jose, CA, United States) and Igor Pro 8.04 (Wavemetrics, Portland, OA, United States) with the NeuroMatic package (Rothman and Silver, 2018).

Oxygen sensing

To obtain 3D maps of oxygen tension distributions in cerebral organoids during culture, a recently presented 3D optical oxygen mapping method based on tissue integrated oxygen microsensor beads mapped by phosphorescence lifetime microscopy, described in detail in our previous publication (Wesseler et al., 2022), was adapted for organoid cultures. To generate conventional brain organoids, oxygen sensor microbeads (0.5 mg/ml CPOx-50-Ptp, Colibri Photonics GmbH, Germany) were mixed with single cell suspension of hPSCs (160k cells/mL), seeded in an ultra-low attachment 96-well plate (50 µl suspension/well, Costar, round bottom, REF 7007) and supplemented with mTeSR1 with 10 µM Y-27632 to reach a final volume of 250 µl/well. To generate silk organoids, a single cell suspension at higher concentration was prepared (15,000 cells/µL in mTeSR1 with 10 µM Y-27632, 2.5 mg/ml CPOx-50-Ptp) and dispersed homogeneously throughout the silk scaffold. Both organoid systems were then differentiated as described in the section "Human cerebral organoid differentiation". For co-localized imaging of live cells and oxygen sensor microbeads, organoids were stained with 2 µg/ml calcein AM in terminal differentiation medium prior to optical oxygen mapping. Imaging analysis and visualization

was performed with custom programmed Matlab software (Mathwork, United States), available upon request through aforementioned publication.

Statistics and reproducibility

Statistical analysis of qRT-PCR data was performed using two-tailed unpaired *t*-test and *p*-values<0.05 were considered significant. Data were statistically analyzed with the GraphPad Prism nine software and presented as mean ± SEM except where stated otherwise. For box-plots representing oxygen distribution in individual organoids, the average value, 25th - 75th percentiles and minimum – maximum values are represented as red line, box and whiskers respectively. Statistical analysis of sequencing data was conducted using two-tailed Wilcoxon rank-sum test (Seurat v4) in R v4.1.0. For all figures: $*p < 0.05$, $**p < 0.01$, $***p < 0.001$. Immunohistochemical staining images are representative of 6–12 sections from at least four biologically independent organoids.

Data availability statement

The datasets presented in this study can be found in online repositories. The names of the repository/repositories and accession number(s) can be found below: https://www.ncbi.nlm.nih.gov/geo/, GSE196423, https://www.ncbi.nlm.nih.gov/geo/, GSE202993.

Author contributions

AF, MP conceived the project and interpreted data; ES, AF, JK designed, performed, and analysed results; AB and DO performed, and interpreted electrophysiology experiments. MW. and NL designed, performed, and interpreted oxygen mapping experiments. FN, MB performed experiments, interpreted data; ES and PS performed bioinformatic analysis. AF, MP JK and ES wrote the paper with input from all authors.

Funding

New York Stem Cell Foundation (MP) European Research Council (ERC) under ERC Grant Agreement 771427 (MP) European Union funded project NSC-Reconstruct (European Union, H2020, GA no 874758, 2020-23) (MP) Swedish Research Council (2016-00873) (MP) Swedish Parkinson Foundation (Parkinsonfonden, 1347/21) (AF) Swedish Brain Foundation (MP) Strategic Research Area at Lund University Multipark (MP) Knut and Alice Wallenberg Stiftelse (KAW 2018-0040) (MP) Independent Research Fund Denmark (grant number 7017-00366B) (NL) Technical University of Denmark, Department of Health Technology (NL) Thorsten and Elsa Segerfalk Foundation (AF) Anna-Lisa Rosenberg Foundation (AF).

Acknowledgments

We thank BioLamina for providing Biosilk. We thank Prof. My Hedhammar, Prof. Anders Björklund and Therese Kallur for helpful comments and discussions, and Ulla Jarl, Sol Da Rocha Baez and Marie Persson Vejgården for technical assistance. Lund University Bioimaging Centre (LBIC), Lund University, is gratefully acknowledged for providing experimental resources for SEM. MP is a New York Stem Cell Foundation Robertson Investigator.

Conflict of interest

MP is the owner of MP Cells AB and co-inventor of the following patents WO2016162747A2, WO2018206798A1, and WO2019016113A1. MP is a paid consultant, steering group member and performers commissioned research for Novo Nordisk AS Cell Therapy Research and Development unit and a member of Arbor Bio SAB.

The remaining authors declare that the research was conducted in the absence of any commercial or financial relationships that could be construed as a potential conflict of interest.

Publisher's note

Supplementary material

The Supplementary Material for this article can be found online at: https://www.frontiersin.org/articles/10.3389/fcell.2022.1023279/full#supplementary-material

References

Ao, Z., Cai, H., Havert, D. J., Wu, Z., Gong, Z., Beggs, J. M., et al. (2020). One-stop microfluidic assembly of human brain organoids to model prenatal cannabis exposure. *Anal. Chem.* 92, 4630–4638. doi:10.1021/acs.analchem.0c00205

Arlotta, P., and Pasca, S. P. (2019). Cell diversity in the human cerebral cortex: from the embryo to brain organoids. *Curr. Opin. Neurobiol.* 56, 194–198. doi:10.1016/j.conb.2019.03.001

Asif, A., Garcia-Lopez, S., Heiskanen, A., Martinez-Serrano, A., Keller, S. S., Pereira, M. P., et al. (2020). Pyrolytic carbon nanograss enhances neurogenesis and dopaminergic differentiation of human midbrain neural stem cells. *Adv. Healthc. Mater.* 9, e2001108. doi:10.1002/adhm.202001108

Bagley, J. A., Reumann, D., Bian, S., Levi-Strauss, J., and Knoblich, J. A. (2017). Fused cerebral organoids model interactions between brain regions. *Nat. Methods* 14, 743–751. doi:10.1038/nmeth.4304

Bennett, M. L., Song, H., and Ming, G. L. (2021). Microglia modulate neurodevelopment in human neuroimmune organoids. *Cell Stem Cell* 28, 2035–2036. doi:10.1016/j.stem.2021.11.005

Bhaduri, A., Andrews, M. G., Mancia Leon, W., Jung, D., Shin, D., Allen, D., et al. (2020). Cell stress in cortical organoids impairs molecular subtype specification. *Nature* 578, 142–148. doi:10.1038/s41586-020-1962-0

Cakir, B., Xiang, Y., Tanaka, Y., Kural, M. H., Parent, M., Kang, Y. J., et al. (2019). Engineering of human brain organoids with a functional vascular-like system. *Nat. Methods* 16, 1169–1175. doi:10.1038/s41592-019-0586-5

Cederquist, G. Y., Asciolla, J. J., Tchieu, J., Walsh, R. M., Cornacchia, D., Resh, M. D., et al. (2019). Specification of positional identity in forebrain organoids. *Nat. Biotechnol.* 37, 436–444. doi:10.1038/s41587-019-0085-3

Cho, A. N., Jin, Y., An, Y., Kim, J., Choi, Y. S., Lee, J. S., et al. (2021). Microfluidic device with brain extracellular matrix promotes structural and functional maturation of human brain organoids. *Nat. Commun.* 12, 4730. doi:10.1038/s41467-021-24775-5

Di Lullo, E., and Kriegstein, A. R. (2017). The use of brain organoids to investigate neural development and disease. *Nat. Rev. Neurosci.* 18, 573–584. doi:10.1038/nrn.2017.107

Eiraku, M., Takata, N., Ishibashi, H., Kawada, M., Sakakura, E., Okuda, S., et al. (2011). Self-organizing optic-cup morphogenesis in three-dimensional culture. *Nature* 472, 51–56. doi:10.1038/nature09941

Faustino Martins, J. M., Fischer, C., Urzi, A., Vidal, R., Kunz, S., Ruffault, P. L., et al. (2020). Self-Organizing 3D human trunk neuromuscular organoids. *Cell Stem Cell* 26, 172–186. doi:10.1016/j.stem.2019.12.007

Fiorenzano, A., Pascale, E., D'Aniello, C., Acampora, D., Bassalert, C., Russo, F., et al. (2016). Cripto is essential to capture mouse epiblast stem cell and human embryonic stem cell pluripotency. *Nat. Commun.* 7, 12589. doi:10.1038/ncomms12589

Fiorenzano, A., Birtele, M., Wahlestedt, J. N., and Parmar, M. (2021a). Evaluation of TH-Cre knock-in cell lines for detection and specific targeting of stem cell-derived dopaminergic neurons. *Heliyon* 7, e06006. doi:10.1016/j.heliyon.2021.e06006

Fiorenzano, A., Sozzi, E., Birtele, M., Kajtez, J., Giacomoni, J., Nilsson, F., et al. (2021b). Single-cell transcriptomics captures features of human midbrain development and dopamine neuron diversity in brain organoids. *Nat. Commun.* 12, 7302. doi:10.1038/s41467-021-27464-5

Fiorenzano, A., Sozzi, E., Parmar, M., and Storm, P. (2021c). Dopamine neuron diversity: Recent advances and current challenges in human stem cell models and single cell sequencing. *Cells* 10, 1366. doi:10.3390/cells10061366

Fleck, J. S., Sanchis-Calleja, F., He, Z., Santel, M., Boyle, M. J., Camp, J. G., et al. (2021). Resolving organoid brain region identities by mapping single-cell genomic data to reference atlases. *Cell Stem Cell* 28, 1177–1180. doi:10.1016/j.stem.2021.03.015

Johansson, U., Widhe, M., Shalaly, N. D., Arregui, I. L., Nileback, L., Tasiopoulos, C. P., et al. (2019). Assembly of functionalized silk together with cells to obtain proliferative 3D cultures integrated in a network of ECM-like microfibers. *Sci. Rep.* 9, 6291. doi:10.1038/s41598-019-42541-y

Kajtez, J., Wesseler, M. F., Birtele, M., Khorasgani, F. R., Rylander Ottosson, D., Heiskanen, A., et al. (2021). Embedded 3D printing in self-healing annealable composites for precise patterning of functionally mature human neural constructs. *bioRxiv* 9 (25), e2201392. doi:10.1002/advs.202201392

Kanton, S., Boyle, M. J., He, Z., Santel, M., Weigert, A., Sanchis-Calleja, F., et al. (2019). Organoid single-cell genomic atlas uncovers human-specific features of brain development. *Nature* 574, 418–422. doi:10.1038/s41586-019-1654-9

Kelava, I., and Lancaster, M. A. (2016). Stem cell models of human brain development. *Cell Stem Cell* 18, 736–748. doi:10.1016/j.stem.2016.05.022

Kelava, I., Chiaradia, I., Pellegrini, L., Kalinka, A. T., and Lancaster, M. A. (2022). Androgens increase excitatory neurogenic potential in human brain organoids. *Nature* 602, 112–116. doi:10.1038/s41586-021-04330-4

Kim, J., Koo, B. K., and Knoblich, J. A. (2020). Human organoids: model systems for human biology and medicine. *Nat. Rev. Mol. Cell Biol.* 21, 571–584. doi:10.1038/s41580-020-0259-3

Kirkeby, A., Nolbrant, S., Tiklova, K., Heuer, A., Kee, N., Cardoso, T., et al. (2017). Predictive markers guide differentiation to improve graft outcome in clinical translation of hESC-based Therapy for Parkinson's disease. *Cell Stem Cell* 20, 135–148. doi:10.1016/j.stem.2016.09.004

Lancaster, M. A., and Knoblich, J. A. (2014). Generation of cerebral organoids from human pluripotent stem cells. *Nat. Protoc.* 9, 2329–2340. doi:10.1038/nprot.2014.158

Lancaster, M. A., Renner, M., Martin, C. A., Wenzel, D., Bicknell, L. S., Hurles, M. E., et al. (2013). Cerebral organoids model human brain development and microcephaly. *Nature* 501, 373–379. doi:10.1038/nature12517

Lancaster, M. A., Corsini, N. S., Wolfinger, S., Gustafson, E. H., Phillips, A. W., Burkard, T. R., et al. (2017). Guided self-organization and cortical plate formation in human brain organoids. *Nat. Biotechnol.* 35, 659–666. doi:10.1038/nbt.3906

Lindborg, B. A., Brekke, J. H., Vegoe, A. L., Ulrich, C. B., Haider, K. T., Subramaniam, S., et al. (2016). Rapid induction of cerebral organoids from human induced pluripotent stem cells using a chemically defined hydrogel and defined cell culture medium. *Stem Cells Transl. Med.* 5, 970–979. doi:10.5966/sctm.2015-0305

Madhavan, M., Nevin, Z. S., Shick, H. E., Garrison, E., Clarkson-Paredes, C., Karl, M., et al. (2018). Induction of myelinating oligodendrocytes in human cortical spheroids. *Nat. Methods* 15, 700–706. doi:10.1038/s41592-018-0081-4

Makrygianni, E. A., and Chrousos, G. P. (2021). From brain organoids to networking assembloids: Implications for neuroendocrinology and stress medicine. *Front. Physiol.* 12, 621970. doi:10.3389/fphys.2021.621970

Mansour, A. A., Goncalves, J. T., Bloyd, C. W., Li, H., Fernandes, S., Quang, D., et al. (2018). An *in vivo* model of functional and vascularized human brain organoids. *Nat. Biotechnol.* 36, 432–441. doi:10.1038/nbt.4127

Mansour, A. A., Schafer, S. T., and Gage, F. H. (2021). Cellular complexity in brain organoids: Current progress and unsolved issues. *Semin. Cell Dev. Biol.* 111, 32–39. doi:10.1016/j.semcdb.2020.05.013

Miura, Y., Li, M. Y., Birey, F., Ikeda, K., Revah, O., Thete, M. V., et al. (2020). Generation of human striatal organoids and cortico-striatal assembloids from human pluripotent stem cells. *Nat. Biotechnol.* 38, 1421–1430. doi:10.1038/s41587-020-00763-w

Nilsson, F., Storm, P., Sozzi, E., Hidalgo Gil, D., Birtele, M., Sharma, Y., et al. (2021). Single-cell profiling of coding and noncoding genes in human dopamine neuron differentiation. *Cells* 10, 137. doi:10.3390/cells10010137

Pasca, A. M., Park, J. Y., Shin, H. W., Qi, Q., Revah, O., Krasnoff, R., et al. (2019). Human 3D cellular model of hypoxic brain injury of prematurity. *Nat. Med.* 25, 784–791. doi:10.1038/s41591-019-0436-0

Pellegrini, L., Bonfio, C., Chadwick, J., Begum, F., Skehel, M., and Lancaster, M. A. (2020). Human CNS barrier-forming organoids with cerebrospinal fluid production. *Science* 369, eaaz5626. doi:10.1126/science.aaz5626

Qian, X., Nguyen, H. N., Song, M. M., Hadiono, C., Ogden, S. C., Hammack, C., et al. (2016). Brain-region-specific organoids using mini-bioreactors for modeling ZIKV exposure. *Cell* 165, 1238–1254. doi:10.1016/j.cell.2016.04.032

Qian, X., Su, Y., Adam, C. D., Deutschmann, A. U., Pather, S. R., Goldberg, E. M., et al. (2020). Sliced human cortical organoids for modeling distinct cortical layer formation. *Cell Stem Cell* 26, 766–781. doi:10.1016/j.stem.2020.02.002

Quadrato, G., Nguyen, T., Macosko, E. Z., Sherwood, J. L., Min Yang, S., Berger, D. R., et al. (2017). Cell diversity and network dynamics in photosensitive human brain organoids. *Nature* 545, 48–53. doi:10.1038/nature22047

Renner, M., Lancaster, M. A., Bian, S., Choi, H., Ku, T., Peer, A., et al. (2017). Self-organized developmental patterning and differentiation in cerebral organoids. *EMBO J.* 36, 1316–1329. doi:10.15252/embj.201694700

Rising, A., Widhe, M., Johansson, J., and Hedhammar, M. (2011). Spider silk proteins: recent advances in recombinant production, structure-function relationships and biomedical applications. *Cell. Mol. Life Sci.* 68, 169–184. doi:10.1007/s00018-010-0462-z

Rothenbucher, T. S. P., Gurbuz, H., Pereira, M. P., Heiskanen, A., Emneus, J., and Martinez-Serrano, A. (2021). Next generation human brain models: engineered flat brain organoids featuring gyrification. *Biofabrication* 13, 011001. doi:10.1088/1758-5090/abc95e

Rothman, J. S., and Silver, R. A. (2018). NeuroMatic: An integrated open-source software toolkit for acquisition, analysis and simulation of electrophysiological data. *Front. Neuroinform.* 12, 14. doi:10.3389/fninf.2018.00014

Rouleau, N., Cantley, W. L., Liaudanskaya, V., Berk, A., Du, C., Rusk, W., et al. (2020). A Long-living bioengineered neural tissue platform to study neurodegeneration. *Macromol. Biosci.* 20, e2000004. doi:10.1002/mabi.202000004

Simsa, R., Rothenbucher, T., Gurbuz, H., Ghosheh, N., Emneus, J., Jenndahl, L., et al. (2021). Brain organoid formation on decellularized porcine brain ECM hydrogels. *PLoS One* 16, e0245685. doi:10.1371/journal.pone.0245685

Sood, D., Tang-Schomer, M., Pouli, D., Mizzoni, C., Raia, N., Tai, A., et al. (2019). 3D extracellular matrix microenvironment in bioengineered tissue models of primary pediatric and adult brain tumors. *Nat. Commun.* 10, 4529. doi:10.1038/s41467-019-12420-1

Sozzi, E., Nilsson, F., Kajtez, J., Parmar, M., and Fiorenzano, A. (2022). Generation of human ventral midbrain organoids derived from pluripotent stem cells. *Curr. Protoc.* 2, e555. doi:10.1002/cpz1.555

Tang-Schomer, M. D., White, J. D., Tien, L. W., Schmitt, L. I., Valentin, T. M., Graziano, D. J., et al. (2014). Bioengineered functional brain-like cortical tissue. *Proc. Natl. Acad. Sci. U. S. A.* 111, 13811–13816. doi:10.1073/pnas.1324214111

Tiklova, K., Nolbrant, S., Fiorenzano, A., Bjorklund, A. K., Sharma, Y., Heuer, A., et al. (2020). Single cell transcriptomics identifies stem cell-derived graft composition in a model of Parkinson's disease. *Nat. Commun.* 11, 2434. doi:10.1038/s41467-020-16225-5

Velasco, S., Kedaigle, A. J., Simmons, S. K., Nash, A., Rocha, M., Quadrato, G., et al. (2019). Individual brain organoids reproducibly form cell diversity of the human cerebral cortex. *Nature* 570, 523–527. doi:10.1038/s41586-019-1289-x

Wesseler, M. F., Johansen, M. N., Kiziltay, A., Mortensen, K., and Larsen, N. B. (2022). Optical 4D oxygen mapping of microperfused tissue models with tunable *in vivo*-like 3D oxygen microenvironments. *chemRxiv*. doi:10.1039/D2LC00063F

Widhe, M., Shalaly, N. D., and Hedhammar, M. (2016). A fibronectin mimetic motif improves integrin mediated cell biding to recombinant spider silk matrices. *Biomaterials* 74, 256–266. doi:10.1016/j.biomaterials.2015.10.013

Xu, X., Smorag, L., Nakamura, T., Kimura, T., Dressel, R., Fitzner, A., et al. (2015). Dppa3 expression is critical for generation of fully reprogrammed iPS cells and maintenance of Dlk1-Dio3 imprinting. *Nat. Commun.* 6, 6008. doi:10.1038/ncomms7008

Zafeiriou, M. P., Bao, G., Hudson, J., Halder, R., Blenkle, A., Schreiber, M. K., et al. (2020). Developmental GABA polarity switch and neuronal plasticity in Bioengineered Neuronal Organoids. *Nat. Commun.* 11, 3791. doi:10.1038/s41467-020-17521-w

Zeisel, A., Hochgerner, H., Lonnerberg, P., Johnsson, A., Memic, F., van der Zwan, J., et al. (2018). Molecular architecture of the mouse nervous system. *Cell* 174, 999–1014. doi:10.1016/j.cell.2018.06.021

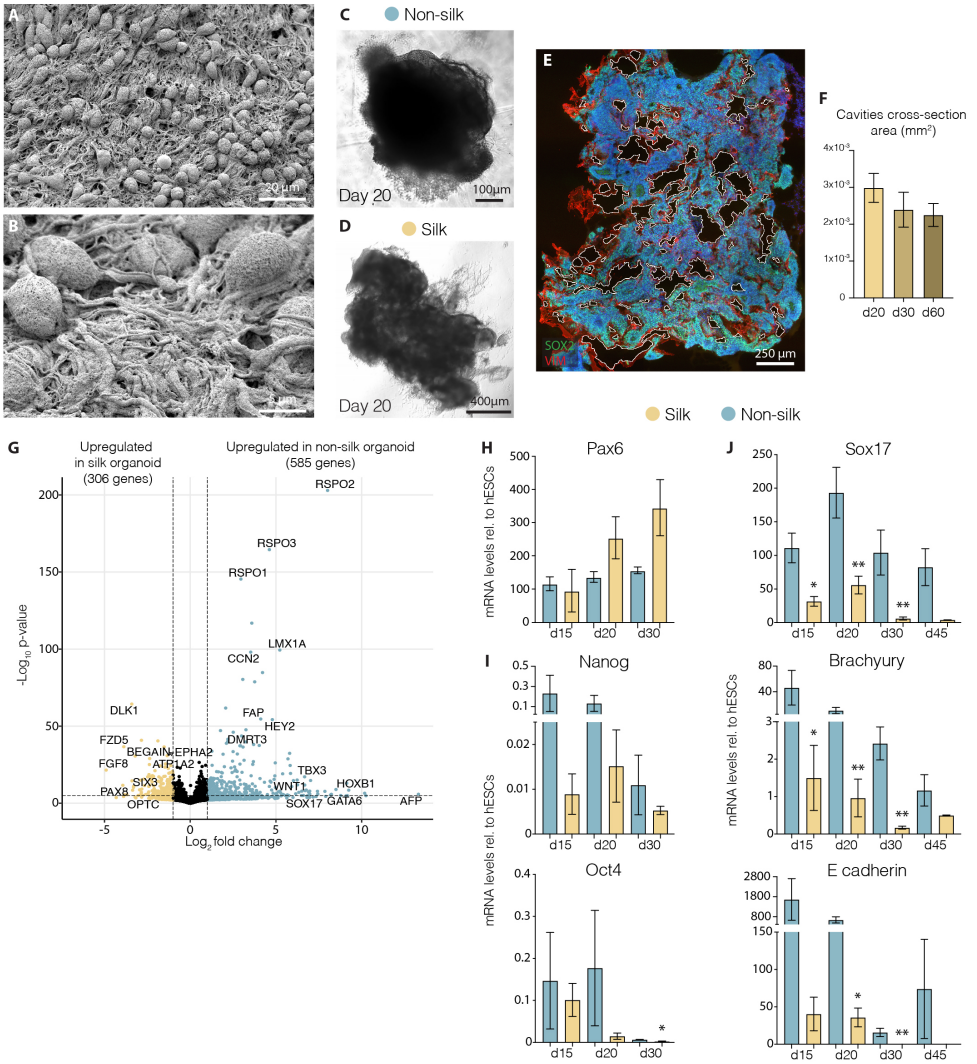

Supplementary Figure 1. A,B) Scanning electron images (SEM) images showing neuronal cell morphology and network formation within cerebral organoids at day 60. Scale bars 20 µm A) and 5 µm B). **C,D**) Representative bright-field images of non-silk C) and silk D) brain organoids at day 20. Scale bars 100 µm C) and 250 µm D). **E**) Immunohistochemistry of SOX2/VIM in silk organoid at day 20 with internal cavities highlighted in white. Scale bar 250 µm. Nuclei were stained with DAPI. **F**) Cross sectional area of the cavities in silk brain organoids over time. Data represent mean ± SEM obtained from 3 individual organoids per time-point. **G**) Volcano plot of statistical significance versus fold change of differentially expressed genes ($p < 0{,}05$, log2FC >1) between silk and non-silk organoids, with manually selected genes named. **H-J**) RT-qPCR analysis of neuroectodermal marker PAX6 H), stem cell markers NANOG and OCT4 I) and non-neural lineage markers SOX17, Brachyury and E-Cadherin J) during cerebral organoid differentiation. Values are given as fold change relative to undifferentiated hPSCs. * $p<0.05$, ** $p<0.01$, two-tailed unpaired t-test.

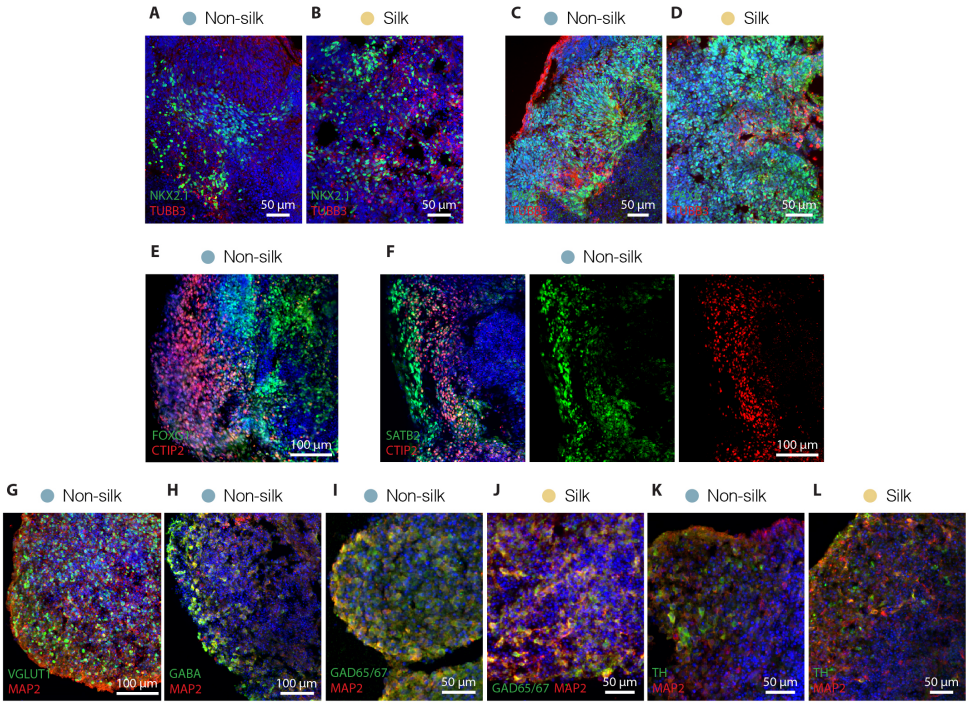

Supplementary Figure 2. A-D) Immunohistochemistry of NKX2.1/TUBB3 A,B) and PAX6/ TUBB3 C,D) in organoids grown with or without silk scaffold at day 30. Scale bars 50 µm. **E**) Cryosection of non-silk brain organoid at day 60 showing FOXG1/CTIP2 double staining. Scale bar 100 µm. **F**) Immunohistochemistry of SATB2/CTIP2 showing cortical layer formation in non-silk brain organoid at day 120. Scale bar 100 µm. **G,H**) Cryosections of non-silk brain organoids at day 120 showing VGLUT1/MAP2 G) and GABA/MAP2 H) double staining. Scale bars 100 µm. **I-L**) Immunohistochemistry of GAD65-67/MAP2 I,J) and TH/MAP2 K,L) in organoids grown with or without silk scaffold at day 120. Scale bars 50 µm. Nuclei were stained with DAPI.

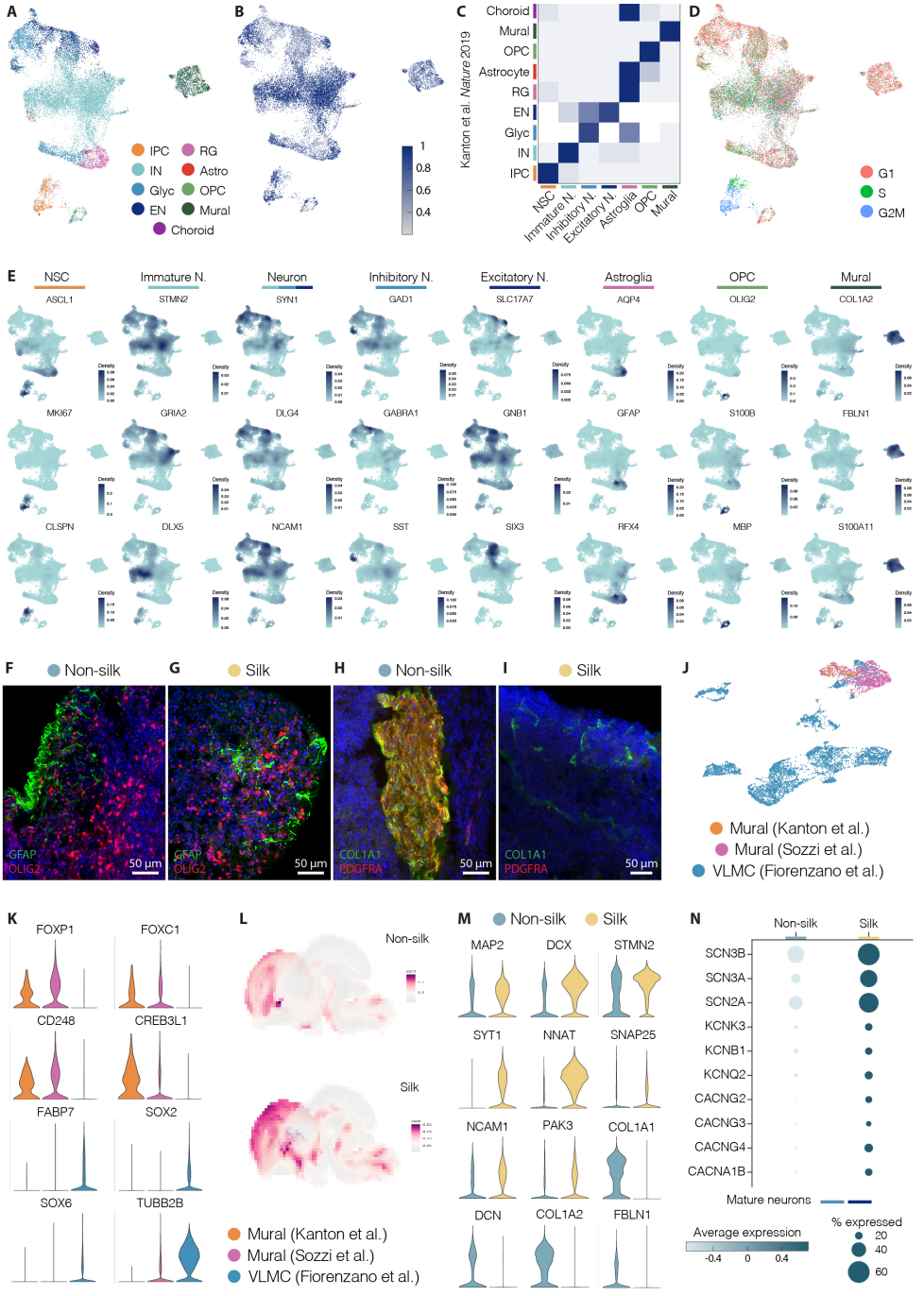
A
IPC
IN
Glyc
EN
RG
Astro
OPC
Mural
Choroid
B
1
0.8
0.6
0.4
C
Kanton et al. Nature 2019
Choroid
Mural
OPC
Astrocyte
RG
EN
Glyc
IN
IPC
NSC
Immature N.
Inhibitory N.
Excitatory N.
Astroglia
OPC
Mural
D
G1
S
G2M
E
NSC
Immature N.
Neuron
Inhibitory N.
Excitatory N.
Astroglia
OPC
Mural
ASCL1
STMN2
SYN1
GAD1
SLC17A7
AQP4
OLIG2
COL1A2
MKI67
GRIA2
DLG4
GABRA1
GNB1
GFAP
S100B
FBLN1
CLSPN
DLX5
NCAM1
SST
SIX3
RFX4
MBP
S100A11
F
Non-silk
G
Silk
H
Non-silk
I
Silk
GFAP
OLIG2
50 µm
COL1A1
PDGFRA
J
Mural (Kanton et al.)
Mural (Sozzi et al.)
VLMC (Fiorenzano et al.)
K
FOXP1
FOXC1
CD248
CREB3L1
FABP7
SOX2
SOX6
TUBB2B
L
Non-silk
Silk
Mural (Kanton et al.)
Mural (Sozzi et al.)
VLMC (Fiorenzano et al.)
M
Non-silk
Silk
MAP2
DCX
STMN2
SYT1
NNAT
SNAP25
NCAM1
PAK3
COL1A1
DCN
COL1A2
FBLN1
N
Non-silk
Silk
SCN3B
SCN3A
SCN2A
KCNK3
KCNB1
KCNQ2
CACNG2
CACNG3
CACNG4
CACNA1B
Mature neurons
Average expression
-0.4
0
0.4
% expressed
20
40
60

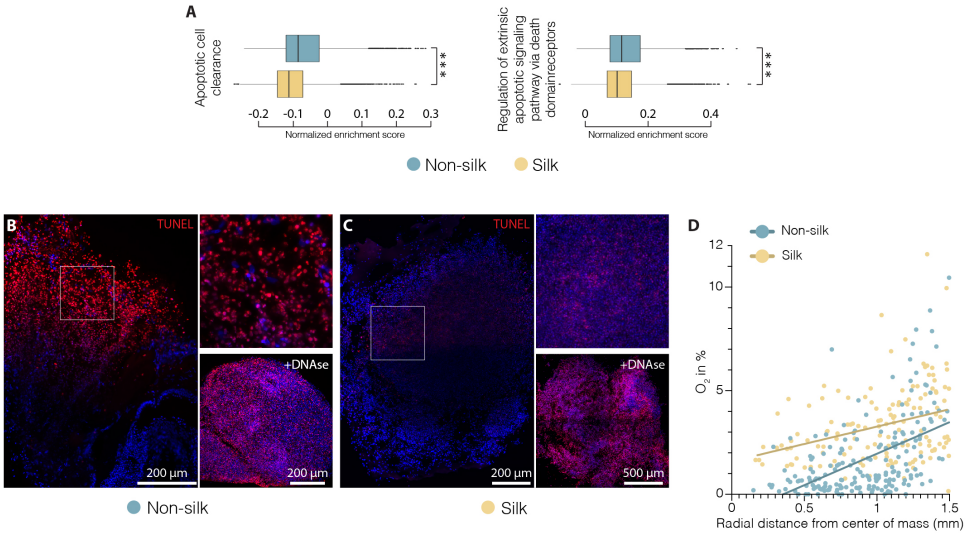

Supplementary Figure 4. A) Gene set enrichment analysis (GSEA) showing a statistically significant different score for apoptotic signalling pathway terms in non-silk and silk brain organoids. *** p<0.001, two-tailed Wilcoxon rank sum test. **B-C**) TUNEL staining of non-silk B) and silk C) organoids after 4 months in culture, including magnification of selected areas (upper panel) and positive control treated with DNAse I for 30min (lower panel). Scale bars 200 µm B), 200 µm C) left and 500 µm C) right. Nuclei were stained with DAPI. **D**) Relation of oxygen tension to distance from organoid center of mass in silk and non-silk organoids, including trendline obtained through simple linear regression.

Supplementary Figure 3. A-C) UMAP plots showing predicted cell types A), prediction score B) and relative overlapping quantification C) using published cerebral organoid dataset as reference (Kanton et al. Nature 2019). IPC, Intermediate progenitor; IN, Immature neuron; Glyc, Glycinergic neuron; EN, Excitatory neuron; RG, radial glia; Astro, Astrocyte; OPC, Oligodendrocyte precursor. **D**) UMAP embeddings showing the predicted cell cycle phase using Seurat CellCycleScoring function. **E**) Density feature plots visualizing specific gene expression across clusters. **F-I**) Immunohistochemistry of F,G) GFAP/OLIG2 and H,I) COL1A1/ PDGFRa in organoids grown with or without silk scaffold at day 120. Scale bars 50 µm. **J**) UMAP plots of mural cells from cerebral organoids (this study, purple, Kanton et al. Nature 2019, orange) and vascular leptomeningeal cells (VLMC) detected in ventral midbrain patterned organoids (Fiorenzano et al. Nature Comm. 2021, light blue). **K**) Expression of representative mesoderm and neurogenesis associated markers in perivascular cell types from distinct datasets. **L**) Spatial similarity maps of silk and non-silk brain organoids generated using VoxHunt with E13.5 mouse embryos (Allen Brain Atlas). Scores were calculated using average gene expressions for all cells using Pearson correlations. **M**) Expression of representative neuronal and vasculature-associated markers in human brain organoid grown with or without silk scaffold after 4 months in culture. **N**) Dot plot showing expression levels of selected genes coding for ion channels in silk and non-silk brain mature neuronal clusters. Nuclei were stained with DAPI.

Table S1.
Primary antibodies

Antigen	Specie	Company	Cat. no	Dilution
BRACHYURY	Goat	R&D Systems	AF2085	1:300
Cleaved CASP3	Rabbit	Cell Signaling	9661	1:500
COL1A1	Sheep	R&D Systems	AF6220	1:500
CTIP2	Rat	Abcam	AB18465	1:500
E-CADHERIN	Mouse	BD Biosciences	610182	1:300
FOXG1	Rabbit	Novus	NBP1-56594	1:300
GABA	Rabbit	Sigma-Aldrich	A2052	1:2000
GAD65/67	Rabbit	Abcam	AB49832	1:1000
GFAP	Rabbit	Dako	Z0334	1:1000
MAP2	Chicken	Abcam	AB5392	1:2000
NKX2.1	Rabbit	Abcam	AB133737	1:500
OCT4	Mouse	Santa Cruz	SC5279	1:500
OLIG2	Goat	R&D Systems	AF2418	1:500
PAX6	Rabbit	Abcam	AB195045	1:300
PDGFRa	Rabbit	Cell Signaling	5241S	1:300
SATB2	Rabbit	Abcam	AB34735	1:300
SOX17	Goat	R&D Systems	AF1924	1:300
SOX2	Rabbit	Millipore	AB5603	1:400
TH	Rabbit	Millipore	AB152	1:500
TUBB3	Mouse	BioLegend	801202	1:1000
VGLUT1	Rabbit	SYSY	135303	1:500
VIM	Mouse	Dako	M0725	1:50
ZO1	Mouse	Invitrogen	33-9100	1:300

Table S2.
Sequence of qPCR primers

Gene name	Primer Sequence (fwd/rev)
ACTB	CCTTGCACATGCCGGAG GCACAGAGCCTCGCCTT
GAPDH	TTGAGGTCAATGAAGGGGTC GAAGGTGAAGGTCGGAGTCA
PAX6	TGGTATTCTCTCCCCCTCCT TAAGGATGTTGAACGGGCAG
NANOG	TTGGGACTGGTGGAAGAATC GATTTGTGGGCCTGAAGAAA
OCT4	TCTCCAGGTTGCCTCTCACT GTGGAGGAAGCTGACAACAA
SOX17	CCAGACCGCGACAGGCCAGAAC AGTGAGGCACTGAGATGCCCCGAG
BRACHYURY	ATGCAGTGACTTTTTGTCGTGG ACTGAGGCTGCATTTCCTTCTT
E-CADHERIN	GAGCTACACGTTCACGGTGCCC GGCTGTCCTTTGTCGACCGGTG

PNAS RESEARCH ARTICLE | NEUROSCIENCE OPEN ACCESS

TARGET-seq: Linking single-cell transcriptomics of human dopaminergic neurons with their target specificity

Alessandro Fiorenzano[a,1,2], Petter Storm[a,1], Edoardo Sozzi[a], Andreas Bruzelius[a], Sara Corsi[a], Janko Kajtez[a], Janitha Mudannayake[a], Jenny Nelander[a], Bengt Mattsson[a], Malin Åkerblom[a,b], Tomas Björklund[b], Anders Björklund[a,2], and Malin Parmar[a,2]

Affiliations are included on p. 12.

Contributed by Anders Björklund; received May 27, 2024; accepted October 18, 2024; reviewed by Jun Takahashi and Lachlan H. Thompson

Dopaminergic (DA) neurons exhibit significant diversity characterized by differences in morphology, anatomical location, axonal projection pattern, and selective vulnerability to disease. More recently, scRNAseq has been used to map DA neuron diversity at the level of gene expression. These studies have revealed a higher than expected molecular diversity in both mouse and human DA neurons. However, whether different molecular expression profiles correlate with specific functions of different DA neurons or with their classical division into mesolimbic (A10) and nigrostriatal (A9) neurons, remains to be determined. To address this, we have developed an approach termed TARGET-seq (Tagging projections by AAV-mediated RetroGrade Enrichment of Transcriptomes) that links the transcriptional profile of the DA neurons with their innervation of specific target structures in the forebrain. Leveraging this technology, we identify molecularly distinct subclusters of human DA neurons with a clear link between transcriptome and axonal target-specificity, offering the possibility to infer neuroanatomical-based classification to molecular identity and target-specific connectivity. We subsequently used this dataset to identify candidate transcription factors along DA developmental trajectories that may control subtype identity, thus providing broad avenues that can be further explored in the design of next-generation A9 and A10 enriched DA-neurons for drug screening or A9 enriched DA cells for clinical stem cell-based therapies.

Parkinson's disease | human embryonic stem cells | single-cell sequencing | A9 and A10 dopamine neurons | Axonal projections

Significance

Understanding the molecular basis of dopaminergic (DA) neuron diversity is crucial for both experimental work and clinical applications. Here, we present a comprehensive single-cell dataset identifying 9 distinct molecular human DA neuron subtypes one year posttransplantation in a Parkinson's disease rat model. By developing TARGET-seq, a technology coupling single cell transcriptional profiles of DA neurons with their specific brain target innervations, we link the molecular identities to the classical definition of A9 and A10 DA neurons. This study advances our understanding of human DA neuron molecular diversity and how it relates to neuroanatomical-based classifications, which is relevant for cell-based therapies, disease modeling, and diagnostics for PD and neuropsychiatric disorders.

Dopaminergic (DA) neurons in ventral midbrain (VM) constitute a heterogeneous group of cells with different functions and innervation targets as well as different vulnerability to disease (1, 2). DA neurons in the VM have traditionally been divided into two main subtypes, A9 and A10, based on their anatomical location and projections. The A9 DA neurons that make up the nigrostriatal pathway are located in the substantia nigra pars compacta (SNpc), project to the dorsolateral striatum (dlSTR), and are a key regulator of motor function in the mammalian brain (2–4). This subtype of DA neurons has been well studied due to their selective vulnerability and degeneration in Parkinson's disease (PD). The A10 neurons that make up the mesolimbic system, are located in the ventral tegmental area (VTA), and have a more widespread innervation to targets in the forebrain including the nucleus accumbens, ventral striatum, septum, amygdala, and prefrontal cortex (PFC). The A10 neurons are mainly involved in controlling emotional behavior, addiction, motivation, and reward (5, 6). It is now recognized, however, that the DA neurons giving rise to the nigrostriatal and mesolimbic pathways are not strictly divided between the SN and the VTA, and that more subtypes exist (7–9). Additionally, recent studies based on single-cell RNA sequencing (scRNAseq) have revealed a molecular diversity among midbrain DA neurons that is greater than expected (10–15). Common to the studies published to date on molecular heterogeneity within the DA system is that they are based only on gene expression and while there are points of congruence, there are also key differences in the published datasets, making a unified classification scheme difficult (10, 16). Moreover, the molecular identities of the DA neurons are not directly linked to location or projections of the neurons, which are the landmarks traditionally used for human DA neuron classification. Thus, it remains unclear whether and how the diverse molecular identities converge to delineate functionally distinct DA subtypes within the human dopaminergic system, and it remains to experimentally address how they relate to the topographically defined A9 and A10 identities.

In this study, we used a well-established xenograft model of PD wherein human fetal and stem cell-derived DA neurons are transplanted homotopically into the lesioned rat midbrain (17–19). The function and maturation of the human DA neurons were assessed

Reviewers: J.T., Kyoto Daigaku iPS Saibo Kenkyujo; and L.H.T., The University of Sydney.

Competing interest statement: Malin Parmar performs paid consultancy to Novo Nordisk A/S, Denmark. Tomas Björklund is founder and director of Brave Bioscience AB and co-founder and SAB member of Dyno Therapeutics. Malin Parmar is the owner of Parmar Cells that holds related ip (U.S. patent 15/093,927, PCT/EP17181588). Tomas Björklund is inventor of multiple patents related to gene therapy, founder and director of Brave Bioscience AB and co-founder and SAB member of Dyno Therapeutics.

[1]A.F. and P.S. contributed equally to this work.

[2]To whom correspondence may be addressed. Email: alessandro.fiorenzano@med.lu.se, anders.bjorklund@med.lu.se or malin.parmar@med.lu.se.

This article contains supporting information online at https://www.pnas.org/lookup/suppl/doi:10.1073/pnas.2410331121/-/DCSupplemental.

Published November 14, 2024.

for up to one year in vivo, and the grafted cells were subsequently analyzed using single-nucleus RNA sequencing (snRNAseq) to construct a comprehensive transcriptional map of functionally mature human DA neurons. This revealed a molecular heterogeneity with nine clusters of molecularly distinct human DA neuron subtypes identified. However, like previous studies (10–13, 20), it was not possible to correlate the molecular identity based in snRNAseq with target specificity or function.

To link the transcriptional profile of the DA neurons with their innervation of specific target structures in the forebrain, we therefore developed an approach termed TARGET-seq (Tagging projections by AAV-mediated RetroGrade Enrichment of Transcriptomes). In these experiments, we delivered mCherry molecular barcode via retrogradely transported designer AAVs (MNM008) (21, 22) into two distinct DAergic target areas in the forebrain: the dorsolateral striatum (dlSTR) and the prefrontal cortex (PFC). After injection, mCherry AAVs are subsequently transported back to the grafted human DA neurons in the midbrain, allowing molecular segregation of the DA neurons that project to A9 targets (dlSTR) and DA neurons that project to the PFC which is one of the main targets of A10 DA neurons. Leveraging this technology, we identify molecularly distinct subclusters of DA neurons with a clear link between transcriptome and axonal target specificity, and thus the possibility to infer neuroanatomical-based classification to molecular identity and target-specific connectivity. We subsequently used this dataset to identify candidate transcription factors (TFs) along DA developmental trajectories. These factors were validated using a commonly used in silico approach (23), which suggest a role in DA neuron determination and supports their further exploration to control DA subtype identity.

Results

High Similarity Between Fetal and hPSC-Derived DA Grafts. In order to generate a molecular map of developing and mature human DA neurons at single-cell resolution, we homotopically transplanted human fetal VM tissue and stem cell-derived DA neurons to the midbrain of 6-hydroxydopamine (6-OHDA) lesioned immune-deficient rats. The ability of both fetal and stem cell–derived DA neurons to mediate functional recovery after intranigral grafting was determined by amphetamine-induced rotations, and the rotational asymmetry was found to be progressively corrected over time for both groups (Fig. 1*A*, n = 10 per group) with no significant difference between fetal- or VM-derived DA neurons. 6 of the rats grafted with fetal VM tissue and 9 rats grafted with stem cell-derived DA neurons were perfused and analyzed using histology twelve months following transplantation. Assessments using antibodies for human neural cell adhesion molecule (hNCAM, detecting the transplanted cells) and tyrosine hydroxylase (TH, detecting the DA neurons) confirmed that the grafts had phenotypically matured (Fig. 1 *B* and *C*). Both groups contained grafts of comparable average volume, but with large variation in the fetal grafts (Fig. 1*D*). Quantifications of TH content in the graft confirmed a higher number of DA neurons in the stem cell–derived grafts (3436±1694, mean ±SD) compared to fetal grafts (656±598SD, mean ±SD). In both groups, analysis of fiber innervation based on hNCAM staining showed that the transplanted neurons exhibited the capacity to extend axons from the graft core along the medial forebrain bundle (MFB), forming terminal networks in the ventral/dorsal forebrain, including PFC and amygdala, as well as in the dorsolateral striatum (Fig. 1 *E–H* and *SI Appendix*, Fig. S1 *A* and *B*). Colabeling of TH in combination with mature and subtype-specific DA markers ALDH1A1, GIRK2, and CALB showed that DA neurons expressing one or more of these markers were present in the grafts (Fig. 1 *I* and *J*), as was the molecular machinery required for dopamine reuptake, as detected via DAT (Fig. 1*K*). Additionally, the presence of neuromelanin could be detected as dark granular pigmentation in the long-term grafts, indicating a highly mature DA neuron component (Fig. 1*L*).

The focus of this study was to determine the molecular phenotypes of mature and functional human DA neurons and for this we needed to overcome previous difficulties involved in dissecting and reisolating grafted human neurons for single-cell profiling (24). We developed a pipeline based on single nucleus RNAseq (snRNAseq) to generate an unbiased and comprehensive map of cell type composition from long-term human DAergic xenografts. First, the midbrain (where the graft was located) was sliced into 350 µm thick sections using a vibratome, and then the grafted area was dissected for nuclei extraction followed by 10X genomics droplet-based single nucleus transcriptomic analysis. For the fetal VM grafts, we isolated 15 independent intranigral transplants originating from 5 different embryos of various gestational ages (from weeks 6.5 to 10 postconception), profiling a total of 14,557 nuclei after quality filtering (*SI Appendix*, Fig. S1*C*). After integration using the Harmony approach, five distinct clusters in the grafts were identified using graph-based clustering and visualized using uniform manifold approximation and projection (UMAP; Fig. 1*M*). Identified cell types (Fig. 1*M* and *SI Appendix*, Fig. S1*C*) were automatically annotated based on highly differentially expressed genes (DEGs) and manually selected using canonical cell type markers (*SI Appendix*, Fig. S1 *C* and *D*). UMAP visualized clusters of cells with VM floor plate-like characteristics (FP; *NES*, *FOXA2*, *LMX1A, CORIN*), postmitotic neurons (*TH*, *SLC6A3*, also known as *DAT*), astrocytes (*AQP4*, *GFAP*), and oligodendrocyte progenitors (OPCs; *OLIG1/2*, *SOX10*) and a small cluster of vascular leptomeningeal cells (VLMCs; *COL1A1*, *LUM, FBLN1)* (Fig. 1*M* and quantified in Fig. 1*P*, and *SI Appendix*, Fig. S1 *D–G*). Animals grafted with human pluripotent stem cell (hPSC)-derived DA neurons, were analyzed by snRNAseq at different time points between 6 and 12 mo of in vivo maturation (n = 6 at 6 mo, n = 7 at 9 mo and n = 7 at 12 moFig. 1*N* and *SI Appendix*, Fig. S2 *A–C*). The expression of nuclear GFP-encoding transgenes in transplanted hPSCs facilitated both graft dissection and FACS of human nuclei from the host environment (*SI Appendix*, Fig. S2 *A–C*). Utilizing 10X genomics droplet-based single nucleus transcriptomic analysis of 20 independent hPSC-derived intranigral grafts, profiling a total of 78,000 human nuclei (Fig. 1*N* and *SI Appendix*, Fig. S2*D*). As with the fetal grafts, five distinct clusters in the hPSC-derived grafts were identified and visualized using UMAP and graph-based clustering after Harmony integration (Fig. 1*N* and *SI Appendix*, Fig. S2 *D* and *E*).

Notably, hPSC-derived grafts exhibited much lower sample-to-sample variability (*SI Appendix*, Figs. S1*C* vs S2*D*) and ROGUE analysis (an entropy-based statistic measurement) confirmed higher heterogeneity of the fetal VM grafts (Fig. 1*O*). By quantifying changes in the relative proportion of cell types, we found that the neuron and astrocyte compartments were highly comparable in the hPSC and fetal stem cell sources (Fig. 1*P*). However, while we detected a large percentage of OPCs and a minor presence of VLMCs in the fetal grafts, these proportions were inverted in the hPSC-derived transplants (Fig. 1*P* and *SI Appendix*, Fig. S2 *F* and *G*). We next investigated whether the cell types generated in hPSC-derived grafts were transcriptionally similar to their fetal counterparts by projecting fetal-derived snRNAseq data on hPSC, and then normalized and clustered the gene expression matrix to measure and quantify the percentage of matched cell types

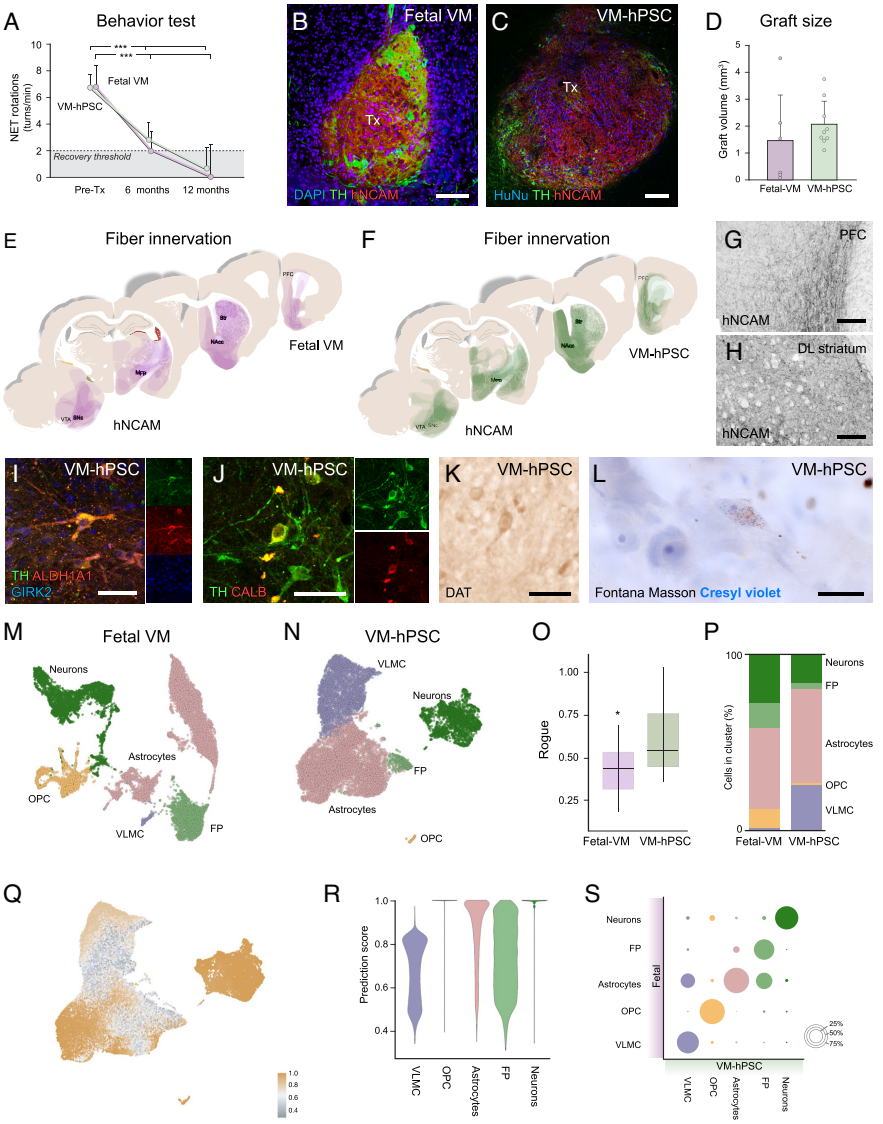

Fig. 1. Cell type composition of 12-mo-old fetal and hPSC-DAergic grafts. (*A*) Amphetamine-induced rotation test indicating functional recovery in transplanted human fetal cell (n = 12) and VM-patterned hPSCs (n = 10) after 6 and 12 mo (one-way ANOVA: ***P < 0.0001 for pre-Tx vs. 6 and 12 mo post-Tx). (*B*) Immunohistochemistry of TH/hNCAM in human fetal cell, and (*C*) VM-patterned hPSCs intranigral grafts 12 mo posttransplantation. (Scale bar, 200 μM.) (*D*) Analysis of graft volume 12 mo posttransplantation. (*E* and *F*) Composite overlay of hNCAM+ fibers from DAB-developed sections from 7 animals transplanted with human fetal cell (purple, *E*) and 9 animals transplanted with VM-patterned hPSC (green, *F*) intranigral grafts, innervating the host brain. G, H, hNCAM$^+$ fibers from DAB-developed sections in *G*, ventromedial PFC and, (*H*) dlSTR. (Scale bar, 200 μm.) (*I*) Immunocytochemistry of TH/ALDH1A1/GIRK2 and (*J*) TH/CALB in VM-patterned hPSC intranigral grafts. (Scale bar, 50 μm.) (*K*) Immunohistochemistry of DAT under bright-field illumination of DAB-developed sections. (Scale bar, 50 μm.) (*L*) Fontana Masson/cresyl violet immunohistochemistry of VM-patterned hPSC intranigral grafts 12 mo posttransplantation. (Scale bar, 20 μm.) (*M* and *N*) Uniform manifold approximation and projection (UMAP) embeddings showing clustering of analyzed cells from (*M*) fetal VM-derived, and (*N*) VM-patterned hPSC intranigral grafts 12 mo posttransplantation. For both graphs the number of cells were randomly downsampled to 15 000. Cell-type assignments are indicated. (*O*) Boxplot showing higher hetereogeneity in fetal derived grafts compared to VM-patterned analyzed samples as indicated by a decreased Rogue score. (*P*) Proportion of each cell type from fetal and VM-patterned hPSC intranigral grafts 12 mo posttransplantation. (*Q*) UMAP colored by projection of fetal snRNA data onto hPSC-derived cells, colored by prediction score. Blue indicates low similarity (score ~0.4) and brown indicates high similarity (score ~1.0). (*R*) Violin plot showing the prediction scores across different cell types derived from VM-hPSC. Higher prediction scores, close to 1.0, indicate a strong resemblance to the corresponding fetal cell types, with neurons, OPC, and astrocytes having the highest scores. (*S*) Dot plot comparing fetal and VM-hPSC-derived cells across various cell types. The size of each dot represents the proportion of cells overlapping.

(Fig. 1*Q*). A detailed comparison between the five clusters detected in hPSC grafts and the five clusters captured in fetal grafts revealed a similar molecular identity (Fig. 1*Q*). The neuron clusters in particular showed a high prediction score confirming a high similarity of neurons sourced from human fetal brain and hPSCs (Fig. 1 *R* and *S*).

Human DA Neuron Diversity. We next focused our analysis on molecular subtypes of human neurons within the grafts, by isolating the neuronal cluster of the hPSC-derived grafts from all 3 to 12 mo (14,606 cells in total). We then reran the integration (Harmony) and clustering analyses with only the neurons (Fig. 2*A*). A UMAP plot visualized seven distinct subclusters (Clusters 1 to 7), all expressing mature and postmitotic neuronal markers, including the synapse-associated genes *SNAP25* and *SYT1* (Fig. 2*B*). snRNAseq highlighted transcriptional diversity within the neuronal populations, revealing that five out of the seven clusters expressed *TH* as well as other characteristic molecular features of midbrain DA neurons, such as *NR4A2* and *SLC18A2* (also known as *VMAT2*) (Fig. 2*B* and *SI Appendix*, Fig. S3*A*). No serotonergic clusters (*SLC6A4*) were detected in the grafts (Fig. 2*A* and *SI Appendix*, Fig. S3*A*) and while some genes expressed by GABAergic and glutamatergic neurons (*GAD1* and *SLC17A6*, also known as VGLUT-2) were expressed in two small clusters (cluster 5 and 1, respectively), these clusters did not correspond to GABAergic or glutamatergic neuronal subtypes. Overall, snRNAseq showed that DA neurons constituted the main neuronal component in the VM-patterned hPSC grafts and highlighted the presence of multiple DA molecular identities. This is in contrast to fetal VM grafts (Fig. 2 *C* and *D*) where ROUGUE variability assessment indicated greater heterogeneity in neuronal molecular identities (Fig. 2*E*), and UMAP plot visualized seven distinct subclusters of neurons, whereof only clusters 5 and 7 were assigned to DA neuron cell types (Fig. 2 *C* and *D*). GABAergic (*GAD1*, *ABAT*) and glutamatergic (*GRID1*, *GRIK5)* neuronal markers were detected in clusters 2, and 3 of fetal grafts and in cluster 1, this latter concomitantly expressing immature molecular features (*NES*) (Fig. 2 *C* and *D*). Cluster 4 in the UMAP comprised a mixture of cell types expressing proliferative and immature neuronal markers (*CCNI, ELF1, FABP7, SOX2*) along with cells with serotonergic signature (FEV, SLC6A4, HTR2A) (Fig. 2 *C* and *D*). A direct comparison of these datasets shows that the hPSC-derived neuronal subclusters are dopaminergic (with varying levels of TH-expression). Notably, we did not find any distinct clusters corresponding to GABAergic, glutamatergic, or serotonergic identities. In contrast, fetal derived neurons show mixed GABAergic/glutamatergic expression profiles and with one cluster clearly mapping to serotonergic neurons (*SI Appendix*, Fig. S3*B*).

We next performed a higher-resolution analysis in order to obtain a more refined and stringent DA diversity map by computationally sort and recluster only TH^+ nuclei from the neuronal population (Fig. 2*F*). The resulting UMAP graph-based clustering revealed nine transcriptionally distinct DA clusters (DA-1 to 9) (Fig. 2*G*) from an analysis of ~6,000 high-quality DA neuron nuclei. Hierarchical relationship analysis showed that all DA subtypes tended to group together, except for DA-7, which exhibited a divergent pattern (Fig. 2*H*). Splitting the UMAP plot into the individual time points from which the grafted cells were reisolated and analyzed (3 to 12 mo) revealed that the DA neuron population acquired greater cellular complexity with progressively defined subtypes over time (Fig. 2*I*). Along the timeline of DA diversification, we detected up- and downregulated of known DA neuron markers, including *DCC, DLK1,* and long noncoding *NEAT1*, but also novel genes such as *NEK7* and *CNTN5* (encoding for a protein kinase and neural recognition molecule, respectively), not previously associated with the DA specification program (*SI Appendix*, Fig. S3*C*).

The filtered TH^+ nuclei all displayed a typical molecular signature of DA neurons, including expression of genes essential for DA maturation and neurotransmission (*NR4A2*/*NURR1*, *SLC6A3*/*DAT*, *SLC18A2*/*VMAT2*, *ALDH1A1*) (Fig. 2 *J* and *K*). Although all nine DA clusters shared highly similar expression patterns, they differed in a small subset of genes, thus a molecular signature distinguishing each DA subtype can be defined (Fig. 2 *J* and *K* and *SI Appendix*, Table S1). DA subtype markers previously identified during development up until adulthood in mice (11) were found to be strongly expressed in our dataset. DA-1 to 4 were particularly enriched in *KCNJ6, VMAT2* (*SLC18A2*), and synuclein protein family member *SNCA*, with the absence of *OTX2* (12, 25, 26) (Fig. 2 *J* and *K*). Specifically, within the DA-2 subcluster we found concomitant expression of *ALDH1A2*, and *VGLUT2* (*SLC17A6*) together with GDNF family receptor alpha1 *GFRA1* (Fig. 2 *J* and *K*). DA-2 also expressed transmembrane protein *TMEM200A* (Fig. 2 *J* and *K*), (10, 27, 28), as well as the nuclear receptor factor *NRIP3* and neurofilament *NEFM* (Fig. 2 *J* and *K*), also found expressed in the DA-3 subcluster. DA-3 was specifically defined by greater expression of *SLC6A3*, *RET*, *SLC18A2*, *KCNJ6*, and the dopamine receptor *DRD2* (Fig. 2 *J* and *K*) compared to the other subclusters. Despite challenges in comparing datasets with postmortem brain tissue, merged clustering revealed that DA-1 to 3 clusters exhibited the highest transcriptional similarity to adult human SN cell populations (13), suggesting vulnerability to degeneration and neuromelanin release (*SI Appendix*, Fig. S3*D*). *SOX6* was also detected in DA-3 and was likewise found highly expressed in DA-4 and DA-5 together with calcium voltage-gated channel *CACNA2D1* (Fig. 2 *J* and *K* and *SI Appendix*, Fig. S3 *E* and *F*). DA-6 and 7 subclusters expressed genes such as *OTX2*, *ZDHCC2*, and *FOXP2* (Fig. 2 *J* and *K*). Additionally, *LM3O* and *NFIB*, recently identified human DA neuron markers enriched in VTA (12, 14), were expressed in DA-7 (Fig. 2 *J* and *K*). Both of these subclusters were also enriched in genes previously identified at single-cell level in developing and adult mouse brain, such as *LYPID1* and *ADCYAP1* (Fig. 2 *J* and *K*) (11, 26). Many of the DEGs detected here have been reported in other similar datasets (11, 12, 14, 27, 29). These DEGs identify partially overlapping subtypes and are suggested to be enriched in A9-like vs A10-like neurons or act as candidate regulators for each subtype. However, the use of different defining markers and naming schemes across studies has made it difficult to consolidate the data and clearly define DA subtypes (10).

TARGET-seq Identifies Distinct DA Neuron Subtypes Based on Projection Pattern. The snRNAseq revealed a heterogeneous composition of DA neurons within the grafts, which reflects the molecular diversity of DA populations previously reported in human and mouse VM. However, as with previously published datasets, it remains to be determined whether and how these molecular subtypes relate to functional characteristics, target specificity, and the classical A9 and A10 DA neuron classification. To generate a transcriptional map of human DA neurons where their molecular identities are linked to their axonal projections in the host brain, we combined intranigral transplantation with injections of mCherry tag delivered using a specifically designed AAV suitable for retrograde transport to DA neurons (MNM008) (22) in a technology that we named TARGET-seq (Fig. 3 *A* and *B*). Here, hPSC-derived DA progenitors were transplanted to the midbrain (Fig. 3 *A* and *B*, step 1). After 11 mo, when the projections of the transplanted

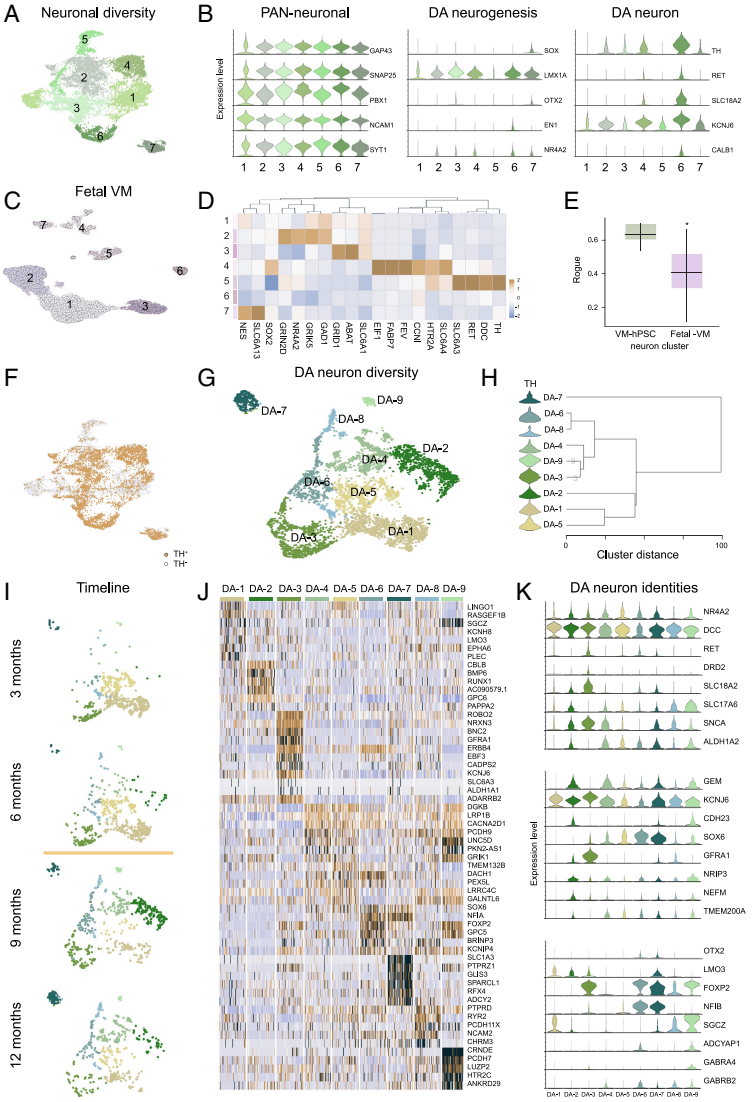

Fig. 2. Human DA neuron composition in hPSC-derived grafts. (*A*) UMAP plot displaying neuron subclusters after reclustering of VM-patterned hPSC intranigral grafts 12 mo posttransplantation (n = 12 509). (*B*) Violin plots illustrating normalized expression levels of indicated genes in each neuronal subcluster (1 to 7). (*C*) UMAP plot revealing neuron subclusters after reclustering of fetal-VM derived neurons 12 mo posttransplantation (n = 3954). (*D*) Heatmap presenting differentially expressed genes and manually selected markers in fetal neuron subclusters (1 to 7). (*E*) Quantification of neuronal subtype diversity between fetal VM-derived and VM-patterned hPSC intranigral grafts 12 mo posttransplantation ($P < 0.01$). (*F*) UMAP of hPSC- derived neuronal cells marked by TH expression (Expression > 0 marked in orange). (*G*) UMAP plot of DA neuron subclusters after TH^+ cells reclustering. (*H*) Dendrogram of unsupervised hierarchical clustering of DA clusters using uncentered Pearson correlation. (*I*) Individual UMAP plot presenting DA cluster diversity within hPSC-derived intranigral graft from 3 to 12 mo. (*J*) Heatmap displaying differentially expressed genes and selected markers for DA neuron subclusters (1 to 9). (*K*) Violin plots showing expression levels of indicated genes in each DA neuron subcluster (1 to 9).

DA neurons in the SN have extended along the nigrostriatal and mesolimbocortical pathways and into their forebrain targets, retrograde AAVs were stereotactically injected into two different forebrain target regions; the dorsolateral striatum (dlSTR) and the prefrontal cortex (PFC) (Fig. 3 *A* and *B*, step 2). The AAVs were engineered to express molecular tags including the red fluorescent mCherry protein for identification of successful axonal tracing as well as barcode sequences consisting of 20 base pairs of semirandom nucleotides, followed by a short library identification sequence, and a polyadenylation signal, all under the control of the same promoter. The polyadenylation signal enables capture of these sequences by standard 10X droplet based sequencing. Thus, once the tags have been transported to the midbrain, the graft can be isolated and TARGET-seq used to link the transcriptional profiled of an individual human DA neurons in the grafts with its specific projection pattern (Fig. 3*A*, step 3). Immunostainings confirmed fluorescent mCherry AAV injected into either PFC (Fig. 3*C*) or dlSTR (Fig. 3*D*), as well as their successfully retrograde transport back to the human DA neurons in the grafts (*SI Appendix*, Fig. S4 *B* and *C*). To perform TARGET-seq, intranigral grafts were isolated and microdissected 12 mo after transplant to the nigra/one month after AAVs injection in axonal target site, and single nuclei extracted for sequencing. The resulting snRNAseq data were mapped to the human genome with the addition of *mCherry* sequence, and the DA

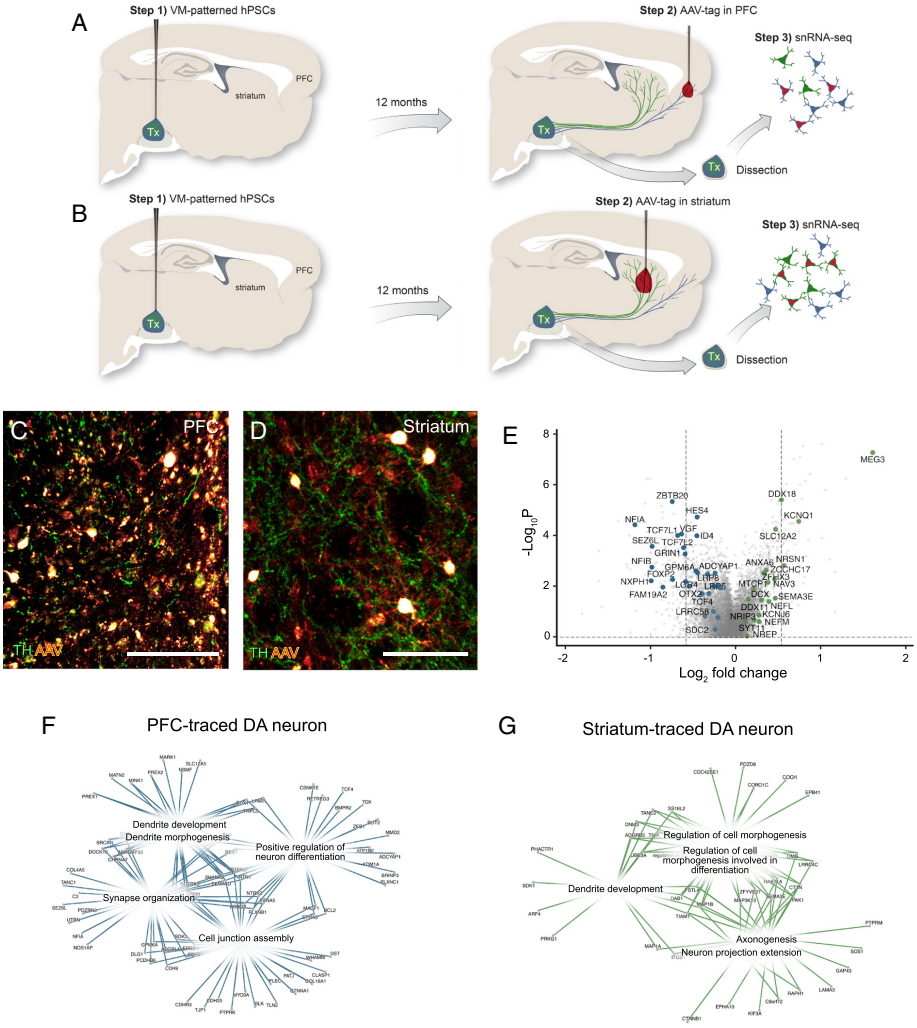

Fig. 3. Axon target-based single cell transcriptomics of DA neuron subtypes. (*A* and *B*) Schematic representation of the TARGET-seq experimental design. Retrograde mCherry AAV injection and tracing from either (*A*) the ventromedial PFC or (*B*) the dlSTR to DA neurons in a 12-mo transplant. (*C*) Detection of retrograde mCherry AAV and TH immunohistochemistry at the ventromedial PFC injection site. (Scale bar, 100 μm.) (*D*) Detection of retrograde mCherry AAVs, TH immunohistochemistry at the dlSTR injection site. (Scale bar, 100 μm.) (*E*) Volcano plot illustrating differential gene expression between dlSTR- and PFC-traced human DA neurons. Selected genes are highlighted in green and blue for dlSTR- and PFC-traced human DA neurons, respectively. Dashed lines indicate *P*-value < 0.05 and |log2-foldchange| > 0.5. (*F* and *G*) Gene Ontology (GO) enrichment analysis displaying of the significant genes ($P < 0.05$) for PFC-traced neurons (*F*) and dlSTR-traced human (*G*) DA neurons. Top five enriched ontology terms are shown including leading edge genes for each gene ontology.

cohort was identified based on *TH* expression at the transcript level. Statistical analysis revealed that TH^+ neurons had a significantly higher number of traced neurons compared to non-DA neurons ($P < 0.05$, chi-square test) indicating that TH^+ neurons are more likely to connect with the interrogated target regions. Biological replicates of three independent grafts for each injection site were analyzed in order to obtain a comprehensive transcriptional profile of human DA neurons based on their innervation target specificity.

We found ~900 differentially expressed protein-coding genes in the two distinct projection-specific DA subtypes (FDR $P < 0.05$, Fig. 3*E*). The PFC-projecting human DA neurons were found enriched in *OTX2* and the nuclear factors *FOXP2* and *NFIA/B* (Fig. 3*E*), all markers previously associated with an A10 molecular identity in VTA (10, 27). Among these differentially expressed genes we also detected the secreted protein *NXPH1*, involved in adhesion between dendrites and axons, and the glutamate receptor *GRIN1*(Fig. 3*E*). In addition, we observed the expression of genes not previously associated with the DAergic lineage, such as the nuclear factor *ZBTB20*, whose deletion leads to cognitive dysfunction and basal ganglia calcification in Primrose syndrome, and the

leucine-rich repeat factor *LINGO1* (Fig. 3*E*) (30, 31). In contrast, *KCNJ6* was found enriched in dlSTR-projected human neurons together with transcription factors *ZCCHHC17* and *DDX11/18*, the long noncoding RNA *MEG3*, and the neurofilaments *NEFM* and *NEFL* (Fig. 3*E*), that have previously been related to an A9 molecular identity in SN (10, 12, 28). Of note, consistent with the axonal retrograde tagging approach used to generate the single-cell datasets, Gene Ontology (GO) analysis revealed that the most enriched terms were linked to terms such as Dendrite Development, Axogenesis, Axon Projection Extension, and Synapse Organization in both PFC- and dlSTR-traced DA neuron subtypes (Fig. 3 *F* and *G* and *SI Appendix*, Fig. S4 *D* and *E*).

To assess the transcriptional similarity of AAV-traced human nuclei and the robustness of the generated projection-specific snRNAseq dataset, we projected PFC- and dlSTR-traced human DA neuron identities onto the overall TH^+ diversity map, encompassing all identified DA subclusters. We found that both dlSTR- and PFC-tracked nuclei specifically mapped to two separate clusters on the TH^+ UMAP plot (Fig. 4 *A* and *B* and *SI Appendix*, Fig. S4 *F* and *G*). The PFC-traced neurons were concentrated in the DA-7 subcluster (chi-square *P*-value 0.001265) (Fig. 4*A* and *SI Appendix*, Fig. S4*F*), which exhibited a molecular signature with expression of *OTX2*, *LMO3*, and *FOXP2* (Fig. 4*C* and *SI Appendix*, Fig. S4*H*). This is also the cluster with the divergent hierarchical pattern of the 9 DA subtypes (Fig. 2*H*). In contrast, dlSTR-traced neurons specifically matched ($P = 0.005557$) to subcluster DA-2 in the TH^+ UMAP plot, characterized by high expression of *KCNJ6*, *GEM*, *VMAT*-2, *NEFM*, and *SNCA*, (Fig. 4*C* and *SI Appendix*, Fig. S4*G*). We then explored these projection-specific subclusters (DA-2 and DA-7) to identify regulatory pathways that may drive specification of DA neuron subtype identities. Gene Set Enrichment Analysis (GSEA) identified WNT Canonical Signaling as one of the most biologically upregulated pathways, with a highly significant enrichment score in the PFC-projected DA cluster (Fig. 4 *D* and *E*). A set of 90 genes encoding both components and downstream targets of WNT pathway were upregulated (adjusted *P*-value < 0.05). High expression of *TCF* and *LEF* transcription factor family members and the cell surface receptors *LGR, FZD*, and *LRP* indicated that WNT pathway was activated in the PFC-traced human DA neuron subtype (Fig. 4*F*). In contrast, signaling components of MAPK cascade were found significantly enriched in the dlSTR-projected DA cluster (Fig. 4 *G* and *H*). More than 50 genes, including *RASA3* and *MRAS*, encoding Ras GTPase-activating proteins, as well as *MAPK4* and *JUN*, encoding protein kinases (adjusted *P*-value < 0.05) were increased, indicating that activation of the ERK cascade occurs in the dlSTR-projected human DA neuron subtype (Fig. 4 *H* and *I*). Importantly, GSEA revealed a significant enrichment of the MAPK signaling pathway in the most vulnerable DA neurons when examining single-cell datasets derived from human postmortem samples [Fig. 4*J*, (13)], linking the population identified using TARGET-seq with in vivo data.

Temporal and Target-Specific Molecular Refinement. We next employed SPRING analysis to infer the dynamics of DA fate decisions (32). Cell trajectories were defined based on transcriptional similarity along a temporal axis spanning up to 12 mo postengraftment. Lineages were delineated by treating clusters of cells as nodes in a graph and constructing a minimum spanning tree between nodes (Fig. 5*A*). SPRING generated a molecular trajectory that temporally mirrored DA neuron clusters sequentially isolated at different time points after transplantation. Notably, the molecular identities obtained at 3 and 6 mo were positioned at the beginning of the trajectory, indicating a gradual acquisition of DA neuron diversity (Fig. 5*A*). Furthermore, when arranging cells based on transcriptional similarity along a temporal axis using a force-directed k-nearest-neighbor graph-based pseudotime trajectory, cluster DA-1 and cluster DA-5 were identified as intermediate molecular identities (Fig. 5*B*). These subsequently segregated into a first branch in cluster DA-9 and a second branch in cluster DA-8. Cluster DA-8 then bifurcated, with one branch passing through the intermediate cluster DA-4 and evolving into cluster DA-2, corresponding to the molecular identities of dlSTR-projecting DA neurons. The other branch evolved into cluster DA-6, ultimately leading to either cluster DA-3 or DA-7, which was identified as containing DA identities projecting to the PFC (Fig. 5*B*). We identified differentially expressed genes along branches in the TH^+ diversity map, including *PLXDC2* (plexin domain-containing protein 2), *SGCZ* (associated with dystonia syndrome), and *KCNH8* (a member of the potassium voltage-gated channel subfamily 8) (Fig. 5*C*). The expression pattern of these genes suggest that they may contribute to determining distinct functions and projection patterns of various human DA subtypes in the brain (Fig. 5 *B* and *C*).

Gene Regulatory Network (GRN) analyses revealed that PFC- and dlSTR-projecting DA clusters were influenced by distinct sets of transcription factors, that are potential candidates to play a role in DA-subtype fate determination (Fig. 5 *D* and *E*). GRN of PFC-cluster highlighted known neuronal markers associated with A10 neurons such as *OTX*2, along with novel genes not previously associated with this DA subtype (Fig. 5*D*). Consistent with GO analysis, transcription factors linked to the WNT pathway were identified as potential regulators of the PFC-projecting neuron fate (Fig. 4 *H* and *I* and Fig. 5*D*). To test these observations and predict their role in cell lineage determination, we employed CellOracle, thus propagating the downstream effect on the direct and indirect targets using the inferred CellOracle GRN (23). In silico perturbation was initially tested on *TCF7L2*, the major endpoint mediator of Wnt signaling. In silico knockout of *TCF7L2* was found to promote the specification of dlSTR-projecting DA clusters (cluster DA-2 and DA-3), with cells in PFC-projecting cluster (cluster DA-6) reverting back (Fig. 5*F*). Interestingly, when in silico *TCF7L2* overexpression was assessed, the opposite trend was observed, with dlSTR-projecting DA clusters reverting back while promoting specification in the PFC-projecting cluster (Fig. 5*F*). This analysis supports that the Wnt pathway is involved in driving specification into human A10-like neurons. We also tested *NFIB*, previously associated with mouse A10 and found enrichment in our PFC cluster. In silico knockout of *NFIB* continued to drive specification in PFC, concurrently promoting the fate of dlSTR clusters (Fig. 5*F*). However, in silico overexpression of *NFIB* reverted dlSTR toward other DA subtypes while promoting the PFC cluster determination (Fig. 5*F*). We also explored TFs significantly involved in dlSTR-projecting DA clusters, assessing *KLF7*, not previously characterized in DA tissue (Fig. 5*G*). In silico *KLF7* knockout impaired dlSTR-cluster specification, favoring the transition to the PFC cluster (Fig. 5*G*). In contrast, In silico *KLF7* overexpression triggered dlSTR-cluster maturation and conversion from cluster 4 (Fig. 5*G*). Similarly, the transcription factor *E2F3* In silico knockout affected cell fate decisions, driving specification to the PFC cluster, while *E2F3* overexpression seemed to enhance DA subtype segregation into the dlSTR-cluster (Fig. 5*G*).

We next investigated the presence of molecular subtypes of DA neurons identified using TARGET-seq in various in vitro human stem cell models (Fig. 5 *H*, *J*, and *L*). First, we used published datasets from 2D cultures (33) and VM organoids (20) (34) and assigned DA identities based on TARGET-seq (Fig. 5 *I* and *K*).

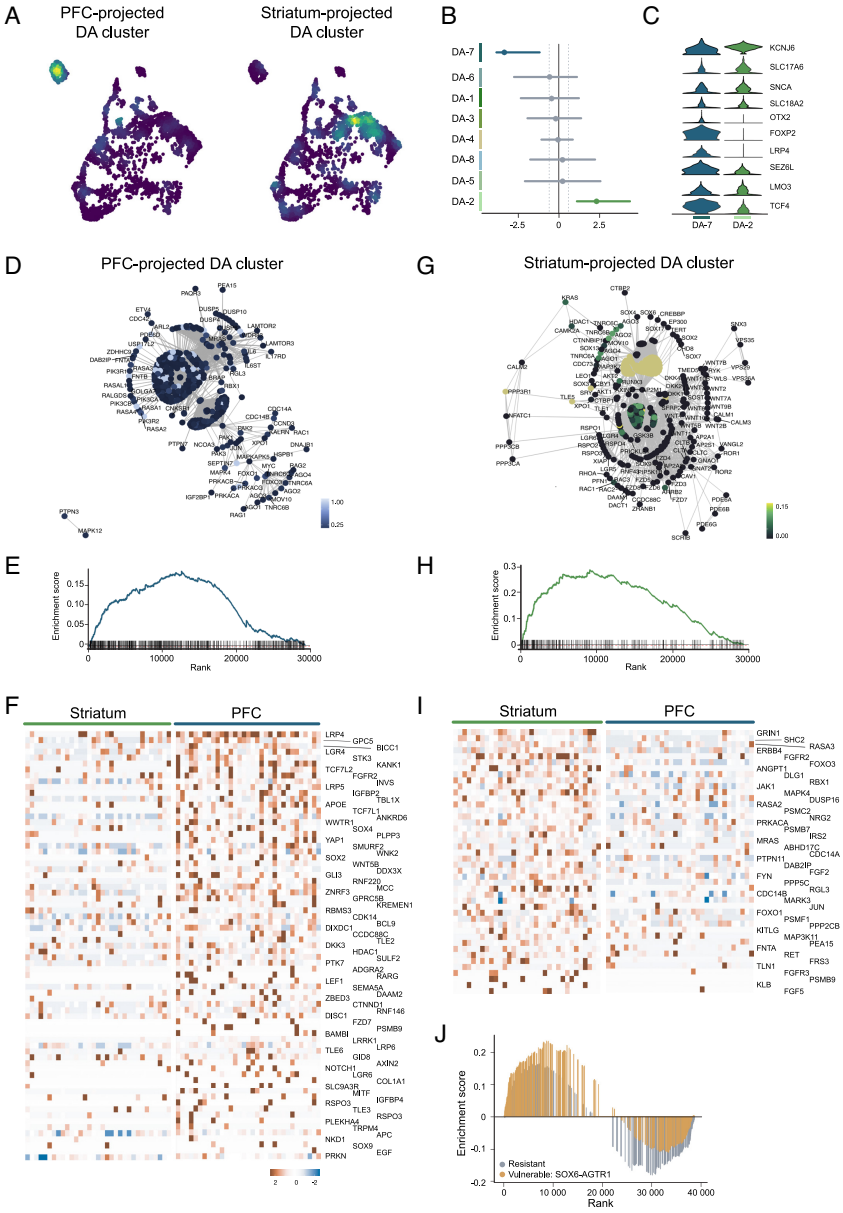

Fig. 4. Gene-set and enrichment pathway analyses in DA subtypes. (*A*) Cell density plot of PFC- and dlSTR-projected DA neurons in the DA UMAP space. (*B*) Permutation test of cluster proportions in PFC- and dlSTR-projected DA neurons. Dot-whiskers marked in blue and green are statistically significant (FDR $P < 0.05$). (*C*) Violin plots illustrating differential expression levels of indicated genes in dlSTR and PFC -projected DA neuron clusters (2 and 6 respectively). (*D*) Active regulons defining PFC-projected DA neuron clusters. (*E*) Gene Set Enrichment Analysis (GSEA) identifying WNT Canonical Signaling in PFC-projected DA cluster (FDR $P < 0.05$). (*F*) Heatmap of differentially expressed ($P < 0.05$) WNT-pathway associated genes between PFC- and dlSTR-projected DA neuron clusters. (*G*) Active regulons defining dlSTR-projected DA neuron cluster. (*H*) GSEA identifying MAPK pathway in the dlSTR-projected DA cluster. (*I*) Heatmap presenting differentially expressed MAPK-pathway associated genes between PFC- and dlSTR-projected DA neuron clusters. (*J*) MAPK-pathway enrichment analysis in the DA vulnerable population from human postmortem ventral midbrain (VM) compared to all other clusters in the same dataset (13).

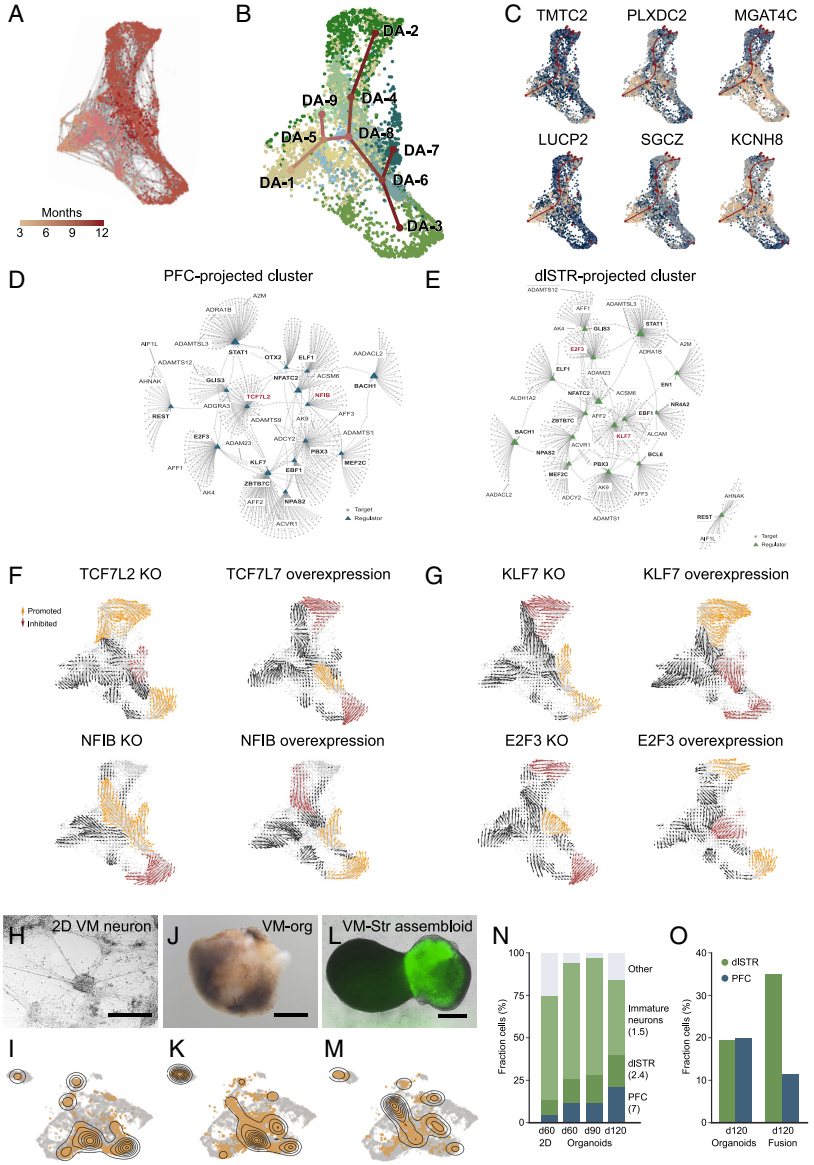

Fig. 5. Novel TFs in Human DA Neuron Subtype Trajectories. (*A*) Force-directed graph (SPRING) identifying the trajectory of DA cluster in stem cell transplant from month 3 to month 12. Cells are color-graded based on months after grafting. (*B*) Trajectory reconstruction by minimum spanning tree (Slingshot) of identified DA neuron clusters along the temporal axis. Branches and molecular specification are visualized with a force-directed layout, where each cell is represented by a point proceeding from 3 to 12 mo. (*C*) Selected markers along the temporal axis showing differential expression along identified trajectories. (*D*) Gene regulatory network underlying PFC-projected, and (*E*) dlSTR-projected DA neuron clusters. GRNs were constructed using Celloracle. (*F*) Quiver plot of CellOracle in silico knockout and overexpression of TFs not previously linked to DAergic neurons with a specific projection pattern: *TCF7L* and *NFIB* for PFC-projected DA cluster, and (*G*) *KLF7* and *E2F3* for dlSTR-projected DA cluster. The effect of the perturbation is shown with projections of cell state transition vectors on each cell's UMAP plot. Yellow or red arrow colors indicate in or out directionality, respectively. (*H*) Representative bright-field image of hPSC-derived DA neurons in 2D culture. (Scale bar ,200 μM.) (*I*) Cell density plot of projected 2D VM culture DA scRNAseq dataset onto hPSC-derived transplants. (*J*) Representative bright-field image of VM organoid. (Scale bar, 1 mm.) (*K*) Cell density plot of projected of VM organoid DA scRNAseq dataset onto hPSC-derived transplants. (*L*) Representative bright-field image of VM-STR assembloid;VM organoid region within assembloid was labeled by GFP. (Scale bar, 100 μM.) (*M*) Cell density plot of projected assembloid DA scRNAseq dataset onto hPSC-derived transplants. (*N*) Quantification of DA developmental trajectories detected in 12 mo hPSC-derived transplants in 2D, VM organoid at different developmental stage (day 60 to 120) datasets. (*O*) Quantification of PFC- and dlSTR-projected DA cluster in VM organoid and VM-STR assembloid DA datasets.

In the 2D cultures we found that the majority of cells mapped to immature DA subtypes (DA-1 and DA-5), but we also observed a small proportion of neurons mapping to the PFC and dlSTR-projecting clusters (DA-7 and DA-2/4 respectively) (Fig. 5 *I* and *N*). To assess DA neurons after longer time points in vitro, we analyzed data from 3D VM organoids that support long-term in vitro maturation (20, 34). When mapping the DA clusters defined by TARGET-seq onto VM organoid datasets we detected the emergence of more DA neurons with identities resembling DA neuron subtypes from long-term i n vivo grafts, including an increase in dlSTR-projecting (DA-2,4) and PFC-projecting DA identities (DA-7), (Fig. 5 *K* and *N*). To assess potential effects of culturing neurons in contact with their correct targets, we generated fused VM-STR assembloids, where VM and striatal organoids are fused after 16 d of differentiation (35, 36) and analyzed using snRNAseq at day 120 (Fig. 5 *L–O*). We then projected this single-cell dataset from assembloids onto the human DA diversity map obtained via TARGET-seq. As for the VM organoid dataset at day 120, we could identify cells with expression profiles of dlSTR-projecting and PFC-projecting transcriptional profiles (Fig. 5*M* and *SI Appendix*, Fig. S4*I*). Quantifying the cells in each cluster showed that in VM-STR assembloids, the proportion of DA neurons resembling dlSTR-projecting neurons increased compared to VM organoids, while the proportion of PFC-projecting neurons decreased (Fig. 5*O*).

Discussion

The use of hPSCs for cell-based treatments is now well established as a scalable resource to generate DA progenitor cells for transplantation in PD patients (35–37). After extensive and sustained research efforts and preclinical validation, hPSC-based therapies for PD have progressed into clinical trials (38–40). The PSC-based differentiation protocols used today generate cells of both A9 and A10 like identities that innervate all DA targets in the forebrain (35, 41–45). In the future, more refined protocols for precise generation of striatum-innervating DA neurons of A9 identity may be beneficial. An essential step toward this goal is a better molecular definition of A9 identity since current markers do not sufficiently discriminate neurons with the capacity to innervate A9 target structures (19). Emerging data from single-cell analyses conducted on mouse mesencephalon at various developmental stages, as well as human fetal and adult brain tissue, have revealed that the DA neuron compartment comprises a molecularly heterogeneous population of DA neurons with multiple subtypes (10–13, 46). However, these molecular identities are not in full agreement between different studies (10) and have not yet been linked to distinct functions or axonal innervation target regions, nor have they been fully integrated with the traditional division of A9 and A10 DA neurons based on their anatomical location in the mesencephalon and their projection patterns in the brain (2).

Here, we homotopically transplanted hPSC-derived DA progenitors into a DA depletion xenograft model to generate intranigral grafts that go on to exhibit mature molecular features and functional properties. The homotopic placement of DA progenitors in the SNpc allows for their differentiation into mature DA neuron subtypes that project over long distances, reaching typical A9 and A10 target regions in the brain (17, 42). We showed that both fetal and hPSC sources generate the same cell types within the grafts, although in different proportions, with high similarity scores between neuronal clusters, indicating that authentic molecular features of endogenous DA neurons are present in the hPSC-derived grafts. Our subsequent analysis of the neuronal compartment of hPSC-derived grafts revealed a predominant presence of DA neurons that can be further divided into distinct DA subclusters. In contrast, fetal VM tissue gave rise to transplants containing DA neurons as well as a variety of neurons typically formed in the mid/hindbrain region, which includes also serotonergic neurons implicated in causing graft-induced dyskinesias (47–50).

In order to correlate human DA subtypes with their projection and thus inferred function, we developed the TARGET-seq approach that enables a link between the molecular identity and target specificity of single neurons. TARGET-seq makes use of molecular tags injected into the axonal target areas, in this case distinct DA neuron targets in the forebrain, delivered using AAVs designed with retrograde tracing capacity and enriched affinity for DA neurons (MNM008) (22). By employing TARGET-seq we were able to identify distinct molecular profiles of human DA neurons projecting specifically to the dlSTR which is the main A9 target and represents the neurons primarily degenerating in PD, as well as DA neurons projection to the PFC, which is one of the A10 target regions. Through TARGET-seq, we found a significant enrichment of the molecular *mCherry* tag in two distinct clusters, DA-2 and DA-7, and each cluster exhibited distinct molecular profiles. Subcluster DA-2, projecting to the striatum, showed enrichment in *KCNJ6*, *VMAT2*, *VGLUT2*, and *SNCA*, as well as activation of the MAPK pathway. This aligns well with the dataset previously obtained in postmortem human brain tissue (13), where the vulnerable dopamine (DA) neuron cluster is enriched in MAPK pathways. In contrast, subcluster DA-7 was enriched in transcription factors such as *OTX2*, *LMO3*, *NFIB,* and *FOXP2*, with robust activation of WNT pathway signaling. The specific expression of OTX2 and WNT-associated factors in this cluster indicates that the previously described OTX2-WNT regulatory loop controlling A10 neuron specification in mouse VM (51–54) is also conserved in the human brain. There were also 5 DA clusters that were not labeled by injections into dlSTR and PFC, which could be either DA neurons projecting to other A10 target regions such as nucleus accumbens, ventral striatum, septum, amygdala, or DA neurons that have not established appropriate connectivity with host targets and may thus represent immature DA neurons or include profiles not necessarily representative of those found in the human brain.

Pseudotime trajectory analysis subsequently showed that the striatum and PFC-projecting subtypes follow two distinct developmental paths, and we identified GRNs likely to be involved in this process as well as distinct sets of transcription factors that are potential candidates to play a role in DA-subtype fate determination. To further study this, we used CellOracle, where gene-regulatory networks inferred from single-cell data combined with chromatin accessibility data were used to perform in silico transcription factor perturbations simulating the consequent changes in cell identity (23). This approach confirmed the GRN analysis and identified candidate transcription factors regulating A9 and A10 identity. These should be further explored in future studies, with the ultimate goal of guiding hPSC differentiation into specific DA neuron subtypes. The data generated can also be used to map and subsequently assess the degree of maturation and diversity of DA neurons generated within different human stem cell-based models as done here in VM organoids, where we use the TARGET-seq profiles to show that DA neurons with identities resembling subtypes from long-term in vivo grafts progressively emerge in VM organoids over time. Furthermore, by comparing DA neurons in VM organoids with VM-STR assembloids we showed that DA neurons that are formed in the presence with their striatal targets refine their mature A9 molecular identity accordingly, which is in line with previous studies that have highlighted the importance of functional target acquisition on DA subtype specification during development and repair in vivo (42).

In this study, we present a comprehensive single-cell dataset identifying distinct human DA neuron subtypes one year after transplantation in a Parkinson's disease (PD) rat model at the stage when the neurons have functionally matured and reached their final targets in the host brain. By developing TARGET-seq, we could also correlate the molecularly distinct subtypes of human DA neurons with their specific innervation targets in the brain. This is a key advancement and serves as an important bridge between molecular heterogeneity, distinct target innervation, and functional specificity, which carries significant implications for generating disease-relevant subtypes of midbrain DA neurons. Thus, this study provides a valuable resource identifying human DA neuron diversity linked to projection and function for studying and treating PD and neuropsychiatric disorders.

Materials and Methods

Human Fetal Tissue Preparation. Human fetal tissues were collected from 6.5 to 10 wk postconception legally terminated embryos at Malmö Hospital (Malmö, Sweden). Ethical approval for using postmortem human fetal tissue was obtained from the Swedish National Board of Health and Welfare, adhering to established guidelines and informed consent from women seeking abortions. Fetal VM tissue was prepared following approved standard operating procedures (SoPs), consistent with those employed in the clinical TRANSEURO trial.

Human Pluripotent Stem Cell Differentiation. GMP-grade RC17 human embryonic stem cells (hESCs), sourced from Roslin Cells Ltd., underwent thawing and expansion in iPS Brew medium (Miltenyi Biotec, GMP-grade) on laminin-521 (1 $\mu g/cm^2$, Biolamina, cell therapy grade). The differentiation of RC17 hESCs into VM-patterned progenitors involved dual SMAD inhibition for neuralization, GSK3 inhibitor-mediated caudalization, and SHH-mediated ventralization, following the detailed protocol outlined in Nolbrant et al. (55). Transplantation was performed after 16 d of differentiation, utilizing only cell preparations meeting preestablished quality criteria.

Surgical Procedures and Cell Transplantation. Lesion of the nigrostriatal pathway in rats was induced by unilateral injection of 6-hydroxydopamine into the right MFB with a volume of 3 µL at a freebase concentration of 3.5 µg/µL to the following coordinates relative to bregma: A/P −4.4; M/L −1.1; D/V (from dura) −7.8, adjusted to flat head. Drug-induced rotations were assessed 4 wk postlesion (D-amphetamine, 2.5 mg/kg, i.p., Apoteksbolaget, Sweden) for 90Â min in automated rotometer bowls. Rotational data were expressed as net turns per minute. Intranigral cell transplantations were made with a total of 150,000 VM progenitors injected over two deposits (75,000 cells per deposit) to the midbrain at the following coordinates AP: −4.9; ML −2.3; DV −5.5/−6.0; TB flat head.

AAV Generation and Delivery. AAV was generated following established protocols (22, 56). Purified AAVs were quantified using qPCR with primers specific to the WPRE sequence. Viral injections were performed under anesthesia (20:1 mixture of fentanyl citrate and medetomidine hypochloride) with a volume of 5 µL with titers ranging from 6E12 to 1.2E13 genome copies per milliliter to the following coordinates relative to bregma: dlSTR: AP = +1.0; ML = −2.9; DV = −3.9. PFC: AP = +2.5; ML = −0.6; DV = −3.5. The capillary was left in position for two minutes before retraction, following all infusions.

Isolation of Xenografts from the Host Brain and Nuclei Extraction. Rat brains were isolated in aCSF containing 119 mM NaCl, 26 mM $NaHCO_3$, 2.5 mM KCl, 1.25 mM NaH_2PO_4, 2.5 mM $CaCl_2$, 1.3 mM $MgSO_4$, and 25 M glucose. Sections of 350 µm thickness (coronal, amplitude 1.7/1 mm, and velocity 0.20/0.16 mm/sec) were cut. Xenografted tissues were transferred to a glass douncer containing 1 ml of nuclei lysis buffer (0.32 M sucrose; 5 mM $CaCl_2$; 3 mM MgAc; 0.1 mM Na2EDTA; 10 mM Tris-HCl, pH 8.0, 1 mM DTT, 0.1% Triton X) on ice.

Prior to transplantation, the hPSC-derived DA progenitors were transduced with nuclear GFP to facilitate the isolation of the graft for single-nucleus RNA sequencing. Following dissection, nuclei were isolated and filtered, then subjected to centrifugation at 900 g for 15 min at 4 °C. The resulting nuclei pellet was collected and washed three times with a cold wash buffer containing 0.1% BSA and 0.4 U/µl RNase inhibitor. Fluorescence-activated cell sorting (FACS) was employed to purify human nuclei based on GFP expression in the hPSC-derived grafts, effectively separating them from rat nuclei. In contrast, fetal-derived grafts were not transduced and therefore not labeled with GFP. Instead, human fetal nuclei were sorted using DRAQ7™, and distinguished from rat nuclei through bioinformatic analysis.

Single Nucleus RNAseq (Alignment, Processing, and Data Analysis). For snRNA-seq, 7,000–10,000 nuclei per sample with a maximum 45 µl total solution volume were collected for snRNA-seq library generation. Single nuclei were captured using Chromium (10X Genomics, PN-120233), a droplet-based scRNA-seq device, according to the manufacturer's recommendations. Successful library preparation was confirmed by Bioanalyzer (DNA HS kit, Agilent) and sequenced on Illumina NovaSeq 5000 2x 100 bp. Cell Ranger (version 6.0, 10x Genomics) together with a combined human/rat reference (Both version 93 from Ensembl) was used for raw data processing. We used a dual-species alignment strategy to differentiate human and rat cells. Specifically, we aligned the snRNAseq reads to a combined reference genome containing both human (GRCh38) and rat (Rnor_6.0) sequences using STAR aligner as implemented in the cellranger pipeline. Nuclei with >80% reads mapping to the human genome were retained for downstream analysis. Although human nuclei from hPSC-derived grafts were labeled and sorted based on GFP, we still employed a dual-species alignment strategy for both types of samples to differentiate human and rat cells. As expected, the proportion of human nuclei (66%) from hPSC-derived grafts was significantly higher than that from fetal grafts, which were not labeled with GFP (31%). Fetal grafts were analyzed separately and cell types were identified using reference annotation from hPSC grafts coupled with canonical marker analysis. Pathway analysis/GSEA was performed using clusterProfiler (60) or fgsea.

TARGET-seq. For identification of retrograde transported barcodes unmapped reads from the Cell Ranger output was extracted (samtools) and remapped to a hybrid genome mCherry inserted. The DA cohort was identified based on *TH* expression at the transcript level to ensure accurate identification of dopaminergic neurons. Statistical analysis revealed that TH^+ neurons had a significantly higher number of traced neurons compared to non-DA neurons ($p < 0.05$, chi-square test). Seurat (version 4.3, R version 4.2.1) was applied to snRNA-seq data for downstream analysis. Ribosomal protein genes and pseudogenes were excluded from analysis. Nuclei with more than 12,000 or less than 500 detected genes as well as those with a mitochondrial transcript proportion greater than 5% were excluded. Data were dimensionally reduced by principal component analysis (n = 30), embedded (Harmony) and used for graph-based clustering. W manually assigned major cell classes to each cluster using a combination of top differentially expressed genes and canonical markers. Force-directed layout of k-nearest-neighbor graphs was generated using SPRING on normalized expression counts using default settings.

Histology. For immunohistochemistry, the brains were coronally sectioned at 35 µm thickness on a freezing microtome in a 1:8 series. Sections were incubated overnight with primary antibodies in 0.1 M KPBS solution containing 0.25% Triton-X and 5% serum specific to the secondary antibody's species. Subsequently, sections were incubated for 1 h with either fluorophore-conjugated antibodies for fluorescent detection or biotin-coupled antibodies for 3,3'-diaminobenzidine (DAB) detection, all in the same solution. Details and list of antibodies for immunohistochemistry are reported in *SI Appendix*, Table S2.

Microscopy, Image Acquisition, and Quantifications. Images were acquired using various platforms, including a flatbed scanner (Epson Perfection V850 PRO), a Leica DMI6000B widefield microscope, and a Leica TCS SP8 laser scanning confocal microscope. Leica LAS X served as the image acquisition software, Number of TH neurons were counted in all sections of a series using Volocity 6.5.1 (Quorum Technologies). Pictures of hNCAM DAB-stained coronal sections were taken at the level of the striatum using an Epson Perfection V850 PRO scanner. To determine the graft volume, the area of the graft core in every eighth section through the graft was measured using ImageJ (version 2.14.0). The measurements were then multiplied by the distance between each measured section. Calibration was performed by associating the number of pixels with a known measurement obtained from a scale.

Data, Materials, and Software Availability. snRNA-seq data have been deposited in Gene Expression Omnibus (GSE233885) (57).

ACKNOWLEDGMENTS. We thank Ulla Jarl, Jenny G Johansson, and Mikael Sparrenius for excellent technical assistance. This work was supported by funding from the New York Stem Cell Foundation, European Research Council (ERC) under ERC Grant Agreement 771427, European Union–funded project NSC-Reconstruct (European Union, H2020, GA no 874758, 2020-23), Swedish Research Council (M.P. 2021-00661 and A.F. 2022-01432), Swedish Parkinson Foundation (Parkinsonfonden), Swedish Brain Foundation, Knut and Alice Wallenberg Stiftelse (KAW 2018-0040), Novo Nordisk A/S, and the Strategic Research Areas at Lund University MultiPark (Multidisciplinary research in Parkinson's disease) and StemTherapy/Lund Stem Cell Center. We would also like to acknowledge Clinical Genomics Lund, SciLifeLab and Center for Translational Genomics (CTG), Lund University, for providing sequencing service.

Author affiliations: [a]Developmental and Regenerative Neurobiology, Wallenberg Neuroscience Center, Lund Stem Cell Center, Department of Experimental Medical Science, Lund University, Lund, Skåne 223 62, Sweden; and [b]Molecular Neuromodulation, Wallenberg Neuroscience Center, Department of Experimental Medical Science, Lund University, Lund Skåne 223 62, Sweden

Author contributions: A.F., A.B., and M.P. designed research; A.F., P.S., E.S., A.B., S.C., J.K., J.M., J.N., B.M., M.A., and T.B. performed research; P.S. and T.B. contributed new reagents/analytic tools; A.F., P.S., E.S., A.B., J.K., J.M., A.B., and M.P. analyzed data; and A.F., P.S., E.S., and M.P. wrote the paper.

1. A. A. Kehagia, R. A. Barker, T. W. Robbins, Cognitive impairment in Parkinson's disease: The dual syndrome hypothesis. *Neurodegener Dis.* **11**, 79–92 (2013).
2. A. Bjorklund, S. B. Dunnett, Dopamine neuron systems in the brain: An update. *Trends Neurosci.* **30**, 194–202 (2007).
3. O. Garritsen *et al.*, Development, wiring and function of dopamine neuron subtypes. *Nat. Rev. Neurosci.* **24**, 134–152 (2023).
4. S. V. Hegarty, A. M. Sullivan, G. W. O'Keeffe, Midbrain dopaminergic neurons: A review of the molecular circuitry that regulates their development. *Dev. Biol.* **379**, 123–138 (2013).
5. B. R. Bloem, M. S. Okun, C. Klein, Parkinson's disease. *Lancet* **397**, 2284–2303 (2021).
6. L. Panman *et al.*, Sox6 and Otx2 control the specification of substantia nigra and ventral tegmental area dopamine neurons. *Cell Rep.* **8**, 1018–1025 (2014).
7. A. Anderegg, J. F. Poulin, R. Awatramani, Molecular heterogeneity of midbrain dopaminergic neurons – Moving toward single cell resolution. *FEBS Lett.* **589**, 3714–3726 (2015).
8. K. Carmichael *et al.*, Diverse midbrain dopaminergic neuron subtypes and implications for complex clinical symptoms of Parkinson's disease. *Ageing Neurodegener Dis.* **1**, 1–26 (2021).
9. M. Azcorra *et al.*, Unique functional responses differentially map onto genetic subtypes of dopamine neurons. *Nat. Neurosci.* **26**, 1762 (2023).
10. J. F. Poulin *et al.*, Classification of midbrain dopamine neurons using single-cell gene expression profiling approaches. *Trends Neurosci.* **43**, 155–169 (2020).
11. K. Tiklova *et al.*, Single-cell RNA sequencing reveals midbrain dopamine neuron diversity emerging during mouse brain development. *Nat. Commun.* **10**, 581 (2019).
12. G. La Manno *et al.*, Molecular diversity of midbrain development in mouse, human, and stem cells. *Cell* **167**, 566–580.e19 (2016).
13. T. Kamath *et al.*, Single-cell genomic profiling of human dopamine neurons identifies a population that selectively degenerates in Parkinson's disease. *Nat. Neurosci.* **25**, 588 (2022).
14. D. Agarwal *et al.*, A single-cell atlas of the human substantia nigra reveals cell-specific pathways associated with neurological disorders. *Nat. Commun.* **11**, 4183 (2020).
15. M. Birtele *et al.*, Single-cell transcriptional and functional analysis of dopaminergic neurons in organoid-like cultures derived from human fetal midbrain. *Development* **149**, dev200504 (2022).
16. A. Fiorenzano *et al.*, Dopamine neuron diversity: Recent advances and current challenges in human stem cell models and single cell sequencing. *Cells* **10**, 1366 (2021).
17. M. Xiong *et al.*, Human stem cell-derived neurons repair circuits and restore neural function. *Cell Stem. Cell* **28**, 112 (2021).
18. A. F., Adler et al., hESC-derived dopaminergic transplants integrate into basal ganglia circuitry in a preclinical model of Parkinson's disease. *Cell Rep.* **28**, 3462 (2019).
19. S. Grealish *et al.*, Human ESC-derived dopamine neurons show similar preclinical efficacy and potency to fetal neurons when grafted in a rat model of Parkinson's disease. *Cell Stem. Cell* **15**, 653–665 (2014).
20. A. Fiorenzano *et al.*, Single-cell transcriptomics captures features of human midbrain development and dopamine neuron diversity in brain organoids. *Nat. Commun.* **12**, 7302 (2021).
21. P. Aldrin-Kirk *et al.*, A novel two-factor monosynaptic TRIO tracing method for assessment of circuit integration of hESC-derived dopamine transplants. *Stem Cell Rep.* **17**, 159–172 (2022).
22. M. Davidsson *et al.*, A systematic capsid evolution approach performed in vivo for the design of AAV vectors with tailored properties and tropism. *Mol. Ther.* **28**, 74–74 (2020).
23. K. Kamimoto *et al.*, Dissecting cell identity via network inference and in silico gene perturbation. *Nature* **614**, 742 (2023).
24. K. Tiklova *et al.*, Single cell transcriptomics identifies stem cell-derived graft composition in a model of Parkinson's disease. *Nat. Commun.* **11**, 2434 (2020).
25. H. J. R. Fernandes *et al.*, Single-cell transcriptomics of Parkinson's disease human models reveals dopamine neuron-specific stress responses. *Cell Rep.* **33**, 108263 (2020).
26. J. F. Poulin *et al.*, Mapping projections of molecularly defined dopamine neuron subtypes using intersectional genetic approaches. *Nat. Neurosci.* **21**, 1260 (2018).
27. A. Saunders *et al.*, Molecular diversity and specializations among the cells of the adult mouse brain. *Cell* **174**, 1015–1030.e16 (2018).
28. P. W. Hook *et al.*, Single-cell RNA-seq of mouse dopaminergic neurons informs candidate gene selection for sporadic Parkinson disease. *Am. J. Hum. Genet.* **102**, 427–446 (2018).
29. J. F. Poulin *et al.*, Defining midbrain dopaminergic neuron diversity by single-cell gene expression profiling. *Cell Rep.* **9**, 930–943 (2014).
30. V. Cordeddu *et al.*, Mutations in cause Primrose syndrome. *Nat. Genet.* **46**, 815–817 (2014).
31. H. Inoue *et al.*, Inhibition of the leucine-rich repeat protein LINGO-1 enhances survival, structure, and function of dopaminergic neurons in Parkinson's disease models. *Proc. Natl. Acad. Sci. U.S.A.* **104**, 14430–14435 (2007).
32. C. Weinreb, S. Wolock, A. M. Klein, SPRING: A kinetic interface for visualizing high dimensional single-cell expression data. *Bioinformatics* **34**, 1246–1248 (2018).
33. F. Nilsson *et al.*, Single-cell profiling of coding and noncoding genes in human dopamine neuron differentiation. *Cells* **10**, 137 (2021).
34. E. Sozzi *et al.*, Generation of human ventral midbrain organoids derived from pluripotent stem cells. *Curr. Protoc.* **2**, e555 (2022).
35. T. Kikuchi *et al.*, Survival of human induced pluripotent stem cell-derived midbrain dopaminergic neurons in the brain of a primate model of Parkinson's disease. *J. Parkinsons Dis.* **1**, 395–412 (2011).
36. A. Kirkeby *et al.*, Predictive markers guide differentiation to improve graft outcome in clinical translation of hESC-based therapy for Parkinson's disease. *Cell Stem. Cell* **20**, 135–148 (2017).
37. S. Kriks *et al.*, Dopamine neurons derived from human ES cells efficiently engraft in animal models of Parkinson's disease. *Nature* **480**, 547 (2011).
38. A. Kirkeby *et al.*, Preclinical quality, safety, and efficacy of a human embryonic stem cell-derived product for the treatment of Parkinson's disease, STEM-PD. *Cell Stem. Cell* **30**, 1299–1314.e9 (2023).
39. J. Piao *et al.*, Preclinical efficacy and safety of a human embryonic stem cell-derived midbrain dopamine progenitor product, MSK-DA01. *Cell Stem. Cell* **28**, 217–229.e7 (2021).
40. D. Doi *et al.*, Pre-clinical study of induced pluripotent stem cell-derived dopaminergic progenitor cells for Parkinson's disease. *Nat. Commun.* **11**, 3369 (2020).
41. M. Maimaitili *et al.*, Enhanced production of mesencephalic dopaminergic neurons from lineage-restricted human undifferentiated stem cells. *Nat. Commun.* **14**, 7871 (2023).
42. N. Moriarty *et al.*, A combined cell and gene therapy approach for homotopic reconstruction of midbrain dopamine pathways using human pluripotent stem cells. *Cell Stem. Cell* **29**, 434 (2022).
43. Z. Alekseenko *et al.*, Robust derivation of transplantable dopamine neurons from human pluripotent stem cells by timed retinoic acid delivery. *Nat. Commun.* **13**, 3046 (2022).
44. T. W. Kim *et al.*, Biphasic activation of WNT signaling facilitates the derivation of midbrain dopamine neurons from hESCs for translational use. *Cell Stem. Cell* **28**, 343 (2021).
45. A. Morizane, Cell therapy for Parkinson's disease with induced pluripotent stem cells. *Inflamm Regen* **43**, 16 (2023).
46. S. Smajic *et al.*, Single-cell sequencing of human midbrain reveals glial activation and a Parkinson-specific neuronal state. *Brain* **145**, 964–978 (2022).
47. C. R. Freed *et al.*, Transplantation of embryonic dopamine neurons for severe Parkinson's disease. *N. Engl. J. Med.* **344**, 710–719 (2001).
48. I. Mendez *et al.*, Cell type analysis of functional fetal dopamine cell suspension transplants in the striatum and substantia nigra of patients with Parkinson's disease. *Brain* **128**, 1498–1510 (2005).
49. C. W. Olanow *et al.*, A double-blind controlled trial of bilateral fetal nigral transplantation in Parkinson's disease. *Ann. Neurol.* **54**, 403–414 (2003).
50. R. A. Barker, T. Consortium, Designing stem-cell-based dopamine Cell Rep.lacement trials for Parkinson's disease. *Nat. Med.* **25**, 1045–1053 (2019).
51. E. Arenas, Wnt signaling in midbrain dopaminergic neuron development and regenerative medicine for Parkinson's disease. *J. Mol. Cell Biol.* **6**, 42–53 (2014).
52. M. Di Salvio *et al.*, Otx2 controls neuron subtype identity in ventral tegmental area and antagonizes vulnerability to MPTP. *Nat. Neurosci.* **13**, 1481–1488 (2010).
53. L. G. Di Giovannantonio *et al.*, Otx2 selectively controls the neurogenesis of specific neuronal subtypes of the ventral tegmental area and compensates En1-dependent neuronal loss and MPTP vulnerability. *Dev. Biol.* **373**, 176–183 (2013).
54. N. Prakash, W. Wurst, Genetic networks controlling the development of midbrain dopaminergic neurons. *J. Physiol.* **575**, 403–410 (2006).
55. S. Nolbrant *et al.*, Generation of high-purity human ventral midbrain dopaminergic progenitors for in vitro maturation and intracerebral transplantation. *Nat. Protoc.* **12**, 1962–1979 (2017).
56. M. Negrini *et al.*, AAV production everywhere: A simple, fast, and reliable protocol for in-house AAV vector production based on chloroform extraction. *Curr. Protoc. Neurosci* **93**, e103 (2020).
57. P. Storm, M. Parmar, A. Fiorenzano, Data from "Single cell sequencing and retrograde barcode tracing reveal human DA neuron identities based on projection patterns in stem cell-derived grafts." Gene Expression Omnibus.https://www.ncbi.nlm.nih.gov/geo/query/acc.cgi?acc=GSE233885. Deposited 1 June 2023.

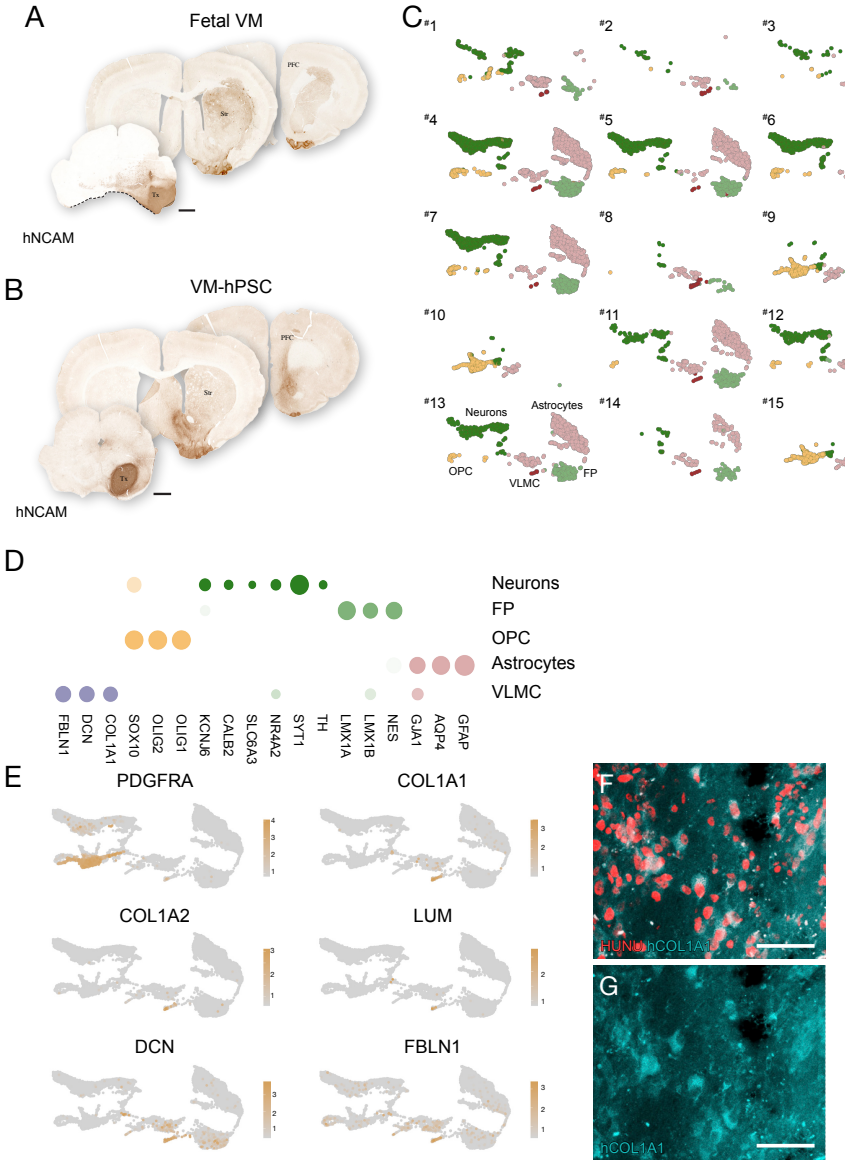

Supplementary Figure 1

A, DAB-developed sections displaying an overview of hNCAM+ fibers from fetal and **B,** VM-patterned hPSC intranigral grafts innervating the host brain. Scale bars 1 mm. **C,** Uniform manifold approximation and projection (UMAP) embeddings showing clusters identified using the Leiden algorithm of individual fetal VM-derived intranigral grafts 12 months post-transplantation. Cell-type assignments are indicated. **D,** Dot plot displaying expression levels of indicated genes in each cluster. **E,** Expression levels of indicated VLMC-associated genes visualized in the UMAP space. F,G, Immunohistochemistry of HUNU/hCOL1A1 in human fetal intranigral graft 12 months posttransplantation. Scale bars 50 µM.

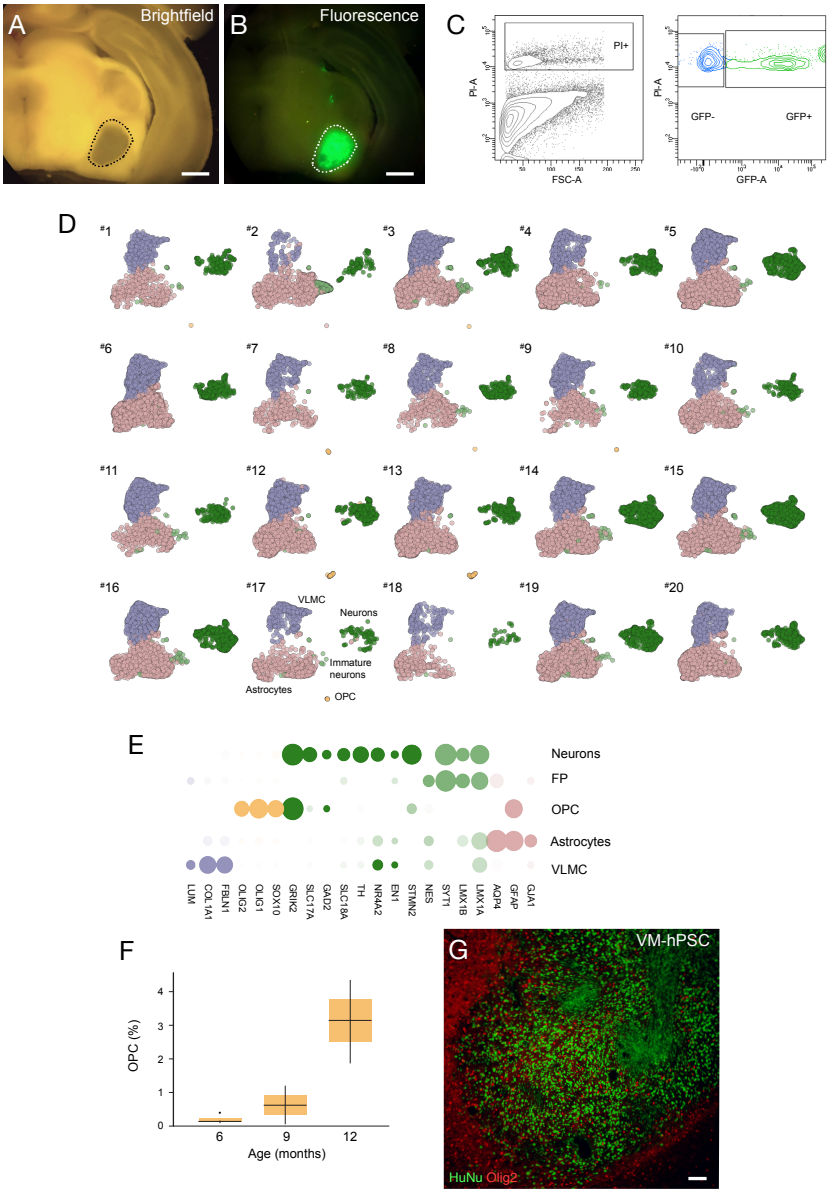

Supplementary Figure 2

A, Bright filed and, **B,** nuclear GFP expression images of live brain before intranigral graft dissection. Scale bars 1 mm **C,** FACS strategy for sorting of the single nuclei based on GFP expression. **D,** UMAP embeddings showing clustering of analyzed cells from VM-patterned hPSC intranigral grafts 12 months post-transplantation. Cell-type assignments are indicated. **E,** Dot plot showing expression levels of indicated genes in each cluster. **F,** Boxplot showing proportion of OPCs at 6 to 12 months after transplantation of human fetal VM tissue. **G,** Immunohistochemistry of HUNU/OLIG2 in VMpatterned hPSC intranigral grafts 12 months post-transplantation. Scale bar 100 µM.

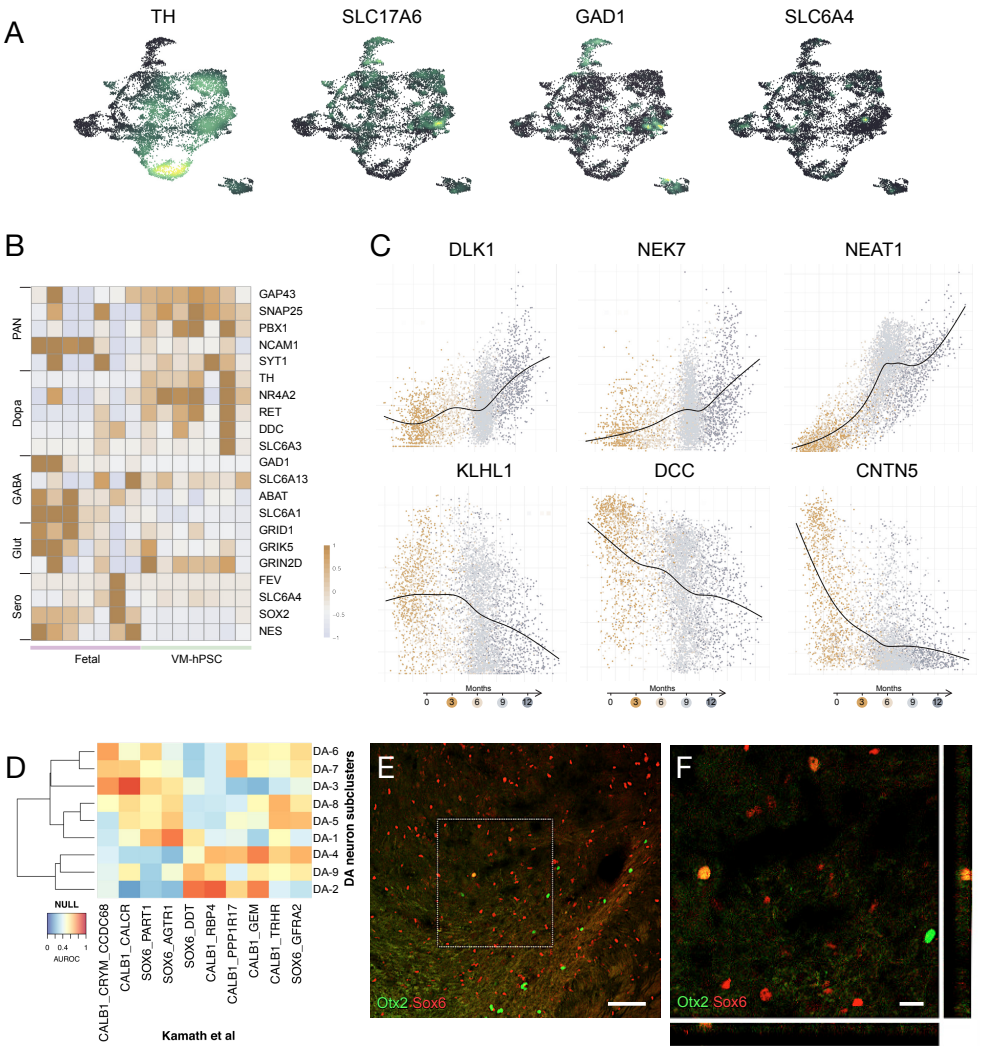

Supplementary Figure 3

A, Density plots visualizing specific gene expression across neuron sub-clusters. Colors indicated expression level. **B,** Heatmap showing the expression levels of the indicated genes in each neuron cluster from VM-patterned hPSC grafts alongside fetal-VM graft. **C,** Identified up- and downregulated DA neuron markers along a pseudotemporal axis during VM-patterned hPSC transplantation. Line indicates mean expression level. **D,** Heatmap of area under the curve receiver operating characteristics (AUROC) scores comparing the similarity after integration of post-mortem brain tissue (columns, Kamath et al., 2022) and VM-patterned hPSC intranigral graft DA neuron clusters (rows). **E, F,** Immunohistochemistry of OTX2/SOX6 in VM-patterned hPSC intranigral grafts 12 months posttransplantation. Scale bar 200 µM.

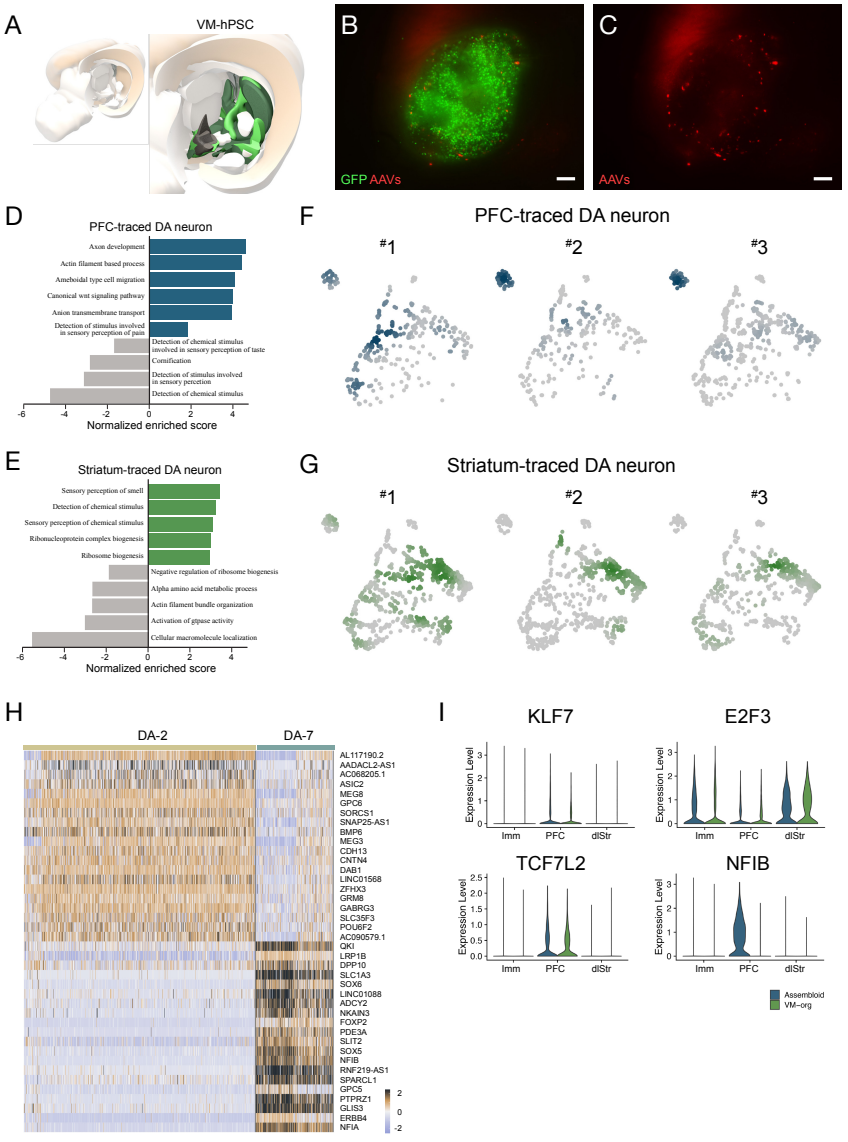

Supplementary Figure 4

A, 3D representation of graft fiber outgrowth, based on the extent of hNCAM immunohistochemistry staining for 1 year-old graft placed in the nigra of 6-OHDA lesioned rats (cumulative data from n = 10 animals). **B, C,** Live image of 1-year intranigral grafts showing GFP expression and mCherry AAV detection before graft dissection. Scale bar 100 µM. **D,** Gene ontology enrichment analysis of PFC- and **E,** dlSTR-projected DA neuron clusters. **F,** Cell density plots of PFC- and **G,** dlSTR-projected DA neurons in the UMAP space from 3 independent 1-year-old grafts. **H,** Heatmap of differentially expressed genes between PFC- and dlSTR-projected DA neuron clusters. **I,** Violin plots depicting the normalized expression levels of KLF7, E2F3, TCF7L2, and NFIB across different neuronal identities (immature, PFC and, dlStr) in VM-org and assembloids.

EDOARDO SOZZI obtained his bachelor's degree in Biotechnology from the University of Pisa in 2018, where he investigated the differentiation of murine stem cells into cortical neurons. Inspired by a research experience at Cambridge University, he pursued a master's degree in Neuroscience at the University of Pisa and Scuola Normale Superiore, focusing on the development of human brain organoids. In 2020, Edoardo began his PhD in Developmental Neurobiology under Prof. Malin Parmar at Lund University. His research explores human dopaminergic neuron development, diversity, and application in cell replacement therapies for Parkinson's Disease, leveraging advanced stem cell systems, including organoids and transplantation models.

Printed by Exakta printing AB, Malmö, Sweden

Doctoral Dissertation Series 2025:12
ISBN 978-91-8021-665-4
ISSN 1652-8220

LUND UNIVERSITY
Faculty of Medicine